

**Pulsed Laser Deposition and Characterisation of Rare
Earth Doped Glass-polymer Optical Materials**

Zhanxiang Zhao

Submitted in accordance with the requirements for the degree
of Doctor of Philosophy



The University of Leeds
School of Process, Environmental and Materials Engineering

July, 2012

The candidate confirms that the work submitted is her own, except where work which has formed part of jointly-authored publications has been included. The contribution of the candidate and the other authors to this work has been explicitly indicated below. The candidate confirms that appropriate credit has been given within the thesis where reference has been made to the work of others.

Most of the results that shown in the papers were obtained by the author of the thesis, and the results that obtained by the other people has been stated in the papers. The author of the thesis also wrote the draft of the papers. The supervisors offered the general idea of this research and also revised all the papers before publicated. All the other authors did some revision submitted.

© 2012 The University of Leeds and Zhanxiang Zhao

Acknowledgements

I would like to devote my sincere gratitude to many individuals who helped me on my study in these three years. First of all, I fully acknowledge my primary supervisor, Prof. Animesh Jha, who brought me to this fantastic optical materials research area and gave me a continuous support for my study. It was a very precious experience to work with Prof. Animesh Jha and learnt valuable academic skills from his instructions. My thanks also go to my co-supervisors Dr. Gin Jose and Dr. Paul Steenson, who trained and instructed me directly on the experiments and academic writing, including this thesis writing. Whenever I met problems, they were there to help me out. Without all the supervisors' guidance, it is impossible for me to finish this work smoothly. I would also like to acknowledge Dr Andy Brown and Dr Tom Brown to be my examiners.

Besides, I would like to thank the lab support staff Mr Mo Javed and research fellow Dr Billy Richards who were very supportive on the experimental instruments and the trainings. I would also like to acknowledge Mr John Smith, Dr Michael Ward, Dr. Richards Walshaw and Dr Timothy Comyn for their help of TEM measurement, SEM training and XRR measurements, respectively. I also would like to show my appreciation to my friends and also my colleagues, these are Mr Mehrdad Irannejad who helped me a lot in the whole study period, Dr Toney T. Fernandez for the help of waveguide writing, Miss Fangyuan Zhu for the help of XRD measurements. I also would like to offer my thanks to the senior laboratory staff Mrs Diane Cochrane and all the secretaries in the department for their continuous assistant.

Finally, I would like to devote this thesis to my whole family as a gift for all their love, especially my husband, Wenfei Wang. Without their encouragements and unconditional supports, I cannot imagine running out these three tough years and finishing my thesis.

I would like to acknowledge RCUK Basic Technology Project for the financial support of this research and the studentship.

Abstract

Tellurite glass is well known for its excellent optical properties in the application of optical fiber and planar waveguide devices, particularly for optical amplifiers. This thesis is focused on the design, fabrication and characterisation of tellurite glass in both bulk and thin films (glass, glass and polymer thin films) used as optical materials. It consists of four major parts, including the fabrication and characterisation of rare earth doped tungsten lanthanum modified tellurite (TWL) glasses, TWL glass thin films, glass and polymer composite thin films as well as the fabrication of channel waveguide structures on the surface of thin films.

One of the main objectives of this research is to engineer rare earth doped glass and polymer composite thin films using pulsed laser deposition (PLD). Thin films are the main form of the prototype for planar devices. Two dissimilar materials with comparable refractive indices have been deposited alternatively to obtain a periodic layer by layer structures using PLD. These two materials, namely, phosphate modified tellurite (PT) glass and siloxane polymer (PDMS), are both excellent optical materials with low propagation loss at the optical communication window. One of the merits of PT-polymer composite is that it could combine the advantages of the good characteristics of both PT glass and siloxane polymer as optical materials. The success of this fabrication opens a door to engineering composite thin films using a simple and low cost technique with a precise control.

The second objective of this research is to fabricate rare earth doped tungsten and lanthanum modified tellurite (TWL) glass thin films on polymer coated silica to produce another kind of glass-polymer composite. The TWL glass has a significantly different refractive index to siloxane polymer. It is not suitable for fabricating multilayer thin films. Here, dual layer composite thin films were produced by depositing rare earth doped TWL glass onto polymer coated silica substrate using PLD.

Furthermore, to optimize the composition of rare earth doped TWL glass and the deposition parameters of the fabrication of TWL glass thin films, a series of rare

earth doped TWL glasses and series of TWL glass thin films on silica were produced and characterized in detail.

Finally, to study the feasibility of making optical devices on these thin films, reactive ion etching (RIE) and fs laser micromachining techniques were utilized to create a ridge waveguide which is the primary structure of optical amplifiers. The SEM images of the ridge waveguide and depths of the waveguides were studied. In addition, the mode profile and propagation loss of the ridge waveguide obtained using fs laser micromachining were investigated.

Contents

Abstract	I
Contents.....	III
List of Figures.....	VII
List of Tables.....	XIV
List of Abbreviations and Symbols	XVI
List of Publications	XIX
Chapter 1 Introduction	1
1.1 Overview	1
1.2 Materials for planar optical amplifiers	2
1.3 Objectives and scope of the thesis	4
1.3.1 Objectives	4
1.3.2 Scope of the thesis.....	4
Chapter 2 Literature review.....	6
2.1 Waveguide optical amplifiers	6
2.1.1 History and development.....	6
2.1.2 Advantages and disadvantages.....	8
2.1.3 Working principles and applications of optical amplifiers.....	9
2.2 Rare earth ions in glasses.....	10
2.2.1 Atomic physics of rare earth ions.....	10
2.2.2 Radiative transitions	12
2.2.3 Nonradiative transition	16
2.3 Tellurite glass and tellurite glass thin film	19
2.3.1 Tellurite glass	19
2.3.2 Tellurite glass thin films	26
2.4 Polymer and polymer-glass composite thin films.....	27

2.4.1 Optical polymer materials.....	28
2.4.2 Glass and polymer composite thin films	30
2.5 Techniques for thin film fabrication.....	33
2.5.1 Chemical vapor deposition	33
2.5.2 Sol-gel coatings	35
2.5.3 Spin coating.....	36
2.5.4 Thermal evaporation.....	37
2.5.5 Molecular beam epitaxy.....	39
2.5.6 Sputter deposition.....	41
2.5.7 Pulsed laser ablation	43
2.6 Techniques for waveguide fabrication	47
2.6.1 Photolithography	47
2.6.2 Wet etching	48
2.6.3 Embossing.....	49
2.6.4 Electron beam direct writing.....	51
2.6.4 Reactive ion etching	52
2.6.5 Laser micromachining	55
2.7 Summary.....	59
Chapter 3 Fabrication and characterisation of tellurite glass	60
3.1 Experimental design for glass melting and fabrication.....	60
3.1.1 Raw materials and compositions of the glasses	60
3.1.2 Glass melting process	61
3.2 Results of glass characterisations.....	63
3.2.1 Density measurement	63
3.2.2 Thermal analysis.....	64
3.2.3 Optical properties	70
3.2.4 Structural analysis	94

3.3 Discussion of glasses for thin film fabrication	100
3.3.1 The role of Yb ³⁺ and Ce ³⁺ codoping.....	100
3.3.2 Structural analysis	101
3.4 Conclusions.....	105
Chapter 4 Fabrication and characterisation of tellurite glass thin film on silica substrate.....	107
4.1 SEM and XRD techniques for thin film investigation	108
4.1.1 SEM-Energy dispersive X-Ray (SEM-EDX)	108
4.1.2 XRD.....	111
4.2 Optimization of the parameters for tellurite glass thin film fabricated on silica substrate.....	113
4.2.1 Laser fluence optimization.....	113
4.2.2 Optimization of the O ₂ pressure	115
4.2.3 Temperature optimization.....	117
4.3 Results and discussions of the thin films obtained at optimal conditions	120
4.3.1 Optical properties	120
4.3.2 Topography	123
4.3.3 Structure and composition analysis.....	124
4.4 Conclusions.....	127
Chapter 5 Fabrication and characterisation of composite thin films	129
5.1 Transmission electron microscopy (TEM).....	130
5.1.1 Sample preparation.....	130
5.1.2 FEG-TEM measurement.....	132
5.2 Fabrication and characterisation of tellurite glass thin films on polymer coated silica substrates	134
5.2.1 Fabrication of tellurite glass thin films on polymer coated silica substrates	135

5.2.2. Results and discussions of tellurite glass thin film on polymer coated silica substrate.....	135
5.3 Fabrication and characterisation of PT glass and polymer composite thin film on silica	138
5.3.1 Fabrication of PT glass and polymer composite thin film on silica	139
5.3.2 Results and discussions of composite thin film	140
5.4 Conclusions.....	150
Chapter 6 Fabrication of ridge waveguides.....	153
6.1 Fabrication of ridge waveguides on tellurite thin films on silica.....	155
6.2 Fabrication of ridge waveguides on composite thin films.....	159
6.3 Conclusions.....	165
Chapter 7 Conclusions and future work.....	167
7.1 Conclusions.....	167
7.1.1 Tellurite glasses	167
7.1.2 Tellurite glass thin films	168
7.1.3 Glass and polymer composite thin films	169
7.1.4 Channel waveguides on composite thin films.....	170
7.2 Future work.....	171
7.2.1 $\text{Er}^{3+}/\text{Yb}^{3+}/\text{Ce}^{3+}$ triply doped TWL glasses	171
7.2.2 TWL glass thin film on silica substrate and polymer coated silica substrate.....	172
7.2.3 Channel waveguides on glass-polymer composite thin films.....	172
Chapter 8 Appendix	173
8.1 Optical gain.....	173
8.2 Judd-Ofelt theory	174
References	177

List of Figures

Figure 2-1 The process of waveguide fabrication[37], (1) substrate, (2) coating cladding layer,(3) core layer on cladding material with a mask layer protection, (4) after exposure to the UV light, (5) after etching, (5) coating top cladding layer	8
Figure 2-2 The stimulated emission process of the rare earth ions. Dashed line represent process that will happen, solid line means process that really happen, empty dot is the position that ions stayed before emission, black filled dot is the excited ions.....	9
Figure 2-3 The schematic of the amplification of light signal	10
Figure 2-4 Schematic of the energy splitting of 4fN electrons under the perturbation of atomic interaction and crystal field environment [38].....	12
Figure 2-5 The schematic of (a) up-conversion and (b) cross relaxation processes. Dashed line represent process that will happen, solid line means process that really happen, empty dot is the position that ions stayed before energy transfer, black filled dot is the excited ions.....	19
Figure 2-6 The calculated configuration of the groups related to TeO_2 in tellurite glass. Large circles are Te atoms, small circle are O atoms.(a) fourfold coordinated Te atom, TeO_4 in tellurite glass, enclosed in the dash line is the TeO_4 structural unit. (b) Threefold coordinated Te atom, $\text{O}=\text{TeO}_2$, in tellurite glass, O_n is nonbridging oxygen, O_b is bridging oxygen between $\text{O}=\text{TeO}_2$ and TeO_4 units, enclosed in the dash line is the $\text{O}=\text{TeO}_2$ structural unit[80].....	23
Figure 2-7 The calculated configuration of groups related to WO_3 in tellurite glass, large circles are Te atom, middle circles are W atmos, small circles are O atoms. (a) The single sixfold coordinated W atom, $\text{O}=\text{WO}_5$, in tunstate-tellurite glass, O_n is nonbridging oxygen, O_b is bridging oxygen between $\text{O}=\text{WO}_5$ and TeO_4 units, enclosed in the dash line is the $\text{O}=\text{WO}_5$ structural unit; (b) The paired sixfold coordinated W atom, $2(\text{O}=\text{WO}_5)$, in tunstate-tellurite glass, O_n is nonbridging oxygen, O_b is bridging oxygen between $2(\text{O}=\text{WO}_5)$ and TeO_4 units, enclosed in the dash line is the $2(\text{O}=\text{WO}_5)$ structural units [80].....	24
Figure 2-8 The equilibrium phase diagram for the TeO_2 – WO_3 system[81], red dotted line represents the phase transition with temperature when the concentration of WO_3 is 17mol%.....	25

Figure 2-9 The glass-forming region of $\text{TeO}_2\text{-WO}_3\text{-K}_2\text{O}$ system [82]. (○) glass	25
Figure 2-10 The schematic setup of chemical vapor deposition [142].....	34
Figure 2-11 The schematic setup of the dip sol-gel coating process[155]. Processes (a) drawing, (b) chemical reaction, (c) baking.	36
Figure 2-12 The schematic process of the spin coating process [158]. Step 1, put substrate on the chuck, turn on the vacuum, and put solution on the substrate, step 2, leave for a while to obtain a smooth liquid surface, step 3, turn on the machine, rotate the substrate to get thin film	37
Figure 2-13 The thermal evaporation process: ES: evaporation source; S: substrate; H: heater; EB: electron beam [139]......	38
Figure 2-14 Various thermal evaporation sources. a: the crucible source with external tungsten soil heater; b to e: coil heater used for evaporation of metal wires, a dimple tungsten boat used for shot or powders, a chromium rod and a specialized source for evaporation of SiO_2 ; f:the tungsten boat used for metal shot or powder[141]......	39
Figure 2-15 The schematic setup of a MBE system [130].....	40
Figure 2-16 Diagram of sputtering process represent sputtered atoms[139], represent incident ions. Due to the ion implant phenomenon, there are some gas ions in the deposited films.	41
Figure 2-17 The schematic setup of the sputtering system [141].....	42
Figure 2-18 The schematic setup of PLD system.....	44
Figure 2-19 The schematic of the photoresist behaviour[186].....	47
Figure 2-20 The schematic process of anisotropic wet etching: (a) isotropic, (b) partially anisotropic and (c) completely anisotropic[187].	49
Figure 2-21 The schematic process of fabricating a waveguide using the embossing technique[190]. (a) a glass fiber used as an embossing die; (b) embossing the groove; (c) the embossed groove ready for filling; (d) a filled groove forming the final waveguide structure.	50
Figure 2-22 Schematic of the embossing process at room temperature[191]. (a), schematic embossing apparatus, Dip coated film F on substrate S is pressed against the blazed master grating M, (b) embossing grating: γ , blaze angle, Λ , grating period	51
Figure 2-23 Schematic setup of the electron beam writing system [194].....	52
Figure 2-24 Schematic of RIE working system[201]	54

Figure 2-25 The phenomena in the reactive ions etching process[200]: (a), ion bombardment; (b) pure chemical reaction; (c) chemical reaction; (d) chemical process.....	54
Figure 2-26 The schematic setup of the laser direct writing system [209].....	56
Figure 2-27 The comparison of the micromachining result on the metal (a) using nanosecond laser (b) using fs laser[215].....	57
Figure 3-1 The Schematic process of glass preparation	62
Figure 3-2 The tools used for the glass melting and glass obtained after polishing. 1. Mortar; 2. Glass mould; 3. Alumina crucible; 4. Glass after polishing.....	62
Figure 3-3 Schematic of the pycnometer: 1. sample chamber, 2. fill valve indicator, 3. expansion valve indicator, 4. expansion chamber, 5. vent valve indicator.....	63
Figure 3-4 Setup of the DTA instrument. 1, purge tube, 2 and 3 are thermocouples for sample (left) and reference (right), respectively, and 4, protection tube.....	65
Figure 3-5 DTA curves of the TWL1, TWL4, TWL6 in (a),(b),(c), respectively.....	67
Figure 3-6 The schematic of the component in the DMA 7 for the thermal expansion coefficient measurement	69
Figure 3-7 Coefficient of thermal expansion curve of the tellurite glass	70
Figure 3-8 Schematic setup of the FTIR system	72
Figure 3-9 Schematic setup of the interferometer in the IR spectrometer system	72
Figure 3-10 Schematic setup of the UV/VIS/IR spectrometer.....	73
Figure 3-11 Schematic of a monochromator. A: light source, B and F: slit, D: rotatable grating, C and E: mirrors	74
Figure 3-12 The schematic of the total internal reflection. α increases slowly, and when $\alpha=\theta_c$, all light beam is reflected and θ_c is the critical angle. The angle between black light and normal line is θ_c	75
Figure 3-13 The schematic setup of the prism coupler.....	76
Figure 3-14 Energy transition schematic in a fluorescence process, S1 and S2 are excited states.....	77
Figure 3-15 The schematic of the fluorescence spectrometer.....	78
Figure 3-16 IR Cutoff edge of the glasses with different dopants.....	79
Figure 3-17 Dependence of $\ln\alpha$ on absorption frequency ν . Point line is the experiment result, and solid line with the same colour is the fitting line. (To make	

the figure more clear, curves of glass TWL2 and TWL4 which have similar composition as glass TWL3 are hidden.).....	80
Figure 3-18 UV/VIS/NIR absorption coefficient of the glasses from TWL1 to TWL6 , the inset figure is the UV/VIS/NIR absorption of the glasses TWL0	81
Figure 3-19 The short wavelength absorption of glasses TWL0, TWL1, and TWL4-TWL6	83
Figure 3-20 Dependence of $\ln\alpha$ on photon energy $h\nu$ for rare earth doped tellurite glasses TWL0-TWL6. Solid lines are the fitting curves.....	83
Figure 3-21 Dependence of $(\alpha h\nu)^{1/2}$ on photon energy $h\nu$ for rare earth doped tellurite glasses TWL0-TWL6. Solid lines are the fitting curves.....	84
Figure 3-22 The fitting curve of refractive index of TWL glasses, solid lines are the fitting curves	85
Figure 3-23 The fluorescence around 1535nm and the bandwidth of the glasses.....	88
Figure 3-24 Up-conversion spectra of the glasses doped with different rare earth ions	93
Figure 3-25 Schematic energy level diagram of Er^{3+} , Yb^{3+} and Ce^{3+} ions. The energy transfer processes between these ions were also depicted	93
Figure 3-26 Schematic of light scattering	96
Figure 3-27 Schematic of Raman spectrometer	96
Figure 3-28 FTIR absorption spectroscopy of the glasses measured using reflection mode.....	97
Figure 3-29 Raman spectra with deconvolution of undoped TWL glasses	99
Figure 3-30 The schematic of the structural units of TeO_4 and TeO_3 [79, 80]. Bond lengths in TeO_4 : $\text{Te}-\text{O}_1 = \text{Te}-\text{O}_4 > 0.20$ nm, $\text{Te}-\text{O}_2 = \text{Te}-\text{O}_3 < 0.20$ nm; Bond lengths in TeO_3 : $\text{Te}-\text{O}_1$ and $\text{Te}-\text{O}_2 < 0.20$ nm $\text{Te}-\text{O}_3 = 0.20$ nm.....	102
Figure 3-31 The schematic of structural unit WO_6 [78, 80]. Black circle represents W atom, grey circles represent oxygen atoms. Bond length $\text{W}-\text{O}_1 < 0.20$ nm, $\text{W}-\text{O}_2 = \text{W}-\text{O}_3 = \text{W}-\text{O}_4 = \text{W}-\text{O}_5 > 0.20$ nm, $\text{W}-\text{O}_6 > 0.20$ nm.	103
Figure 3-32 Schematic of local structure of TWL glasses. Blue circles represent Te atoms, grey circles represent oxygen atoms, and black circles represent W atoms.	105
Figure 4-1 The schematic of the SEM system [264].	110
Figure 4-2 The schematic of electron interaction volume, depth for secondary electrons: 5-50 nm, backscattered electrons: 500-1000 nm, X-ray: 1-2 μm	111

Figure 4-3 (a) The schematic of the X-ray production. From inner orbit to outer orbit: nuclear, 1s, 2s, sp, 3p. (b) Schematic for derivation of Bragg's law	112
Figure 4-4 The transparencies of the thin films on silica substrate prepared using different laser energy	114
Figure 4-5 Images of thin films on silica substrate deposited at 300 °C (a) the images at low magnification (b) image of the area between the cracks at high magnification	115
Figure 4-6 SEM images of the samples deposited using various O ₂ pressure in the range of 120-160 mTorr	116
Figure 4-7 Transparencies of thin films deposited on silica substrate using various O ₂ pressures in the range of 120-160 mTorr	116
Figure 4-8 SEM images of films deposited at different substrate temperatures, and other conditions are shown in Table 4-3. Inset image in right top picture is the same sample at higher magnification. (a) 50 °C, (b) 100 °C, (c) 120 °C. (d) 300 °C	118
Figure 4-9. SEM images of film prepared at 300 °C and cooling down with rate of 0.5 °C/min when deposition finished, other deposition conditions are shown in Table 4-3, (a) low magnification, (b) high magnification	119
Figure 4-10 Transmittences of films deposited on silica substrate at different temperatures with other deposition conditions shown in Table 4-3.	119
Figure 4-11 Optical transmittance spectra of the TWL glass thin films deposited using 193 nm laser on silica substrates at 100 °C and 300 °C in the range of 350 nm to 2500 nm.	121
Figure 4-12 The room temperature PL spectra of the TWL thin films deposited on silica substrate using 193 nm laser at 100 °C (solid) and 300 °C (dashed), all the other deposition conditions are listed in Table 4-3.	122
Figure 4-13 The OH absorption peak in the TWL thin film deposited using PLD and bulk glass.	123
Figure 4-14 SEM images of thin films deposited on silica substrate using 193 nm laser at (a) 100 °C, (b) 300 °C.	124
Figure 4-15 Comparison of the Raman spectra of undoped TWL glass and undoped TWL glass film deposited on silica substrate at 100 °C, red lines are deconvolution peaks based on Raman spectrum of TWL glass.	125

Figure 4-16 XRD of samples: (a) target glass, (b) glass film on silica deposited at 100 °C, (c) glass film on silica deposited at 300 °C.....	127
Figure 5-1 Schematic of LMIS and FIB setup[274].....	131
Figure 5-2 TEM Sample preparation process using FIB. (a) choose a thin slice by removing the material around it, (b) take the thin slice out using the micromanipulation, (c) the thin slice on the sample grid (d) the final thin sample	132
Figure 5-3 Schematic of TEM system [275].....	134
Figure 5-4 SEM images of TWL glass thin films on polymer substrates: a) at 100 °C in O ₂ gas, b) at 100 °C in a gas mixture of 96 vol% O ₂ and 4 vol% He.	136
Figure 5-5 UV-visible-NIR transmittance spectra of the TWL glass thin films deposited in pure oxygen and oxygen/He mixtures on PDMS coated silica substrates	137
Figure 5-6 Room temperature PL spectra of TWL glass films, deposited at 100 °C on PDMS coated silica substrates in O ₂ and O ₂ /He atmospheres.	138
Figure 5-7 TEM images of a cross section of the superlattice thin film fabricated using at, a) lower magnification and b) higher magnification. (c) image showing particle diffusion between layers, deposition conditions: laser fluence 0.4 J/cm ² , substrate temperature 100 °C, background gas pressure 5 mTorr, laser repetition rate 20 Hz.....	143
Figure 5-8 Interlayer intensity profile of composite thin film layers thick extracted using Image J software.....	143
Figure 5-9 High resolution SEM image of the surface of the PT glass-polymer composite thin film	144
Figure 5-10(a) The X-ray reflectivity (XRR) curve of the superlattice thin film, (<i>inset</i> : the XRR curves for polymer film (black), PT glass film (red) and composite film with 10 deposition cycles(blue) depicting the shift in the absorption edge), (b) the TEM images of the cross-section of the same film	145
Figure 5-11 (a) HAADF images of thin films (b) Si X-ray mapping images in the composite thin film, white dots	146
Figure 5-12 Diffraction pattern of PT glass-polymer composite thin films measured using TEM.....	146
Figure 5-13 XRD curve of PT glass and polymer composite thin film.....	147

Figure 5-14 FTIR spectra of bulk polymer (black), target glass (red), glass-polymer composite thin film (blue) recorded using the reflection mode.	148
Figure 5-15 The optical transmittance of the glass only (black) and composite (red) thin film from 350 nm to 2200 nm	149
Figure 5-16 M-line spectra of the glass only and composite thin film on silicate substrate.....	150
Figure 5-17 The fluorescence spectra of the $\text{Er}^{3+}: {}^4\text{I}_{13/2} \rightarrow {}^4\text{I}_{15/2}$ transition in the PT glass, glass film and composite films	150
Figure 6-1 The schematic of three layer planar waveguides[297]	154
Figure 6-2 The mode profiles for TE ₀ (single mode) and TE ₁ (double modes) [298]	155
Figure 6-3 SEM images of channel waveguide on the tellurite glass thin film fabricated using RIE. Etching conditions are listed as 1-1 in Table 6-2.....	159
Figure 6-4 The picture of fs laser writing system.....	160
Figure 6-5 SEM images of channel waveguide structures on the composite thin film obtained in No.1 experiments (a) 4 μJ , 4 mm/s (b) 5 μJ from left to right: 0.1 mm/s, 0.5, 1, 1.5, 2, 4 mm/s, (c) 7 μJ , from the second one left to right: 0.1 mm/s, 0.5, 1, 1.5, 2, 4 mm/s, (d) 8 μJ 1mm/s.....	162
Figure 6-6 Localized pore formation along the laser beam scan direction.....	162
Figure 6-7 SEM images of waveguide structure on composite thin film obtained in No. 2 experiments. (a) 7 μJ 3 mm/s, (b) 7 μJ 4 mm/s, (c) 8 μJ 3 mm/s, (d) 8 μJ 4 mm/s.....	163
Figure 6-8 Raman spectra of composite thin film trench of ablated area with double scan of fs laser and silica substrate.....	163
Figure 6-9 Correlation between width of trench area and writing parameters, blue bars represent.....	164
Figure 6-10 SEM image of waveguides used for light propagation.....	164
Figure 6-11 Mode profile of channel waveguides with 18 μm width and 11 mm length.....	165
Figure 8-1 The schematic of the experimental setup of the gain measurement with an optical spectrum analyzer[38]	174

List of Tables

Table 2-1 The intensity parameters of Ωt for different glass hosts	14
Table 2-2 Spectroscopic properties of Er^{3+} doped glass in different hosts.....	26
Table 2-3 The thermal and optical properties of various polymers.....	29
Table 2-4 The application of glass and polymer composites in varioius areas.....	33
Table 2-5 The different group of CVD depends on different classification basis.....	35
Table 2-6 Etching materials and the etched gases used [187].....	55
Table 3-1 Description of composition of various tungsten oxide modified tellurite glasses in mole percent and the use of crucibles	62
Table 3-2 Densities of TWL glasses.....	64
Table 3-3 List of the thermal properties of glasses, T_g , T_x , and ΔT	67
Table 3-4 FTIR absorption edge of glasses with different dopants.....	79
Table 3-5 The electronic transitions from the optical spectra for Er^{3+} , Yb^{3+} and Ce^{3+} codoped TWL glasses[38].....	81
Table 3-6 Calculated energy gap and energy tails of glasses TWL0-TWL6	83
Table 3-7 The refractive indices of the glasses at different wavelengths	85
Table 3-8 Sellmeier coefficient of TWL glasses with different rare earth dopants at room temperature.....	85
Table 3-9 The bandwidth and the flat gain of TWL glasses	87
Table 3-10 The lifetime for glasses at different states	88
Table 3-11 Er^{3+} ions concentration in the glasses calculated using glass density	89
Table 3-12 Reduced matrix elements of $U^{(\lambda)}$ between chosen intermediate coupled states of Er^{3+} ions [44]	89
Table 3-13 Calculated Judd-Ofelt parameters for Er^{3+} in TWL glass system.....	89
Table 3-14 The values of the measured experimental oscillator strengths f_{exp} (10^{-6}) and theoretical oscillator strengths f_{cal} (10^{-6}) of Er^{3+} in TWL glass systems.....	90
Table 3-15 Values of radiative transition probabilities, calculated lifetimes and quantum efficiency of transition ${}^4I_{13/2} \rightarrow {}^4I_{15/2}$ in Er^{3+} ions	90
Table 3-16 The theory energy gap of various transitions in the rare earth ions of Er^{3+} , Yb^{3+} , and Ce^{3+}	92
Table 3-17 The assignment of the IR absorption peaks measured using reflection modes	98

Table 3-18 The assignment of the Raman peaks of TWL glasses.....	99
Table 3-19 The bond lengths and angles between the bonds in the glass structure [80]	104
Table 4-1 Deposition parameters for thin film on silica substrate using different laser fluence.....	114
Table 4-2. Deposition parameters of thin films on silica substrate prepared at room temperature under different O ₂ pressures.....	116
Table 4-3 Deposition parameters for films using different temperatures.....	118
Table 4-4 Optical and spectroscopic properties of TWL bulk glass and thin films deposited on plain and polymer-coated silica substrates.....	122
Table 4-5 The intensity of peak 279 cm ⁻¹ , 652 cm ⁻¹ and 758 cm ⁻¹ of TWL thin film and bulk glass.....	125
Table 4-6 Compositions of target and thin films in atomic% measured using EDX	126
Table 4-7 Compositions of target and thin films in mol% converted using the data in above table, ignoring the existence of Al ₂ O ₃ in the samples.....	126
Table 5-1 Refractive indices, thickness and fluorescence decay and lifetime of transition ⁴ I _{13/2} → ⁴ I _{15/2} in Er ³⁺ ions.....	138
Table 5-2 Composition (in atomic %) of target and glass thin films on polymer coated silica substrates under different gas environments measured using EDX ...	138
Table 5-3 The properties of PT glass and siloxane polymer.....	139
Table 6-1 List of the conditions used during the photolithography process.....	157
Table 6-2 RIE parameters used for thin films patterning.....	158
Table 6-3 Writing parameters used during channel waveguide structure writing process on the composite thin films.....	161

List of Abbreviations and Symbols

ASE	amplified spontaneous emission
AWG	arrayed waveguide
CVD	chemical vapor deposition
CCVD	catalytic chemical vapor deposition
CTE	coefficient of thermal expansion
CB	conduction band
CW	continuous wave
DSC	differential scanning calorimetry
DTA	differential thermal analysis
DMA	dynamic mechanical analyser
dc	direct current
EDFA	erbium doped fiber amplifier
EPSRC	Engineering and Physical Sciences Research Council
ET	energy transfer
FEG	field emission gun
FIB	focused ion beam
fs	femtosecond
FTIR	Fourier transform infrared red spectrometer
FWHM	Full width half maximum
HAADF	high angle annular dark field
IPA	isopropyl alcohol
J-O	Judd-Ofelt
LMIS	liquid metal ions source
LD	laser diodes
LPCVD	low pressure chemical vapour deposition
MBE	molecular beam epitaxy
MMA	methylmethacrylate
MOCVD	metalorganic chemical vapour deposition
MEMS	Microelectromechanical systems
NA	numerical aperture
POF	polymer optical fibers

PVD	physical vapor deposition
PLD	pulsed laser deposition
PMMA	polymethylmethacrylate
PT	phosphate modified tellurite
PL	photoluminescence
PDMS	poly(dimethylsiloxane)
PEC	photoelectrochemical
PECVD	plasma enhanced chemical vapor deposition
PCB	printed circuit boards
PMT	photomultiplier tube
RCUK	Research Councils UK
RIE	reactive ion etching
RT	room temperature
RF	radio frequency
SI	step index
SEM	scanning electron microscopy
TMA	thermo- <i>mechanical</i> analysis
TEM	transmission electron microscopy
TE	transverse electric
TWL	tungsten lanthanum modified tellurite
TZN	TeO ₂ -ZnO-Na ₂ O
tbps	trigonal bipyramids
3D	three dimension
UHV	ultra-high vacuum
UV/VIS/IR	ultra-violet-visible-infrared spectrometer
VB	valence band
XRR	X-ray reflectometry
A	transition rate
c	the light velocity (2.998×10^8 m/s)
d	Molar concentration of ions
e	the electron charge (1.6×10^{-19} C)
E _{opt}	optical energy gap
f	oscillator strength

h	Plank's constant (6.63×10^{-23})
H	Harmoltonian operator
J	total angular quantum number
k	the Bolzman constant
m	mass of electron (9.11×10^{-31} kg)
n	refractive index
N	rare earth ion concentration (ion/m^{-3})
r.m.s	root mean square
S_{ed}	line strength of the electric dipole transitions
S_{md}	line strength of the magnetic dipole transitions
T_g	glass transition temperature
T_x	starting temperature of glass crystallization
T_p	peak temperature of glass crystallization
T_m	glass melting temperature
t	Thickness of glass
W	relaxation rate
v	Light velocity in the medium
Z	atomic number
Ω_t	Judd-Ofelt parameters
$\alpha(\lambda)$	absorption coefficient
β	branching ratio
ϵ	molar extinction coefficient
θ	angle
$\bar{\lambda}$	average wavelength
μ	reduced mass of the molecule
τ_{ra}	radiative lifetime
χ_{ed}, χ_{md}	correction terms of the local field
ψ	phase shift
ω	phonon angular frequency
\hbar	reduced Plank constant

List of Publications

Journals:

- ❖ Zhanxiang Zhao et al. Active glass-polymer superlattices for novel photonic integration. *Nanotechnology*, 2012, Volume 23, 225302
- ❖ Zhanxiang Zhao, Gin Jose, Paul Steenson, Nikos Bamiedakis, Richard V Penty, Ian H White and Animesh Jha, Tellurite glass thin films on silica and polymer using UV (193 nm) pulsed laser ablation. *Journal of Physics D: Applied Physics* 2011. Volume 44(9), 095501.
- ❖ M.Iraanejad, Z. ZHAO, G. Jose, D.P.Steenson, A.Jha, A short review on the pulsed laser deosition of Er^{3+} ion doped oxide glass thin films for integrated optics. *Trans.Ind.Ceram.Soc.*, 69 (4)207-221 (2010).
- ❖ Joshi Purushottam, Irannejad Mehrdad, Zhanxiang Zhao et al., Erbium-ion doped tellurite glass fibers and waveguides-devices and future prospectives, submitted to *International Journal of Applied Glass Science*

Conferences:

- ❖ Zhanxiang Zhao, Gin Jose, Animesh Jha, Nikos Bamiedakis, Jianji Dong, Richard, Penty, Ian H White Tellurite glass on polymer planar waveguides, 15th *European Conference on Integrated Optics*, Cambridge, 7th -9th April, 2010.
- ❖ Zhanxiang Zhao, Gin Jose, Mehrdad Irannejad, Paul Steenson, Nikos Bamiedakis, Richard Penty, and Ian White , Animesh Jha. Er^{3+} -doped glass-polymer composite thin films fabricated using combinatorial pulsed laser deposition. in *CLEO/Europe and EQEC 2011 Conference Digest*: Optical Society of America
- ❖ Zhanxiang Zhao, Gin Jose, Animesh Jha, Nikos Bamiedakis, Jianji Dong, Richard, Penty, Ian H White Fabrication and characterisation of tellurite

glass thin film waveguides using UV pulsed laser deposition, in *17th International Symposium on Non-Oxide and New Optical Glasses (ISNOG)*, Ning Bo, China, 2010.

- ❖ Zhanxiang Zhao, Gin Jose, Animesh Jha, Structure and optical properties of $\text{TeO}_2\text{-WO}_3\text{-La}_2\text{O}_3$ glasses co-doped with $\text{Er}^{3+}/\text{Yb}^{3+}/\text{Ce}^{3+}$, in *Society of Glass annual conference*, Lancaster, UK, 2009.

Chapter 1 Introduction

1.1 Overview

The replacement of electrical communication systems by optical fiber communication systems in long-haul networks boosted the data rates of the communication systems significantly. However, the electrical components, such as the backplanes and interconnects in the servers, routers and computing systems in local or metro networks, still cause serious difficulties to obtain data rates higher than 10 Gb/s due to the shortcomings i.e. electromagnetic interference size density, power and heat dissipation at high operating frequencies. The optical links can overcome the disadvantages and improve the bandwidth of the products [1, 2]. Therefore, all optical interconnects and circuits in the servers, routers and computing systems are desirable.

Generally, planar waveguide optical amplifiers in the optical interconnects and optical circuits are used to amplify the strength of signal to a satisfied intensity, for example, compensating the coupling losses, waveguide losses or the power division in the optical splitters[3]. Optical amplifiers have many applications in optical communication system. To meet the need for all these applications, different requirements include high gain and output power, low noise, broad band and high reliability in addition to the low cost and compactness are needed[4].

Currently, the main challenge of the optical amplifiers is to fabricate an amplifier with very high gain and small size while operating at a low pump power [5]. The maximum gain of the amplifiers that may be achieved depends on the concentration and the pumping efficiency of the active components in the host material, while the pump power required is based on the optical loss and any other attenuations of the host material. Therefore, to engineer an amplifier with quality approaching these requirements, the host materials and active components should be chosen carefully.

As a result of the limitation of the geometries of the planar waveguide optical amplifiers, high rare earth concentrations are required to achieve a high gain. Therefore, host materials that are used to engineer planar waveguide optical

amplifiers should be able to dope with high rare earth concentration without clustering (larger than 5000 ppm). In addition, broad bandwidth and relatively high flatness of the emission spectra are also necessary to obtain a high quality planar optical amplifier [6].

Vast amounts of research on materials for planar optical amplifiers has been done previously, for example, Er^{3+} doped alumina glasses with compositions of Al_2O_3 , Na_2O , La_2O_3 , and P_2O_5 were utilised to fabricate a strip-waveguide amplifier, and a net gain of 4.1 dB/cm at 1535 nm are attained with a 1480 nm diode laser at the power of 23 mW [5]. Hottari et al. [7] demonstrated an erbium doped silica-based planar waveguide amplifier with a length of 23 cm using sol-gel technique, the highest net gain obtained is 9.8 dB at the wavelength of 1533 nm when pumped by a 980 nm $\text{Ti}:\text{Al}_2\text{O}_3$ laser with pump power of 99 mW. Liu and his colleagues [8] reported an erbium doped phosphosphate glass waveguide amplifier fabricated using focused proton beam writing. An optical gain of 1.7 dB/cm at the wavelength of 1534 nm using the amplifier were achieved when pumped by a 975 nm laser diode at power of 100 mW.

In spite of the advances that have been achieved, there is still a long way for the planar waveguide amplifiers to approach the performance of the optical fiber amplifiers.

1.2 Materials for planar optical amplifiers

As mentioned in the previous section, the host material plays a key role in determining the quality of the optical waveguide amplifiers. Hence, the research on the materials used for the planar optical amplifiers needs to be paid more attention to meet the requirements of high performance amplifiers.

Common rare earth doped host materials include crystals [9], semiconductors[10], glasses[11], and polymers[12]. Among the materials, glass is compatible with the existing fiber-optic systems, and also has the advantage of high transparence [13]. Polymer as a cost effective and easy to process material can be integrated with printed circuit boards (PCB) and also is compatible with the traditional polymer

optical fibers [2]. Thanks to these attractive advantages, glass and polymer are considered as attractive materials for optical devices, i.e. amplifiers.

Although polymer is a brilliant candidate for the fabrication of a passive device, it is not promising to make active devices due to the rare earth ions clustering problem. Much research has been focused on how to reduce the concentration quenching of rare earth ions in the polymers. Wong et al. [14] demonstrated an erbium doped polymer planar waveguide fabricated using electron beam direct writing. To compensate the quenching problem of Er^{3+} ions and improve the quantum efficiency, they codoped Yb^{3+} ions. The waveguide of 1.8 cm they obtained exhibited an optical gain of 13 dB at 1550 nm when pumped using 980 nm laser diode at power 110 mW. Slooff and coworkers [12] encapsulated Er^{3+} ions into an organic ligand which can offer enough coordination sites to bind Er^{3+} ions, and then dispersed the resulting complex in a polymer film. The calculated net gain of the waveguide they fabricated was as high as 1.7 dB/cm at pump power 1.4 mW. They also fabricated an amplifier using silica colloid doped polymer, in which Er^{3+} ions were implanted into silica colloid to increase the doping concentration. The calculated net gain for this amplifier was 12 dB for a 15 cm long silica colloid polymer waveguide. The polymer waveguide reported above has a short emission lifetime in an order of μs . Therefore, further research needs to be performed to achieve polymer waveguides with high net gain and long fluorescence lifetime.

Based on the advantages of both materials, glass and polymer composites as a novel material combine the advantages of glass and polymer. They are believed to be an excellent choice for optical device fabrication, and have the potential to meet the stringent requirements of the present short distance communication and computing systems. In addition, the adjustable refractive index of glass and polymer makes it possible to design a refractive index matching glass and polymer composite which has a relatively low Rayleigh scattering [15].

Furthermore, the properties of glass and polymer composites may be fabricated using various ratios between the glass and polymer, which may further expand the application of this kind of composite material [16]. Consequently, glass and polymer

composite can satisfy the application of optical materials in a wide range with extended functionality and integrated capability at a reasonable expense[17], and may have a promising future in application of the interconnects and computing system.

1.3 Objectives and scope of the thesis

1.3.1 Objectives

This thesis is based on the RCUK Basic Technology Project, which aims to demonstrate integrated optical devices and circuits using epitaxially grown inorganic semiconductor, polymer and glass-based materials for components engineering. This project was carried out by the Leeds materials group collaborated with four other universities, namely, the Universities of Cambridge, Sheffield, St Andrews and Heriot-Watt University. The research reported in this thesis is focused on the preparation of tellurite glass and polymer composite thin films using pulsed laser deposition (PLD), and the fabrication of planar channel waveguides using suitable waveguide writing techniques on the thin film obtained.

Precisely, there are four major parts of the research work in this thesis: a), prepare high quality bulk tellurite glasses and investigate their properties, b), optimized the fabrication parameters of tellurite glass thin film and characterize the thin films obtained at optimal conditions, c), fabricate glass and polymer composite thin films and fully characterise their properties, d), write ridge or stripe waveguides on the high quality thin films to study their suitability for engineering optical amplifiers.

1.3.2 Scope of the thesis

This thesis is organised as follows:

Chapter 1 gives an introduction of the research work in this thesis, which includes the background, objectives and materials that are used for optical amplifier, especially glass and polymer in this thesis are discussed.

Chapter 2 presents the planar optical amplifiers (including the history and development, advantages and disadvantages, and working principle of amplifiers)

and details of the materials used in this thesis. Rare earth ions in the glasses which consist of the atomic physics of the rare earth ions, radiative and nonradiative transitions are also discussed. The techniques used for the fabrication of thin films and waveguides are reviewed in detail.

Chapter 3 demonstrates the process of bulk glass designing and melting, the instruments used for glass characterisation and their working principles. The results of thermal, structural and optical properties of the bulk glass are also discussed in this chapter.

Chapters 4 and 5 discuss the PLD experiments and the corresponding results which include the optimized process of thin film deposition, the discussions and results of the thin film properties, namely, the topographic and optical properties.

Chapter 6 describes the experimental optimization processes of two waveguide engineering techniques: reactive ion etching (RIE) and femtosecond (fs) laser micromachining. The obtained waveguides written on both tellurite glass thin films and composite thin films are demonstrated.

Chapter 7 summarises the conclusions of each chapter and proposes the work plan for the future including the improvement of the quality of the thin films and further study of the ridge waveguides.

Chapter 2 Literature review

Planar waveguide optical amplifier is one of the main components in the integrated optical circuits for all on chip systems. The research on this topic involves host materials, fabrication techniques of thin films and waveguides etc. The purpose of this chapter is to study the waveguide optical amplifiers, atomic physics and optical properties of the rare earth ions in the glasses, the materials and techniques used for thin film and waveguide fabrication in detail. Among these techniques, PLD used for thin film deposition (section 2.4), while waveguide fabrication techniques RIE and laser micromachining (section 2.5) which were employed in this study were discussed in particular.

2.1 Waveguide optical amplifiers

After the introduction of the first erbium doped fiber amplifiers (EDFA) optical fibre amplifiers in 1987[18], a rapid development has continued even since, replacing the electronic repeaters. EDFAs are now commercially available and widely used in the long haul transmission system. However, it is difficult to integrate the fibre amplifier with other components in the application of local communication system due to the limitation of its geometric structure which makes the EDFA packaging highly expensive and restricts its further application. Planar waveguide amplifiers are usually fabricated on a planar substrate and therefore easy to integrate with other components. As a result, the researches on fabrication and application of planar waveguide amplifiers have attracted more and more attention recently.

2.1.1 History and development

In 1969, Miller proposed the concept of integrated optics[19]. Since then, research on waveguide multifunctional devices on chip has intensified for designing amplifiers because of their promising application in the optical communication system.

In 1972, Yajima and his colleagues[20] demonstrated the first Nd^{3+} doped glass thin film waveguide which could be used as an amplifier at 1060 nm, and they measured the amplification properties in which the light power amplitude increased 28%

(equal to an optical gain of 0.36 dB/cm). This experiment encouraged people to do more research to increase the gain and reduce the loss through modifying the glass host and doping with different rare earth ions. However, in early 1970s when optical communication was not fully developed, the most sought after wavelength for the optical communication was the 1310-1320 nm. In this wavelength region, the silica fibre has zero dispersion at wavelength near 1317 nm. Since all the communication system was optimized for signal transmission in the range of 1310-1320 nm for terrestrial operation, the Nd^{3+} doped waveguide amplifier operating at 1325 nm was not acceptable because the peak of bandwidth in Nd^{3+} doped silicate host was outside the 1310-1320 nm window. The gain of Nd^{3+} doped amplifier at 1325 nm reduced because the 1060 nm amplified spontaneous emission (ASE) is five times stronger than the gain at 1325 nm. The research on waveguide optical amplifier has no breakthrough till the research group from Southampton invented the EDFAs in 1987[18]. In 1991, Kitagawa et al.[21] from Japan demonstrated the first erbium doped waveguide optical devices and showed the emission spectra of erbium around 1550 nm and described the potential application as a laser or an amplifier. The same group [22] and researchers Shmulovick and his colleagues [23] from AT&T Bell laboratory demonstrated the erbium doped silicate glass waveguide amplifiers on silicon in 1992, independently. In these papers, they reported a waveguide amplifier with a total gain of 21 dB using a 2.4 cm long thin film at a pump power of 120 mW. Although the gain obtained was not comparable with the fibre devices, it showed a promising future of realizing the ultra-short length integrated amplifiers on silicon. A year after, the same research group from Japan showed the erbium doped silica-based glass waveguide optical amplifier using the 980 nm pump laser diode for the first time [7], and in the same year, they demonstrated the phosphate modified silicate glass waveguide amplifiers which were prepared from the thin films deposited using plasma enhanced chemical vapor deposition (PECVD) technique. The waveguide was fabricated using RIE [24]. With this amplifier, they demonstrated a maximum net gain of 5 dB and gain coefficient of about 0.67 dB/cm using 980 nm laser diode pump.

The multiple steps involved in the fabrication process of a waveguide optical amplifier are shown in Figure 2-1. It is evident that the quality of waveguide optical

amplifier not only depends on the techniques of thin film and waveguide fabrication, but also based on the host materials used. Different materials have been studied for waveguide optical amplifiers, including semiconductor materials [25], glass materials [24, 26-29] nanocrystalline [30, 31] and polymer materials [32] etc. In addition, some new thin film fabrication techniques, namely sol-gel [33, 34], molecular beam epitaxy MBE [35], and PLD [36] have been used for different materials. Several techniques for waveguide fabrication will be discussed in detail later in this chapter.

From the point of view of gain per unit length, the dielectric waveguide amplifier is still in its immature state in comparison with a semiconductor optical amplifier. In this respect, the very first step in cost reduction for broadband network is to engineering a dielectric optical amplifier with a gain of few dBcm⁻¹.

2.1.2 Advantages and disadvantages

Compared to the fiber optical amplifiers, the following features are the main advantages for waveguide optical amplifiers [9].

1. More compact size
2. Much more suitable to integrate with other devices
3. Lower cost
4. Better reliability
5. Better mechanical and thermal stability

However, the waveguide optical amplifiers have a complex fabrication process as shown in Figure 2-1, and therefore, it is hard to control the quality of the amplifier which further makes it difficult to engineer a planar optical amplifier with a low loss and high gain at low cost.

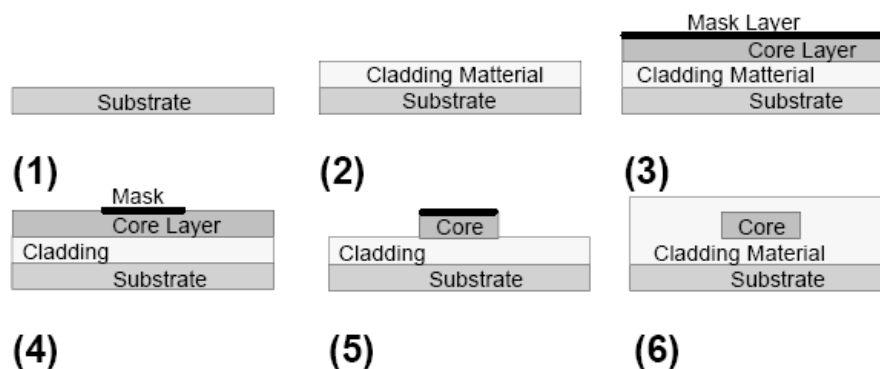


Figure 2-1 The process of waveguide fabrication[37], (1) substrate, (2) coating cladding layer, (3) core layer on cladding material with a mask layer protection, (4) after exposure to the UV light, (5) after etching, (6) coating top cladding layer

2.1.3 Working principles and applications of optical amplifiers

There is a number of energy states included in the $4f^N$ configuration in the rare earth ions. The lowest energy state is called ground state, while any other higher energy states are called excited states. With the help of the energy from other devices, electrons in the higher energy levels can be more than the electrons in the ground state. This phenomenon is known as population inversion which is the precondition for lasing.

Electrons in the higher energy level can release the energy and transition from the excited states to the ground states automatically. This process is called spontaneous emission which can happen whenever there are electrons at the excited levels. If there is an outside photon with energy $h\nu$ triggering a resonance with the excited atoms (an incident light beam interact with the medium), the electrons at the excited states will leave this state and transition to the ground states with another photon with the same energy $h\nu$ emitted. This process is known as stimulated emission which is schematically shown in Figure 2-2. The working principle of optical amplifiers is based on the theory of the stimulated emission process happened to the electrons in the rare earth ions when they are excited within the $4f$ energy states. When the light signals come through a medium with electrons in the population inversion state, the electrons at the excited level will release photons in forms of light with the same wavelength of the passing signal. The input signal has no changes in this process, and the total signal is increased as shown in Figure 2-3.

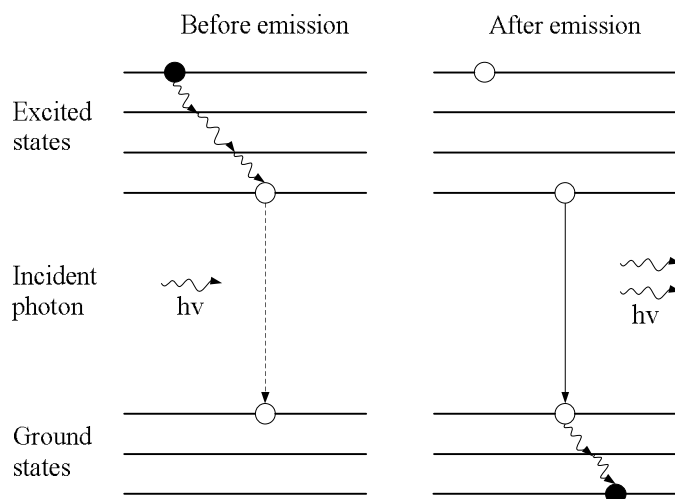


Figure 2-2 The stimulated emission process of the rare earth ions. Dashed line represent process that will happen, solid line means process that really happen, empty dot is the position that ions stayed before emission, black filled dot is the excited ions

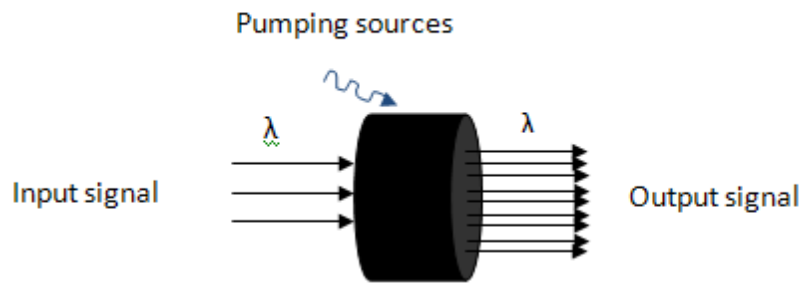


Figure 2-3 The schematic of the amplification of light signal

Design of optical amplifiers is based on its expected functions and corresponding requirements. Three main types of optical amplifiers are preamplifiers, power amplifiers and line amplifiers. The preamplifier is used to amplify signals when the source signal is too low to be processed in the next step. It usually is installed before the receiver or inside an instrument such as musical instrument or microphones. Therefore, the noise performance of a preamplifier is very critical [38]. The power amplifier is usually used to amplify the source signals, for example, to increase the power of source signal from 2 mW to the fiber power range 100-200 mW. As a result, the gain of the power amplifier is very important while the noise figure is not critical. The line amplifier is usually used in the long haul transmission system which plays the same role as the repeater. This type of amplifier requires much tougher performance requirements including higher gain and low noise figure. Hence, many factors need to be considered in the designing process, such as polarization mode dispersion, chromatic dispersion and noise[38]. Optical amplifier works based on pump (eg. laser diode), while laser amplifies the signal based on the stimulated emission process.

2.2 Rare earth ions in glasses

Rare earth (RE) trivalent ions have a unique characteristic due to the 4f electrons. In this section, the atomic physics of the RE ions, radiative transition, nonradiative transition, and Judd-Ofelt parameters will be discussed in detail.

2.2.1 Atomic physics of rare earth ions

Rare earth ions are classified into two groups, lanthanides and actinides. The former is characterized by the filling of 4f shell which starts from cerium (Ce atomic number $Z=58$) and ends with lutetium (Lu, $Z=71$). The latter which fills 5f shell lies

from thorium ($Z=90$) to Lawrencium ($Z=103$) [38]. Only the first group is considered here because the rare earth ions in this group have a wide-range of optical spectrum and many laser transitions happen. The most common form of rare earth ions is the trivalent state $(Ln)^{3+}$ and a neutral lanthanide element has an atomic form of $[Xe]4f^N6s^2$ or $[Xe]4f^{N-1}5d^16s^2$, in which $[Xe]$ represents the xenon core. The ionization of lanthanide elements is to remove two loose electrons in shell 6s and then either a 4f or 5d electron. The electrons in 4f shell can only be excited inside 4f states due to the shields of the electron shells 5s and 5p. Therefore, the energy levels are insensitive to the host and have only a small host-induced energy splitting. This results in narrow or sharp lines for the optical transitions between 4f states and a high efficiency emission, which is different from other optical ions (transition metals) that have broad and strong emission and absorption bands due to the influence of the host materials [39].

As the 4f electrons only interact weakly with the electrons in other ions, the Hamiltonian operator H which describes the wavefunctions of the 4f electrons including atomic interactions of the free ions and the interaction of electrons with the crystal field can be written as follows for an individual rare earth ion:

$$H = H_{\text{atomic}} + H_{\text{cf}} \quad (2.1)$$

where H_{atomic} is the free ion Hamiltonian in central field which includes the kinetic energy and the Coulomb interaction of the nucleus with electrons in 4f state as well as the mutual Coulomb repulsion and spin orbit interactions of the 4f electrons. The first two terms which are spherically symmetrical will not induce degeneracy of the energy level, while the third and fourth terms can cause spread of 4f electron energy level. H_{cf} is the crystal-field Hamiltonian. In this scheme, the configurations of the atomic electrons of the rare earth ions are considered as a set of one-electron orbital since the shielding shell are inert with regard to the optical excitation [38].

The $4f^N$ energy level is split into many sublevels due to the atomic interaction between the electrons. And a further splitting of the energy level can happen when the rare earth ions are placed in a crystal field environment. The splitting of the energy level is drawn in Figure 2-4[38].

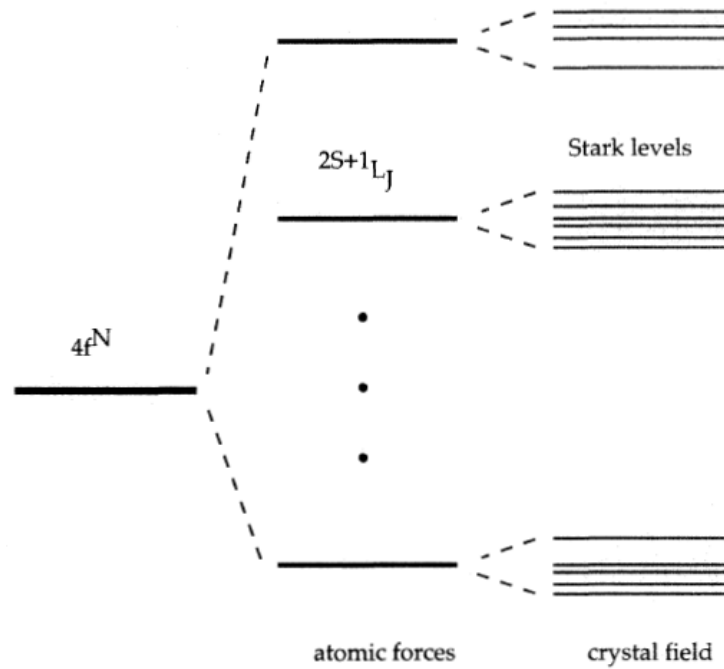


Figure 2-4 Schematic of the energy splitting of $4f^N$ electrons under the perturbation of atomic interaction and crystal field environment [38]

In multi-electron atoms, the states of an electron in the orbitals can be described using four quantum numbers, n , l , m_l , m_s , which is principle quantum number, orbital quantum number, magnetic quantum number and spin quantum number, respectively. There are many schemes for explaining the multi-electron atoms, and for rare earth ions, it usually employs the Russell Saunders Coupling Scheme (L-S coupling). In this scheme, the $4f$ configuration can be written as $^{2S+1}L_J$, in which L is the total orbital angular momentum, S is the total spin angular momentum of all electrons in the system, and J is the total angular momentum [39].

2.2.2 Radiative transitions

The optical spectral lines are yielded by the transitions between $4f^N$ electrons in different energy levels. The positions of these levels depend on a combination of the Coulomb interactions among electrons, spin-orbital coupling and crystal electric field. The electronic interactions are responsible for degenerating the energy level and yielding terms ^{2S+1}L which have a separation of 10^4 cm^{-1} in magnitude. At the same time, the spin orbital couplings can degenerate the energy level into J states which have a splitting distance of 10^3 cm^{-1} . However, the J degeneracy of the free ions can finally be removed by the crystal electric field, and yields splitting energy levels with a magnitude of few hundred cm^{-1} , which is known as the Stark splitting.

The radiative transitions can take place from one Stark component $\{L, S, J\}$ to another Stark component $\{L', S', J'\}$ [40].

The energy difference between the two states in radiative transition is emitted in the form of photons. The dynamic interaction of Hamiltonian terms is time-dependent and usually treated using perturbation theory, for example the influence of crystal field can be treated as perturbations. The interaction between electron charge and electric field, and interaction between electron spin and magnetic field can yield radiative transitions including absorption and emission of photons.

The intensity of the transition including electric dipole and magnetic dipole transition can be expressed using oscillator strength f for each a $\{L, S, J\} \rightarrow b \{L', S', J'\}$ process. The experimental oscillator strength can be calculated using the integrated absorption cross section of the transitions between different multiple states $^{2S+1}L_J$ as shown below [41]:

$$f_{exp(a \rightarrow b)} = \frac{4\varepsilon_0 mc^2}{Ne^2 \bar{\lambda}^2} \int \alpha(\lambda) d\lambda \quad (2.2)$$

where ε_0 is the permittivity of free space, c is the light velocity (2.998×10^8 m/s), N is the rare earth ion concentration (ion/m^3), e (1.609×10^{-19} C) and m (9.11×10^{-31} kg) are the charge and mass of electron, $\alpha(\lambda)$ is the absorption coefficient ($\frac{-\ln(I/I_0)}{d}$) at a wavelength of λ and d is the thickness of the sample, average wavelength $\bar{\lambda} = \int \lambda \alpha(\lambda) / \int \alpha(\lambda)$.

In 1962, Judd and Ofelt [42, 43] proposed a theory to calculate the intensity of the radiative transitions independently, known as Judd-Ofelt theory. This theory can be used to calculate the oscillator strength of the transitions, the radiative transition rate, and radiative lifetime [38, 40, 41], etc. The theoretical oscillator strength of the transition from state a $\{L, S, J\}$ to state b $\{L', S', J'\}$ can be written as follows:

$$f_{cal(a \rightarrow b)} = \frac{8\pi^2 mc}{3h(2J_a + 1)\lambda n^2 e^2} (\chi_{ed} S_{ed} + \chi_{md} S_{md}) \quad (2.3)$$

where S_{ed} and S_{md} are line strength of the electric dipole and magnetic dipole transitions, respectively, which are defined as

$$S_{ed} = e^2 \sum_{t=2,4,6} \Omega_t |\langle a \| U^{(t)} \| b \rangle|^2 \quad (2.4)$$

$$S_{md} = \left(\frac{eh}{4\pi mc} \right)^2 |\langle a \| L + 2S \| b \rangle|^2 \quad (2.5)$$

where $\chi_{ed} = n(n^2+2)^2/9$ and $\chi_{md} = n^3$ are the correction terms of the local field which stand for the increase of the electric field around the rare earth ions due to the polarizability of the host medium, J is the total angular quantum number for this transition, n is the refractive index of the host medium at the average wavelength, h is the Plank constant, the reduced matrix $|\langle a \| U^{(t)} \| b \rangle|^2$ was tabulated by Weber [44] and $|\langle a \| L + 2S \| b \rangle|^2$ can be calculated using the equation offered by Carnall [45]. $\Omega_2, \Omega_4, \Omega_6$ are known as the Judd-Ofelt intensity parameters. The magnetic dipole strength is zero when the transition is satisfied with the selection rule: $\Delta J = \pm 1, \Delta S = 0, \Delta L = 0, \Delta l = 0$, otherwise it is non-zero and can be calculated using equation 2.5. Combining $f_{exp} = f_{cal}$, and equations 2.3, 2.4 and 2.5, Judd-Ofelt parameters $\Omega_2, \Omega_4, \Omega_6$ can then be obtained by fitting the combined equation. The J-O parameters for various Er^{3+} doped glasses are listed in Table 2-1.

Table 2-1 The intensity parameters of Ω_t for different glass hosts

Glass	Compositions (mol%)	Ω_2 (10^{-20} cm^2)	Ω_4 (10^{-20} cm^2)	Ω_6 (10^{-20} cm^2)
TWL[46]	70TeO ₂ -20WO ₃ -10La ₂ O ₃ -1.0 wt% Er ₂ O ₃ -5.0 wt%Yb ₂ O ₃	7.93	2.18	0.97
Tellurite[47]	70TeO ₂ -2.5BaO-7.5SrO-20Nb ₂ O ₅ - 1.0wt%Er ³⁺	6.07	1.71	0.77
Phosphate[48]	10Na ₂ O- 50 PbCl ₂ - 40P ₂ O ₅ - 1.0wt%Er ³⁺	4.11	0.47	1.16
Germanate[49]	55GeO ₂ -25(BaO+ZnO+K ₂ O)-15PbO- 5PbF ₂ -1Er ₂ O ₃	5.15	1.36	0.59
Fluoride glass[50]	20ZnF ₂ -20SrF ₂ -2NaF-16BaF ₂ -6GaF ₃ - 35InF ₃ -1ErF ₃	2.17	2.31	0.89
silicate[51]	5Na ₂ O-20Sb ₂ O ₃ -35B ₂ O ₃ -39SiO ₂ - 1Er ₂ O ₃	4.22	1.85	1.62
Bithmuth[52]	60Bi ₂ O ₃ - 35B ₂ O ₃ -5Na ₂ O-1wt%Er ₂ O ₃	3.86	1.52	1.17

For glasses, the calculated Judd-Ofelt parameters are average values from a variety of sites for rare earth ions in different environments. The Judd-Ofelt parameters are correlated with the site environment and the amount of covalent bonding. Among these parameters, value of Ω_2 depends on the degree of the covalence of the host material which means it is small for ionic host material, e.g. fluoride glasses as

shown in Table 2-1, while is large for covalent host materials, such as silicate glasses. The accuracy of the Judd-Ofelt theory is in the range of 15-25%[39] and largely depends on the number of transitions considered for the reduced tensor matrix analysis. Usually a large number of optical transitions, e.g. in Er-ions, can reduce the error and vice-versa. This theory is useful to estimate the strength of the unreachable transitions. The validity of the intensity parameters can be evaluated using a deviation parameter: root-mean-square (r.m.s.) which is given by [41]:

$$r. m. s. = \left[\frac{\sum (f_{cal} - f_{med})^2}{N_{Tran} - N_{Param}} \right]^{1/2} \quad (2.6)$$

where N_{Tran} is the number of the transitions used in the calculation, N_{Param} is the number of the parameters, here the value is 3.

Once the intensity parameters are determined, they can be used to calculate the individual radiative transition rate, its lifetime, the branching ratio and quantum efficiency for any transitions [41]. The radiative transition rate for transitions $b\{L', S', J'\}$ (b is excited state) to state $a\{L, S, J\}$ can be expressed as follows:

$$A_{b \rightarrow a} = \frac{16\pi^3}{3h\epsilon_0(2J'_b + 1)\lambda^3} (\chi_{ed}S_{ed} + \chi_{md}S_{md}) \quad (2.7)$$

The radiative lifetime τ_{ra} can be given by

$$\frac{1}{\tau_{ra}} = \sum_a A_{b \rightarrow a} \quad (2.8)$$

The branching ratio β can be expressed as

$$\beta = \frac{A_{b \rightarrow a}}{\sum_a A_{b \rightarrow a}} \quad (2.9)$$

The branching ratio is an important parameter for the performance of the device at a specific transition and it influences the threshold of the laser and the efficiency of the amplifier.

The quantum efficiency η is given by:

$$\eta = \beta \frac{\tau_{exp}}{\tau_{ra}} \quad (2.10)$$

where τ_{exp} is the measured lifetime.

2.2.3 Nonradiative transition

Apart from radiative transition which are caused by the interaction with the electromagnetic field (absorption or emission of photons), rare earth ions can also experience transition due to the interaction with vibration of the host material (absorption and emission of phonons). The process of rare earth ions relaxing to a lower electronic state by emitting multiple phonons is known as a nonradiative transition. The probability of the nonradiative transition depends on the number of phonons needed to bridge the energy gap[39, 41]. When the energy gap can be bridged by one or two phonons, the nonradiative transition rate can be fast. On the other hand, if the energy gap is large, the transition probability is reduced significantly. The ratio between radiative and nonradiation transition rate determines the efficiency of the fluorescence. Therefore, nonradiative transitions are undesirable for the application of the amplifier.

A nonradiative process may involve multiphonon relaxation and ion-ion interaction. The theory of multiphonon relaxation process for rare earth ions was first proposed by Kiel[53] and then further developed by Reisberg and his colleagues[54] for crystals. There are three predictions in this theory, the exponential dependence of multiphonon relaxation rate on energy gap, the predominant contribution of the highest phonon energy of the host material and dependence of the multiphonon decay on the temperature. This theory is complex and needs to be explained by perturbation theory. As the nonradiation transition is correlated with the energy gap and number of phonons needed to bridge the gap, maximum phonon energy plays a key role in this nonradiative process. The multiphonon relaxation theory has been successfully used for crystal materials and also proved to be useful for glasses [55].

The rate of multiphonon relaxation which depends on host materials is independent of the nature of the electronic states can be written as [39]:

$$W_{mp} = B(n(T) + 1)^p \exp(-\alpha\Delta E) \quad (2.11)$$

where $n(T)$ is the Bose-Einstein occupation number for the effective phonon mode and p is the phonon numbers required to bridge the energy gap which can be given by

$$n(T) = \frac{1}{\exp(\hbar\omega/kT) - 1} \quad (2.12)$$

$$p = \frac{\Delta E}{\hbar\omega} \quad (2.13)$$

where \hbar is the reduced Plank constant, k is the Boltzman constant, ω is the phonon angular frequency, ΔE is the energy gap between two electronic states. The parameter $\alpha = -\ln(\gamma)/\hbar\omega$ is correlated with the coupling constant with interaction γ . Parameters B , $\hbar\omega$ or p and α are usually used as the empirical terms to describe the nonradiative decay in practice. They strongly depend on the host material but are independent on rare earth ions in the same host medium. Their values can be obtained by fitting equation 2.11 and the nonradiative decay rate obtained experimentally for variety of transitions.

The total transition rate for rare earth ions in a state is the sum of the radiative transition rate $A_{a \rightarrow b}$ and the nonradiative transition rate W_{nr} including the nonradiative decay yielded by multiphonon process W_{mp} and ion-ion interaction $W_{ion-ion}$. Therefore, the total transition rate can be given by:

$$A = A_{a \rightarrow b} + W_{nr} = A_{a \rightarrow b} + W_{mp} + W_{ion-ion} \quad (2.14)$$

As it is known that devices with low RE ion concentrations have relatively high efficiency than those with higher RE ions density. This is because the ion-ion interactions can reduce the quantum efficiency via increasing the probability of the nonradiative transitions in the devices. Even in the devices with low RE ion concentration, ion-ion interaction still can happen when the local rare earth ion concentration is comparatively high. Therefore, ion-ion interaction is not desirable for devices like amplifiers or lasers, while it is helpful in some other applications, e.g. infrared pumped visible lasers. Energy transfer is the main manifestation of ion-ion interaction, which can occur between the same rare earth ions or different rare earth ions, such as the energy transition between $Yb^{3+} \rightarrow Er^{3+}$ [41].

If reactions occur between two electrons, one of the electrons will be excited to a higher level, and the other will come down to the ground state, and this process is known as upconversion. Upconversion is the main source of concentration quenching. Therefore, any increase in the concentration of the rare earth ions can

reduce the quantum efficiency [38]. The process of upconversion is shown in Figure 2-5 (a), in which two rare earth ions are pumped to a metastable energy state, and then one of the ions passes its energy to another and promotes it to an even higher energy state. At the same time, it cascades down to the ground state.

There are many mechanisms that can cause the upconversion phenomenon, one of which is the energy transfer. In this process, two photons in excited level could interact with each other with one of the photons promoted to a higher energy level and the other one cascaded down to the ground level through energy transfer. If the energy changes of these two photons are the same, then there will be no energy absorption or loss, and this process is known as the resonant energy transfer. Energy transfer can also happen even if the energy changes of these two excited ions are different which is defined as the nonresonant energy transfer. This transfer needs the assistance of the photons or phonons to complete [38]. Energy transfer between the same types of rare earth ions is known as cross-relaxation process. Cross relaxation is a process where an excited ion passes part of its energy to a nearby ion, but it relaxes to a lower energy level at the same time, and then decays to the ground state nonradiatively. There is energy loss in this process [38]. The cross relaxation process is shown in Figure 2-5 (b).

Concentration quenching is an effect that the quantum efficiency of rare earth ions is reduced due to an increase in RE ion concentration. Both upconversion and cross-relaxation can give rise to concentration quenching which is detrimental to the performance of devices. In waveguide devices, the concentration of rare earth ions needs to be high for large gain. In this case, it is necessary to reduce the concentration quenching effect by choosing a glass host of high rare earth solubility.

For Er^{3+} doped glasses, the concentration quenching mainly comes from the upconversion and impurity quenching. The energy transfer has a small influence in this case, and can be ignored during the analysis. When there are more than one RE ions doped in the glass, the energy transfer phenomena will become significant. The dominant impurity quenching in the Er^{3+} doped glasses is the OH⁻ quenching which brings about severe reduction to the quantum efficiency of the devices. Therefore, it

is important to control the OH⁻ concentration in the glass to fulfill the requirements of the high performance devices [40].

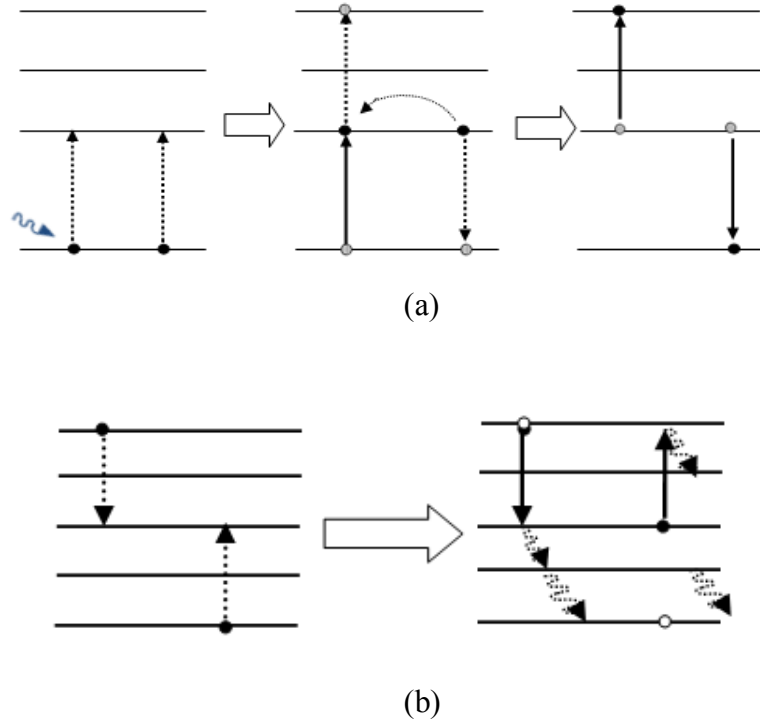


Figure 2-5 The schematic of (a) up-conversion and (b) cross relaxation processes. Dashed line represent process that will happen, solid line means process that really happen, empty dot is the position that ions stayed before energy transfer, black filled dot is the excited ions

2.3 Tellurite glass and tellurite glass thin film

Tellurite glass has attracted much attention in the research community thanks to its high refractive index and RE ions solubility [56, 57]. The excellent optical properties of tellurite glasses and their applications in the optical communication system have been demonstrated extensively [56, 58-60] for tellurite glass fiber [61] and optical amplifiers [62], etc. In this section, the tellurite bulk glass and thin films for planar waveguides are reviewed.

2.3.1 Tellurite glass

According to Pauling's theory, only the elements with electronegativity values in the range of 1.7-2.1 on the Pauling scale could be regarded as excellent glass former [63, 64]. This pattern is observed in silicon (1.8), phosphorus (2.1), and boron (2.0) which form silicate, phosphate and borate glasses, respectively. Based on this statement, tellurium which has electronegativity value of 2.1 can be used as glass

former. However, pure tellurium oxide glasses had not been successful using the traditional melting process for a long time. During 1956-1957, Barady [65] combined TeO_2 and Li_2O together to fabricate a tellurite glass. He reported X-ray analysis in the article, and found that the tellurium oxide glass had a local structure similar to that of TeO_2 crystal. Following this work, he presented the structure of tellurium oxide glass in some detail in later work, and concluded that the main building block in the crystal was preserved when transformed into a glass. As a result, the pure tellurium oxide glass has a similar unit group like that of the TeO_2 crystal. The authors also found that adding more than 10% modifiers like Na_2O or Li_2O are necessary to avoid crystallisation when fabricating tellurium oxide glass using a general glass making process. However, it is easy to make a pure SiO_2 glass. This can be explained from the difference of the transformation scheme. There is a simple distortion of the corner tetrahedral Si-O-Si angle in the formation process of SiO_2 glass from SiO_2 crystal, while in the formation of TeO_2 glass, there are breakdown of the corner sharing which will require additional O⁻ ions to balance the coordination[66].

Koen's research group [67] fabricated the first erbium doped tellurite glass and discovered that the erbium ions in this glass could affect the magnitude and speed of photochromic effects, and a small amount of Yb_2O_3 doping can enhance the absorption peak around 980nm. Wang et al. [56] studied the spectroscopic properties of TeO_2 - ZnO - R_2O glasses doped with various RE ions (Pr^{3+} , Nd^{3+} , Er^{3+} , Tm^{3+}) and their suitabilities of fabricating fibers. They also reported that tellurite glass exhibits many advantages: (a) comparatively wide transmission range, (b) good thermal stability and corrosion resistance, (c) nonlinear refractive indices. Mori et al.[29] studied the fluorescence spectra of tellurite glass fiber and calculated the emission cross-section. Their results illustrated that this glass has potential applications in fiber lasers and amplifiers if the propagation loss can be reduced to a suitable range. Le Neindre[68] investigated the optical and thermal properties of tellurite glass with various $\text{Na}_2\text{O}/\text{Li}_2\text{O}$, $\text{Na}_2\text{O}/\text{K}_2\text{O}$ and $\text{K}_2\text{O}/\text{Li}_2\text{O}$ ratios and calculated the Judd-Ofelt parameters of these glasses which can be used to calculate the transition rate, radiative transition lifetime and branching ratios. The results

showed that this kind of glass has a potential for using as a broadband amplifiers around 1.5 μm .

Dimitriev and his colleagues [69-74] studied the phase diagrams of the formation of glasses using tellurium oxide mixed with other metal compounds systematically, including the equilibria in the binary mixtures $\text{TeO}_2\text{-PbO}$, $\text{TeO}_2\text{-Ag}_2\text{O}$ and $\text{TeO}_2\text{-GeO}_2$, in addition to ternary glass systems of $\text{TeO}_2\text{-CuO-V}_2\text{O}_5$, $\text{TeO}_2\text{-Na}_2\text{O-V}_2\text{O}_5$ and $\text{TeO}_2\text{-Ag}_2\text{O-V}_2\text{O}_5$. Besides the phase diagram investigation, this group also has investigated the structure of various tellurite glasses, for example the structure of glasses $\text{TeO}_2\text{-V}_2\text{O}_5$ [75], $\text{TeO}_2\text{-MoO}_3$ [76]and $\text{TeO}_2\text{-WO}_3$ (TW) [77]. They postulated that there are deformed TeO_4 trigonal bipyramids (tbps) in the tellurium oxide glass. When adding WO_3 inside the glasses, the WO_4 polyhedra will substitute part of the TeO_4 groups, and form Te-O-W bonds consequently. With the increase of WO_3 content, WO_6 groups are formed and TeO_4 tbps and WO_4 polyhedra will be reduced subsequently. Kozhukharov [78] proposed a structural model of this TW glasses, and assumed that there are TeO_4 tbps, WO_4 tetrahedra, and WO_6 octahedra in the TW glasses.

However, Sekiya and his colleagues [79] disagreed with the above discussed models, he pointed out that the TeO_4 tbps is difficult to be substituted by WO_4 due to the lone electron pair in the sp^3d hybrid orbitals. Therefore, they doubted the existence of WO_4 tetrahedra in the TW glass because it is not stable to have two W=O bonds. Based on the crystal chemistry, they believed that W^{6+} with W=O bonds is in six coordination instead of four, and WO_6 shares the corner with TeO_{3+1} polyhedra by forming Te-O-W linkages. Till now, this argument still remains sustained.

All the above studies on the tellurite glass structure were based on the structure of crystal. In 2006, Sokolov[80] studied the structure of TW glass and made a structural model based on the vibrational properties of the glass. The calculated configuration of TeO_4 , TeO_3 and WO_6 are shown in Figure 2-6 and Figure 2-7.

In 1999, Blanchandin and his colleagues [81]verified the formation range of $\text{TeO}_2\text{-WO}_3$ system, and the phase equilibrium diagram of this system is shown in Figure

2-8. The limits of the formation range of glasses depends on the melting temperature and quenching conditions. From this phase equilibrium diagram, it is clear that the high quality $\text{TeO}_2\text{-WO}_3$ glass could be obtained when the concentration of WO_3 is in the range of 10 mol% to 30 mol% under the traditional preparation conditions.

There is no phase equilibrium diagram of TWL glass system available till now. However, the glass forming region of $\text{TeO}_2\text{-WO}_3\text{-K}_2\text{O}$ system proposed by Kosuge could be used as a reference [82]. The phase equilibrium diagram of $\text{TeO}_2\text{-WO}_3\text{-K}_2\text{O}$ glass system is shown in Figure 2-9. It can be seen that the glass formation region is 20-90 mol % for TeO_2 , 0-70mol % for WO_3 and 0-60 mol % for K_2O .

Adding WO_3 to the tellurium oxide glass can improve its thermal and optical properties. It has been proved by many researchers that adding heavy metal oxides such as WO_3 and La_2O_3 can increase the glass transition temperature and reduce the thermal damage at high optical intensities[46, 83-85]. Furthermore, when WO_3 is added as a network modifier, it can connect with TeO_4 in the TW or TWL glasses transferring part of TeO_4 unit groups to TeO_3 groups and creates more sites for dopants. As a result, adding WO_3 can broaden emission spectrum of Er^{3+} ions[85]. Large percentage of La_2O_3 addition in the modified glass also is advantageous to dope high concentration of rare-earth ions, erbium ions in this work. Er^{3+} doped tellurite glasses have wide applications in lasers and amplifiers operating in the wavelength range of 1530 -1620 nm. The absorption of Er^{3+} ions around 980nm is weaker compared with the absorption of Yb^{3+} . Therefore the addition of Yb_2O_3 to glass could enhance the pumping efficiency of 980 nm laser diodes(LD) through the energy transfer (ET) from Yb^{3+} to Er^{3+} [86]. Furthermore, the Ce^{3+} ions could improve the internal gain and pump inversion efficiency through shortening the 980 nm fluorescence lifetimes[87].

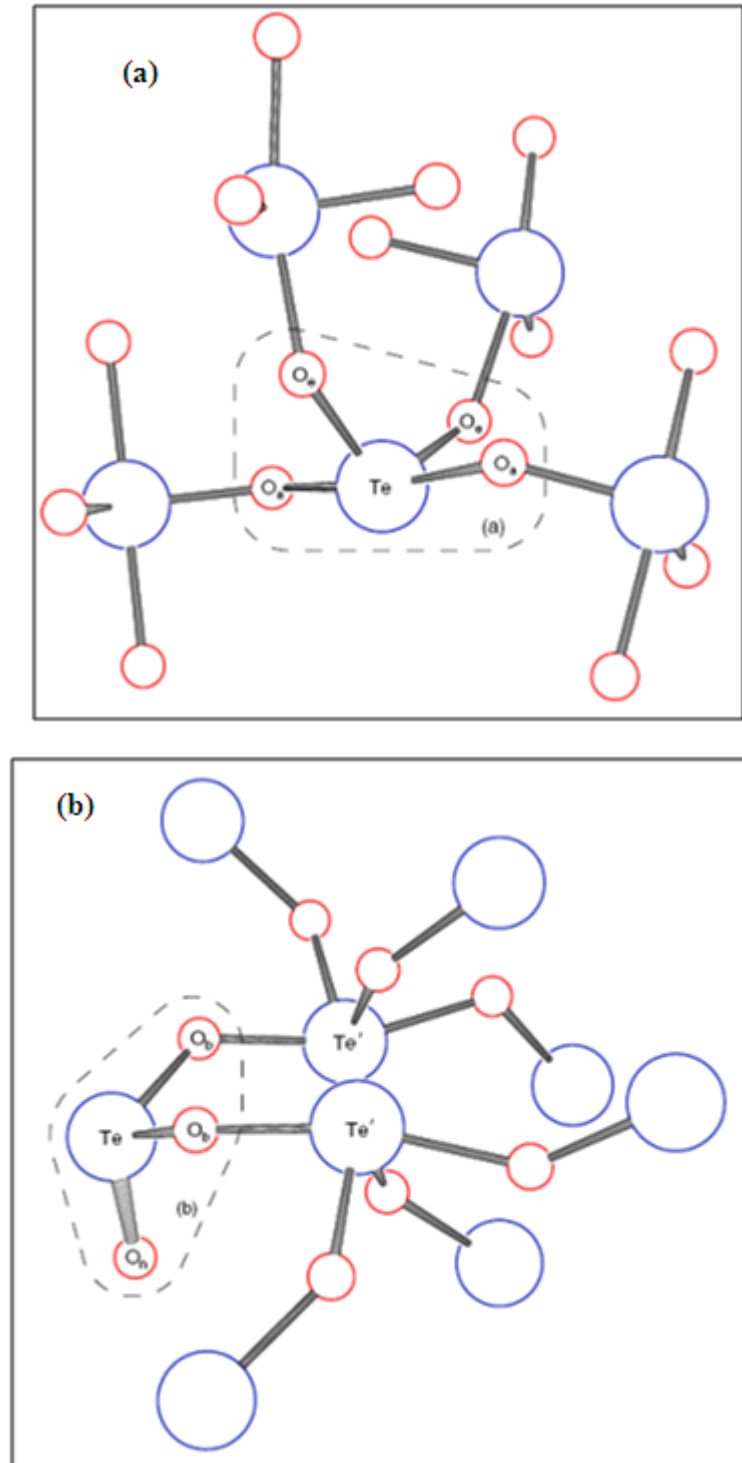


Figure 2-6 The calculated configuration of the groups related to TeO_2 in tellurite glass. Large circles are Te atoms, small circle are O atoms. (a) fourfold coordinated Te atom, TeO_4 in tellurite glass, enclosed in the dash line is the TeO_4 structural unit. (b) Threefold coordinated Te atom, $O=TeO_2$, in tellurite glass, O_n is nonbridging oxygen, O_b is bridging oxygen between $O=TeO_2$ and TeO_4 units, enclosed in the dash line is the $O=TeO_2$ structural unit[80].

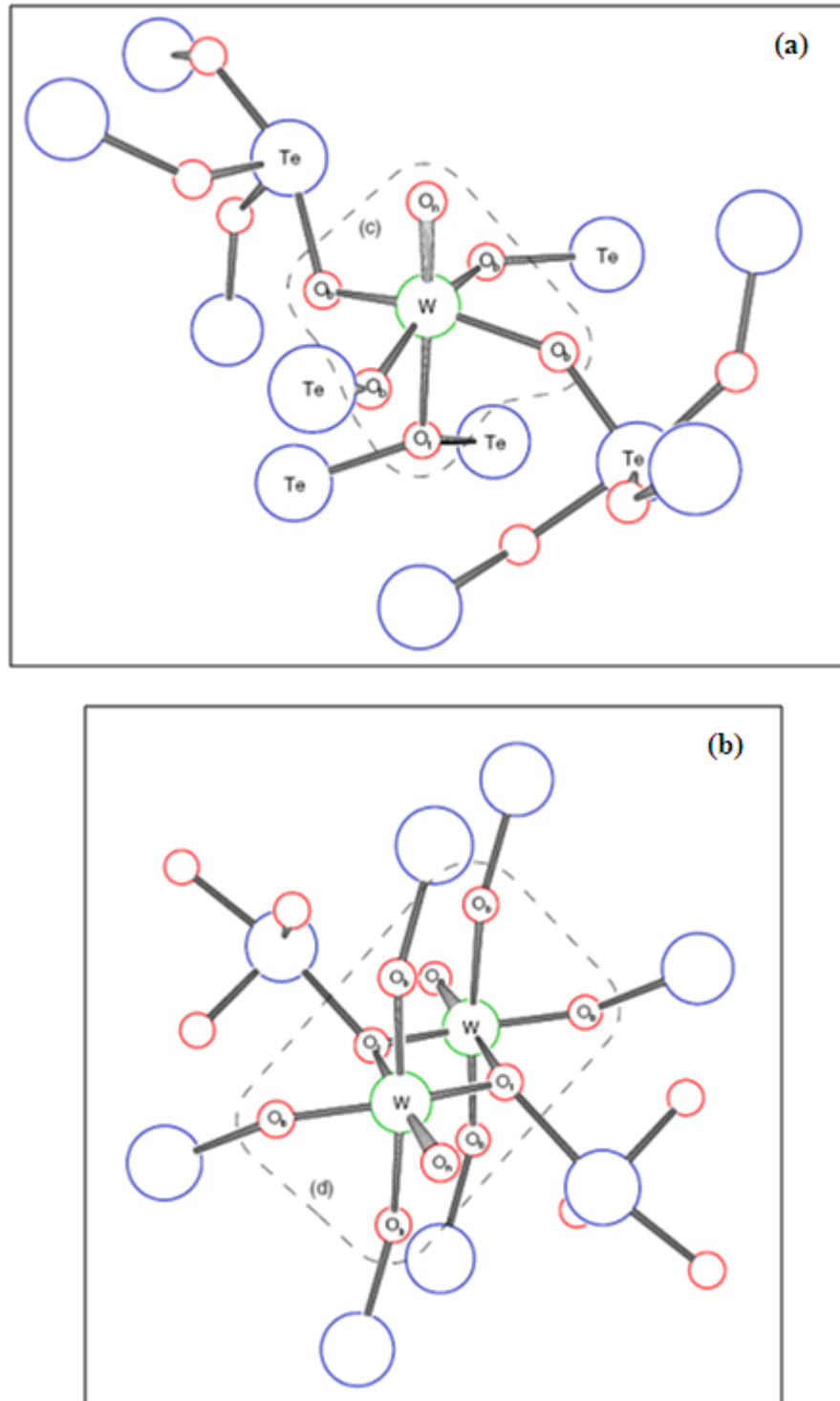


Figure 2-7 The calculated configuration of groups related to WO_3 in tellurite glass, large circles are Te atom, middle circles are W atoms, small circles are O atoms. (a) The single sixfold coordinated W atom, $\text{O}=\text{WO}_5$, in tungstate-tellurite glass, O_n is nonbridging oxygen, O_b is bridging oxygen between $\text{O}=\text{WO}_5$ and TeO_4 units, enclosed in the dash line is the $\text{O}=\text{WO}_5$ structural unit; (b) The paired sixfold coordinated W atom, $2(\text{O}=\text{WO}_5)$, in tungstate-tellurite glass, O_n is nonbridging oxygen, O_b is bridging oxygen between $2(\text{O}=\text{WO}_5)$ and TeO_4 units, enclosed in the dash line is the $2(\text{O}=\text{WO}_5)$ structural units [80]

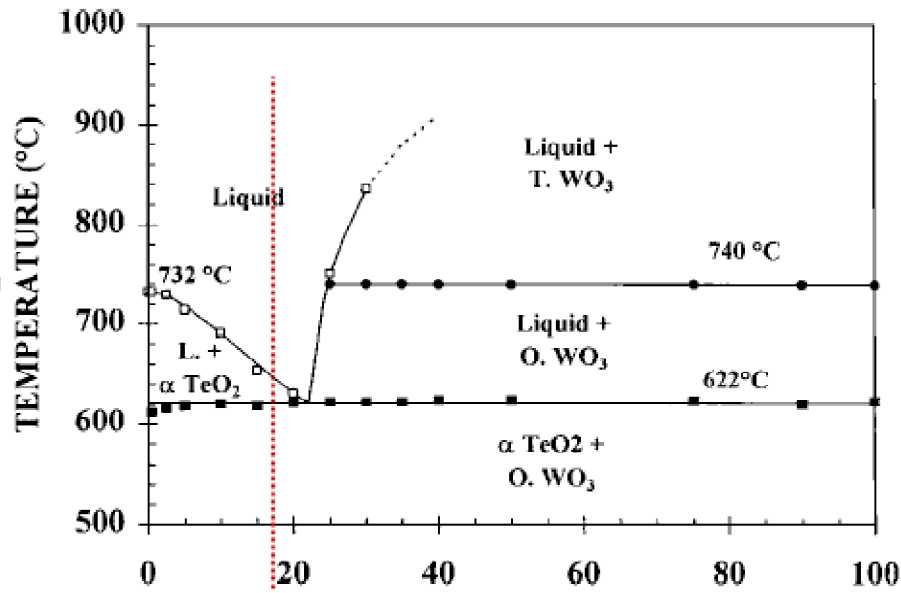


Figure 2-8 The equilibrium phase diagram for the $\text{TeO}_2\text{-WO}_3$ system[81], red dotted line represents the phase transition with temperature when the concentration of WO_3 is 17mol%

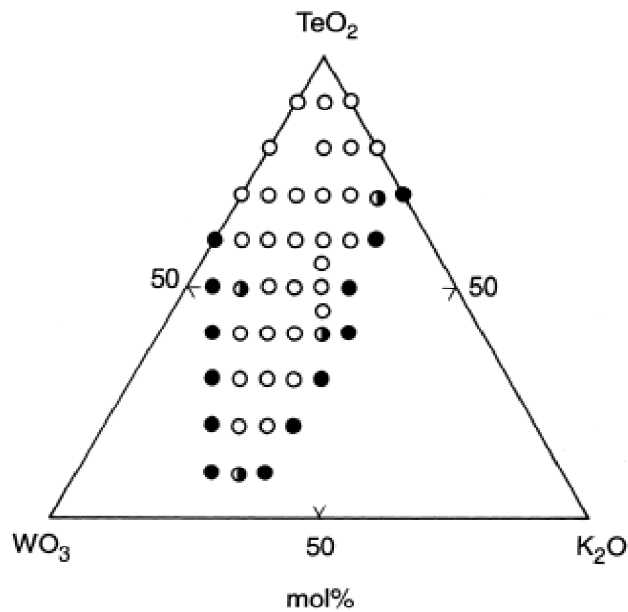


Figure 2-9 The glass-forming region of $\text{TeO}_2\text{-WO}_3\text{-K}_2\text{O}$ system [82]. (○) glass

(◐)partially crystallized, (●)crystallize.

Tungsten modified tellurite glass has been studied extensively. Feng et al.[83] investigated $\text{TeO}_2\text{-WO}_3$ glasses doped with Yb^{3+} and then studied the thermal properties, the absorption and emission cross-section of $\text{TeO}_2\text{-WO}_3\text{-La}_2\text{O}_3$ glasses. Their results showed that these glasses have good glass forming ability and the absorption and emission data indicated a potential for Yb^{3+} doped material as a 1.02 μm laser source. Churbanov et al. [61] fabricated $\text{TeO}_2\text{-WO}_3$ and $\text{TeO}_2\text{-WO}_3\text{-La}_2\text{O}_3$

glasses in 2005, and the results indicated that these kind of glasses have potential applications of fiber laser. However as far as the present work is concerned, the glasses co-doped simultaneously with the three rare-earth oxides (Er_2O_3 , Yb_2O_3 , CeO_2) to modify their optical properties have not previously been reported.

2.3.2 Tellurite glass thin films

Compared to crystalline materials, glassy materials have numerous merits, such as low price, easy production in large quantities and the quality can be modified easily by adding other modifiers[88]. Moreover, tellurium oxide-based thin films have dominant advantages among the glass materials: optical non-linearity, high transparency, broad fluorescence bandwidth, comparatively high fluorescence decay lifetime and also high thermal and chemical stability. The comparison of thermal and optical properties of erbium doped glass with different host materials are listed in Table 2-2. Based on the above mentioned advantages, tellurite glass also has a promising potential for applications in integrated optical devices.

Table 2-2 Spectroscopic properties of Er^{3+} doped glass in different hosts

Glass compositions (mol%)	FWHM (nm)	Emission cross section ($\times 10^{-21} \text{cm}^2$)	Lifetime $^4\text{I}_{13/2}$ (ms)	Refractive index	$T_g(^{\circ}\text{C})$	CTE ($\times 10^{-6}/^{\circ}\text{C}$)
72TeO ₂ -17WO ₃ -10.5La ₂ O ₃ -0.5 Er ₂ O ₃	73	6.5	5.3	2.10	436	13
80TeO ₂ -10ZnO -10Na ₂ O-1wt%Er ₂ O ₃ [85]	65	8	5.0	2.00	290	0.55
70.7SiO ₂ -1.5Al ₂ O ₃ -12.0CaO-1.5Li ₂ O-10.5Na ₂ O-3.9K ₂ O-0.005Er ₂ O ₃ [89]	45	5.5	10.0	1.45	1200	12-15
60Bi ₂ O ₃ -35B ₂ O ₃ -5Na ₂ O-0.5Er ₂ O ₃ [52]	73	7.0	1.90	1.95	435	6
64P ₂ O ₅ -12Al ₂ O ₃ -3.5(Er ₂ O ₃ +La ₂ O ₃)-20.5BaO [90]	37	6.4	8.0	1.54	365	9-25

Tellurite glass thin films were produced using different fabrication techniques in the past. For example, Nayak et al.[88] fabricated the tellurium oxide glass thin films using radio frequency (RF) reactive sputtering, and the thin films obtained exhibited a large band gap and a high refractive index value (2.042-2.052) with low dispersion over a wavelength range of 500-2000 nm. Thus, it is appropriate for application in optical waveguides. Intyushin and coworkers [91] prepared erbium doped tungsten-

tellurium oxide glass thin films by radio-frequency magnetron sputtering deposition method. They measured the optical properties and PL of the resultant thin film, and also calculated the Judd-Ofelt parameters. Their papers provided rich information on tungsten-tellurium oxide glass thin films which can be used to compare with the thin films obtained by PLD. Lecomte et al.[92] prepared the TeO_2 thin films by sol-gel methods.

Generally, tellurite glass thin films were prepared using many different techniques as discussed above, while fabrication of tellurite glass thin films using PLD approach is rare although thin films produced using the PLD technique is quite common, especially for ZnO thin films [93-96]. Wang et al.[97] investigated the optical properties of ZnO modified tellurite thin film fabricated by PLD and MBE, and their results showed that with the incorporation of high oxygen pressure, the thin film exhibits increased transparency and more TeO_x amorphous formation. Martino et al.[98] deposited erbium doped TeO_2 -ZnO- Na_2O thin films and obtained high quality thin films. Even though PLD has the advantages of simplicity, excellent composite preservation, and high deposition speed, it is a complex process. There are no optimal deposition conditions for all the materials are reported so far. As a result, the research on thin film fabrication using PLD has a large room to develop.

2.4 Polymer and polymer-glass composite thin films

Compared to conventional inorganic materials, polymers can be processed easily with adjustable properties[99]. In addition, the polymer thin films may be fabricated using various techniques, namely, dip coating, spinning coating, film casting and printing, etc, which are low cost and less complex techniques. Furthermore, polymers have a high transparency and low propagation loss which are crucial optical properties for devices. As results of these merits, polymer materials have been used to fabricate a variety of optical devices, such as splitters, couplers, filters, modulators, and amplifiers. The advantages of the polymer waveguides include compatibility with the board-level electronic packaging, lower production cost, easy fabrication of complex structures, compatibility with silicon (Si) and gallium arsenide (GaAs) fabrication technologies, good dielectric properties as well as the good mechanical and chemical stabilities[100]. Therefore, the optical polymers are

considered as attractive materials in the field of optical engineering due to the above mentioned advantages.

2.4.1 Optical polymer materials

There are many kinds of polymers with different applications according to their mechanical, physical and chemical properties. Among these polymer materials, one group which exhibits high resistance properties, low propagation loss and many other excellent optical properties is known as optical polymer and can be used to fabricate optical devices. Generally, the optical polymer materials can be divided into several groups, namely, acrylates, siloxanes, polyimides, polycarbonates and olefins [101].

In the early history of optical polymer research, acrylates were a popular choice for most of the optical material research groups as the candidate of polymer materials for optical devices application. In the late 1960s, DuPont demonstrated the first step index (SI) polymer optical fibers (POF) and from then the research of the POF became prevalent for several decades [102]. Another crucial polymer used as the core of the fiber is polymethylmethacrylate (PMMA). As a result of the strong C-H absorption and Rayleigh scattering, the minimum loss of PMMA fiber is as high as 100dB/km. The only way to reduce the loss of the PMMA material is to replace the hydrogen by heavier atoms, like fluorine [102]. Besides the loss property, the other two key factors of the polymer materials for POF system are to have excellent thermal stability and long-term reliability [103]. Therefore, the research on the optical polymer materials was focused on the improvement of their optical, thermal and resistant properties. Koike and coworkers [103] prepared a perfluorinated polymer-based POF and their results showed that attenuation of perfluorinated polymer (45dB/km@ 1.3 μ m) improved significantly compared to that of PMMA material (\geq 100dB/km). An alternative polymer material with better stability is polycarbonate with glass transition temperature as high as 150 °C compared to that of PMMA 105 °C [104].

Among these polymers, siloxane polymer as a new developing optical material is a special category which can be seen as a hybrid of inorganic and organic materials. Siloxane polymer exhibits excellent thermal stability, chemical resistance, adjustable

refractive index and mechanical properties in addition to relatively low optical loss and high transpance [1, 105]. The main properties for different polymers are compared in Table 2-3.

Moreover, the optical mechanical and electrical properties of siloxane polymer may also be tailored according to the specific application. Based on this knowledge, it became easier to choose suitable siloxane polymer for different applications. For example, if the siloxane polymer is used in bio-optic application like creating contact lens, a diphenyl functionalized siloxane polymer with refractive index between 1.43 and 1.46 is required. Brunchi [106] investigated the properties of some polysiloxanes, and concluded that the refractive index could be adjusted by changing the ratio of molar refraction to molar volume, and the transmittance of the siloxane polymer is also possible to be modified by changing the end groups.

Table 2-3 The thermal and optical properties of various polymers

Polymers	loss dB/cm	Refractive index	Transmittance	Operating temperature(°C)	CTE (x10 ⁻⁶)
Siloxane polymer[105]	≤0.01@850 nm	1.4-1.5@633 nm	85%@248 nm 60 μm thick	150	300
PMMA[107, 108]	0.2@1060 nm	1.49@633 nm	78%@250-500 nm	85	200-300
Polycarbonate[109]	0.2@633 nm	≈1.60@1550 nm	99%@350-1500 nm 3 μm thick	120	70
Fluorinated polyimide[110]	0.1@1550 nm	1.52@1330 nm	≈97%@1300 and 1550 nm	≤300	80

The use of siloxane polymer for optical applications has been demonstrated extensively in the literature. Brown [111] fabricated siloxane polymer planar optical waveguide using spinning coating technique, and studied the optical properties of the thin films. Watanabe [112] presented a directional coupler, an arrayed waveguide (AWG) multi/demultiplexer and a thermo-optic switch using siloxane polymer material. Ingham and coworkers [113] proposed a multichannel waveguide using siloxane polymer material by directly spin coating on PCB substrate and the waveguide obtained exhibits a low loss of 0.03-0.05 dB/cm at 850 nm. Dangel et al. [114] illustrated optical waveguides, namely, transmitter and receivers using siloxane polymer by laser writing technique for the application of optical

interconnect linkage. Bamiedakis and his colleagues [1] demonstrated siloxane polymer channel waveguides which loss was 0.04 dB/cm. All the waveguides discussed above are used as passive devices due to the shortage of active elements.

To engineer active waveguide devices, siloxane polymers with active components are required. Basically, there are two kinds of active components, the organic dyes and rare earth ions. Diré et al. [115] prepared a dye doped siloxane polymer using sol-gel technique and obtained strong emission spectrum from this material. Siloxane polymer doped with a variety of rare earth ions using sol-gel technique has been demonstrated [116, 117], and the optical properties of the rare earth doped siloxane polymer were investigated as well. These materials with dye or rare earth ions could be used to make active optical device. However, organic dyes are susceptible to photobleach and have a high quenching rate resulting in a low radiation lifetime in an order of nanosecond [118] compared to that for RE ions of microsecond [12]. Therefore, the researchers prefer to use the RE ions as the active elements instead of organic dyes. However, due to their different chemical and structural properties, it is difficult to dope high concentrations of Er-ions in the polymer without concentration quenching which yields a short radiative lifetime of less than 1 ms for the $^4I_{13/2}$ to $^4I_{15/2}$ transition [117].

Therefore, one of the main motivations in this work is to fabricate polymer composite thin films to overcome the problem of radiation quenching caused by clustering in the RE doped polymers. As a part of the overall investigation, the thesis also investigated the techniques for the formation of glass-polymer composite.

2.4.2 Glass and polymer composite thin films

Organic and inorganic hybrid materials have been prepared extensively using one of the prevalent methods, sol-gel technique, in which the monomer solvents were diffused into the pores of the inorganic materials and then polymerized. This kind of composite material has been engineered for the applications of lasing, optical power limiters, optical switches and optical storages.

Glass and polymer, as two crucial materials for the optical devices, nowadays have been applied comprehensively to manufacture a range of optical devices due to their

excellent thermal, mechanical and optical properties as mentioned in Chapter 1, section 1.2. Different glasses have been developed for active and passive optical devices, like amplifiers [11], lasers [29] and switches [119]. On the other hand, polymers as an optical material possess many advantages over traditional materials, like glasses, or semiconductors, and hence they are good candidates for passive optical devices application. However, its ability for engineering active devices is restricted due to their immiscibility with rare earth salt precursors [120] as mentioned in the above section.

There is no single optical material which is capable of meeting all the necessary requirements for optical properties in a complex optical circuit. As summarized in Table 2-2 and Table 2-3, the excellent optical and thermal properties of glass and polymer prompted people to try to make glass and polymer composites to combine their advantages and minimize their limitations. However, the mismatch of the thermal expansion and refractive index between glass and polymer used can cause cracking and delamination of the composite. Therefore, it is important to choose glass and polymer with similar properties to reduce the dispersion loss.

Glass-polymer composites have been engineered to meet the requirement of the novel materials in many areas as summarized in Table 2-4. O'Brien and coworkers [121] prepared glass and polymer composite for military application by infiltrating nanoporous glass with methyl methacrylate (MMA) and then polymerized the monomers in situ. The obtained composite is transparent, lightweight with excellent optical and mechanical properties. Glass-polymer composite has been fabricated to overcome the brittleness and low conductivity of the glass [122]. Furthermore, polymer and glass composites has been used as scaffolds materials to make bone grafts for sake of their improved mechanical properties and compatibility with other human tissues[123]. Iba and his colleagues [124] demonstrated a glass and polymer composite which has improved mechanical properties (increased tensile strength and Young's modulus) and comparable transmittance (as high as 50%) by filling the glass fiber into the epoxy matrix.

As mentioned previously, the fabrication of hybrid organic-inorganic siloxane polymer composites is based on the sol-gel technique [125, 126]. The quality of composite materials obtained using this technique is diminished by the O-H (3400 cm^{-1}) or C-H (2950 cm^{-1}) quenching due to their energy resonance with the transition $^4I_{13/2} \rightarrow ^4I_{15/2}$ (6500 cm^{-1}) in rare earth ions [12]. Herein, we utilized a novel technique (PLD) to engineer composite thin films which could solve this problem properly. PLD is a fast and efficient technique to prepare thin films suitable for various compositions and has a precise control over the thickness of the layers. Furthermore, this technique could be used to make multilayer thin films using more than two target materials. Part of our work in this dissertation is to make a dual layer glass and polymer thin film which was prepared using PLD by depositing the glass onto the polymer substrate. This polymer substrate was prepared by directly spinning coating onto silica substrates [127]. Another way is to deposit both glass and polymer materials commutatively and produce multilayer composite thin films used as optical materials, which is a new concept.

If the multilayer composite thin film has a structure of two materials, deposited alternately in spatially periodic layers with thicknesses of each layer on a scale of 1-10 nm, this composite thin film can be treated as a superlattice [128]. Since the first report on a superlattice structure of dissimilar crystalline materials Nb and Cu in 1980 [129], there have been innumerable examples of such structures with reference to the control of the electronic properties of crystalline semiconductor materials. The advent of MBE has enabled the lattice-matched superlattice structures of GaAs and AlAs for making AlGaAs devices [130, 131]. Other types of superlattices investigated in the past include amorphous silicon [132], polymer only [133], and superconductors [134]. Pulsed laser deposition is one of the most important techniques used for growing superlattices of crystalline materials [135]. This approach can be extended to several applications involving the growth of composite materials of polymer and carbon [136], graphene and silica [137] as well as glass and polymer [121, 138]. In this thesis, a superlattice structure of phosphate modified tellurite glass (PT) glass and siloxane polymer composite thin film was prepared using PLD technique. It is worth mentioning that the incorporation of RE ions with active optical functionality is reported for the first time in a glass-polymer

superlattice structure, which is especially important for engineering a structurally stable and compatible glass-poly(dimethylsiloxane) (PDMS) amplifying medium. Also, in a polymer waveguide, continuous pumping at IR wavelengths increases the photo-sensitivity which can be minimized in a superlattice structure of Er-ion doped glasses and undoped PDMS, for example.

Table 2-4 The application of glass and polymer composites in varioius areas

Glass and polymer composition	Fabrication technique	Improved properties	Application area
Porous silicate glass and PMMA[121]	Infiltration and curing	Strength, lightweight and transmittance	Military application
Lithium-boronated glass and polyethethylene [122]	Mixed and cured	Conductivity and flexibility	Electrolyte application
PLAGA and BG[123]	solvent-casting	Biocompatibility and strength	Medical application
Silicate glass and epoxy[124]	Filled and cured	Tensile strength and Young's modulus	Engineering application

Note: PLAGA: Polylactide-*co*-glycolide 50:50 co-polymer; BG: 45S5 bioactive glass

2.5 Techniques for thin film fabrication

Thin film deposition techniques are widely used in the manufacture of electronics, optics, packaging and other fields. They can be divided into three groups, namely, chemical vapor deposition (CVD), chemical reaction and physical vapor deposition (PVD). CVD is a process in which the volatile compounds are vaporized and the vapor is decomposed or reacted with a gas or other vapours to produce nonvolatile products [139]. Sol-gel thin film deposition belongs to a chemical reaction. PVD is a thermal evaporation, which includes fabrication techniques such as MBE, sputtering deposition and pulsed laser deposition (PLD). All these deposition techniques will be discussed in this section.

2.5.1 Chemical vapor deposition

Chemical vapor deposition (CVD) is a reaction process between one or more gaseous species on a substrate and one of the products is solid which can reach and condense on the substrate to form a thin film. There are several steps in this process [140]:

1. transfer the reaction species to the surface of the substrate
2. the reaction species adsorps or chemisorps on the surface of the substrate

3. species react with each other. In this process, the substrate can be used as a catalyst
4. gaseous byproducts desorb from the substrate and the solid products are condensed on the substrate; and
5. remove byproducts away from the substrate

A CVD system consists of a reactive chamber, thermal heating or plasma energy source, gas carrier and source materials [141]. The schematic setup is shown in Figure 2-10.

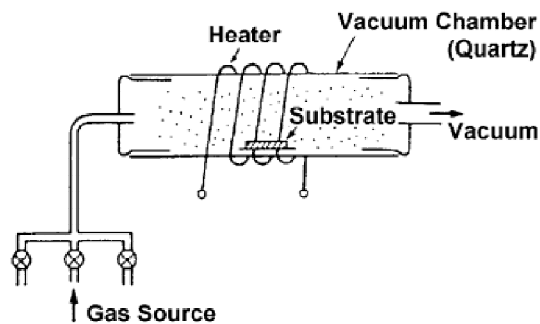


Figure 2-10 The schematic setup of chemical vapor deposition [142]

The CVD process offers advantages to produce excellent uniform thin films around whole substrates which might be difficult to achieve using PVD deposition techniques. In addition, the risk of contamination is reduced due to the presence of favourable chemical specimens, e.g. the presence of chlorine and oxygen gas mixture can reduce the contamination when fabricated silica thin film using SiCl_4 . Furthermore, it has a high deposition rate and a low vacuum level requirement in this process. The disadvantages for CVD are that the precursors are generally highly toxic and some of the byproducts are hazardous. Moreover, there are some limitations for the substrates due to their high deposition temperature [143].

CVD system can be modified according to the requirement of the thin film fabrication based on the main CVD techniques and be classified into different groups. Depending on the pressures used, the CVD may be divided into low pressure CVD (LPCVD)[144] and ultra-high vacuum CVD (UHV CVD)[145]. According to the precursor used, there are metalorganic CVD (MOCVD)[146]. Based on the energy source, there are plasma enhanced CVD (PECVD) which was used extensively [24,

147] and microwave plasma CVD [148]. There are some other CVD methods which are not used widely, like catalytic CVD (CCVD)[149] and atomic layer CVD[150]. The different CVD classifications are listed in Table 2-5.

In terms of applications, CVD is a versatile deposition technique which could be used to prepare nano-tube and nano-fibers [151], semiconductor thin films [152], diamond thin films [153] and light emitting diodes [154].

Table 2-5 The different group of CVD depends on different classification basis

Types of CVD	Classification based on	Materials	Others
LPCVD[144]	pressures	diamond and cubic boron nitride,	Superhard materials
UHV CVD [145]		Silicon	Epitaxial channel technology
MOCVD[146]	Precursor	Mg-doped p-InGaN	high-quality Mg-doped III-nitrides
PECVD[24, 147]	energy	Carbon nanotubes	Well aligned
microwave plasma CVD[148]		Carbon nanotips	High aspect ratio carbon nanotips

2.5.2 Sol-gel coatings

Sol-gel coating is a method using metal compounds in alcoholic solutions to make thin films through hydroxylation and polycondensation at the temperature of about 500 °C[155]. Together with sol-gel material preparation, the process of sol-gel coating is carried out via dip coating and spin coating processes. These processes are used to coat on different shape substrates, for instance, the dipping process is used for rod, tube, pipe or fiber coating, while spinning coating is used for plane disk. Among these processes, dip coating process, with the schematic setup shown in Figure 2-11[155], is used more extensively in the sol-gel coating applications. In sol-gel process, a complex reaction between the compounds, and different processes for specific thin film materials have their own mechanical principles [156].

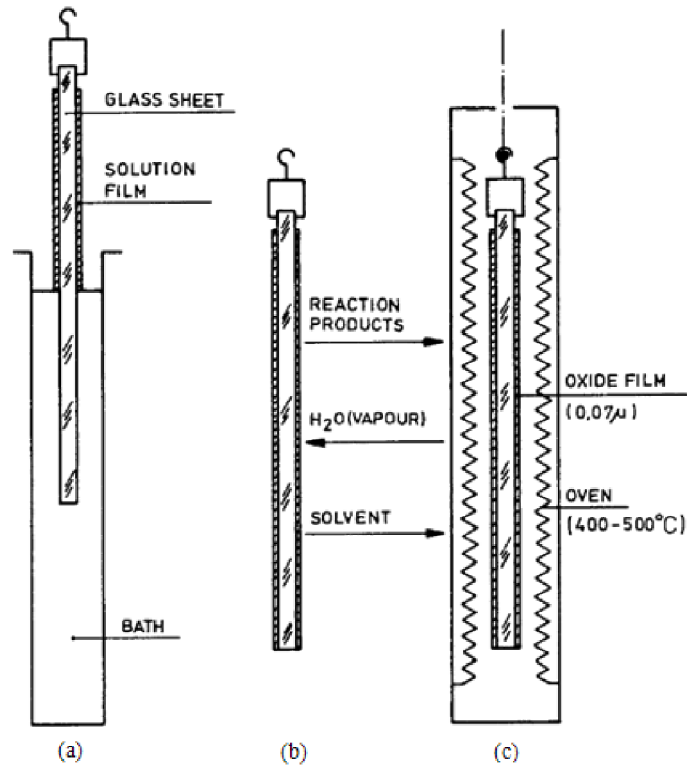


Figure 2-11 The schematic setup of the dip sol-gel coating process[155]. Processes (a) drawing, (b) chemical reaction, (c) baking.

The sol-gel technique which is still immature offers a low cost thin film fabrication method. In addition, the samples obtained using sol-gel have a high purity and chemical homogeneity. Furthermore, the sol-gel process allows atomic scale mixing with an opportunity to control the microstructure. Although the sol-gel was derived from materials in a gel state, its application was extended significantly for applications in engineering optics, protective and porous films in addition to optical coatings [157].

2.5.3 Spin coating

Spin coating is a simple and widely used thin film fabrication technique. It is a process in which the liquid material is dropped onto a rotating disk and then spreaded into a uniform film under the centrifugal force. The resulting thin film is condensed on the substrate with the help of baking and evaporation to release the volatile matters. It usually includes three steps [158]:

1. drop solution onto substrate which is fixed by the vacuum.
2. wait until the solution spreads around the surface of the substrate uniformly and in this process, the air bubbles could be removed as well; and

- turn on the spinner and the trunk with substrate will rotate with the set speed, and then transfer the substrate with films to the hotplate to vaporize the versatile solvent and the solid uniform thin films obtained.

These steps are shown schematically in Figure 2-12.

The thicknesses of the thin films obtained relate to rotation speed, viscosity and density of the solution, and the spinning duration. Precisely, it is proportional to the viscosity and density of the solution and inversely proportional to the rotation speed and spinning duration. This indicates when the viscosity and density of the liquid increase, the thicknesses of the thin films increase accordingly, while when the rotation speed and spinning duration rise, the thicknesses of the films reduce in contrast.

The spinning coating technique was widely used on the microelectronic industry for the photoresist coating on the silicon, like S1813, PMMA, and SU8. Nowadays, this method also is used to prepare the sample before etching to make channel waveguide in the RIE which will discussed in detail in Chapter 6.

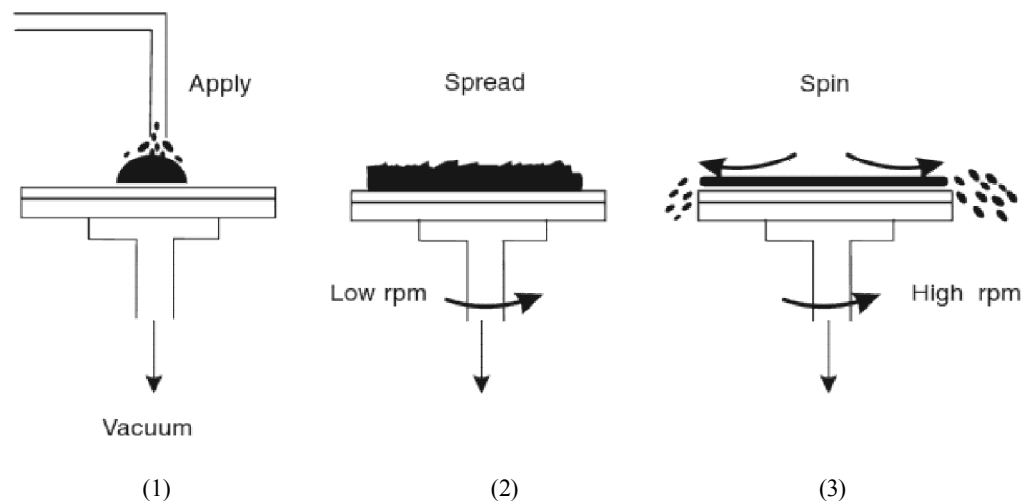


Figure 2-12 The schematic process of the spin coating process [158]. Step 1, put substrate on the chuck, turn on the vacuum, and put solution on the substrate, step 2, leave for a while to obtain a smooth liquid surface, step 3, turn on the machine, rotate the substrate to get thin film

2.5.4 Thermal evaporation

Thermal evaporation is a method to vaporize materials in a vacuum chamber using heat energy. Michael Faraday was the first person who employed this technique using metal wires as the target in vacuum in his experiments[141].

Two primary evaporation sources for this technique are resistance and electron beam heating. The setup of this technique is shown schematically in Figure 2-13. The equipment for this technique include a vacuum chamber and source material holder or container. The holders, containers are generally wire coils and boats made of refractory materials such as tungsten (W), molybdenum (Mo), tantalum (Ta) with or without ceramic coatings. Another container form is crucible which is usually made of quartz, or alumina, or boron-nitride [139]. These holders or containers and the source materials are shown in Figure 2-14. When there is electric current passing through the source material holder, the heat produced by the resistance can melt and evaporate the source material. Finally, the vaporized material condenses on the substrate to form a thin film, subsequently.

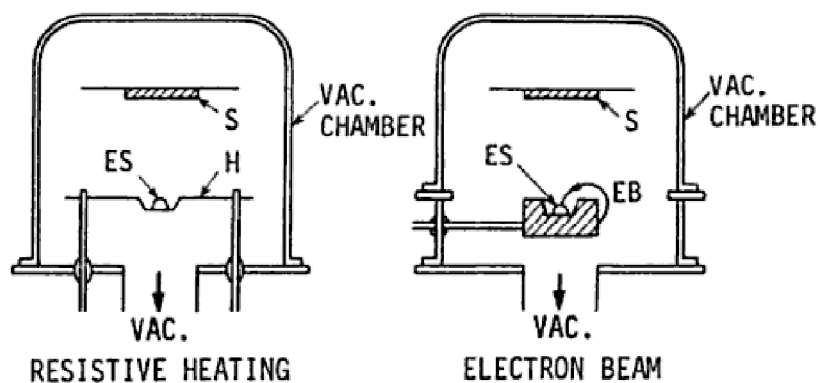


Figure 2-13 The thermal evaporation process: ES: evaporation source; S: substrate; H: heater; EB: electron beam [139].

Thermal evaporation has advantages of simplicity and low cost of implementation. However, the rate of deposition cannot be changed very rapidly and the temperature is limited in this technique because both the entire source material and container should be heated to the same temperature. Furthermore, it is difficult to eliminate contamination [141]. There is an alternative evaporation technique, namely electron beam evaporation which may be used for controlling the deposition rate easily and also could reduce the contamination and obtain highly-purity thin films.

Nowadays, thermal evaporation is still being used because of its convenience and low expense. Its applications include fabrication of nanostructures [159], sensors [160, 161], nanostructural functional oxide thin films applied in electronic, optical and optoelectronic nanodevices [162].

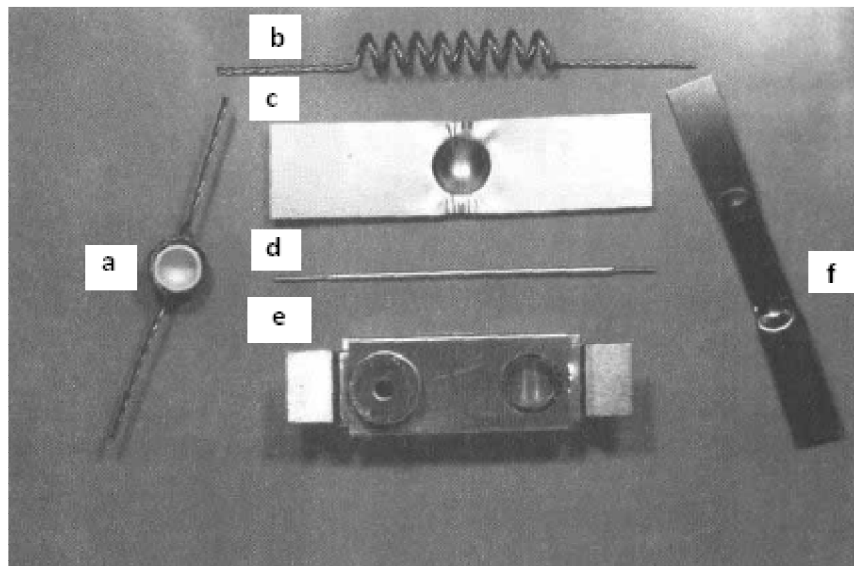


Figure 2-14 Various thermal evaporation sources. a: the crucible source with external tungsten coil heater; b to e: coil heater used for evaporation of metal wires, a dimple tungsten boat used for shot or powders, a chromium rod and a specialized source for evaporation of SiO_2 ; f: the tungsten boat used for metal shot or powder [141].

2.5.5 Molecular beam epitaxy

MBE is a technique widely used for precise and controlled growth of single crystal thin film of semiconductor materials. This technique uses a beam of atoms or molecules in an ultra-high vacuum as the source of energy to deposit target materials onto the surface of the substrates. Epitaxial means the crystalline structure of films obtained is ordered with respect to that of the substrates, on which film is grown [130].

In fact, the invention of MBE was motivated by the requirement of the surface-vapor interaction research. It was a coincidence that the researchers found this technique could be used to grow very perfect and controlled crystalline structures by means of depositing the materials with single atom layers [130]. In 1969, Cho [163] demonstrated the first GaAs crystalline thin films grown using MBE techniques, and his results showed that MBE could grow atomically, flat and well arranged layers. These results opened a door of using MBE to produce thin films with various materials.

MBE has much more stringent requirements than any other deposition techniques. As a result of the difficulty of maintaining an ultra-high vacuum and a strictly

cleanliness requirement for the monolayer growth, MBE system is designed with separate chambers for individual experiments, namely, substrate preparation, actual growth and film analysis. The separated chamber, internal surfaces of which are polished to minimize the adsorption of moisture and gas by the chamber walls are made of stainless alloys[141]. The side cutaway view of the MBE system is shown in Figure 2-15.

To meet the high cleanliness requirement of the MBE grown environment, the substrates should be cleaned very carefully before use. First of all, the substrates need to be degreased and then chemically etched to eliminate the contamination on their surfaces. Afterwards, the surface of the substrates should be protected by a passivation layer of oxide to inhibit the reaction between the substrates and the atmospheric gases [141]. The strict requirements of the ultra-high vacuum and cleanliness make this technique higher expense compared to other deposition techniques.

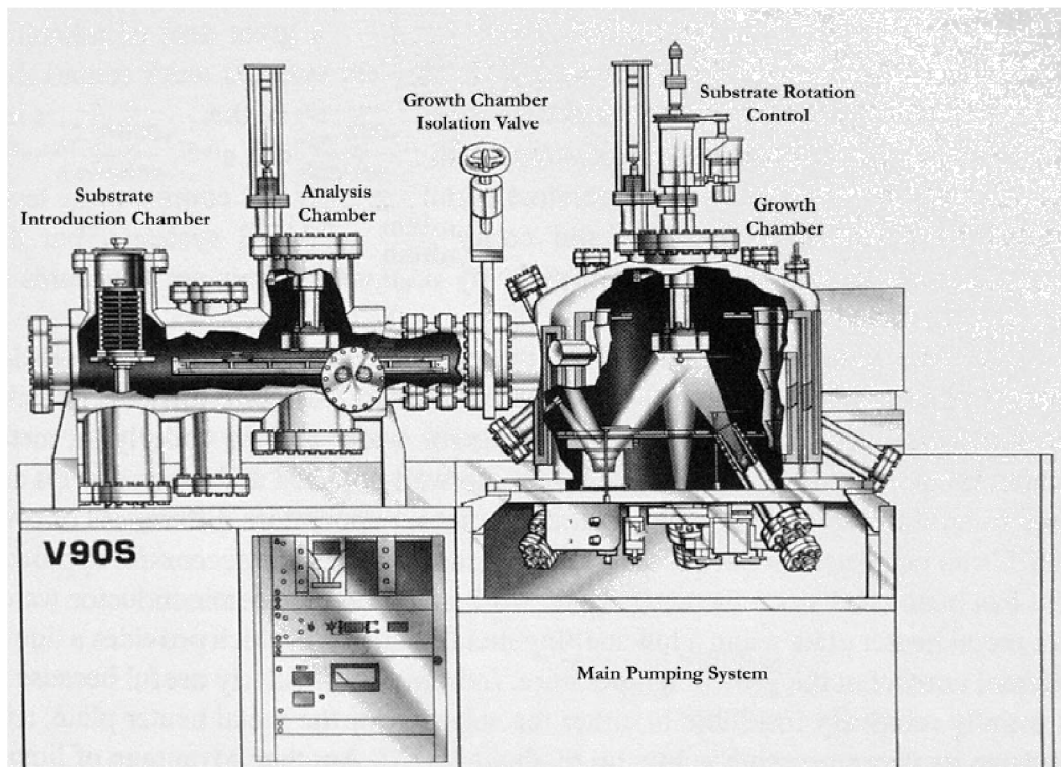


Figure 2-15 The schematic setup of a MBE system [130].

MBE is a slow material growth process with extremely precise dimension control. It can control both the composition and dopants on an atomic scale which is almost unfeasible using any other thin film fabrication techniques. In addition to the

aforementioned advantage of this technique, its growth process has a comparatively simple growth mechanism and is possible to be analysed in situ before, during and after the growth processes. This feature, which saves the time of optimizing the growing parameters, was proved to be invaluable for comprehending and modifying the deposition process [164].

Thanks to all the advantages above mentioned, MBE is used extensively for high-quality crystalline thin film deposition and nanostructural devices engineering. For instance, it was used for growing semiconductor thin films [165], superconducting thin films [166], photodiodes [167], optoelectronic diodes [168], and laser diodes [169]. All in all, MBE is a suitable and excellent choice for the engineer of crystalline thin film and devices with precise nanostructure.

2.5.6 Sputter deposition

Different from any other PVD techniques, such as thermal evaporation and MBE, sputtering deposition is a process of bombardment instead of thermal evaporation. Sputtering deposition was developed in order to deposit refractory materials which have very high melting temperatures and are difficult to deposit using traditional thermal evaporation. It is a physical vapor process in which the target material is removed by the bombardment of the positive ions emitted from the rare gas discharge [141]. The removal happens via the momentum transfer between ejected atoms with surface atoms caused by a series of collisions [170]. The sputtering process is shown schematically in Figure 2-16.

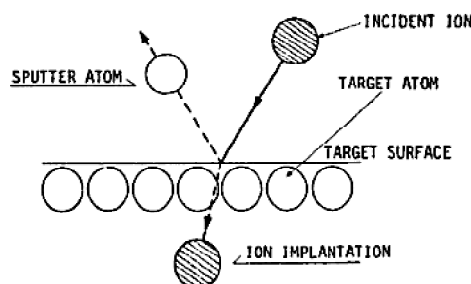


Figure 2-16 Diagram of sputtering process ○ represent sputtered atoms[139], ⊗ represent incident ions. Due to the ion implant phenomenon, there are some gas ions in the deposited films.

According to the power supply, sputtering deposition is divided into three categories, direct current (DC) diode sputtering, radio-frequency (RF) sputtering and magnetron sputtering.

A DC sputtering system consists of a cathode with target material and an anode with substrate, both of which are placed in a vacuum chamber. Basically, inert gas such as argon is filled in the chamber. When the discharged gas ions are incident on the target surface, high accelerated ion-ion bombardment occurs, and the target material is deposited onto the substrate. When the chamber is filled with reactive gases, namely oxygen or nitrogen, chemical reaction happens and produces compound thin films with proper metal targets. This sputtering process is known as reactive sputtering [139].

DC sputtering is a basic sputtering model which is usually used for the conductor materials. However, with respect to the deposition of insulator material, the sputtering glow discharge cannot be maintained because of the formation of the surface charge from positive ions on the front side of the insulator material. As a result, magnetron sputtering was developed to sort this problem out [139].

Basically, a sputtering system includes a vacuum chamber, sputtering source, vacuum sensor, substrate holder and a pumping system. The schematic setup of the equipment is shown in Figure 2-17.

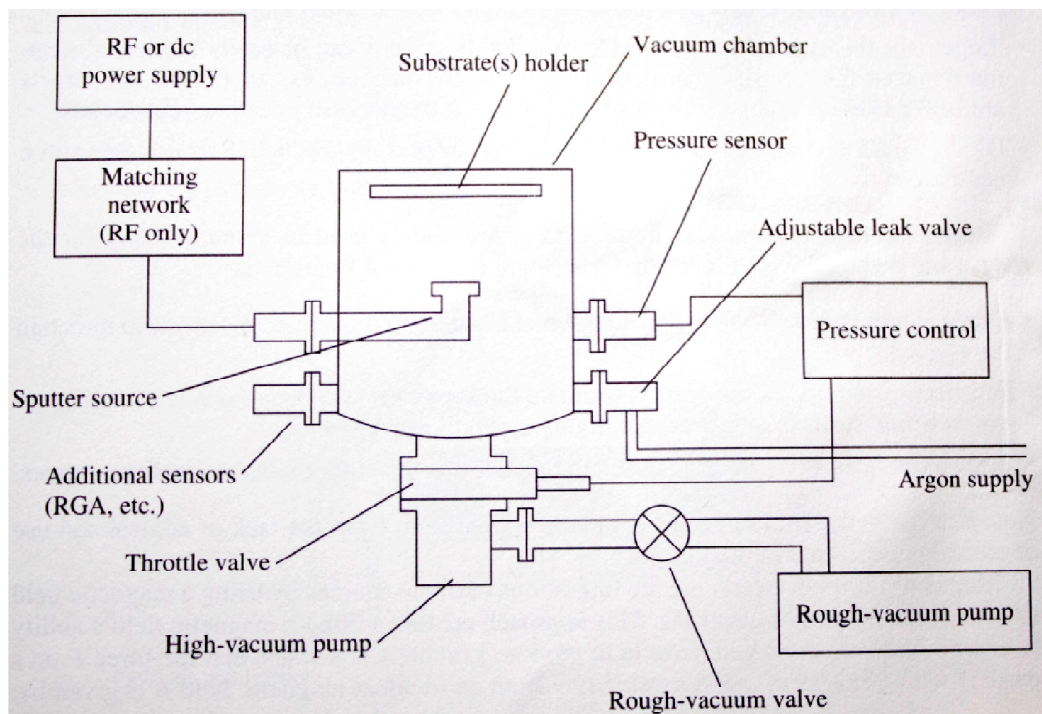


Figure 2-17 The schematic setup of the sputtering system [141]

Sputtering deposition has become one of the most versatile thin film fabrication techniques till now. It is especially useful when large area thin films are required. As a result of such a physical deposition process, refractory materials, i.e. W, Ta and Mo thin films may be prepared easily at much lower temperature than their melting point. Therefore, most of the refractory material thin films were obtained utilizing this technique [141]. In addition, this technique also can be used for superconductor and alloy materials [171, 172].

2.5.7 Pulsed laser ablation

As a thin film fabrication technique, PLD employs either a nano or fs laser as the energy source to ablate the target material and produce thin films. Primary sputtering mechanism includes collisional, thermal, electronic and exfoliation sputtering as well as a condensation process. In a PLD process, all the four ablation mechanisms are involved, however, the main mechanism is believed to be thermal sputtering in all nano second pulsed laser ablation process[173].

The PLD technique was first demonstrated by Smith and Turner in 1965[174], however the development of this technology remained at a standstill until the first major breakthrough made in the 1970s when the electronic Q-switch was developed which delivered short pulses with very high peak power density. This impressive progress broadened the area of deposition available materials using PLD. Nevertheless, it was the second breakthrough which initiated the rapid growth of PLD by successfully growing the high T_c superconducting thin films in 1987, boosted PLD development and accelerated it to become a popular technique for thin films fabrication [173].

From 1987 to the present, PLD has experienced a rapid development and massive related literature have been published. However, thin film deposition using PLD is such a complex process that there are many factors affecting the quality of the thin films obtained. As a result, the application of PLD is still relatively restricted.

There are three main factors which make the application of PLD quite difficult: firstly, the surface of the thin film may have a high roughness because of some particles produce Secondly, it is presently difficult to make a large area thin film

using PLD which restricts the application of this method to research laboratories. Finally, due to the limited knowledge on the process dynamics, it is impossible to sort out optimal conditions for all the materials, even for the unary materials and their binary variants.

The PLD process can be splitted into three steps: 1) high power laser beam is incident on a target; 2) the target is ablated into a gas phase to form a plasma plume which includes electrons, atoms, ions and particles; 3) the plasma plume reaches a substrate and the material is deposited onto the substrate which is near and vertically above the target. The schematic setup of the PLD system is shown in Figure 2-18.

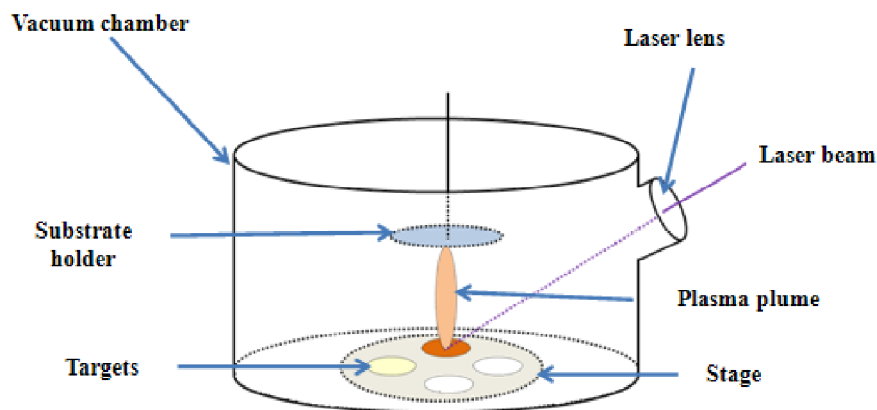


Figure 2-18 The schematic setup of PLD system

From the description of the PLD process, it is obvious that the crucial factors which influence the quality of the thin films are the laser fluence, wavelength, pulse repetition rate as well as the substrate temperature, oxygen pressure, and the distance between the target and the substrate.

Laser fluence and wavelength are two of the most important factors affecting the size and density of the particulates formed on the thin film[173] and also the deposition rate. Laser fluence is related to the laser power and spot size. With an increase in fluence, the size of the particle will increase. For example, Kokai et al.[175]found that both the size and shape of the particles on their boron carbonide thin films are affected by the variation of laser energy. It was also found that the atomic ratios and bonding states also correlated with the laser fluence. Another group found that shorter wavelength lasers could produce better thin films than longer wavelength

lasers[93]. Take semiconductor thin films as an example, the nanocrystallite dimension of the thin films was increased with an increase of wavelength[176].

The substrate temperature choice tends to be as low as possible to minimize the problem associated with thermal mismatch. Typically, the substrate temperature should be lower than the melting point of the material. With an increase in the substrate temperature, the film surface roughness tends to be higher. Sucheai et al.[177] found that the surface roughness of their ZnO thin films increased with the rise in substrate temperature. Zhao et al.[178] also investigated the influence of substrate temperature on their ZnO films, and they not only found that the surface roughness increased with the increase in substrate temperature, but also found it was easier to have defects at higher substrate temperatures.

Oxygen pressure has a decisive effect on the fundamental properties of the oxide glass thin films produced by PLD, such as the composition, bonding and chemical structures[179]. Therefore, oxygen pressure plays a key role on the properties of the obtained thin film. For example, when the oxygen pressure increases, the transmittance and crystalline orientation of the ZnO thin film can be improved while the surface roughness increases as well[180, 181]. In addition, oxygen pressure can also influence the deposition rate by changing the shape of the plasma plume[182].

The distance between target and substrate affects the thickness and uniformity of the films. For a given deposition time, the shorter the distance, the thicker the film becomes. On the other hand, if the distance is too large, the deposition flux of ablated material in the plume that reaches the substrate will decrease dramatically. Furthermore, if the distance is increased beyond 5.5 cm, the number of the larger particulates will rise accordingly. However, if the distance changes within a maximum range of 5.5cm, the size of the particulates appears to show no obvious differences [183].

The pulse repetition rate affects the amount and dimension of the particulates on the thin film. While the deposition rate is kept constant, thicker films could be obtained at higher repetition rate. In addition, with an increase in the repetition rate, the size of

the particulates on the thin film surface goes up gradually. Take the thin film deposition of diamond as an example, the reported crystallite diameter tended to increase slowly when the repetition rate rises, i.e. the crystallite diameter was in the range of 100-200 nm when the repetition rate was 5 Hz, while the repetition rate increased to 50Hz, the crystallite diameter rised to 1 μm [184].

There are many other parameters which affect the quality of the thin films, such as roughness of the target surface, the target and substrate rotation rate, the stability of the laser plume, and the atomosphere in the chamber. Roughness of the target surface is possible to decrease by optical surface finishing for minimizing the splashing and, consequently, the size and quantity of the particulates on the films can be decreased[173].

Looking at the development over the last 20 years, PLD nowadays has become a unique, thin film fabrication technique which is much simpler than MBE and shows more opportunities than sputtering for obtaining high film quality and better composition control. Even though, PLD has the feature of target sthoichiometry, however, there are two main drawbacks of PLD. One of them is the stoichiometric uneven ablation leading to a nonuniformity diversity of material in the plume. The other is the difficulty of preparing large area uniform films. The latter could be solved easily by rotating the substrates and the target. Many efforts have been made to reduce nonuniform ablation, e.g. to filter out mechanically the large particles, or to control the plume and polishing target surface. Poor beam quality could produce nonstoichiometric films and some droplets as well [173].

In summary, PLD can be employed for a range of applications[27, 185], for example, waveguide fabrication and carbon nano-tube production. Although PLD technique has so many applications, one of the shortcomings of this method is film nonuniformity which means that there is much more work required to fully understand the mechanism in detail to produce a variety of thin films with different materials successfully.

2.6 Techniques for waveguide fabrication

There are a variety of techniques to “write” microstructures such as the channel waveguide on a planar substrate. For the light sensitive materials, photolithography is thought as one of the best choices to pattern on the thin film. While for the light insensitive material, etching techniques including wet etching and dry etching are usually the good options. This section is focused on an overview of the patterning technologies.

2.6.1 Photolithography

Photolithography is a patterning technique which uses UV light as the “energy source” to write waveguide onto the photosensitive material (known as photoresist) with the help of a developer. There are two types of photoresists, namely, positive photoresist and negative photoresist. The positive photoresist means that the solubility of the material in developer becomes higher after exposure to light. Conversely, the negative photoresist has a lower solubility in the developer after exposure to light [186]. The schematic of the photoresist behaviour is shown in Figure 2-19.

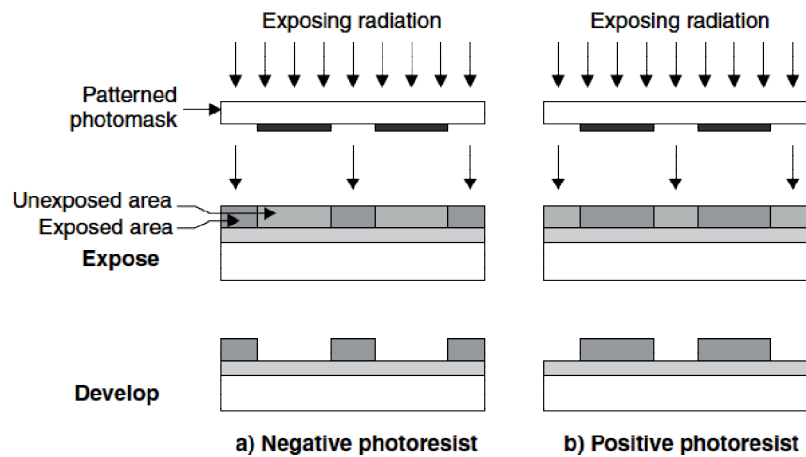


Figure 2-19 The schematic of the photoresist behaviour[186]

There are several steps to pattern the materials which are listed below.

1. spinning coating: the resist is spun coated on a cleaned substrate.
2. baking: after spin coating, the substrate is baked for 1-2 min to solidify the resist.
3. exposure: after baking, the substrate is exposed to the UV light (usually in the range of 200 nm to 350 nm) with the protection of the mask.

4. developing: after exposure, the sample is dipped into developer to remove part of the materials, and patterns obtained.

The above steps may be used to make microstructures on the photo sensitive materials. However, for the light insensitive materials, the etching needs to be carried out to obtain the pattern. The energy sources of the etching may be plasma, electron beam, or chemical solution.

2.6.2 Wet etching

Wet etching is a primitive technique of microstructural fabrication on the planar samples with low cost. It is based on the chemical reaction using etchants, for instance, hydrogen fluoride (HF) solution for the metal oxide, potassium hydroxide (KOH) for metal.

Before the etching processes, the sample needs to be patterned using photolithography technique to protect the areas not suppose to be etched. Once the expected structures obtained, the sample is immersed into the etchant solution for a proper period, and the material in the area without resist protection will be removed while the material in the resist protective area left intact. In such a way, the patterns are transferred to the substrate. After etching, the residual resist is removed to obtain the channel waveguide structure on a substrate.

Traditional wet etching is an isotropic process which means that the material is etched in both vertical and lateral direction as shown in Figure 2-20. As a result, wet etching is not reliable for high resolution pattern transfer. On the other hand, anisotropic etching process is possible when etching depth is small. The schematic process of anisotropic etching is shown in Figure 2-20 as well. Besides, etchants should have a high selectivity. Take silicon as an example, the etchant should etch the silicon much faster than etch the resist. There are three solutions for silicon etching, potassium hydroxide (KOH), ethylenediamine pyrocatechol (EDP) and trimethyl ammonium hydroxide (TMAH). KOH has the highest etching rate for silicon among the three of them, but KOH can etch oxide material fast as well. EDP has a higher selectivity and a limited anisotropic but unfortunately the products are

toxic. TMAH has a reasonable etching rate and a high selectivity which is considered as the most suitable etchant for silicon [187].

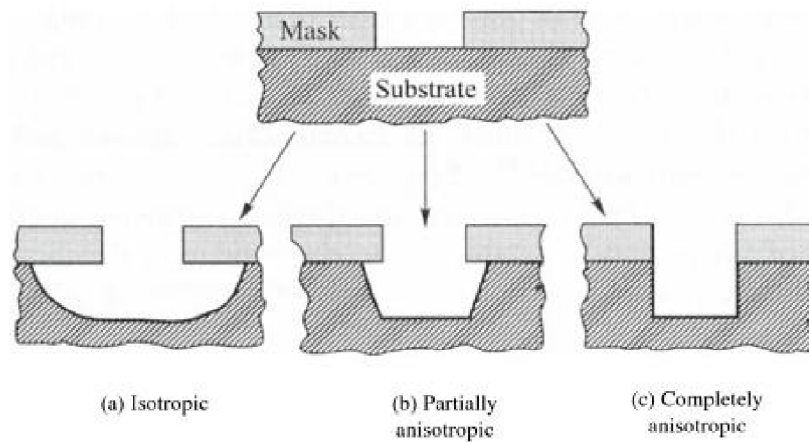


Figure 2-20 The schematic process of anisotropic wet etching: (a) isotropic, (b) partially anisotropic and (c) completely anisotropic[187].

According to the mechanism, wet etching is divided into electrochemical etching and chemical etching. Wet etching includes an anodic, electroless and a photoelectrochemical (PEC), while chemical etching includes conventional etching in aqueous etchants and selective etching [188].

Wet etching is a simple method compared to other etching techniques. Furthermore, it is a highly selective etching method which may help reduce the damage of the sample subsurface. Wet etching can be used not only for semiconductor patterning, but also for defect characterisation, polarity and polytype identification by means of observing photoluminescence (PL) spectra, TEM and SEM images[188, 189].

2.6.3 Embossing

Embossing was first used to fabricate waveguides by Ulrich in 1972 [190]. In his paper, the fabrication process of this technique as shown in Figure 2-21 was explained in detail. First of all, a simple die, e.g. a glass fiber die, needs to be prepared. The glass fiber is put onto the PMMA film, and then a microscope glass slide is put on the glass fiber. At the same time, another glass slide is put under PMMA. This sandwich structure is taken into the embossing press carefully. During the embossing press, a force of around 140 N is exerted on the sample. After that, the sample is heated to above 100 °C in 1 min, and then cooled down to 50 °C in 3 mins. Taking the sample out after all these processes are finished, the fiber is removed

from the PMMA, and there will be a groove on the PMMA sheet as shown in Figure 2-21 (c). This groove is filled with liquid polymer with refractive index higher than substrate to form the waveguide structure [190].

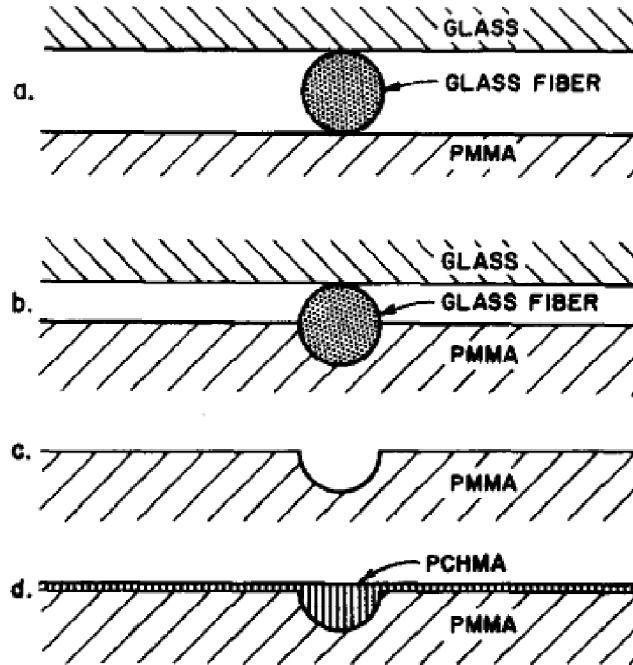


Figure 2-21 The schematic process of fabricating a waveguide using the embossing technique[190]. (a) a glass fiber used as an embossing die; (b) embossing the groove; (c) the embossed groove ready for filling; (d) a filled groove forming the final waveguide structure.

It is clear that embossing is suitable for soft materials like polymers. However, it is very hard to be used for inorganic materials. In 1983, Lukosz [191] demonstrated a method of engineering waveguides with inorganic materials using embossing techniques. The principle of this experiment is to make an organometallic film using sol-gel first, and then emboss the deformable gel thin films at room temperature (RT) as shown in Figure 2-22. The sample is baked at a high temperature, and then the film transferred to an inorganic material with the obtained structure conserved.

Embossing is also a simple and low cost way to make microstructures on a thin film. However, it is limited to be used for a few materials, like polymer or inorganic materials which could be produced through organometallic precursors [192, 193]. This disadvantage restricts this technique to be used widely.

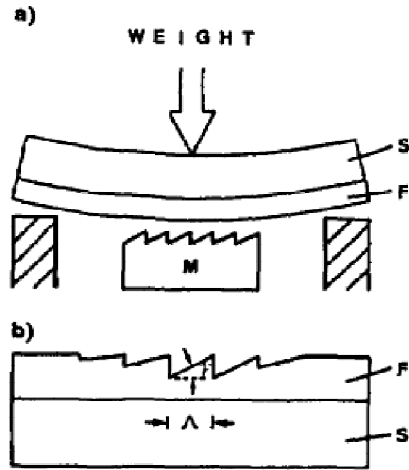


Figure 2-22 Schematic of the embossing process at room temperature[191]. (a), schematic embossing apparatus, Dip coated film F on substrate S is pressed against the blazed master grating M, (b) embossing grating: γ , blaze angle, Λ , grating period

2.6.4 Electron beam direct writing

Electron beam direct writing, as the name suggests, is to use the energy of an electron beam to write high resolution microstructures on thin films or bulk samples without the help of a mask. The electrons are accelerated at a high voltage and focused by electrostatic and magnetostatic lenses. In this way, the diameter of the electron beam is limited to a reasonable size and will not diffract because the wavelength of the electron is an order of angstrom level. The size of the beam is influenced by the uniformity of the electrostatic and magnetostatic lenses. The shape of the electron beam is various, for example, point beam, Gaussian beam or rectangle beam etc. [194]. The schematic setup of the electron beam writing system is shown in Figure 2-23.

The process of electron beam direct writing is similar to that of photolithography. It may be used for the fabrication of microstructures like channel waveguides in bulk samples through modifying the materials to change their refractive index or writing microstructures on a thin layer through changing the solubility of the materials in the developer.

Electron beam direct writing is widely used in the electronic industry, optical devices, and biology, microphotonics and quantum devices [195]. Due to its working principle, this technique is only suitable for electron sensitive materials or materials

with electron sensitive prototype, for instance, organic materials, semiconductor or glasses [196-198].

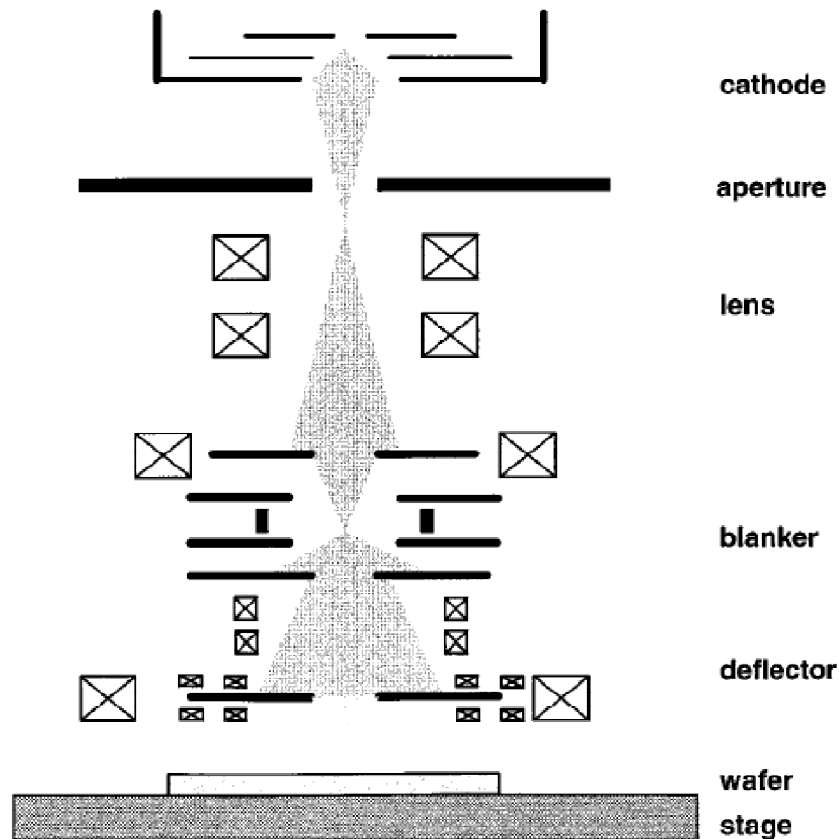


Figure 2-23 Schematic setup of the electron beam writing system [194].

2.6.4 Reactive ion etching

RIE is one of the most widely used techniques for microstructure fabrication. Unlike other microstructural fabrication techniques, RIE process involves both physical and chemical mechanisms to remove material with ion bombardment and chemical reaction[199]. Ionization of the etching gas molecules and sputtering away the material from the surface of the sample are physical processes while transferring material into a versatile compound is a chemical processes [187].

Basically, RIE is carried out in a vacuum chamber with two parallel plates, one of which is connected with the ground and the other is connected with an electrode [200]. The electrons move much faster than the ions, and an electric field can be produced subsequently. As a result, the electrode is negatively charged and consequently positive ions are produced to hit the materials and form ion bombardment [187, 201].

There are several steps in the RIE process [201]:

1. activate the gases into particles including radicals, positive and negative ions, electrons, and neutrals. DC bias is produced to accelerate these ions.
2. active ions hit the material being etched with an extremely fast speed. During this process, some of the materials are bombarded away, and some “active sites” are produced which are useful for the next step.
3. active ions are adsorbed on the surface of the material to be etched
4. the adsorbed ions react with the surface to etch the material and
5. the volatile products in the reaction process desorb from the surface of the materials being etched and are pumped away through the vacuum system.

A schematic of the RIE system is shown in Figure 2-24.

RIE is a complex process including physical ion bombardment and chemical reaction. The phenomena involved in the RIE process are shown schematically in Figure 2-25. It can be seen from this figure that there are four basic kinds of reactions between the ions and the surface of the materials. Process (a) in the figure is showing a pure physical process of removing materials. In this process, the non-volatile products are removed and some “active sites” are obtained which are useful for the chemical reaction process. Process (b) is a pure chemical reaction process in which the reactive ions react with etching material directly and the volatile products are removed by the flowing gas. Process (c) is a chemical reaction process as well however, there is no materials removed in this process. It produces some radicals which adsorbs on the surface of the material subsequently for process (d) in which the radicals react with material to be etched to produce volatile products. These volatile products will be flowed away by the vacuum system [187].

During the RIE process, chemical reaction processes are selective which means it can remove one type of material without affecting other types of materials at the same time. Physical bombardment is an anisotropic process indicating that it removes the material from the depth direction while leaving the same materials on the lateral direction [202]. As a combined process of these two mechanisms, it is necessary to optimize the parameters, namely, the reaction gas flow rate, pressure in

the chamber, and etching gas species to obtain high selective and anisotropic etching results.

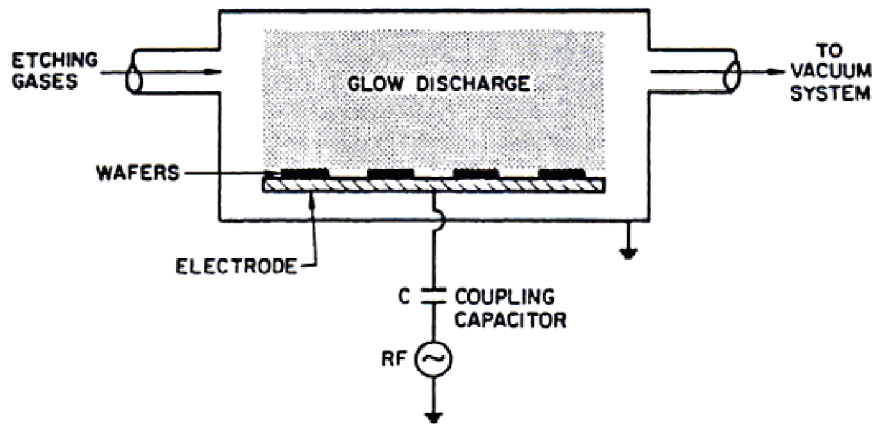


Figure 2-24 Schematic of RIE working system[201]

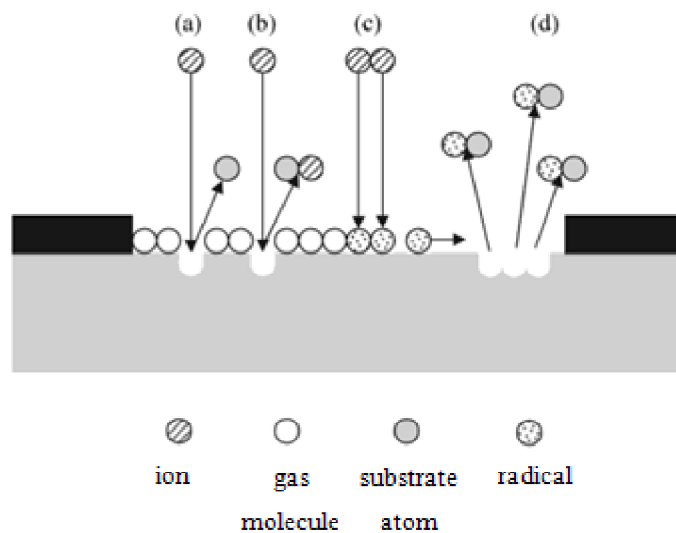


Figure 2-25 The phenomena in the reactive ions etching process[200]: (a), ion bombardment; (b) pure chemical reaction; (c) chemical reaction; (d) chemical process

In the RIE process, ion bombardment is not dominant while chemical reaction is the main source of the etching. Most RIE processes use halogen ions to produce the plasma due to their excellent reaction with most of the inorganic materials. Among these halogen ions (F, Cl, Br, I), F was used more often due to its ability of yielding volatile products at RT temperature when reacted with most inorganic materials [187].

RIE was initially developed for etching materials in the silicon industry, and this is still the main application of this technique. However, the application of RIE has been extended to many other materials, for example, ceramics [203], semiconductor [204] and glass [205]. The gases used and their corresponding etched materials are listed in Table 2-6.

Table 2-6 Etching materials and the etched gases used [187].

Materials to be etched	Chemical gases (multi choices)
Single-crystal silicon	CF ₃ Br, HBr/NF ₃ , SF ₆ /O ₂
Polysilicon	SiCl ₄ /Cl ₂ , BCl ₃ /Cl ₂ , HBr/Cl ₂ /O ₂ , HBr/O ₂ , Br ₂ /SF ₆
Al	SiCl ₄ /Cl ₂ , BCl ₃ /Cl ₂ , HBr/Cl ₂
Al-Si-Cu, Al-Cu	BCl ₃ /Cl ₂ + N ₂
W	SF ₆ , NF ₃ /Cl ₂
TiW	SF ₆
WSi ₂ , TiSi ₂ , CoSi ₂	CCl ₂ F ₂ /NF ₃ , CF ₄ /Cl ₂
SiO ₂	CCl ₂ F ₂ , CHF ₃ /CF ₄ , CHF ₃ /O ₂ , CH ₃ CHF ₂
Si ₃ N ₄	CF ₄ /O ₂ , CF ₄ /H ₂ , CHF ₃ , CH ₃ CHF ₂
GaAs	SiCl ₄ /SF ₆ , SiCl ₄ /NF ₃ , SiCl ₄ /CF ₄
InP	CH ₄ /H ₂
Photoresists	O ₂

Thanks to its high selectivity and anisotropic, the resulting structure fabricated using RIE has a smooth surface and vertical sidewall. As a result, this technique is used widely to make microelectronic devices [206], optoelectronic devices [207] and various semiconductors.

2.6.5 Laser micromachining

Laser micromachining is a technique of fabricating micro/nano structures on the surface of the materials directly using laser beam without the help of a mask. This technique is quite similar to the ion beam direct writing, which has the advantages of maskless writing of microstructures, chemistry reaction in low temperature, and good selectivity. However, there are still many differences between these two techniques. First of all, they have different energetic particles. In the case of beam direct writing, the energetic particles are electrons, protons and ions, while for laser direct writing, the energetic particles are photons. Secondly, the fundamental principle of the interaction of the photon with materials in the laser micromachining is different from that of the beam direct writing. The physical bombardment is necessary in the beam direct writing process, but laser micromachining could finish the writing using only a photochemical reaction [208]. The schematic setup of the laser micromachining is shown in Figure 2-26.

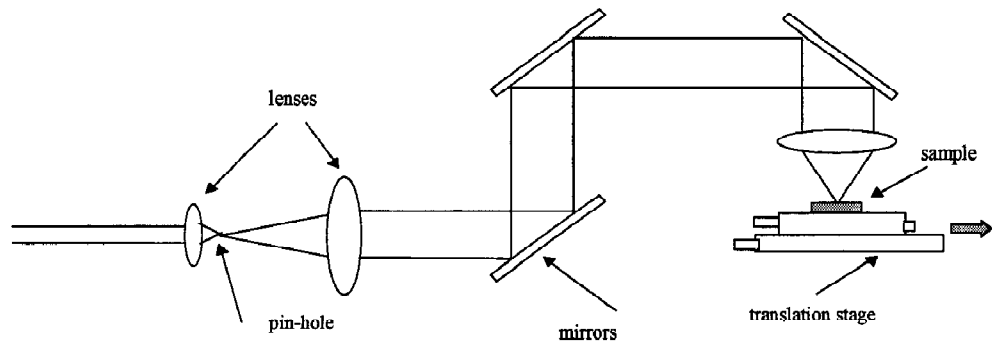


Figure 2-26 The schematic setup of the laser direct writing system [209].

According to the pulse duration, lasers can be divided into five groups: microsecond laser (pulse duration: 10^{-6} s), nanosecond laser (pulse duration: 10^{-9} s), picosecond laser (pulse duration: 10^{-12} s), fs laser (pulse duration: 10^{-15} s), and attosecond laser (pulse duration: 10^{-18} s). Among these lasers, attosecond laser is not commercially available, and therefore, our discussion is focused on the first four classifications. The nano second lasers are widely used to pattern polymers and high quality patterns have been demonstrated [210-212]. However, regarding to the dielectric materials such as glass and ceramics etc., it is not practical to be used due to the absorption of the UV laser (nano second laser) and formation of cracks during the micromachining process[213, 214].

When using lasers with pulse duration of longer than a few tens of picoseconds, it is easy to cause melting and boiling of the dielectric materials as the thermal heat will be transferred to the remaining bulk materials before the pulses expired. This phenomenon is known as thermal shock which could bring about cracks and damage to the patterned structures. fs laser has a much shorter pulse duration, thus the heat has no opportunity to conduct into the bulk materials [214]. For this reason, a fs laser can be employed to engineer micro/nano structures with a precise control of the processing and can manage some writing work which cannot complete using nanosecond lasers.

The micromachining of the bulk metal has been a tough job using nanosecond laser because of the effect of the melting around the writing area which reduces the precision of the micromachining. Thanks to the short pulses of the fs laser, the melting problem was overcome and high quality nano structures can be

achieved[215]. The comparison of the micromachining results on the metal using nanosecond laser and fs laser is shown in Figure 2-27.

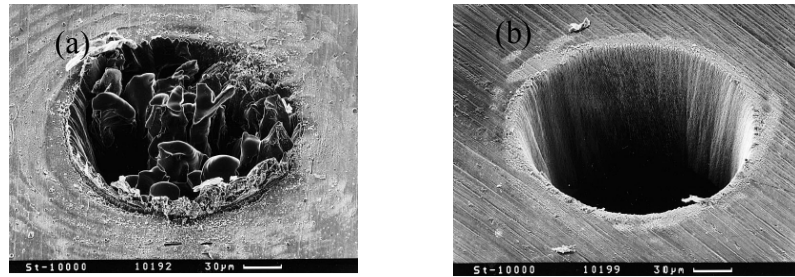


Figure 2-27 The comparison of the micromachining result on the metal (a) using nanosecond laser (b) using fs laser[215].

Furthermore, a fs laser has a specific application in fabricating a waveguide structure inside a bulk glass. There are many other applications in which a fs laser is superior over the nanosecond laser, for example, the machining of a diamond, laser smoothing, and mask repairing application [216]. As a result, fs laser has become one of the most crucial types of lasers used for the micromachining of various materials nowadays.

There are three types of fs laser systems categorized according to the range of the repetition rate: the amplified Ti:Sapphire system which repetition rate ranges from 1kHz to 200 kHz, long-cavity Ti: Sapphire oscillators which work in the repetition rate of 4-25MHz, and the last one, Yb-based lasers which have only one repetition rate at around 1 MHz. The amplified Ti:Sapphire system was used widely due to the broad availability in research laboratories. It works in the low-frequency region in which materials modification is induced by single pulses. Although this system can be used to engineer various materials, it has some disadvantages like making small changes of material refractive index and complex setup. Laser oscillators which work in a long frequency region with cumulative effects have a high repetition rate allowing faster and more efficient fabrication. Therefore, they are more convenient and economic. However, the limited intensity range restricts the application of this system. Compared to the first two lasers, the Yb-based laser system shows better results with a high fabrication speed and good waveguide quality. In addition, this system can be set up with a low price but it exhibits high writing efficiency which makes it attractive for the industrial application [217-221].

As discussed above, a fs laser can fabricate waveguides inside bulk materials by focusing the laser energy inside the transparent material, and the energy of the laser is combined in the focal volume thanks to the nonlinear absorption. When the laser intensity is high enough, the structure of the materials will change permanently and the refractive index changed consequently [217]. The mechanism of the refractive index change is not fully understood till now, and several possible mechanisms have been assumed, namely, melting material is resolidified which causes the change in the density of the materials [218], colour center formation [222], direct photostructural change due to, for example, chemical bond reorganization in the glass matrix[223], and photochemical modification in the polymers[224].

Laser refractive index modification and microablation on the surface of the sample are two main applications of the fs laser micromachining. The former is to change the lattice structure inside the sample and form microstructures through the changes of the refractive index. The latter however, is to remove materials on the top of the sample to form nanostructure by means of ion bombardment and chemical reaction.

The threshold energy which is the minimum pulse energy E that the nonlinear is absorption required to drive the electrons is a critical parameter in the fs laser micromachining. When the pulse energy E is close to the energy threshold, the energy could be confined in the focal volume causing a localized change of the refractive index. This is the main application of the fs laser. With the increase of the pulse energy, the affected area and the average plasma energy rise at the same. When the plasma energy is large enough, voids can be formed because of the Coulomb repulsion caused by the reducing of the ion shielding [225]. This is the basic principle of the fs laser microablation.

Fs laser microablation was developed in the 1990s later than the development of fs laser refractive index micromachining. In 1997, Glezer [226] investigated micro-explosions using the fs laser impinging which exploited a novel method of material ablation using fs laser on the surface of the sample. Beinhorn et al. [227] in 1999, demonstrated the microablation experimental results using a fs UV laser, in which they fabricated submicron gratings on the surface of Ta₂O₅ thin films using a fs KrF-

laser system. Microgratings on SiO₂ prepared using fs laser ablation has also been demonstrated in 2001[228]. Fs laser microblation is still in its developing period. Meyaji et al. [229] studied the origin of the periodicity of the microstructure on the thin films, and they explained that the periodic structure may be produced due to the excitation of the surface plasmon polaritons in the surface layer.

Laser micromachining which is also called laser direct writing is widely used to fabricate micron or submicron structures in biotechnologies, microelectronics, optical communication, MEMS and medical application. The materials micromachined like metals, ceramics, and polymers etc. have been demonstrated successfully[230].

2.7 Summary

An overview of the waveguide optical amplifiers, RE ions in the glasses, materials used in this thesis, and techniques for thin film and waveguide structure fabrication were given in this chapter. In particular, the development of tellurite glass and siloxane polymer, thin film fabrication technique PLD, and waveguide patterning techniques RIE and fs laser micromaching that are used in this thesis were discussed in detail.

Chapter 3 Fabrication and characterisation of tellurite glass

The study of $\text{TeO}_2\text{-WO}_3\text{-La}_2\text{O}_3$ (TWL) glasses with different dopants has attracted much attention of several research groups to explore their thermal and optical properties as well as the possibility of fiber drawing of this type of glasses [46, 61, 231]. However, according to our knowledge, no results have been reported on the thin films deposition of TWL glasses so far.

In this chapter, the design and characterisation of TWL glasses codoped with Er^{3+} , Yb^{3+} , Ce^{3+} are presented to investigate their suitability for thin film deposition. The focus is put on the properties of the glasses, namely thermal, optical, and structural properties. Various instruments, such as differential thermal analyser (DTA), dynamic mechanical analyser (DMA), Fourier transform infrared red spectrometer (FTIR), ultra-violet-visible-infrared spectrometer (UV/VIS/IR), fluorescence spectrometer, Raman spectrometer and prism coupler etc were employed to obtain the necessary data. The analysed results reported in this chapter help to choose the most suitable glass composition as a target for thin film deposition presented in Chapter 4.

3.1 Experimental design for glass melting and fabrication

3.1.1 Raw materials and compositions of the glasses

First, a series of TWL glasses were melted using oxide compounds TeO_2 , WO_3 , La_2O_3 and rare earth oxides Er_2O_3 , Yb_2O_3 , CeO_2 with purity of higher than 99.998% and 99.99%, respectively. The compositions and chemicals of the glasses are listed in Table 3-1.

Based on the main compositions of $72\text{TeO}_2\text{-}17\text{WO}_3\text{-}(11\text{-}x)\text{La}_2\text{O}_3$ (mol %)- $x\text{R}_2\text{O}_3$, x is the total concentration of the rare earth oxides R_2O_3 doped in the glasses. The thermal, optical and structural properties of the resultant glasses were analysed and compared to determine a suitable composition for thin film fabrication and waveguide engineering.

3.1.2 Glass melting process

Glasses were fabricated using a traditional glass melting and quenching technique, and the glass fabrication process is illustrated schematically in Figure 3-1. First of all, the weight of each compound in the batch (total weight 20 g) of the glass were measured using a high resolution balance (± 0.0001 g, Oertling, NA 114). The oxide powders with precise weights were transferred to a mortar (top left in Figure 3-2), and then were ground for a couple of minutes to obtain a uniform and fine powder mixture. This step is critical for the fabrication of high quality glass. After that, the mixture was transferred into a crucible which was then put into a muffle glass melting furnace at a temperature of 975 °C. During the melting process, dry O₂ with a flow rate of around 1 ml/min was used to purge away the moisture in the furnace and make sure there was no deficiency of O₂ in the glass. After 2.5 hrs melting, the melt in the crucible was cast into a preheated stainless mould (top right in Figure 3-2) immediately, this was maintained in a Pyrotherm annealing chamber (Pyro Therm) with temperature 430 °C (close to the T_g of the glass) for more than 2 hrs. During the above process, the crucible containing the melt was shaken after 1.5 hrs to remove any gas bubbles and obtain a homogeneous mixture. Subsequently, the mould plus melt was put back into the annealing furnace to eliminate internal stress to further improve the fracture strength. After further 3 hrs, the temperature of the annealing furnace was cooled down to RT at a rate of 0.5 °C/min. The tools used in the glass fabrication process are shown in Figure 3-2.

The obtained glasses prepared using 20 g powder have dimensions of 2×3×0.45 cm³ after using a polishing machine (Buehler, Motopol 2000) with SiC paper (Buehler, Grit P1200, P2500, P4000) and the final finish is around 6 μm for the PLD targets. It can be seen that the glasses obtained are very transparent as shown at the bottom right in Figure 3-2.

Table 3-1 Description of composition of various tungsten oxide modified tellurite glasses in mole percent and the use of crucibles

Name	TeO ₂ /mol%	WO ₃ /mol%	La ₂ O ₃ /mol%	Er ₂ O ₃ /mol%	CeO ₂ /mol%	Yb ₂ O ₃ /mol%
purity	99.9995%	99.998%	99.999%	99.99%	99.99%	99.99%
TWL0	72	17	11	0	0	0
TWL1	72	17	10.5	0.5	0	0
TWL2	72	17	8.875	0.125	1	1
TWL3	72	17	8.75	0.25	1	1
TWL4	72	17	8.5	0.5	1	1
TWL5	72	17	9.75	0.25	0	1
TWL6	72	17	9.75	0.25	1	0

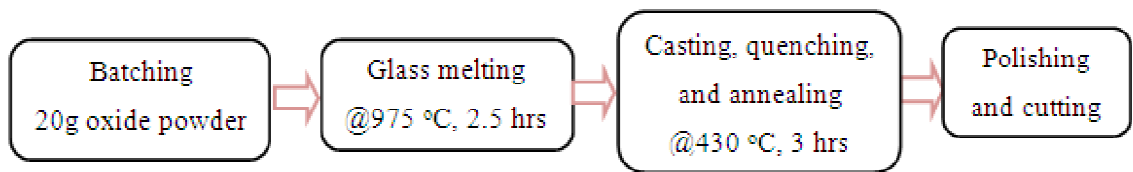


Figure 3-1 The Schematic process of glass preparation

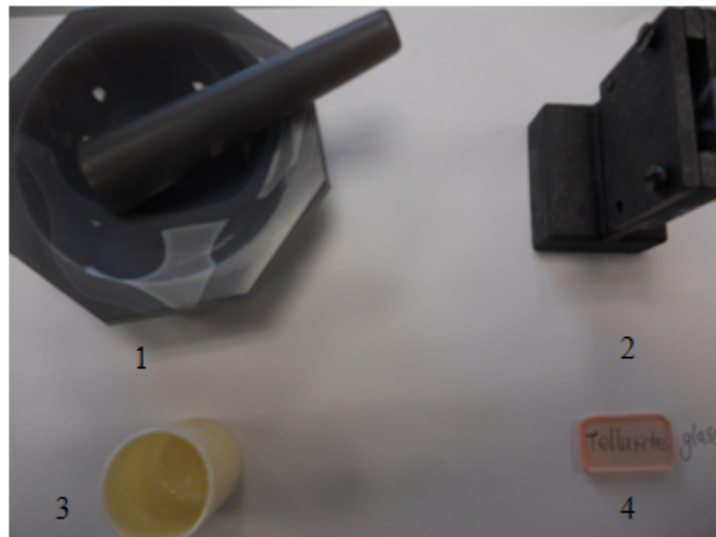


Figure 3-2 The tools used for the glass melting and glass obtained after polishing. 1. Mortar; 2. Glass mould; 3. Alumina crucible; 4. Glass after polishing

3.2 Results of glass characterisations

The thermal, optical and structural properties of the glasses were characterized using various instruments which were detailed in this section.

3.2.1 Density measurement

Density is a critical parameter in the study of the material which can be used to calculate some important parameters, such as the RE ions concentration in the glasses.

All the densities in this work were measured using an Accupyc 1330 pycnometer. The main components of the pycnometer include a cell chamber, expansion chamber, fill valve, expansion valve and vent valve indicators. The schematic is shown in Figure 3-3.

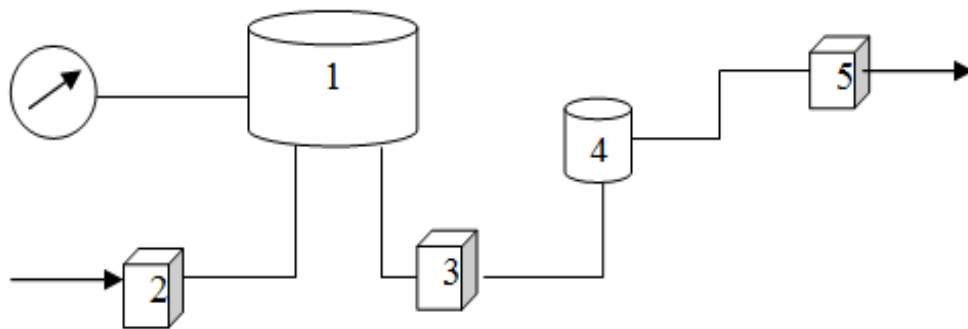


Figure 3-3 Schematic of the pycnometer: 1. sample chamber, 2. fill valve indicator, 3. expansion valve indicator, 4. expansion chamber, 5. vent valve indicator

The pycnometer decides the density and volume through calculating the pressure change of the helium gas in a calibrated volume. Before the measurement, the pycnometer should be calibrated to make sure that it works well with an error of within 0.006. And a precise weight of a sample needs to be imputed before the measurements. After that, the system could calculate the density of the sample using the weight provided and the volume obtained through the measurement of the helium pressure change automatically, and print the results out when the measurement finished with a connecting printer. All the densities and molar volumes of the glasses are listed in Table 3-2.

Table 3-2 Densities of TWL glasses

Samples	TWL0	TWL1	TWL2	TWL3	TWL4	TWL5	TWL6
Density ($\pm 0.006 \text{ g/cm}^3$)	5.995	5.984	6.024	6.047	6.031	6.056	5.727

3.2.2 Thermal analysis

Thermal analysis is critical to characterize some important parameters of glass thermal properties, such as the glass transformation temperature, crystallisation temperature, and thermal stability [232], which are useful to guide the thin film fabrication and waveguide engineering.

Differential thermal analysis (DTA) and differential scanning calorimetry (DSC) are two of the most common techniques that are used to measure the thermal properties of the glasses. Limited by the platinum as cell materials for DSC experiments, the thermal properties of tellurite glass discussed herein could only be measured using DTA since platinum cells are readily attacked by tellurite glasses.

3.2.2.1 DTA measurements

The principle of the DTA technique is easy to understand. Two thermo couples are installed in the instrument with beads connected with the sample and inert reference crucibles, respectively. When the sample experiences a transformation or melting process, its temperature will standstill due to the endothermic process, while the temperature of the reference will continue to increase. The temperature difference (ΔT) between the sample and reference under the same heating process is recorded versus the temperature, which is known as the DTA curve. Furthermore, the glass transformation temperatures and crystallisation temperatures can be determined using the curves.

Basically, the following parameters are used to characterise the thermal properties of the glasses, namely, glass transformation temperature T_g correlated with the stiffness of the glass structure, the onset crystallisation temperature T_x representing the starting point of the glass crystallisation, and the temperature difference ΔT between T_x and T_g related to the stability of the glasses. Two other important parameters are the peak temperature of the glass crystallisation T_p and the onset melting temperature

T_m . Among these phase transformations, the glass transformation and melting are endothermic processes because the glass needs to absorb heat to break networks in the glasses, while the crystallisation is an exothermic process in which glass emits heat to rearrange and bond structural units in the glass.

In this work, a Perkin Elmer DTA 7 was utilized to perform the DTA measurements. As shown in Figure 3-4, this system consists of a sample holder, reference holder, two thermo couples and a purge tube. The left thermo couple is used to heat the sample, while the right one is for the reference. The sample cup is put into the sample holder on the top of the thermocouple. The purge tube behind the thermocouple is used to provide gas to keep the sample dry and also promote the thermal equilibrium.

The measurements were carried out at a heating rate of 10 °C/min starting from 100 °C to 1000 °C. The obtained data are listed in Table 3-3. The DTA curves of the chosen representative candidates TWL1, TWL4 and TWL6 are shown in Figure 3-5a, 3-4b and 3-4c, respectively.



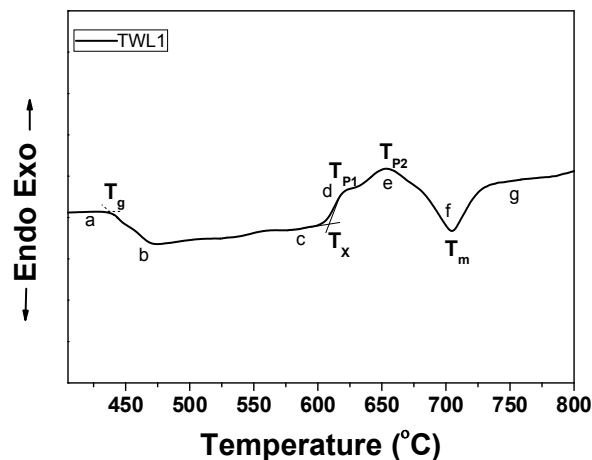
Figure 3-4 Setup of the DTA instrument. 1, purge tube, 2 and 3 are thermocouples for sample (left) and reference (right), respectively, and 4, protection tube

In Figure 3-5 (a), the glass phase transition processes were divided into different parts. Part a-b shows a slope change in the baseline indicating the heat change caused by the transformation from solid state to the glassy state. Following the a-b

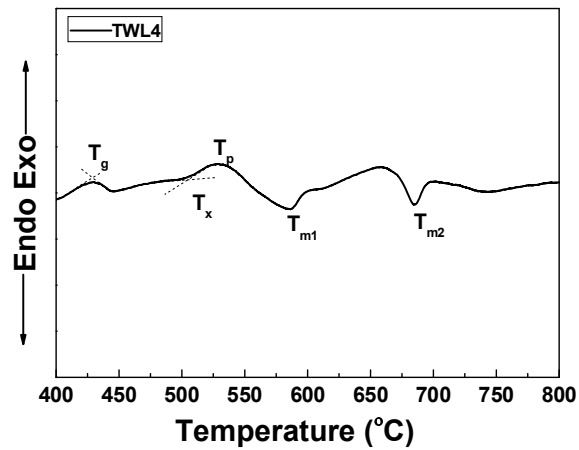
region, the part b-c shows the raised baseline yielded by the fluctuation of the instrument. Part c-d implies a part crystallisation process which is finished in part d-e. These two crystallisation processes are exothermic process during which the sample of glass releases heat. The starting point of the process c-d is the onset crystallisation temperature T_x , while the peak temperatures are known as the peak crystallisation temperature T_{p1} and T_{p2} . On the other hand, part e-f is an endothermic process in which crystallized glass is melted completely, followed by part f-g caused by the instrument. The peak temperature of the melting process is defined as the melting temperature T_m .

In Figure 3-5 (b), the first phase transition known as the glass transformation is also an endothermic process. It is then followed by an exothermic process which is the glass crystallisation process. It is the same as the analysis of glass TWL1, the start temperature in this process is the onset crystallisation temperature, while the peak temperature is the peak crystallisation temperature. It is obvious that there are two melting endothermic peaks T_{m1} and T_{m2} in this triply doped glass which might be contributed to the melting processes of different crystalline phases in the glass.

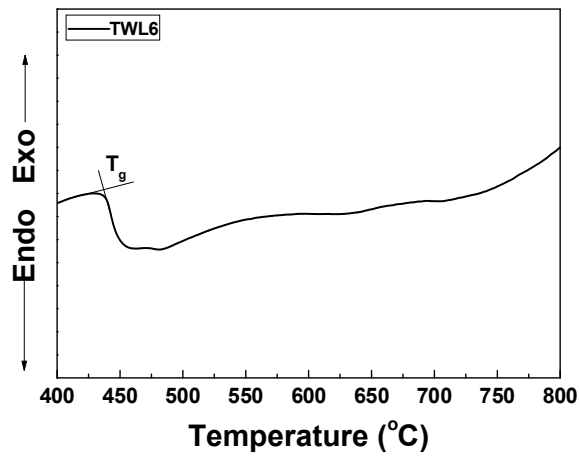
It should be noted, however, there is only one endothermic process representing the glass transformation process in Figure 3-5 (c), and no obvious crystallisation and melting peaks for glasses TWL5 are displayed, which indicates that the glass shows excellent stability.



(a)



(b)



(c)

Figure 3-5 DTA curves of the TWL1, TWL4, TWL6 in (a),(b),(c), respectively

Table 3-3 List of the thermal properties of glasses, T_g , T_x , and ΔT

Sample	T_g (°C)	T_x (°C)	T_p (°C)	T_{m1}	T_{m2} (°C)	ΔT (°C)
TWL0	436	586	632	-	703	150
TWL1	436	615	654	-	706	179
TWL2	438	517	543	587	691	79
TWL3	430	493	529	586	684	63
TWL4	433	509	529	587	684	76
TWL5	438	-	-	-	-	-
TWL6	436	-	-	-	-	-

From Table 3-3, it can be seen that the transformation temperatures T_g of all the glasses are in the range of 430 ~ 438 °C. In particular, the T_g (436 °C) of glass TWL0 with the composition of 72TeO₂-17WO₃-11La₂O₃ is the same as that of the glass with a similar composition 75TeO₂-15WO₃-10La₂O₃ reported by Feng[83], and is slightly lower than that of the glass with composition 69TeO₂-23WO₃-8La₂O₃ (>440 °C) measured using differential scanning calorimetry (DSC) reported by Dorofeev[233]. The differences between T_g of all the alike composition glasses may be caused by different thermal histories and measuring techniques used. When doped with rare earth ions, the T_g of the glasses TWL1 to TWL6 has minor changes, while T_x and ΔT vary significantly when codoped with different rare earth ions. For instance, in the case of Er³⁺ doped glass TWL1, T_x and ΔT is about 29 °C and 19 °C higher compared to the undoped glass TWL0, respectively. While for glasses codoped with Er³⁺, Yb³⁺ and Ce³⁺, both T_x and ΔT are at least 70 °C lower than that of glass TWL0. As the decrease of the T_x in triply doped glasses, the glass stability factor ΔT reduced consequently, which indicates that Yb³⁺ and Ce³⁺ codoping increases the crystallized tendency of TWL glasses.

3.2.2.2 Thermal expansion analysis

To fabricate a glass thin film on the substrates, glasses having matched thermal expansion properties with that of the substrates are necessary to obtain crack free thin films. This is why the thermal expansion analysis of the glass is important.

The coefficient of thermal expansion (CTE) which is inversely proportional to the stiffness of a sample material reflects the relationship between the changes of volume of the glass and that of the temperature. It describes the dimension changes corresponding to the temperature changes [232]. When the temperature of the glass increases, the bond length between the atoms in the glass increases, and consequently the glass expands [234]. Basically, there are three methods to describe the thermal expansion of a material: linear thermal expansion, area thermal expansion, and volumetric thermal expansion. In this thesis, the linear thermal expansion was measured.

The CTE of glass TWL1 was measured using a DMA (Perkin Elmer, DMA7e). There are many components in the DMA system and it can be used to perform

thermomechanical analysis (TMA) which could measure the dimensional changes of the sample as a function of temperature. As shown in Figure 3-6, there were two silica discs where the sample with a known geometry (with a thickness of L) was sandwiched in between, a static force of 1 mN was utilized to deform the shape of the sample at different temperatures, the change of the dimension (ΔL) of the sample and the temperature (T) are recorded, and used to calculate the CTE values.

$$a = \frac{\Delta L/L}{\Delta T} \quad (3.1)$$

where ΔL is the change of the sample dimension, L is the thickness of the sample, $\Delta T = T_2 - T_1$ as show in Figure 3-7. The CTE of the glasses were measured from 30 °C to 450 °C at a heating rate of 10 °C/min.

It is clear to see from Figure 3-7 that the CTE of glass increases with the increase in temperature. From the beginning at 50 °C to around 180 °C, the CTE of the glass TWL1 is calculated to be $12.3 \times 10^{-6} \text{ } ^\circ\text{C}^{-1}$ (12.6 ppm). While the CTE of this glass in the temperature range of 180- 430 °C is calculated to be $14.0 \times 10^{-6} \text{ } ^\circ\text{C}^{-1}$ (14.0 ppm). The CTE value of the glass increases suddenly around 430 °C which is corresponding to the glass transition temperature, at which the glass will undergoes transformation from a hard brittle substance to a plastic material. The obtained T_g using DMA measurement is consistent with the glass transformation temperature obtained using the DTA measurement. Excluding CTE values around T_g temperature region, average CTE value of glass TWL1 is measured to be about $13 \times 10^{-6} \text{ } ^\circ\text{C}^{-1}$ (13 ppm/K).

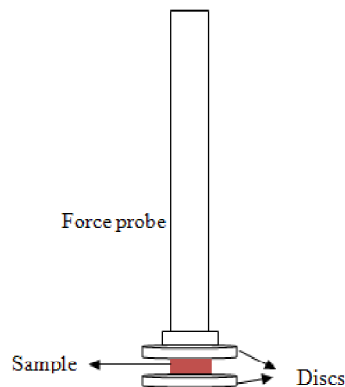


Figure 3-6 The schematic of the component in the DMA 7 for the thermal expansion coefficient measurement

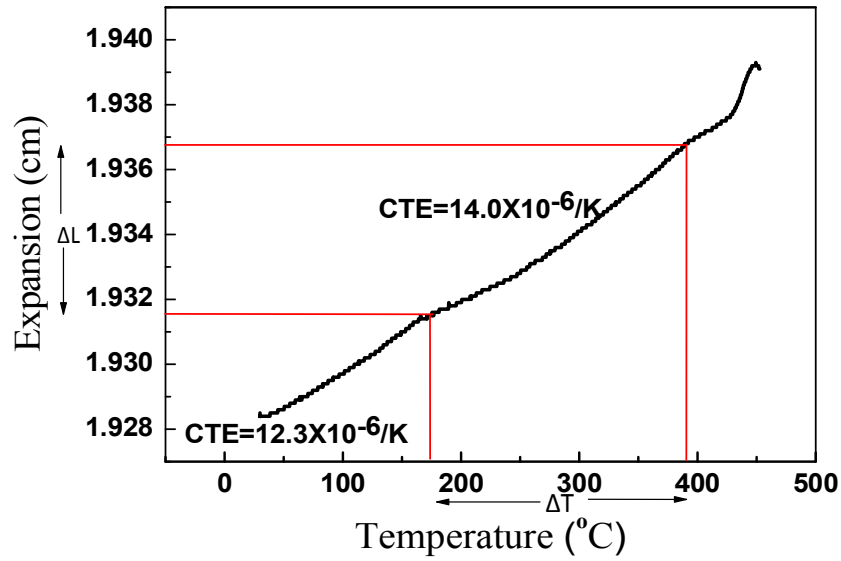


Figure 3-7 Coefficient of thermal expansion curve of the tellurite glass

3.2.3 Optical properties

In this section, the optical properties of the TWL glasses are reported. The details of the various techniques employed in the experiments are described first, and followed by the results and discussions.

3.2.3.1 Experiments

Absorption spectroscopy

IR spectroscopy is a commonly used tool to study the absorption properties of the glasses. It works based on the fact that the lattice vibrations in the molecules absorb specific light that has similar energy as that of the vibration (known as resonance). The wavelengths of IR spectra which lie between $2.5 \mu\text{m}$ (4000 cm^{-1}) to $15.4 \mu\text{m}$ (649 cm^{-1}) known as the fundamental region are generally used to identify the bonding groups in the molecules [235].

The intensity of absorbed incident light is directly proportional to the number of the molecules in the sample. According to the Beer-Lambert law [235], the absorbance is given by:

$$-\text{Log}_{10} \left(\frac{I}{I_0} \right) = \epsilon dt \quad (3.2)$$

where $-\text{Log}_{10}\left(\frac{I}{I_0}\right)$ is the absorbance, I/I_0 is the transmittance, d is the molar concentration of ions, t is the thickness of the sample. ϵ is the molar extinction coefficient. Moreover, the absorption coefficient of glasses equals to the absorbance divided by the thickness of the glasses.

$$a = \frac{-\text{Ln}(I/I_0)}{t} \quad (3.3)$$

FTIR can also be used to investigate the contamination in the materials, such as free OH, or bonded OH. Generally, water contamination comes from the raw material used, or absorbs from the air during the melting process. To reduce the water in the materials, all the raw materials used in this study are dried properly before melting. In addition, the furnace was filled with dry O_2 to reduce water absorption during the melting process.

The instrument used here is a Bruker Vertex FTIR spectrometer 1725x which consists of an IR source, interferometer, sample compartment and a detector. The schematic setup of this system is shown in Figure 3-8. All measurements were carried out at RT and used air as a reference.

The main component of the FTIR spectrometer is the interferometer as shown in Figure 3-9. The IR signal is incident on a beamsplitter which splits light into two beams: one of them is reflected to a fixed mirror, and the other beam passes through a moving mirror. These two beams will be reflected back to the beamsplitter and produces interferences due to the different path caused by the moving mirror. The interference signal then passes through the sample where it is absorbed at different wavelengths by various molecular groups. The signal measured by the detector as a function of the optical path difference will be processed using the Fourier Transform technique, and then IR spectra are obtained.

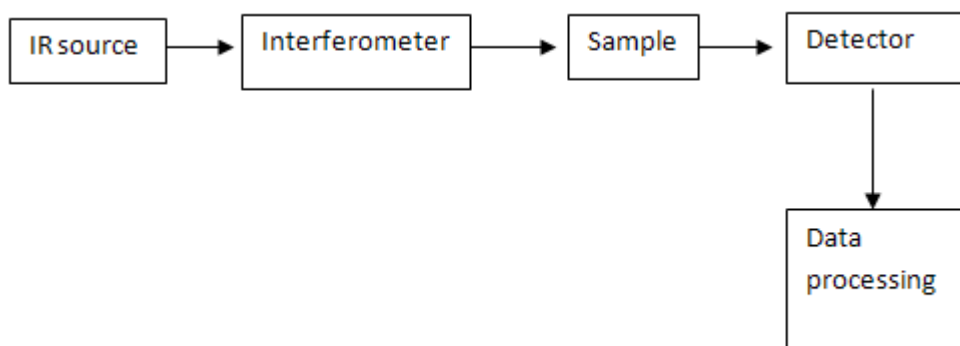


Figure 3-8 Schematic setup of the FTIR system

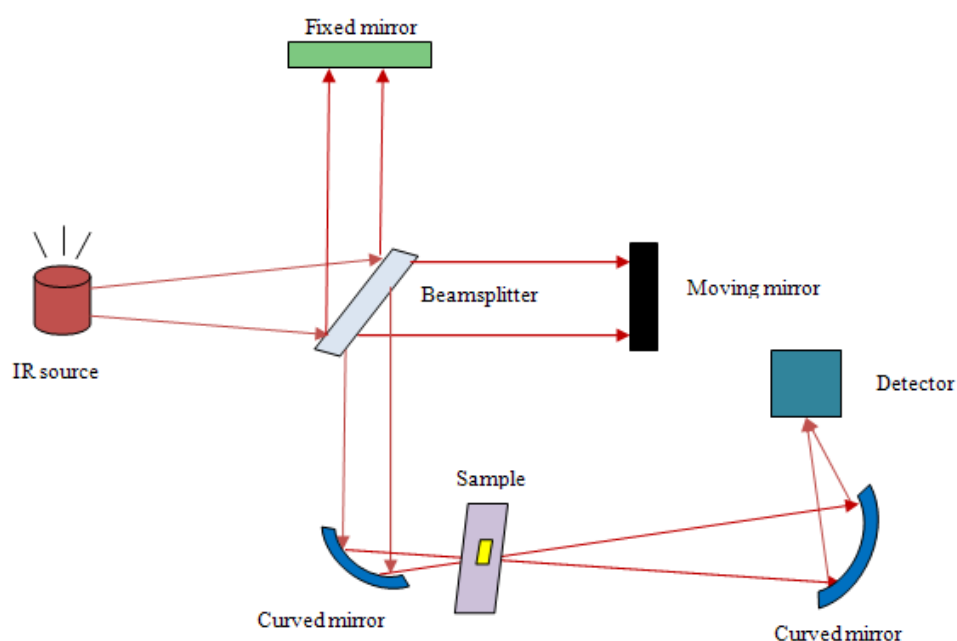


Figure 3-9 Schematic setup of the interferometer in the IR spectrometer system

Absorption in the UV/VIS region takes place when the band energy of the electronic transition is resonant with the energy of the passing light. At this condition, some photons are absorbed and electrons are promoted from the ground state to excited states in the atom, while others are transmitted. The intensity of the absorbed incident light is proportional to the number of photons absorbed[235]. The UV/visible spectra also obey the Beer-Lambert law, therefore, the absorption coefficient is also calculated using equation (3.3).

In this study, the UV/VIS absorption measurements were carried out using a Perkin-Elmer UV/VIS/NIR Lambda-19 which includes two lamps (Deuterium lamp for NIR

range and Halogen lamp for VIS range), two monochromators and detectors (one photomultiplier tube for UV/VIS and the other lead sulphide cell for IR). A schematic for the Perkin-Elmer UV/VIS/NIR spectrometer is shown in Figure 3-10, where monochromators which could split the light into signals with a range of wavelengths are the primary components. The schematic of the monochromator is shown in Figure 3-11, a white light beam A is focused on a slit B and then is collimated by a mirror C. The collimated light beam will be split into a series of lights with different wavelengths using a rotatable grating D. After that, the light with different wavelengths is focused on another slit F by a mirror E. The wavelength of the light passing through slit F is determined by the angle of the rotatable grating D.

After the monochromator, the signal is split into two beams by a beamsplitter as shown in Figure 3-10 . One light beam passes through a reference and reaches a detector with intensity of I_0 , while the other beam passes through a sample and reaches the detector with intensity of I . The curve of the UV/VIS spectra can be plotted using $-\log \frac{I}{I_0}$ versus the wavelengths. In this work, the polished glass samples were scanned from 200 nm to 2500 nm with a scanning rate of 60 nm/min to obtain absorbance spectra. Air was used as references in all the measurements.

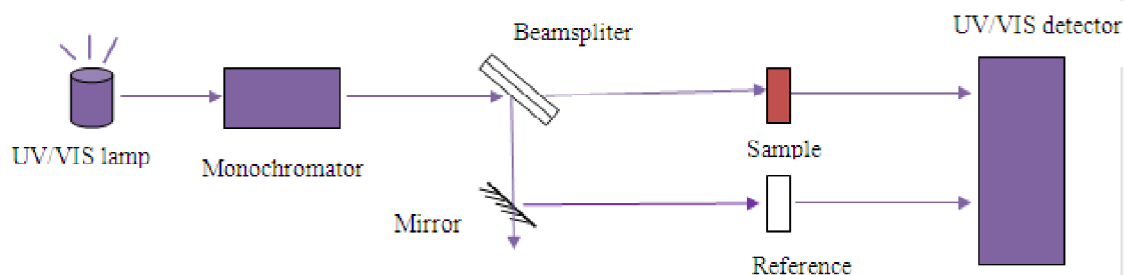


Figure 3-10 Schematic setup of the UV/VIS/IR spectrometer

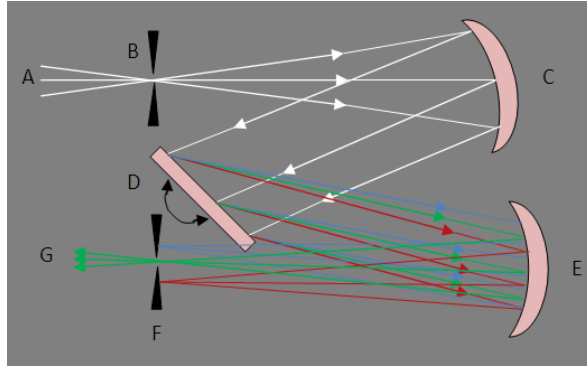


Figure 3-11 Schematic of a monochromator. A: light source, B and F: slit, D: rotatable grating, C and E: mirrors

Prism coupler

The refractive index is the ratio of the speed of light travelling in the vacuum and that in the medium as given by:

$$n = c/v \quad (3.4)$$

where n is the refractive index, c and v are the velocity of propagating light travelling in vacuum (2.998×10^8 m/s) and a medium, respectively. The refractive index is an important parameter for optical materials.

Snell studied the relation between the ratio of incident angle, the refraction angle and the refractive index of the medium, obtaining the following formula known as Snell's law [236].

$$\frac{\sin \theta_1}{\sin \theta_2} = \frac{n_1}{n_2} = \frac{v_1}{v_2} \quad (3.5)$$

where n_1, n_2 are the refractive indices of medium 1 and 2, and θ_1 is the incident angle while θ_2 is the refractive angle, v_1 and v_2 are the light travelling speeds in media 1 and 2, respectively.

According to Snell's law, when light is incident on a medium with refractive index of n_1 from another medium with refractive index of n_2 ($n_1 > n_2$), as shown in Figure 3-12, there is an angle, where all light signals are reflected at the interface of these media (the black light beam in the Figure 3-12). This angle is known as the critical angle, and the reflection at this angle is known as total internal reflection.

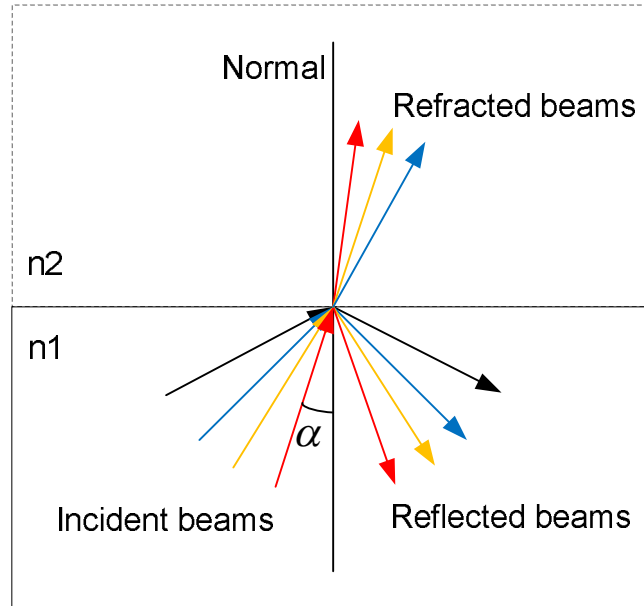


Figure 3-12 The schematic of the total internal reflection. α increases slowly, and when $\alpha = \theta_c$, all light beam is reflected and θ_c is the critical angle. The angle between black light and normal line is θ_c .

Refractive indices of materials can be measured using a prism coupler, where a coherent light beam is incident onto a prism with comparable high refractive index. The sample is placed very close to the base of the prism. The coupler used in this work is a Metricon 2010 prism coupler. A light beam is incident on the prism and reaches its base. The incident angle of the light beam could be changed by rotating the table where the prism, coupling head, photodetector and sample are mounted. At some angle θ (known as the critical angle), the light can reach the sample across an air gap between the prism and sample by forming an evanescent field and the light coupling into one of the propagating mode in the sample will cause a sudden reduction of the light intensity. As a result, there is a significant drop in the intensity that the photodetector collected. The intensity of the signal versus the effective indices could be obtained consequently [237]. The schematic of the prism coupler is shown in Figure 3-13.

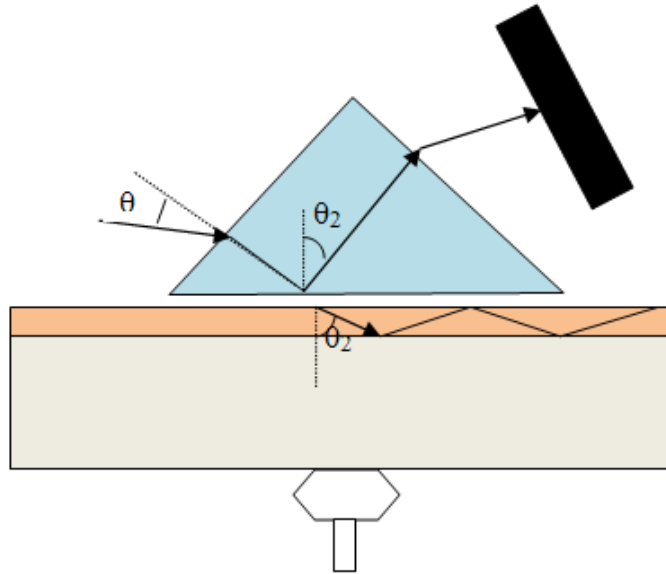


Figure 3-13 The schematic setup of the prism coupler

If the sample is film, the thickness of the thin film can then be calculated using the following equation once two modes have been obtained [238].

$$\left(\frac{2\pi}{\lambda}\right) * n \cos(\theta_2) * T + \varphi_{10} + \varphi_{12} = m\pi \quad (3.6)$$

where λ is the wavelength of the incident light, T is the thickness of the thin film, n is the refractive index of the film, φ_{10} and φ_{12} are the Fresnel phase shifts at the film-air and film-substrate interfaces, respectively.

Fluorescence spectroscopy

As discussed in the last section, absorption of photons can promote the electrons at ground state to an excited state. Electrons at the excited state can cascade down to the ground state and emit energy. The energy emitted in the form of a photon through radiative transition is called fluorescence as shown in Figure 3-14. The energy of the emission photons has lower energy than the absorbed photons. However, the wavelength of the emission spectra is not depending on the excitation wavelength but is determined by the energy difference between the start energy state and the final state. For example, if the energy difference between the two energy states is E , then the relation between E and the emission wavelength λ is $E=hc/\lambda$.

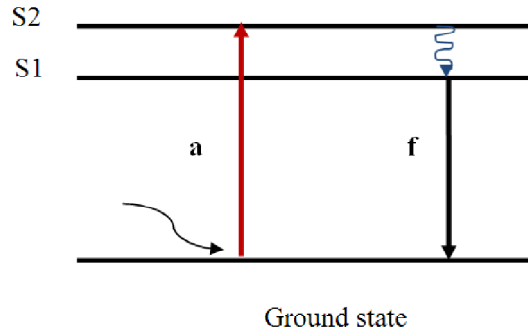


Figure 3-14 Energy transition schematic in a fluorescence process, S1 and S2 are excited states

Fluorescence has extensive applications in various areas, namely, clinical chemistry, biochemical industry, life and material science etc. Herein, the discussion focuses on the application of fluorescence in the characterisation of RE-ion doped glasses and thin films.

Fluorescence spectra were collected using the Edinburgh Fluorospectrometer F900 which consists of sample compartment, emission monochromator, excitation monochromator, InGaAs detector for infrared light and its cooling unit, as well as PMT detector for visible light etc. The schematic of this spectrometer is shown in Figure 3-15.

First, the sample was placed in the compartment of the system. The light beam with wavelength 980 nm produced by a laser diode was focused on the sample as a pump. The emission signal was collected by InGaAs detector through a scanning spectrometer. Then the computer recorded the signal at each wavelength, and the emission intensities were plotted against wavelength in nm to obtain the fluorescence spectra. Regarding lifetime measuring, a laser pulse generator was used to activate pulsed signals which can be checked by an oscilloscope. The pulsed signal was focused on the sample through a chopper. The signal intensity which was recorded by a computer was plotted against the decay time. The lifetime was determined by fitting the exponential curves using the software F900 in the computer. For the measurement of upconversion spectra, InGaAs detector was used to collect the emission signal.

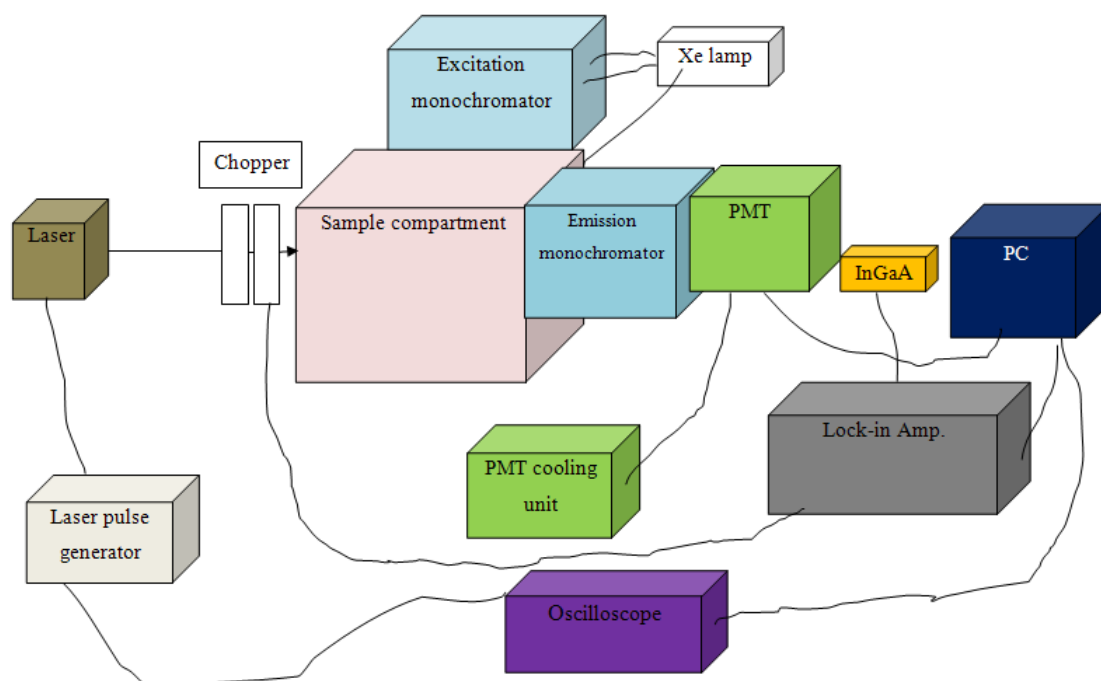


Figure 3-15 The schematic of the fluorescence spectrometer

3.2.3.2 Results and discussion

FTIR spectroscopy

As introduced in the last section, IR absorption is produced due to the molecular vibration and is a critical factor in determining the transparency region and structure of the materials. The IR spectrum consists of fundamental and multiphonon regions [40]. The fundamental resonance, which is related to the intense vibration, can be used to determine the glass structure, and will be discussed in section 3.2.3. The multiphonon absorption which determines the transparency of the materials at lower frequency region is produced when a high energy photon interacts with more than one phonon.

The multiphonon absorption at shorter wavelength can be obtained using a spectrometer in transmission mode. The IR spectra measurements of TWL glasses were carried out using a Bruker Vertex FTIR spectrometer 1725x in the region of 1750 to 2000 cm^{-1} (5.0 μm to 5.7 μm). The obtained absorption spectra of the TWL glasses are shown in Figure 3-16. IR absorption cutoff edge is defined as the wavenumber when absorption is 2 cm^{-1} [239] and the values of the different glasses are listed in Table 3-4.

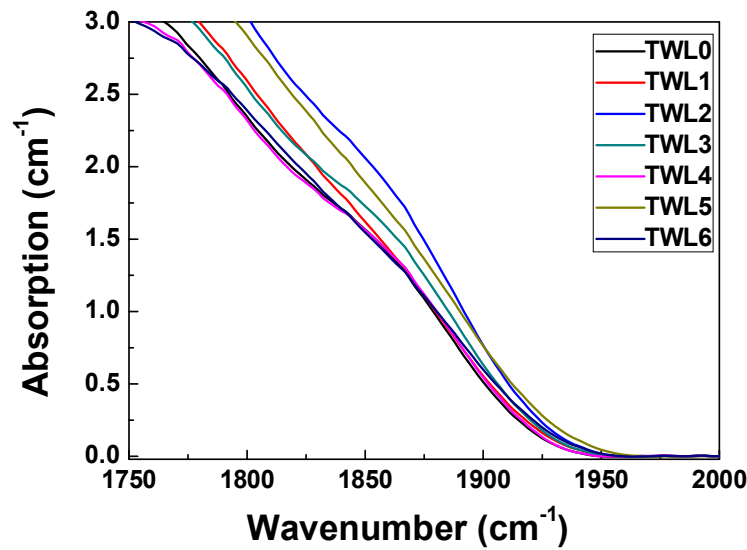


Figure 3-16 IR Cutoff edge of the glasses with different dopants

Table 3-4 FTIR absorption edge of glasses with different dopants

sample	TWL0	TWL1	TWL2	TWL3	TWL4	TWL5	TWL6
FTIR cutoff edge (cm ⁻¹)	1818	1829	1852	1830	1817	1845	1822
FTIR cutoff edge (μm)	5.500	5.467	5.400	5.464	5.503	5.420	5.488

From Figure 3-16 and Table 3-4, it is obvious that the rare earth dopants has little influence on the IR edge absorption which implies the rare earth dopants not change the transparent property of the glasses in IR region.

At shorter wavelength, the relation of the absorption of the multiphonon edge tails and the frequencies can be given by the following the equation [240]:

$$\alpha(\omega) = A \exp\left(\frac{-\gamma\omega}{\omega_0}\right) \quad (3.7)$$

where A and γ are constants, ω_0 is the fundamental optical phonon frequency. Using this equation, the dependence of absorption on the multiphonon edge tail was fitted with the curves shown in Figure 3-17. It is clear that the experimental data and the fitting curve are in good agreement. This exponential dependence of absorption on frequency was also reported in some ionic crystals, including alkali halides and fluorides. McGill believed [241] that this exponential dependence caused by the superpositions of a number of multiphonon processes. These results indicate that

these TWL glasses do display an intrinsic multiphonon process in the transparent region.

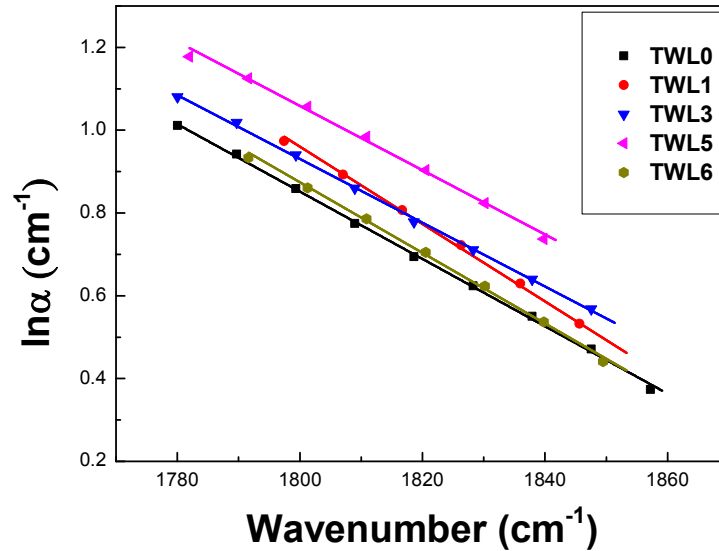


Figure 3-17 Dependence of $\ln\alpha$ on absorption frequency ν . Point line is the experiment result, and solid line with the same colour is the fitting line. (To make the figure more clear, curves of glass TWL2 and TWL4 which have similar composition as glass TWL3 are hidden.)

UV/visible spectroscopy

UV/VIS spectra were used to investigate the transmittance of the thin film and the transition of rare earth ions in the glasses or thin films which is useful for the waveguide engineering.

The main absorption peaks in the range of 400 nm to 1700 nm of glasses obtained using Perkin-Elmer UV/VIS/NIR Lambda-19 are shown in Figure 3-18, where each of them corresponds to transition from ground state to different excited state in Er^{3+} and Yb^{3+} ions as shown in the energy level diagram. The absorption peaks at 794 nm, 650 nm, 540 nm and 520 nm are attributed to the transitions from ground state $^4I_{15/2}$ to $^4I_{9/2}$, $^4F_{9/2}$, $^4S_{3/2}$ and $^4H_{11/2}$ in Er^{3+} ions, respectively[38]. The absorption at around 980 nm results from both $\text{Yb}^{3+}: ^2F_{7/2} \rightarrow ^2F_{5/2}$ and $\text{Er}^{3+}: ^4I_{15/2} \rightarrow ^4I_{11/2}$ transitions. However, the glasses TWL2 to TWL4 co-doped with Yb^{3+} and Er^{3+} have much higher absorption around 980 nm than the glass TWL1 which was not doped with Yb^{3+} . This is due to the transition of $\text{Yb}^{3+}: ^2F_{7/2} \rightarrow ^2F_{5/2}$ which occurs between two broadband states with absorption band ranges from 870 nm to 1060 nm. Moreover, the absorption cross-section of $\text{Yb}^{3+}: ^2F_{7/2} \rightarrow ^2F_{5/2}$ is approximately 10 times larger than that of $\text{Er}^{3+}: ^4I_{15/2} \rightarrow ^4I_{11/2}$ [242]. The absorption peak around 1535 nm belongs to

the transition of Er^{3+} ions from ${}^4I_{15/2}$ to ${}^4I_{13/2}$. All the electronic transitions discussed above are listed in Table 3-5.

Table 3-5 The electronic transitions from the optical spectra for Er^{3+} , Yb^{3+} and Ce^{3+} codoped TWL glasses[38]

Rare earth ions	Transitions	Absorption Peaks (nm)
Er^{3+}	${}^4I_{15/2} \rightarrow {}^2H_{11/2}$	520
	${}^4I_{15/2} \rightarrow {}^4S_{3/2}$	540
	${}^4I_{15/2} \rightarrow {}^4F_{9/2}$	650
	${}^4I_{15/2} \rightarrow {}^4I_{9/2}$	794
	${}^4I_{15/2} \rightarrow {}^4I_{11/2}$	980
	${}^4I_{15/2} \rightarrow {}^4I_{13/2}$	1535
Yb^{3+}	${}^2F_{7/2} \rightarrow {}^2F_{5/2}$	980

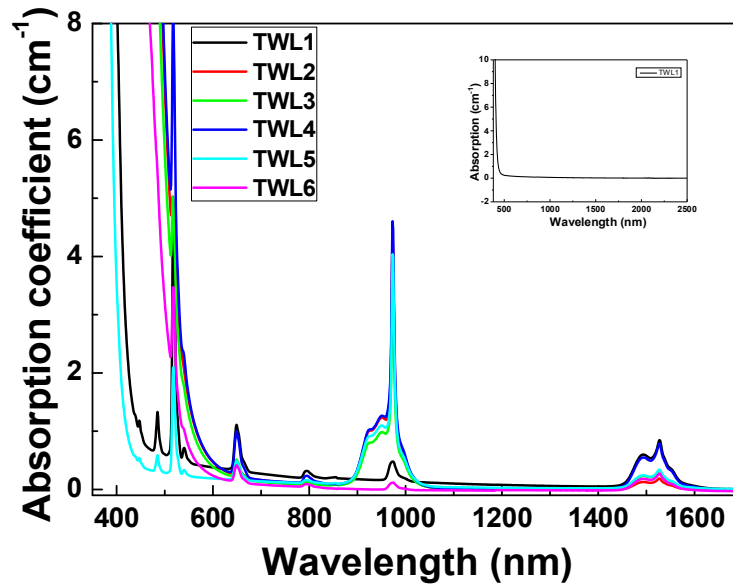


Figure 3-18 UV/VIS/NIR absorption coefficient of the glasses from TWL1 to TWL6, the inset figure is the UV/VIS/NIR absorption of the glasses TWL0

It is known that a smooth exponential tail in the absorption curve is a characteristic of amorphous materials or disordered semiconductors. This tail is named as the Urbach edge, and the exponential dependence rule is known as the Urbach rule [243] which can be written as:

$$\alpha(\omega) = B \exp\left(\frac{\hbar\omega}{\Delta E}\right) \quad (3.8)$$

where α is the absorption coefficient, B is a constant, \hbar is the reduced Planck's constant, ω is the frequency, ΔE is the width of band tails at the localized states. This edge occurs due to the photon transitions from the valence band (VB) to the

conduction band (CB). There are two kinds of transitions at this edge, direct and indirect transition. Both transitions involve interaction of electromagnetic wave with electrons in the VB, which is then raised up to the CB across the fundamental edge or Urbach edge [244].

Figure 3-20 shows the plot of $\ln\alpha$ against the photon energy $\hbar\omega$. The linear relationship indicates that these factors α and $\hbar\omega$ have an exponential dependence, which means the Urbach rule is obeyed. The inverse slope of the linear part of the curve represents the optical energy tail E_{tail} which relates to the amorphous nature of the material [245, 246]. The values obtained from these curves for glass TWL0-TWL6 are listed in Table 3-6.

The Urbach rule was found to be obeyed by numerous amorphous and glassy materials at lower ranges of absorption edge. While for absorptions at higher range, another relationship as the following form:

$$\alpha(\omega) = B(\hbar\omega - E_{\text{opt}})^n / \hbar \quad (3.9)$$

where B is a constant, E_{opt} is the energy gap of the material, $n=1/2$ and 2 for direct and indirect forbidden transitions, respectively. The optical energy gap E_{opt} of the material is the energy difference between the maximum of the valence band and the minimum of the conduction band [247]. This value related to the host materials, the ionic radius of the rare earth ions etc. In this study, all the glasses have the same host materials. E_{opt} can be calculated from the intersect of the slope of the $(\alpha\hbar\omega)^{1/2}$ against $\hbar\omega$. If a straight line cannot be achieved, then the representation of $(\alpha\hbar\omega)^{1/3}$ against $\hbar\omega$ can be used[244]. The dependence of $(\alpha\hbar\omega)^{1/2}$ on photon energy $\hbar\omega$ is plotted in Figure 3-21, and the values of E_{opt} obtained from these curves are reported in Table 3-6. From the square of the correlation coefficient R^2 ($R^2 = 1$, is perfect fitting), it is obvious that all the curves are fitted well even though not perfectly. This result indicates that all glasses TWL0-TWL6 have a direct band gap.

From Figure 3-21 and Table 3-6, the optical energy gaps of undoped glass TWL0 and Er^{3+} doped glass TWL1 are very close to each other, while glasses codoped with Yb^{3+} have a slightly higher optical energy gap. On the other hand, glasses TWL2-TWL4, and TWL6 codoped with Ce^{3+} have relatively lower energy gaps. This

indicates that Ce^{3+} could reduce the energy gap while Yb^{3+} codoping can make it raised. The change of the optical energy gaps of the glasses is believed to be the result of the rearrangement of the glass structure [246].

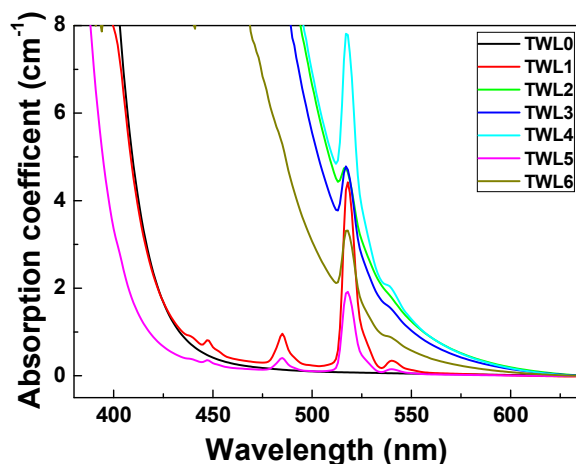


Figure 3-19 The short wavelength absorption of glasses TWL0, TWL1, and TWL4-TWL6

Table 3-6 Calculated energy gap and energy tails of glasses TWL0-TWL6

Glasses	E_{opt}	Correlation coefficient R^2	E_{tail}	Correlation coefficient R^2
TWL0	2.969	1.0000	2.863	0.9995
TWL1	2.946	0.9986	2.860	0.9992
TWL2	2.339	0.9989	2.189	0.9989
TWL3	2.369	0.9988	2.224	0.9997
TWL4	2.350	0.9989	2.181	0.9992
TWL5	3.087	0.9987	2.967	0.9996
TWL6	2.401	0.9990	2.319	0.9996

Note: the fitting is perfect when the correlation coefficient $R^2=1$.

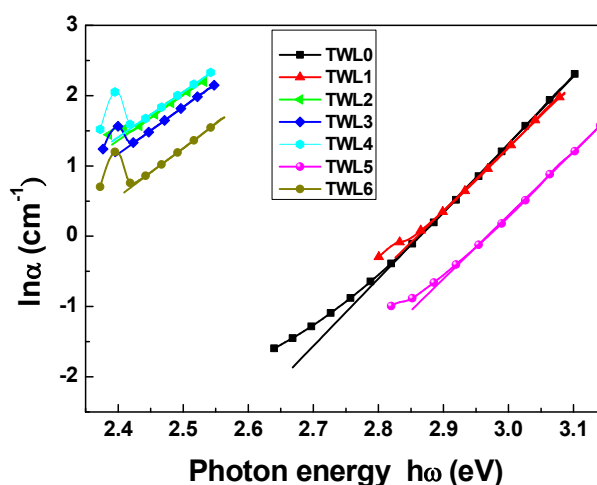


Figure 3-20 Dependence of $\ln\alpha$ on photon energy $h\omega$ for rare earth doped tellurite glasses TWL0-TWL6. Solid lines are the fitting curves

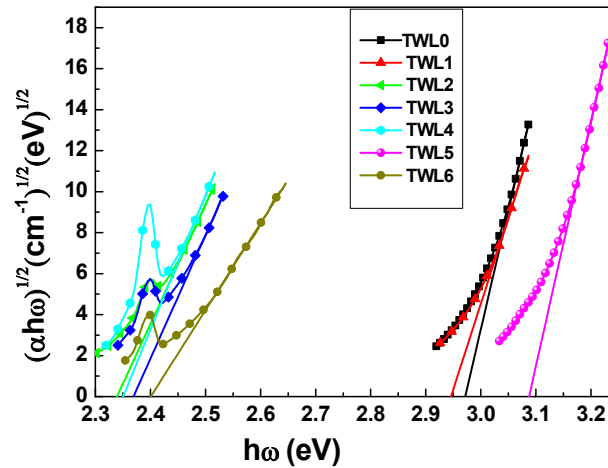


Figure 3-21 Dependence of $(\alpha h\omega)^{1/2}$ on photon energy $h\omega$ for rare earth doped tellurite glasses TWL0-TWL6. Solid lines are the fitting curves

Refractive indices

The refractive indices of the glasses were measured at different wavelengths using the prism coupler. The obtained values are listed in Table 3-7. The refractive index dispersion which is the variation of the refractive index with changes of wavelength can be given by the two-pole Sellmeier equations [248]:

$$n^2(\lambda) = A + B/(1 - C/\lambda^2) + D/(1 - E/\lambda^2) \quad (3.10)$$

where $n(\lambda)$ represents the refractive index at the wavelength of λ with unit μm , and A, B, C, D, E are the constant parameters which can be obtained by fitting the experimental refractive index data with the above equation. Among these parameters, A and B represents the contribution of the higher-energy and lower-energy band gaps of electronic absorption to the refractive index, D stands for the decrease of the refractive index due to lattice absorption. E , which is not very critical, is usually determined using the IR transition cutoff edge. For the glasses in this thesis, for which IR transition cutoff edge is about $5.5 \mu\text{m}$, and E is a square of 11, twice the IR transition region $5.5 \mu\text{m}$ ($E = (5.5 \times 2)^2 = 121$) [248]. All the parameters were obtained by the fitting function in Origin. As shown in the table, most of the experimental data were fitted well using this model.

The Sellmeier parameters can be used to calculate the refractive indices of the glass at any wavelength, especially for those beyond the measurable wavelength region. In addition, these parameters are correlated with chromatic dispersion which is an

important factor for waveguide design and engineering. The values of all the Sellmeier parameters of the TWL glasses obtained are listed in Table 3-8. The graph regarding the spread of experimental data and fitting curves of TWL glasses are depicted in Figure 3-22, from which it can be seen that the refractive indices decrease with the increasing of the wavelengths.

Table 3-7 The refractive indices of the glasses at different wavelengths

Samples	Refractive index (± 0.0004)							
	633nm	808nm	1321nm	1476nm	1523nm	1540nm	1550nm	1560nm
TWL0	2.1022	2.0752	2.0507	2.0485	2.0459	2.0463	2.0465	2.0463
TWL1	2.0976	2.0720	2.0462	2.0448	2.0436	2.0424	2.0425	2.0421
TWL2	2.1041	2.0782	2.0528	2.0509	2.0488	2.0490	2.0488	2.0485
TWL3	2.1039	2.0783	2.0524	2.0504	2.0486	2.0485	2.0487	2.0485
TWL4	2.1036	2.0768	2.0513	2.0501	2.0486	2.0485	2.0485	2.0483
TWL5	2.0354	-	1.9888	1.9862	1.9847	1.9845	1.9843	1.9842
TWL6	2.0330	-	1.9889	1.9867	1.9852	1.9854	1.9854	1.9849

Table 3-8 Sellmeier coefficient of TWL glasses with different rare earth dopants at room temperature

Samples	Sellmeier Coefficients					Correlation coefficient R^2
	$n^2(\lambda) = A + B / (1 - C / \lambda^2) + D / (1 - E / \lambda^2)$					
	A	B	C	D	E	
TWL0	3.34757	0.82912	0.09175	1.10403	121	0.9990
TWL1	2.91476	1.24205	0.06643	1.00183	121	0.9985
TWL2	2.95135	1.23053	0.006743	1.00152	121	0.9992
TWL3	2.71165	1.4681	0.05834	1.00188	121	0.9992
TWL4	3.2311	0.95108	0.08231	1.03872	121	0.9982
TWL5	2.50962	1.41656	0.05388	1.03562	121	0.9997
TWL6	2.45628	1.47445	0.04905	1.03989	121	0.9992

Note: when $R^2=1$, the fitting is perfect

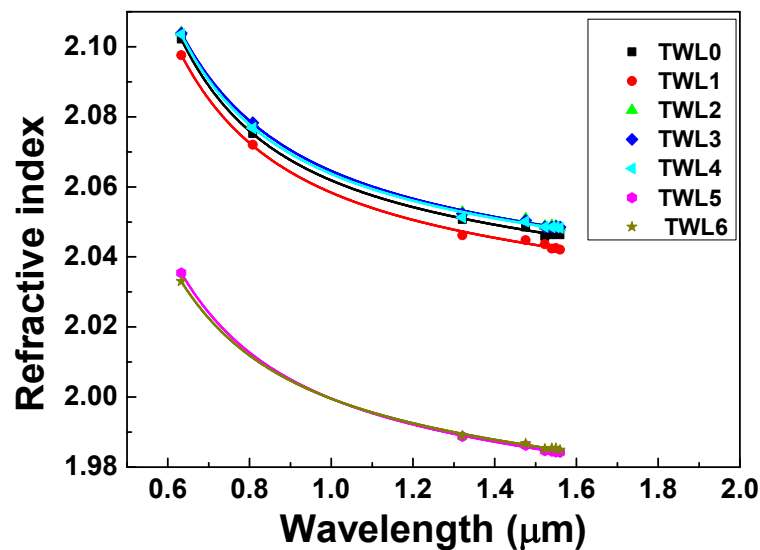


Figure 3-22 The fitting curve of refractive index of TWL glasses, solid lines are the fitting curves

Fluorescence spectroscopy

The fluorescence around 1535 nm which is due to the transition of ${}^4I_{13/2} \rightarrow {}^4I_{15/2}$ in Er^{3+} ions was measured using a photoluminescence spectrometer excited with the 980 nm laser diodes at RT. This transition is important since the emission wavelength around 1500 nm is corresponding to the high gain and low loss optical communication windows. The emission intensities of the transition ${}^4I_{13/2} \rightarrow {}^4I_{15/2}$ for the TWL glasses with different rare earth dopants were normalised with respect to the peak values around 1535 nm as shown in Figure 3-23.

It can be seen from the figure that the fluorescence bandwidths of the glasses TWL5 (Er^{3+} and Yb^{3+} codoped) and TWL6 (Er^{3+} and Ce^{3+} codoped) exhibit comparable values with that of glass TWL1 (Er^{3+} doped only). It is also important to mention that when the glass was codoped with $\text{Er}^{3+}/\text{Yb}^{3+}/\text{Ce}^{3+}$, the bandwidth of the emission spectra would increase significantly to 88 nm as shown in Table 3-9. This indicates that $\text{Yb}^{3+}/\text{Ce}^{3+}$ codoping could enhance the fluorescence of the TWL glass. The same effect was also reported in $\text{Er}^{3+}/\text{Yb}^{3+}/\text{Ce}^{3+}$ codoped fluoride glasses $53\text{ZrF}_4-19\text{BaF}_2-7\text{LaF}_3-3\text{AlF}_3-18\text{NaF}$ mol% (ZBLAN) [249].

The ratio of emission intensities around the shoulder 1490 nm and peak 1535 nm I_{1490}/I_{1530} can be employed to characterise the flat gain properties of the optical devices[40]. As shown in Table 3-9, the I_{1490}/I_{1530} of glass TWL1 (Er^{3+} doped only) and glass TWL5 (Er^{3+} and Yb^{3+} codoped) are 0.4 and 0.39, respectively, which are close to each other. Regarding glasses TWL6 and TWL4 which are codoped with Ce^{3+} ions, the ratios I_{1490}/I_{1530} increase to 0.43 and 0.57, respectively, which indicates that Ce^{3+} codoping in the TWL glasses can increase the ratio I_{1490}/I_{1530} , and Ce^{3+} and Yb^{3+} codoping can boost this ratio further. This may be due to the fact that energy transfer (ET) processes increase the population of the upper Stark levels of ${}^4I_{13/2}$ and thus leads to more radiative transitions from state ${}^4I_{13/2}$ to the ground state.

As discussed in Chapter 2, section 2.2.2, the fluorescence decay life time which relates to the transitions of photons between two different energy levels is inversely proportional to the photon decay rate, (i.e. the radiative and non-radiative relaxation from the excited) as shown in the following equation:

$$\frac{1}{\tau} = A + W_{nr} + W_{ET} \quad (3.11)$$

where A is the total decay rate, W_{nr} is the single ion nonradiative rate due to the multiphonon energy relaxation, and W_{ET} is the effective nonradiative rate due to the energy transfer. In the tellurite glass, the nonradiative decay rate for the transition ${}^4I_{13/2} \rightarrow {}^4I_{15/2}$ can be neglected at RT. The above equation then can be written as:

$$\frac{1}{\tau} = A + W_{ET} \quad (3.12)$$

The lifetime of the glasses at different states are reported in Table 3-10. It is clear that the lifetime at 980 nm for glass TWL5 (Yb^{3+} codoped) is much larger than that of glass TWL1 (Er^{3+} doped only). This is due to much slower relaxation rate of level ${}^2F_{7/2}$ in excited Yb^{3+} ions compared to that of the level ${}^4I_{11/2}$ in Er^{3+} ions. Moreover, the energy transfer from Yb^{3+} to Er^{3+} can also reduce the relaxation rate of ${}^4I_{11/2}$. The lifetime at 980 nm for glass TWL1 (Er^{3+} doped only) is smaller than that of glass TWL6 codoped with $\text{Er}^{3+}/\text{Ce}^{3+}$, which might be caused by the energy transfer from $\text{Er}^{3+} {}^4I_{13/2}$ to $\text{Ce}^{3+} {}^2F_{7/2}$ that makes the radiative decay rate of level ${}^4I_{11/2}$ increase [250]. Furthermore, the combined effects of energy transfer from Yb^{3+} to Er^{3+} and from Er^{3+} to Ce^{3+} result in a small increase in the lifetime of state ${}^4I_{11/2}$ in glass TWL4 ($\text{Er}^{3+}/\text{Yb}^{3+}/\text{Ce}^{3+}$). The lifetimes of state ${}^4I_{13/2}$ at 1535 nm shown in Table 3-10 indicate that Yb^{3+} and Ce^{3+} codoping can enhance the upconversion emission without sacrificing the lifetime of state ${}^4I_{13/2}$.

Table 3-9 The bandwidth and the flat gain of TWL glasses

Samples	Bandwidth of the emission at 1535 (nm)	Flat gain (I_{1490}/I_{1530})
TWL1	73	0.4
TWL5	75	0.39
TWL6	80	0.43
TWL4	88	0.57

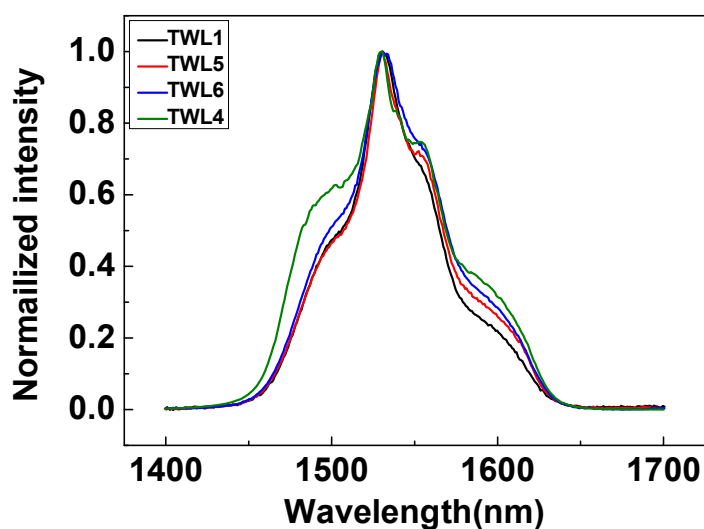


Figure 3-23 The fluorescence around 1535nm and the bandwidth of the glasses

Table 3-10 The lifetime for glasses at different states

Sample	Lifetime (ms)	
	1535nm	980nm
TWL1	5.35	0.03
TWL4	5.57	0.17
TWL5	5.36	0.86
TWL6	5.71	0.01

Judd-Ofelt parameters

As discussed in Chapter 2, section 2.2.2, Judd-Ofelt parameters Ω_t are important factors for the investigation of local structure of glass and the environment of rare earth ions in the glass system. Using the absorption spectra in Figure 3-18 and the Er^{3+} ions concentration (please refer to section 8.2 in Appendix for the calculation details) in Table 3-11, Judd-Ofelt parameters Ω_2 , Ω_4 , Ω_6 of TWL glasses with different rare earth ions can be determined from the least-squares fit to the experimental oscillator strength and the theoretical strength that calculated using equations 2.2 and 2.3. The reduced matrix elements $U^{(\lambda)}$ used in the calculation and the obtained intensity parameters are listed in Table 3-12 and Table 3-13, respectively. The reduction of Ω_2 indicates the decrease of the covalency between Er^{3+} ions and the oxygen ions. When codoped with other rare earth ions, such as Yb^{3+} and Ce^{3+} , the number of oxygen electrons that are available to coordinate with

Er^{3+} ions reduced, which caused the decrease of the covalency between Er-O oxygen bonds [46]. Therefore, Ω_2 reduced for glasses codoped with Yb^{3+} and Ce^{3+} as shown in Table 3-13. Ω_6 is correlated with the rigidity of the glasses, while Ω_4 is affected by the factors of changing both Ω_2 and Ω_6 [251, 252]. It can be seen that Ω_6 of the TWL glasses with different RE dopants are similar to each other, which means the RE codoping has little influence on the rigidity of the glass. This result is consistent with the thermal analysis.

Table 3-11 Er^{3+} ions concentration in the glasses calculated using glass density

Glasses	N (10^{20} cm^{-3})
TWL1	1.88
TWL2	0.47
TWL3	0.95
TWL4	1.90
TWL5	0.95
TWL6	0.90

Table 3-12 Reduced matrix elements of $U^{(\lambda)}$ between chosen intermediate coupled states of Er^{3+} ions [44]

a (S.L.J)	b (S'.L'.J')	U2	U4	U6
${}^4I_{15/2}$	${}^4I_{13/2}$	0.0188	0.1176	1.4617
${}^4I_{15/2}$	${}^4I_{11/2}$	0.0259	0.0001	0.3994
${}^4I_{11/2}$	${}^4I_{13/2}$	0.021	0.11	1.04
${}^4I_{15/2}$	${}^4I_{9/2}$	0	0.1452	0.0064
${}^4I_{15/2}$	${}^4F_{9/2}$	0	0.5655	0.4651
${}^4I_{15/2}$	${}^2H_{11/2}$	0.7056	0.4109	0.0870

Table 3-13 Calculated Judd-Ofelt parameters for Er^{3+} in TWL glass system

glasses	$\Omega_2 (10^{-20} \text{ cm}^2)$	$\Omega_4 (10^{-20} \text{ cm}^2)$	$\Omega_6 (10^{-20} \text{ cm}^2)$
TWL1	7.28	1.49	1.98
TWL2	4.29	1.08	1.92
TWL3	3.75	0.95	1.65
TWL4	5.72	1.31	1.76
TWL5	6.84	1.41	1.45
TWL6	5.22	1.22	1.49

The quality of the fitting of Ω_i parameters can be estimated by the magnitude of the room-mean-square (r.m.s.) deviation given by equation 2.6. The experimental and calculated oscillator strength adjusted after least-square fitting as well as the r.m.s of the fitting are listed in Table 3-14. It is shown that, all the r.m.s. values are in the magnitude of 10^{-6} with a maximum of 0.65×10^{-6} which is comparable with the reported value for TWL glasses [46]. The radiative transition probability, radiative lifetime and quantum efficiency of transition ${}^4I_{13/2} \rightarrow {}^4I_{15/2}$ were calculated with the

help of equations 2.7, 2.8 and 2.10 as shown in Table 3-15. There is only one radiative transition of state ${}^4I_{13/2}$, therefore, the branch ratio of this state is 1.

When compared the measured lifetime of transition ${}^4I_{13/2} \rightarrow {}^4I_{15/2}$ in Er^{3+} ions in Table 3-10 with that of the calculated radiative lifetime of this transition, it is obvious that the measured lifetimes are much longer than the calculated lifetime, which result in quantum efficiencies higher than 100%. This result is caused by the radiative trapping which can lengthen the measured lifetime due to the reabsorption of the photons emitted by the spontaneous emission processes. The phenomena of radiative trapping have been reported for Yb^{3+} phosphate glasses [253].

Table 3-14 The values of the measured experimental oscillator strengths f_{exp} (10^{-6}) and theoretical oscillator strengths f_{cal} (10^{-6}) of Er^{3+} in TWL glass systems

Excited states	TWL1		TWL2		TWL3		TWL4		TWL5		TWL6	
	f_{exp}	f_{cal}										
${}^4I_{13/2}$	3.04	2.79	2.79	2.78	2.43	2.42	2.66	2.65	2.13	2.14	2.28	2.13
${}^4I_{11/2}$	1.07	1.36	-	-	-	-	-	-	-	-	0.26	1.01
${}^4I_{9/2}$	0.50	0.40	0.51	0.30	0.46	0.27	0.59	0.37	0.45	0.37	0.42	0.32
${}^4F_{9/2}$	3.87	3.77	3.18	3.25	2.88	2.96	3.46	3.53	3.11	3.14	2.81	3.27
${}^2H_{11/2}$	17.30	17.31	9.95	9.97	9.37	9.35	13.90	13.91	15.30	15.26	11.90	11.86
rms (10^{-6})	0.27		0.22		0.21		0.23		0.09		0.64	

Table 3-15 Values of radiative transition probabilities, calculated lifetimes and quantum efficiency of transition ${}^4I_{13/2} \rightarrow {}^4I_{15/2}$ in Er^{3+} ions

Glasses	A	T (ms)	η
TWL1	410	2.44	2.19
TWL4	369	2.71	2.06
TWL5	280	3.57	1.50
TWL6	280	3.57	1.60

Upconversion

As mentioned in section 2.2.3 of Chapter 2, reactions between ions can cause upconversion processes. When the local concentration of rare earth ions is high enough, the ion-ion interaction is unavoidable. Therefore, upconversion is one of the main ion-ion interactive effects of the erbium ions. It is a critical factor in materials for erbium doped optical amplifiers, especially erbium doped waveguide amplifiers which require a high rare earth ion concentration due to a compact size. As

aforementioned in Chapter 2, energy transfer and cross relaxation are two main mechanisms that cause upconversion processes, which is also the case for the upconversion phenomena in codoped TWL glasses herein. In this section, red and green upconversion spectra were investigated.

To analyse the upconversion mechanism in RE codoped TWL glasses properly, the energy gaps between different levels in the rare earth ions are listed in Table 3-16. The upconversion spectra of the glasses were obtained using the Edinburgh Fluorospectrometer F900 with a pumping laser diode of 980 nm. They are normalized with respect to the green up-conversion at 545 nm as shown in Figure 3-24. The spectra exhibit three distinct emission bands corresponding to different excitation energy levels in the erbium ions. It can also be seen that the green upconversion is observed at both 520 nm and 545 nm. Referring to the energy level diagram in Figure 3-25, these two green upconversion peaks belongs to the transition of $^2H_{11/2} \rightarrow ^4I_{15/2}$ and $^2S_{3/2} \rightarrow ^4I_{15/2}$ in Er^{3+} ions, respectively. Moreover, the red upconversion fluorescence at 655 nm occurs due to the transition of $^4F_{9/2} \rightarrow ^4I_{15/2}$ in Er^{3+} ions.

The transitions with small energy gaps have a high probability of energy transfer. From Figure 3-25, it can be seen that the erbium ions are excited to state $^4F_{7/2}$ by two energy transfer processes from Yb^{3+} ions. In this process, one Yb^{3+} ion at state $^2F_{5/2}$ transfers its energy to an Er^{3+} ion at the ground state, and promotes it to one of the excited state. At the same time, Yb^{3+} ion is cascaded back down to the ground state. Following this process, the Er^{3+} ion at state $^4I_{11/2}$ is then excited to a higher state $^4F_{7/2}$ by the energy transfer from another excited Yb^{3+} ion. These two energy transfer processes are both resonant energy transfer since the energy donor (transition $^2F_{5/2} \rightarrow ^2F_{7/2}$) has the same energy gap as the energy acceptor (transitions $^4I_{15/2} \rightarrow ^4I_{11/2}$ and $^4I_{11/2} \rightarrow ^4F_{7/2}$ in Er^{3+} ions), as shown in Table 3-16. The other path of $^4F_{7/2}$ state population results from ion interaction between two Er^{3+} ions via a cross-relaxation process. Er^{3+} ions are promoted to state $^4I_{11/2}$ directly by the pumping laser, where one of the Er^{3+} ion states gives its energy to another which is then promoted to state $^4F_{7/2}$ [254]. This transition ($^4I_{11/2} \rightarrow ^4F_{7/2}$) can also happen by absorbing energy from the pumping source. Er^{3+} ions at state $^4F_{7/2}$ are cascaded rapidly down to the state

$^2H_{11/2}$ and $^2S_{3/2}$ via nonradiative decay due to the very small energy gap between these states. Excited Er^{3+} ions at states $^2H_{11/2}$ and $^2S_{3/2}$ then relax down to the ground state producing the green luminescence at 520 nm and 545 nm. In the paths of the population of state $^4F_{7/2}$ in Er^{3+} ions, the process via energy transfer from Yb^{3+} ions is dominant due to their large absorption cross section at around 980 nm [254], which indicates that Yb^{3+} codoping could enhance the efficiency of the green upconversion luminescence.

As mentioned previously, if the energy donor and acceptor have the same energy gap, then resonant energy transfer processes can happen. From the values in Table 3-16, it is obvious that resonant energy process without any phonon involved is difficult to take place for energy transfer processes $^2F_{5/2}$, $^4I_{13/2} \rightarrow ^2F_{7/2}$, $F_{9/2}$ from Yb^{3+} ions to Er^{3+} ions and $^4S_{3/2}$, $^2F_{5/2} \rightarrow ^4F_{9/2}$, $^2F_{7/2}$ from Er^{3+} ions to Ce^{3+} ions. Therefore, phonon-assistant energy transfer is considered instead for these two processes. The phonon energy in TWL glasses is around 920 cm^{-1} according to the Raman spectra in the following section. From Table 3-16, it can be seen that about two phonons are needed to bridge the energy discrepancy between transitions $^2F_{7/2} \rightarrow ^2F_{5/2}$ in Yb^{3+} ions and transitions $^4I_{13/2} \rightarrow ^4F_{9/2}$ in Er^{3+} ions, which is also the case for energy transfer of process $^4S_{3/2}$, $^2F_{5/2} \rightarrow ^4F_{9/2}$, $^2F_{7/2}$ from Er^{3+} ions to Ce^{3+} ions. These two processes increase the population of state $^2F_{7/2}$ and consequently, Yb^{3+} and Ce^{3+} codoping can enhance the red upconversion of the glasses.

Table 3-16 The theory energy gap of various transitions in the rare earth ions of Er^{3+} , Yb^{3+} , and Ce^{3+}

Rare earth ions	Transitions between energy levels	Energy gap ($\times 10^3\text{ cm}^{-1}$)	Wavelengths (nm)
Er^{3+}	$^4I_{15/2} \rightarrow ^4I_{11/2}$	10.2	980
	$^4F_{7/2} \rightarrow ^4I_{11/2}$	10.2	980
	$^4I_{13/2} \rightarrow ^4F_{9/2}$	9.66	1035
	$^4S_{3/2} \rightarrow ^4F_{9/2}$	3.37	2967
	$^4I_{11/2} \rightarrow ^4I_{13/2}$	3.71	2695
	$^2F_{7/2} \rightarrow ^2H_{11/2}$	1.17	8547
	$^2H_{11/2} \rightarrow ^4S_{3/2}$	0.8	12500
Yb^{3+}	$^2F_{5/2} \rightarrow ^2F_{7/2}$	10.2	980
Ce^{3+}	$^2F_{7/2} \rightarrow ^2F_{5/2}$	2	4546

Note: energy gap is defined as the energy difference between the initial and final states

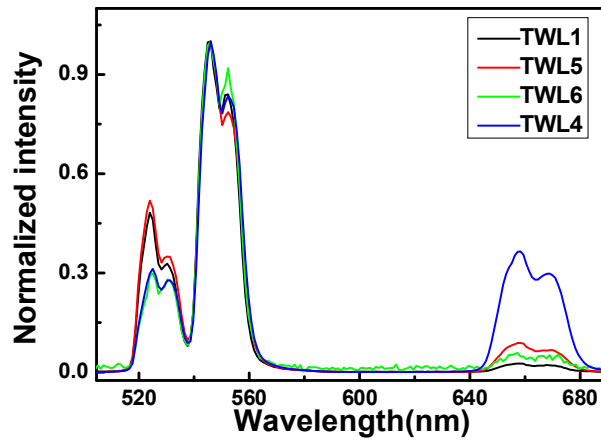


Figure 3-24 Up-conversion spectra of the glasses doped with different rare earth ions

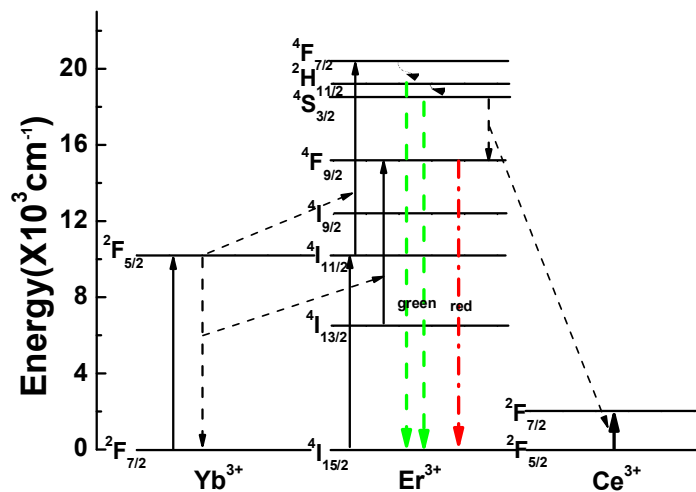


Figure 3-25 Schematic energy level diagram of Er^{3+} , Yb^{3+} and Ce^{3+} ions. The energy transfer processes between these ions were also depicted

Figure 3-24 shows that glasses TWL5 (Yb^{3+} codoping) and TWL6 (Ce^{3+} codoping) have slightly higher red upconversion intensity at around 650 nm. For Er^{3+} / Yb^{3+} / Ce^{3+} codoped glasses, the red upconversion increases significantly due to the influences of both Yb^{3+} and Ce^{3+} ions. These results are consistent with the previous analysis of the energy transfer processes between these rare earth ions.

3.2.4 Structural analysis

3.2.4.1 Experiments

FTIR spectroscopy

IR spectroscopy is a powerful tool to study structural properties of glasses. The IR spectra are plotted using absorbance versus wavenumber ν which could be calculated by the following equation:

$$\nu = \lambda^{-1} = \frac{1}{2\pi c} \left(\frac{k}{\mu} \right)^{\frac{1}{2}} \quad (3.13)$$

where k is the bending or stretching force constant of the bond, c is the speed of light and μ is the reduced mass of the molecule, which is given by:

$$\mu = \frac{m_1 m_2}{m_1 + m_2} \quad (3.14)$$

where m_1 and m_2 represent the atomic masses of the two atoms[246]. It can be seen from this equation that the wave number of the vibrational modes in these spectra is determined by the force constant between the cation-anion bonds and the mass of the atoms in the material.

The IR absorption spectra of glasses in this thesis were measured from 400 cm^{-1} to 2500 cm^{-1} with reflected mode utilizing Bruker Vertex FTIR spectrometer 1725x that is discussed in detail in section 3.2.3.1. The reference used in these experiments was a gold mirror with a perfect smooth surface, and all the measurements were carried out in nitrogen filled atmosphere to reduce the influence of the contamination in the air.

Raman spectroscopy

Raman spectroscopy has proved to be an excellent tool for determining the structural features of amorphous materials, e.g. glasses. Similar to the FTIR spectroscopy, Raman spectroscopy which is produced by vibrations of the molecules in the materials is useful for determining the composition and structure of materials. However, FTIR spectroscopy is related to dipole moment changes in the molecules while the Raman effects occur due to the polarizability changes [255]. Dipole moment is a vector quantity which is used to characterize of a dipole. A dipole is the separation of the centre of positive charges and negative charges. If a vibrational bond in a molecule is symmetrical, the dipole moment will stay constant, and there will be no FTIR spectra yielded. However, the polarizability of the molecule which

relates to distributions of the electron cloud will change and produces Raman spectra. The difference discussed above is the primary difference between FTIR and Raman spectroscopy.

There are many other differences between FTIR and Raman spectroscopy. For example, covalent bonds could produce stronger Raman spectra while ionic bonds produce stronger FTIR spectra; water is a weak Raman scattering material, as a result, the Raman spectra is not influenced by the solvent and is an ideal technique to analyse the structures of compounds in the solution[255].

Raman Effect is a kind of light scattering produced because of the change of polarization in the molecules. There are two types of Raman scattering, Stokes scattering and anti-Stokes scattering. When light interacts with medium, both absorption and emission processes could happen when the energy of photons matching with the differences between energy states of the electrons. When photons are absorbed, the frequency (energy) of scattering light is lower than the incident light, and the scattering in this case is defined as Stoke scattering. While for anti-Stoke scattering, the scattering light has higher frequency than that of original light. Besides Raman scattering, there is another type of scattering known as the Rayleigh scattering. Raman scattering changes the energy or frequency of photons compared to the incident radiation, while Rayleigh scattering keeps these values. The schematic of Raman scattering and Rayleigh scattering is shown in Figure 3-26 .

The vibration frequency of molecules can also be calculated using equation (3-13). Here, Raman spectra were measured using a Renishaw inVia Raman microscope which consists of a laser source, microscope, monochromator, filter, detector and a data processing unit. The schematic of the Raman system is shown in Figure 3-27. The light beam passes through a monochromator which could split the light into a bunch of lights with different wavelength (refer to Figure 3-11). Then the light is focused onto the sample with the help of a microscope. The signal scattered from the sample is reflected to a filter which removes the Rayleigh scattering. Raman scattering that passes through the filter will be collected by the detector. The

wavelength and the intensities of the signal are recorded to obtain the Raman spectra with the help of the data processing unit.

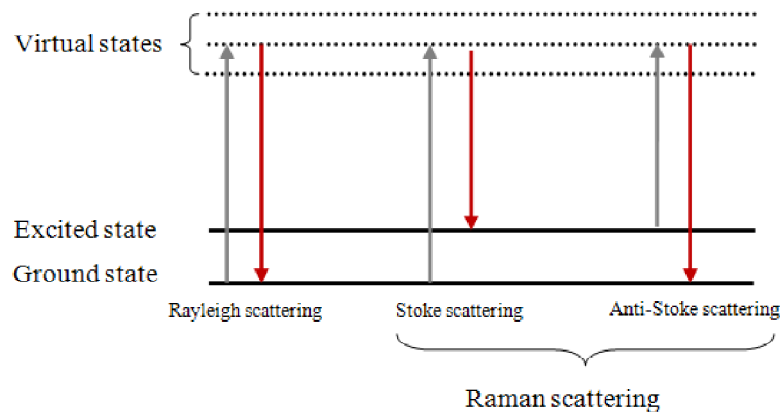


Figure 3-26 Schematic of light scattering

One of the severe disadvantages of Raman spectroscopy is the strong disturbance from fluorescence, thus the excitation wavelength should be chosen carefully to avoid this influence. The excitation wavelength used in the Raman system discussed here is 514 nm, where the fluorescence from erbium has a strong influence. As a result, only the undoped glass TWL0 was studied by Raman spectrometer.

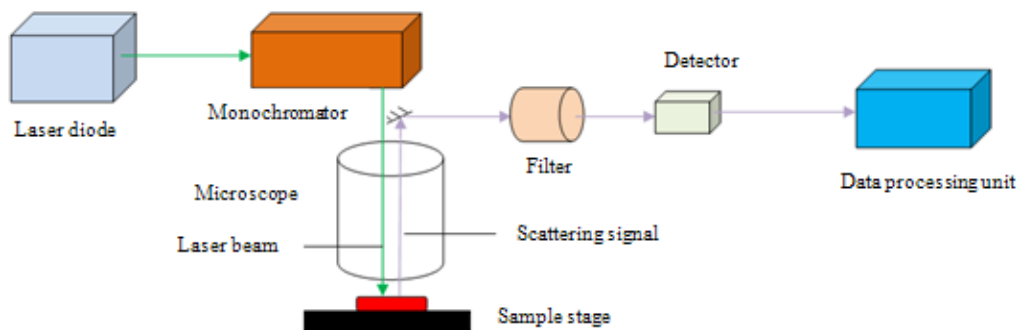


Figure 3-27 Schematic of Raman spectrometer

3.2.4.2 Results and discussions

FTIR

FTIR reflection mode is used in order to collect the absorption spectra of the glass samples with an approximate thickness of 0.4 cm. Unlike the transmittance spectra, the incident light beam does not pass the medium but is reflected directly from the surface of the sample which is why it is not affected by the thickness of the sample. The reflection spectra can then be converted into absorption spectra using the tool in the software.

The IR absorption spectroscopy was measured from 400 cm^{-1} to 2500 cm^{-1} using reflected mode as shown in Figure 3-28. It is clear that there are very strong peaks in the range of 400 to 1200 cm^{-1} which is attributed to the molecular vibration of the glass, while three small peaks in high frequency range are due to electron transitions of the rare earth in the glass or weak molecular vibration of host materials.

The peak around 504 cm^{-1} is attributed to the W-O-W linkages between the paired sixfold coordinate W atoms in groups $[\text{O}=\text{WO}_5]_2$ while the very small weak shoulder at around 733 cm^{-1} is the contribution of a stretching vibration of Te-O-W linkages[80]. A strong peak around 879 cm^{-1} is attributed to the absorption of W-O-W linkages in WO_6 octahedra. Besides this peak, there is another shoulder at around 945 cm^{-1} which is believed to be the contribution of W=O in WO_4 or WO_6 , which is still a disputable topic [77, 80, 256]. The absorption peaks at 2151 cm^{-1} (4649 nm) are corresponding to the transition of $^4I_{5/2} \rightarrow ^4I_{7/2}$ in Ce^{3+} ions [245]. The weak peaks at 1280 cm^{-1} and 1887 cm^{-1} may be attributed to the Te=O overtone vibration in $[\text{TeO}_6]$ groups and O=W overtone vibrations in pair groups of $[\text{O}=\text{WO}_5]_2$ [257, 258], respectively. The overtone vibration of group $[\text{TeO}_6]$ at around 1220 cm^{-1} has been reported by O'Donnell using FTIR spectra [257]. All the assignments of the IR absorption peaks are listed in Table 3-17.

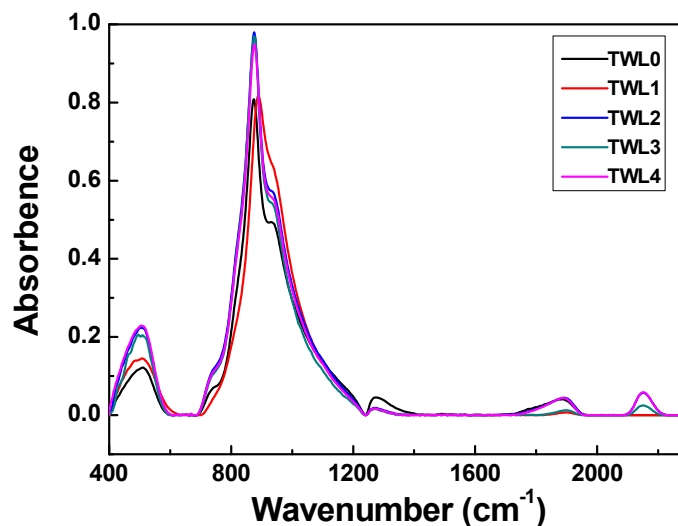


Figure 3-28 FTIR absorption spectroscopy of the glasses measured using reflection mode

Table 3-17 The assignment of the IR absorption peaks measured using reflection modes

Peak position	assignments	References
504 cm ⁻¹	W-O-W	[80]
733 cm ⁻¹	Te-O-W	[80]
879 cm ⁻¹	W-O-W in WO ₆	[77, 80, 256]
945 cm ⁻¹	W=O	[77, 80, 256]
1280 cm ⁻¹	overtone vibrations of group [TeO ₆]	[257]
1887 cm ⁻¹	O=W overtone vibration in [O=WO ₅] ₂	[258]
2151 cm ⁻¹	transition of ⁴ I _{5/2} -- ⁴ I _{7/2} in Ce ³⁺ ions	[245]

Raman spectra

Before the structural analysis of TWL glasses using Raman spectrum, it should be noted that addition of modifier RO (R=K, Li, La, Na etc.) into the TeO₂-WO₃ glasses could break the Te-O-Te bonds and form more Te-O-W bonds. RO will only modify the glass properties, but not affect the glass structure. As a result, the TWL glass has similar elemental groups with the TeO₂-WO₃ glass.

The Raman spectrum of glass TWL0 determined using a Renishaw inVia Raman microscope with a 514 nm laser diode at the power of 25 mW is shown in Figure 3-29. Unlike the Raman spectra of crystalline material with sharp absorption peaks, Raman spectra of glasses have broad absorption peaks. From Figure 3-29, it is evident that the Raman peaks of TWL0 glass are broad which indicates the glass is totally amorphous. The spectrum obtained was deconvoluted using symmetric Gaussian-type function with the help of Origin 7.5. It can be seen that there are peaks at around 279 cm⁻¹, 339 cm⁻¹, 449 cm⁻¹, 652 cm⁻¹, 758 cm⁻¹ and 921 cm⁻¹, which are marked as A, B, C, D, E and F, respectively. The contributions of bands A-F are assigned according to some references. Band A is due to W-O-W bond vibrations in WO₆ octahedrons [259, 260]. Band B is attributed to Te-O-W linkages [261]. Band C is ascribed to be the contribution of symmetric stretching and bending vibrations of Te-O-Te or O-Te-O bonds [256]. Band D represents Te-O-Te bonds between two fourfold coordinated Te atoms in TeO₄ trigonal bipyramid (tbp) [256]. The strength of band E is attributed to stretching vibrations of O=TeO₂ trigonal pyramid (tp) units [80]. The attribution of band F at 921 cm⁻¹ is assigned to O=W bonds in

single six-fold coordinated W atoms in the WO_4 or $\text{O}=\text{WO}_5$ octahedron [80]. Through the discussion above, we could conclude that the TWL glasses prepared contain TeO_4 , TeO_3 and WO_6 or WO_4 groups. All the assignment of the Raman peaks and the references are listed in Table 3-18. It is obvious that the structural analyzing result of Raman spectra is consistent with that of the FTIR spectra.

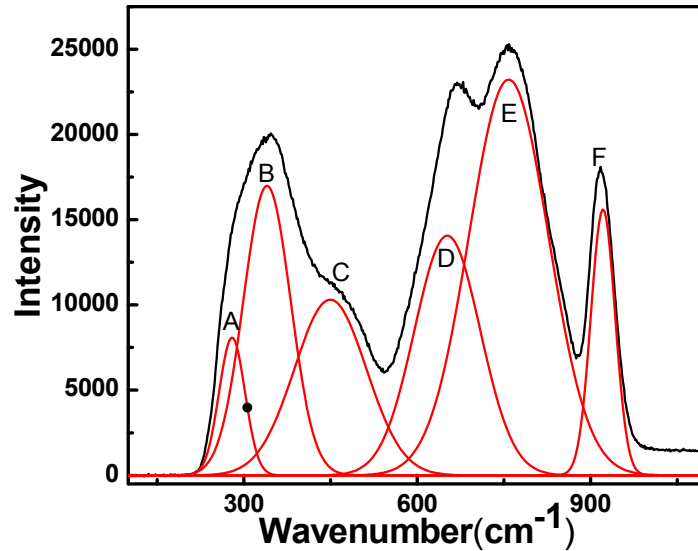


Figure 3-29 Raman spectra with deconvolution of undoped TWL glasses

Table 3-18 The assignment of the Raman peaks of TWL glasses

Peak position(cm^{-1})	assignments	References
279	W-O-W bond in WO_6	[259, 260]
339	Te-O-W linkages	[261]
449	Te-O-Te or O-Te-O bonds	[256]
652	Te-O-Te between two TeO_4	[256]
758	stretching vibrations of $\text{O}=\text{TeO}_2$	[80]
921	O=W	[80]

3.3 Discussion of glasses for thin film fabrication

3.3.1 The role of Yb^{3+} and Ce^{3+} codoping

From Figure 3-5 and Table 3-3, it is clear that the undoped glass TWL0 and Er^{3+} doped glass TWL1 have better thermal stability than glasses codoped with Yb^{3+} and Ce^{3+} , which might be due to the rare earth ions codoping could increase the proportion of non-bridging oxygen and consequently reduce the compactness of the glass structure. From Figure 3-28, it is evident that the intensities of peaks around 504 cm^{-1} and 879 cm^{-1} of codoped glasses TWL2 to TWL4 are higher than Er^{3+} doped glass TWL1, which implies that groups WO_6 have a higher proportion in Yb^{3+} and Ce^{3+} codoped glasses than that in the Er^{3+} doped glasses. As Sokolov proposed in his paper[80], one WO_6 group in the glass will cause the formation of two TeO_3 groups in the glass structure. Therefore, it can be concluded that the fraction of TeO_3 groups in Yb^{3+} and Ce^{3+} codoped glasses are higher than that in the Er^{3+} doped glasses which makes the glass structure much looser as thermal analysis suggested. The trend of the refractive index change with Yb^{3+} and Ce^{3+} codoping also indicates that Yb^{3+} and Ce^{3+} codoping makes the glass structure looser which is also consistent with the conclusion drawn from the above discussion.

From the UV absorption curve in Figure 3-18, it can be seen that the TWL glasses are transparent from 399 nm to 491 nm in the visible range, and in the IR range around 1900 cm^{-1} ($5.26\text{ }\mu\text{m}$). This indicates TWL glasses are transparent in the range of 399 nm to $5.26\text{ }\mu\text{m}$ which is slightly larger than that Dorofeev and his colleagues [233] obtained (of 440 nm to $5\text{ }\mu\text{m}$). On the other hand, Ce^{3+} codoping in the glasses can shift the UV cutoff edge to the longer wavelength which is assumed to be due to the interconfiguration transition between 4f and 5d orbitals that increases the ionic radius and consequently expands the optical energy gap [250].

The results shown in Figure 3-23 illustrate all the fluorescence spectra of the glasses which have very similar linewidth shapes and peak positions. The bandwidths of the fluorescence spectra for triply doped glasses are higher than those for doubly or singly doped glasses which may result from the influences of the energy transfer between the rare earth ions or the different environment around Er^{3+} ions. Upconversion which diminishes the intensity of the emission around 1535 nm is not

desirable for lasers and amplifier devices, as it depletes the efficiency of such devices. However, it has extensive applications in fields of display, sensors and LEDs. Both green (520 nm and 545 nm) and red upconversions are enhanced when codoping Er^{3+} , Yb^{3+} and Ce^{3+} in glasses due to the energy transfer mechanisms between these rare earth ions.

3.3.2 Structural analysis

From the study of TeO_2 crystals, it is believed that the basic structural units in the tellurite crystal can be TeO_4 tbps and TeO_3 tp. Tellurite glass has a distorted structure similar to its crystal, therefore, these two basic structural units are also the main units in tellurite glasses.

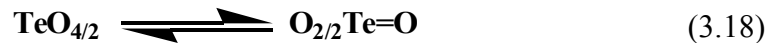
In the binary glasses, when a network modifier oxide is added, two kinds of structural changes are considered[262]. In the first model[262], it is assumed that one of the bridging oxygen (BO) in TeO_4 tbps is transformed to two non-bridging oxygen (NBO) by inserting an oxygen atom from the modifier oxide. This model is similar to what happens in silicate glasses.



In this model, the addition of the modifier leads to the creation of TeO_4 tbps with a non-bridging oxygen atom. The molar ratio of $\text{TeO}_3/\text{TeO}_4$ is independent of composition of the modifier because there is no TeO_3 tp produced [262]. The fraction of NBO in this model is:

$$\text{NBO}/(\text{BO} + \text{NBO}) = \{2[\text{O}/\text{Te}] - 4\} / [\text{O}/\text{Te}] \quad (3.17)$$

In the second model[262], the addition of the modifier oxide changes one of the TeO_4 tbp to TeO_3 tp with NBO atoms. In this case, the oxygen atoms have two kinds of formation, one is single bonded BO and NBO, the other is double bonded oxygen atoms (also a kind of NBO) as shown in the following equilibrium reactions:



where $\text{TeO}_{4/2}$ and $\text{O}_{2/2}\text{Te}=\text{O}$ are similar units that can be represented by TeO_2 , while $\text{O}_{3/2}\text{Te}-\text{O}^-$ and $\text{O}_{2/2}\text{Te}(=\text{O})\text{O}^-$ can be represented as $1/2[\text{Te}_2\text{O}_5]^{2-}$. The reactions in this model can be described as the following equilibriums:



The fraction of NBO is calculated using the following equation:

$$\text{NBO}/(\text{BO}+\text{NBO}) = \frac{\{2[\text{O}/\text{Te}]-3\}[\text{TeO}_3/\text{TeO}_4] + 2[\text{O}/\text{Te}]-4}{[\text{O}/\text{Te}]\{[\text{TeO}_3/\text{TeO}_4]+1\}} \quad (3.21)$$

In this equation, two oxygen atoms in unit $[-\text{Te}(=\text{O})\text{O}^-]$ are considered as equivalent due to the resonance. The molar ratio of $\text{TeO}_3/\text{TeO}_4$ can be calculated using the Raman peak intensity, approximately [262].

For the Raman spectra of TWL glass in this thesis, peaks at 652 cm^{-1} and 758 cm^{-1} represent the vibrations of unit TeO_4 and TeO_3 , respectively, as described in section 3.2.4.2. Therefore, it is assumed that $\text{TeO}_3/\text{TeO}_4$ can be calculated using I_{758}/I_{652} [262]. The presence of peak 758 cm^{-1} confirms the existence of unit TeO_3 . As a result, model 1 which has no unit of TeO_3 produced is not appropriate for the TWL glasses here. The results of Raman and FTIR in the above section indicate that both TeO_4 and TeO_3 are the basic units in the TWL glasses discussed in this thesis. There are three types of $\text{Te}-\text{O}$ bonds: $\text{Te}-\text{O}_{\text{long}}$ ($>0.20 \text{ nm}$), $\text{Te}-\text{O}_{\text{mid}}$ (0.20 nm) and $\text{Te}-\text{O}_{\text{short}}$ ($<0.20 \text{ nm}$) [79]. The schematic of the two basic structural units is shown in Figure 3-30.

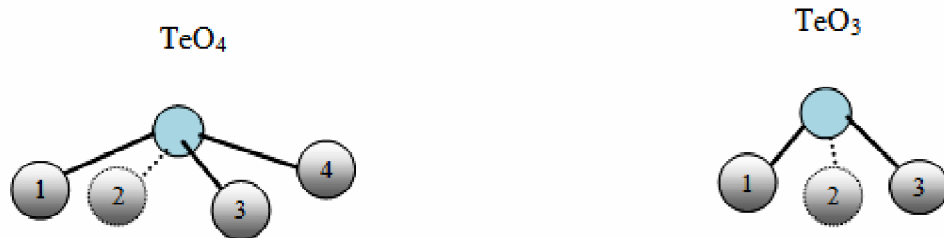


Figure 3-30 The schematic of the structural units of TeO_4 and TeO_3 [79, 80]. Bond lengths in TeO_4 : $\text{Te}-\text{O}_1 = \text{Te}-\text{O}_4 > 0.20 \text{ nm}$, $\text{Te}-\text{O}_2 = \text{Te}-\text{O}_3 < 0.20 \text{ nm}$; Bond lengths in TeO_3 : $\text{Te}-\text{O}_1$ and $\text{Te}-\text{O}_2 < 0.20 \text{ nm}$, $\text{Te}-\text{O}_3 = 0.20 \text{ nm}$

When the modifier WO_3 is added, the coordination number of unit group of W^{6+} has arguments on whether it exists in the formation of WO_4 (coordination is 4) or WO_6 (coordination is 6) in the glasses as discussed in Chapter 2, section 2.3.1. The author of this thesis agrees with Sekiya's statement that the TeO_4 tbps is difficult to be substituted by WO_4 due to the lone electron pair in the sp^3d hybrid orbitals. Therefore, for the TWL glass in this thesis it is assumed that WO_6 is the main formation of W^{6+} . The schematic of this structural unit is shown in Figure 3-31. Actually, in pure WO_3 crystals all the $\text{W}-\text{O}$ bonds have the same length, while when

mixed with other compounds, WO_6 octahedron is deformed. One of the bonds (i.e. $\text{W}-\text{O}_6$) is elongated to connect with other groups and the opposite bond (i.e. $\text{W}-\text{O}_1$) is shortened [78]. Meanwhile, the insertion of WO_6 can break the linkages between two TeO_4 units and change the tellurium atoms to threefold coordinated ones, which means two TeO_3 units can be formed for each WO_6 units insertion [80].

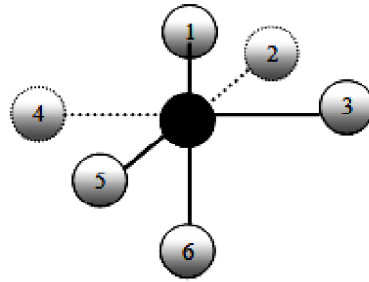
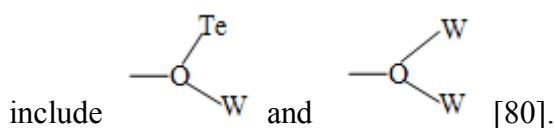


Figure 3-31 The schematic of structural unit WO_6 [78, 80]. Black circle represents W atom, grey circles represent oxygen atoms. Bond length $\text{W}-\text{O}_1 < 0.20 \text{ nm}$, $\text{W}-\text{O}_2 = \text{W}-\text{O}_3 = \text{W}-\text{O}_4 = \text{W}-\text{O}_5 > 0.20 \text{ nm}$, $\text{W}-\text{O}_6 > 0.20 \text{ nm}$.

From the analysis of FTIR spectroscopy, besides the structural units TeO_4 , TeO_3 and single WO_6 , there are also structural units $[\text{TeO}_6]$ and $[\text{O}=\text{WO}_5]_2$ which represent two connected TeO_3 and WO_6 resonant group, respectively, in the TWL glasses. However, pair units $[\text{TeO}_6]$ and $[\text{WO}_6]_2$ could only be detected using the reflection mode FTIR. O'Donnell believed that the weak overtone absorptions are the combinations of fundamental Raman absorptions and Te-O infrared bands that result in IR active modes. It is believed this is the reason why overtone absorptions of $[\text{TeO}_6]$ and $[\text{O}=\text{WO}_5]_2$ groups have not shown in the Raman spectra [257].

The linkages in these structural units include bridging oxygen atoms and threefold coordinated oxygen atoms. The former one includes linkages between TeO_4 unit and its environment: $\text{Te}_I-\text{O}-\text{Te}_I$, TeO_4 and its environment: $\text{Te}_{II}-\text{O}-\text{Te}_{II}$, TeO_4 and TeO_3 : $\text{Te}_I-\text{O}-\text{Te}_{II}$; WO_6 and its environment: $\text{W}-\text{O}-\text{W}$; and linkages between WO_6 and TeO_4 as well as WO_6 and TeO_3 : $\text{Te}_I-\text{O}-\text{W}$, $\text{Te}_{II}-\text{O}-\text{W}$. The threefold coordinated oxygen atom connect groups TeO_4 , TeO_3 and WO_6 together, therefore, the linkages



Based on the above analysis, the local structure of the TWL glasses can be drawn and is shown in **Error! Reference source not found.** The bond lengths and bond angles in the structure are listed in Table 3-19.

Table 3-19 The bond lengths and angles between the bonds in the glass structure [80]

Structural unit	Bond	Bond lengths(nm)	Angle	degrees
TeO ₄	Te-O _a	0.1914	O _a -Te-O _a	105.2
	Te-O _c	0.2150	O _a -Te-O _c	91.2
			O _c -Te-O _c	172.9
TeO ₃	Te-O _n	0.1818	O _n -Te-O _b	97.3
	Te-O _b	0.2000	O _b -Te-O _b	94.3
	Te'-O _b	2.038	Te-O _b -Te'	135.3
	Te-O _n	0.1838	O _n -Te-O _a	101.6
Paired TeO ₃	Te-O _a	0.2042	O _n -Te-O _b	101.9
	Te-O _b	0.1921	O _a -Te-O _b	97.2
	Te'-O _b	0.2326	Te-O _a -Te	127.7
			Te-O _b -Te'	115.3
WO ₆	W-O _n	1.735	O _n -W-O _b	99.4
	W-O _b	0.2025	O _n -W-O _t	176.2
	W-O _t	0.2321	O _b -W-O _t	80.8
				88.5
			O _b -W-O _b	159.4
			W-O _b -Te	114.8
[O=WO ₅]		0.1735	W-O _t -Te	145.2
			O _n -W-O _b	113.8
			O _n -W-O _b	98.1
	W-O _b	0.2059	O _n -W-O _t	101.2
				168.4
	W-O _t	0.2330	O _b -W-O _t	86.2
			O _b -W-O _b	153.8
		W-O _b -Te	88.4	
		W-O _t -Te	136.4	
		W-O _t -Te	109.1	
		W-O _t -W	128.1	
			109.7	

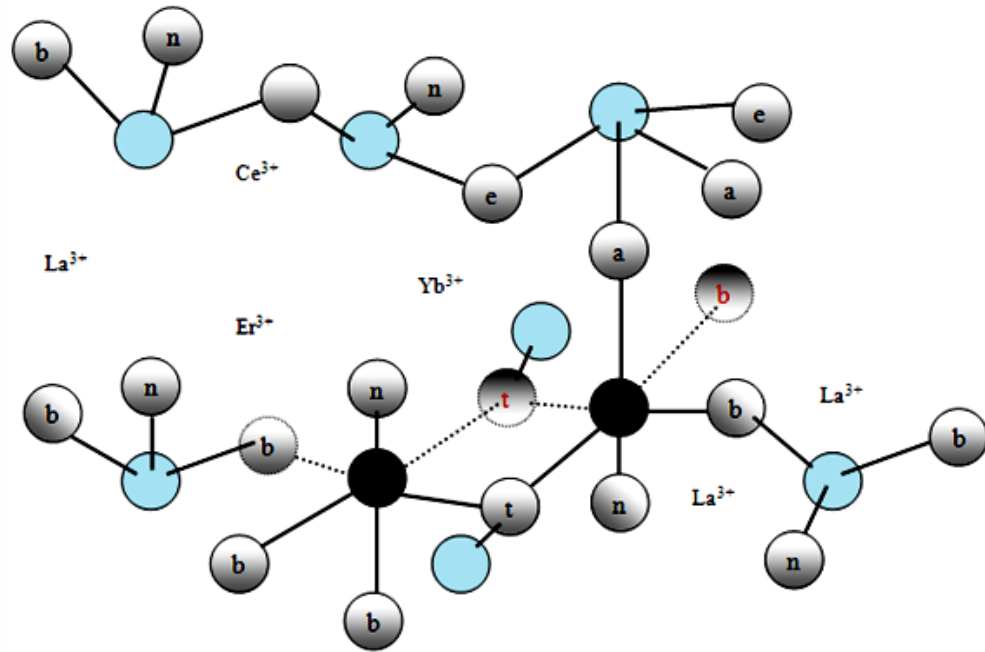


Figure 3-32 Schematic of local structure of TWL glasses. Blue circles represent Te atoms, grey circles represent oxygen atoms, and black circles represent W atoms.

3.4 Conclusions

1. Er^{3+} doped glass TWL1 has a relatively higher stability compared to $\text{Yb}^{3+}/\text{Ce}^{3+}$ codoped glasses TWL2-TWL4.
2. When codoped with Er^{3+} and Yb^{3+} , the optical energy gaps of TWL glass are reduced compared to Er^{3+} doped glass TWL1. While codoped with Er^{3+} and Ce^{3+} , the UV cutoff edges shift to longer wavelength and the optical energy gaps increase. The change of the optical energy gaps of TWL glasses is believed to be due to the rearrangement of the glass structure.
3. From the analysis of reflection FTIR and Raman spectra, the glasses have group units of TeO_4 , TeO_3 , single WO_6 , and pair groups $[\text{WO}_6]_2$ and $[\text{TeO}_6]$. The local structures of TWL glass is drawn according to the structure model and the analysed results.
4. When doped with different rare earth ions, there is no obvious change in the linewidth shape, FWHM, peak position of fluorescence spectra of these glasses.

5. The Judd-Ofelt parameters were calculated using the absorption spectra. The results showed that the Yb^{3+} and Ce^{3+} codoping can reduce the covalency of Er^{3+} ions which caused the reduction of Ω_2 . The long measured lifetime of transition ${}^4I_{13/2} \rightarrow {}^4I_{15/2}$ implies the radiative trapping effect in the TWL glass system. As a result, the calculated lifetime should be referred as the lifetime of the TWL glass.
6. Codoped with Yb^{3+} and Ce^{3+} ions into Er^{3+} doped glasses can enhance the upconversion which could reduce the lasing or amplification ability of the glasses.

Chapter 4 Fabrication and characterisation of tellurite glass thin film on silica substrate

As discussed in Section 2.1 of Chapter 2, that planar channel waveguides have dominant potential advantages over optical fibres. Thin film is a typical planar waveguide which consists of a substrate and a thin layer of dielectric material with larger refractive index than that of the substrate. The cladding layer is usually air. Once thin films are obtained, various devices or nanostructure with different geography can be fabricated on.

According to the analysis in Chapter 3, Er^{3+} doped glass TWL1 has comparatively better properties compared with other Yb^{3+} and Ce^{3+} codoped glasses made in this work. As summarized in Chapter 3, glass TWL1 has better thermal stability and lower upconversion efficiency which is a critical quality for this material to be used in the application of amplifiers and lasers. Therefore, the composition of glass TWL1 (Er^{3+} doping concentration: 1wt% or 0.5 mol%) was chosen as the recipe of target used for thin film deposition in this chapter. All targets used herein were prepared using alumina crucibles.

This chapter focuses on the fabrication of erbium doped TWL glass films on silica substrate. As mentioned in Section 2.5.7 of Chapter 2, the deposition parameters, namely, laser energy fluence and laser repetition rate, oxygen pressure, and substrate temperature in addition to distance between the substrate and the target have critical effects on the quality of the thin film obtained. Therefore, first of all, these deposition parameters are optimized based on the composition of glass TWL1. The properties of obtaining thin films (with thickness of 1-2 μm) deposited at different conditions, especially, at the optimized conditions are investigated in detail using various techniques, such as UV, fluorescence spectroscopy, X-ray diffraction (XRD) and scanning electron microscopy (SEM) etc. These techniques, for example XRD and SEM, and their measurement principles which are not included in Chapter 3, are explained in this chapter as well.

4.1 SEM and XRD techniques for thin film investigation

4.1.1 SEM-Energy dispersive X-Ray (SEM-EDX)

SEM-EDX as an electron microscope fitted with an energy dispersive spectrometer can be used as a powerful technique to investigate the topography, composition or electrical conductive properties of materials. The topography such as particle distribution and size on the top layer of the thin films and the composition of the thin films are crucial factors for determining the quality of the thin films. Therefore, SEM-EDX was utilized to analyse the topography and composition of the thin films in this work.

Compared to the traditional optical microscope, SEM has merits on the study of surfaces of solid samples due to the ultra-high resolution that it can achieve. The maximum resolution of the microscope is correlated with working wavelengths, refractive indices of the surrounding media and distances between lens and sample. The optical microscope uses visible light as the energy source which has a relatively long wavelength, and the surrounding media is usually air which refractive index is restricted to be around 1. In addition, the distance from lens to the sample is limited as well. As results of these limitations, the magnification of the optical microscopy is as low as 1000.

Conversely, SEM uses an electron beam which has a much shorter wavelength than the visible light (about 0.02 nm) as energy source. The shorter wavelength of the electron beam in SEM enables to yield a higher image resolution. As a result, images acquired using this technique have satisfied quality even down to the nanometer level. Additionally, SEM has a large depth of field which is why images obtained using this technique exhibiting a three dimensional (3D) like appearances [263].

The main components in SEM system are lenses, an electron gun, electron collector, visual and photo recording system (view screen) and any other associated electronics. The schematic of this system is shown in Figure 4-1. A high voltage is firstly applied on a filament (usually tungsten), and then electrons escape from the filament to an anode when the voltage reached the value of threshold voltage. With the help of the anode voltage, electrons can form a beam which comes down through the

whole column and is incident on the sample under the alignment of lenses. The interaction between the incident electrons and the sample can yield various electron signals, such as secondary electron and backscattered electron, ions and atoms etc. The imaging detector collects the obtained electron signals point by point, converts them into intensity changes on a viewing screen, and produces images subsequently. There are many factors that correlate with the quality of images that can be achieved, specifically, diameter of final electron beam incident on a specimen (resolution), electron beam current (contrast between image feature and background), angle between electron beam and specimen (focus area), and voltage of the electron beam (field depth) [263].

As aforementioned, once the electron beam is incident on the sample surface, it will interact with the material, and scatter or generate a variety of signals, namely, electrons (back scattering electrons, and secondary electrons), ions and atoms in addition to X-rays. All the scattering effects can be combined together to produce 3D “interaction volume” as shown in Figure 4-2. The depth of the interaction volume is related to the voltage of the electron beam utilised and the properties of the sample. The X-ray signal is a small fraction among these signals produced due to the higher threshold voltage it requires. It is produced when electrons in the inner electron shell is excited leaving a hole. The hole in the inner electron shell can be filled by electrons in the outer shell subsequently, and X-ray is produced in this process. The energy of the X-ray signal is a characteristic of atomic structure and is consistent with the energy difference between these two electron shells. As a result, the composition of sample can be identified by measuring the intensity of the X-ray signal using an energy dispersive spectrometer.

In this work, a field emission gun (FEG) SEM (LEO 1530 FEGSEM) was used to measure topography of thin films on silica substrates. Compared to the traditional thermionic electron gun which has a low brightness, limited lifetime and large energy spread field, FEG is usually a sharp zirconia coated tungsten tip and emit electrons by a thermally assisted field emission process. Therefore, it has a much higher brightness and better capability of yielding high quality images[263].

As all the materials used in this work are dielectric materials, to avoid electron charging which reduces the quality of images, all the samples need to be coated by materials with good conductivity before the measurements. In this work, bulk glasses were coated by gold while thin films were coated by platinum (Pt) of around 10 nm thickness.

When taking images of sample surfaces, the voltage of the electron beam was set as low as 3 kV to obtain a truthful image of the top surface and the working distance was usually set as 3 mm. During the EDX measurement, the electron beam voltage was increased to 20 kV to increase the intensity of the X-ray signal while the working distance was set as 8 mm where the X-ray detector is placed.

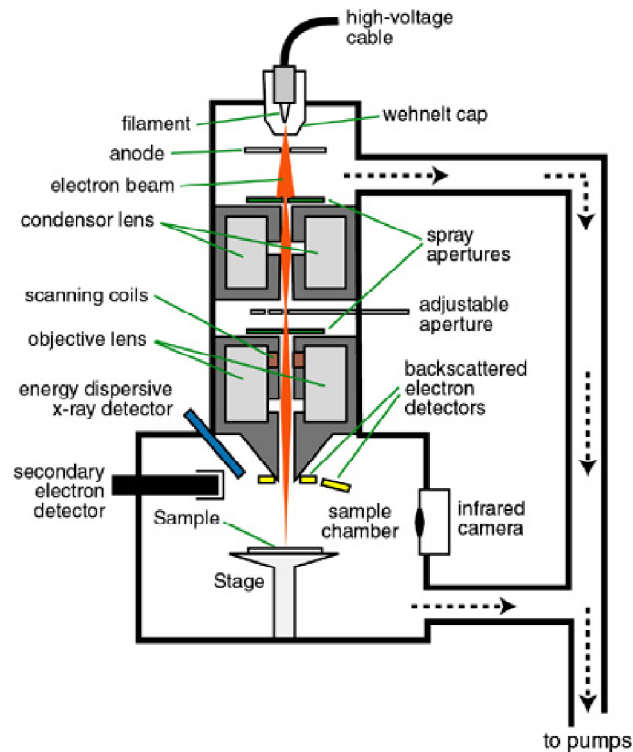


Figure 4-1 The schematic of the SEM system [264].

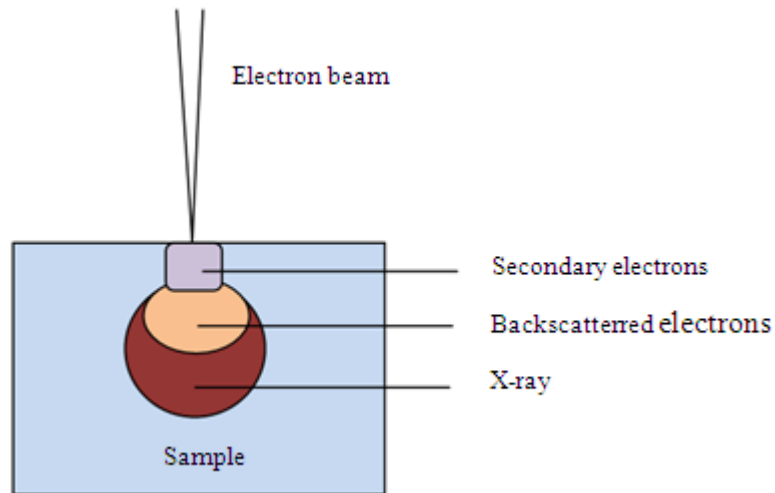


Figure 4-2 The schematic of electron interaction volume, depth for secondary electrons: 5-50 nm, backscattered electrons: 500-1000 nm, X-ray: 1-2 μm

4.1.2 XRD

Crystallisation, which can reduce the transparency of glass thin films, should be avoided in the whole thin film fabrication process. In this chapter, XRD, as a crystalline structural characterisation technique, was employed to examine whether there is crystallisation in the thin film.

In XRD measurements, X-ray radiation is produced by hitting a copper (Cu) target with an accelerated electron beam. As is known, there are many electron orbits around the nucleus of an atom as shown in Figure 4-3. It can be seen from the figure that the energy of the electron beam can ionize some of the electrons in 1s orbit in Cu atoms, and leave a void in this orbit which is filled subsequently by the electrons from the outer orbits, namely 2p, 3p, etc. The energy differences between the 1s orbit and the outer orbits are released in a form of X-ray radiation including K_{α} radiation (transition 2p---1s), and K_{β} radiation (3p---1s). Among these radiations, K_{α} radiation which is much more intense and happens more often than K_{β} is used in the diffraction experiments. To attain a pure K_{α} radiation which, Ni foil which can absorb K_{β} radiation and most of the white radiation is used as a filter [265].

When the X-ray signal that produced in the above process is incident on a sample surface with an adjustable angle, the atomic plane in crystals or plane like features in amorphous materials can yield scattered X-ray photons. If the X-ray photons

produced from adjacent plane is constructively interfere, bright fringes or Bragg reflections can be produced. Otherwise, destructive interference produces.

As shown in Figure 4-3 (b), when the X-ray radiation is incident on the sample with an angle of θ , the light 1 and 2 are scattered from two crystalline planes separately and it is assumed that the scattered X-ray light 1' and 2' are in phase.

Since $AB=BC=d\sin\theta$, and $BC=n\lambda$, then:

$$d\sin\theta = 2n\lambda \quad (4.1)$$

where d is the distance between this two reflection planes and n is the order of the reflection, λ is the wavelength of the incident light. As the incident angle changes, destructive interference which produces low intensity occurs as well and therefore diffraction can be yielded. The above equation is known as Bragg's Law which can be used when the reflected X-rays are in phase. Utilizing this equation, dimension of crystalline lattice, which is a characteristic of the crystals, can be calculated to identify the crystal when the wavelength of the X-ray is known.

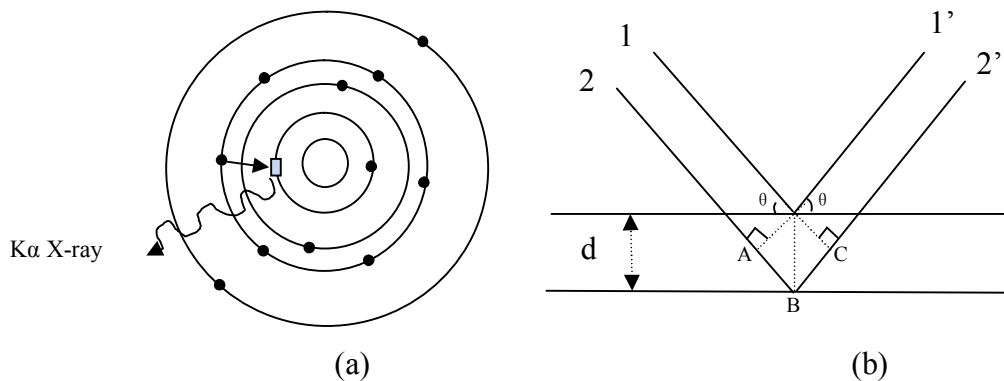


Figure 4-3 (a) The schematic of the X-ray production. From inner orbit to outer orbit: nuclear, 1s, 2s, sp, 3p. (b) Schematic for derivation of Bragg's law

In this work, samples were scanned using Cu $K_{\alpha 1}$ X-ray radiation ($\lambda=0.15406$ nm), and the incident angle is changed from 5° to 95° with a step size of $0.05^\circ/s$. All the XRD measurements were performed with the help of Miss Fangyuan Zhu.

4.2 Optimization of the parameters for tellurite glass thin film fabricated on silica substrate

As described in Chapter 2, PLD is a complex technique of thin film fabrication. To attain TWL glass thin films with excellent optical properties and smooth surfaces, the parameters including laser fluence, O₂ pressure, substrate temperature in addition to laser wavelength, repetition rate, and distance between substrate and target need to be optimized. The wavelength of laser, repetition rate and distance between the substrate and targets used, in this work, are 193 nm, 10 Hz and 55 mm, respectively. In this section, laser fluence, pressure and temperature are optimized through investigation of the transmittance properties of a series of thin films.

4.2.1 Laser fluence optimization

In this section, a series of thin films were deposited using different laser fluence while all the other parameters were kept constant. The deposition parameters used here are listed in Table 4-1. After depositions completed, the substrate temperatures were cooled down to RT at a rate of 50 °C/min.

As aforementioned, the transmittance of a thin film is a crucial property for optical materials and is used as the first criteria of thin film quality evaluation. All the transmittance of thin films obtained using the parameters listed in Table 4-1 are shown in Figure 4-4. It can be seen that there are interference fringes in all the curves of the transmittance of thin films indicating uniform thin films with excellent transparencies. Chrisey[173] pointed out that the lower laser energy used during the deposition process resulted in smaller particle dimensions. In addition that a thin film was obtained using 1.3 J/cm² has a relatively higher transparenance as shown in Figure 4-4. Consequently, this fluence was chosen as a better laser energy.

The transparencies of thin films produced herein are satisfied, therefore, other properties need to be investigated to further understanding of these thin films. Topographies of thin films as the second criteria were examined using an optical microscope first, and then SEM. It is shown that all films in this series have large cracks when investigated under the optical microscope. Images of one of the thin films measured using SEM are shown in Figure 4-5.

SEM images confirm the existence of the large cracks as have been found using the optical microscope. However, the areas between these large cracks when investigated at higher magnification as shown in Figure 4-5(b) reveal no additional small cracks at the 10s of nano meter scale. Cracks in the films may come from the thermal stress between the materials during the cooling down process which is possible to improve or remove through changing cooling rate or the CTE mismatch between the glass materials (12 ppm) and the substrates (0.5 ppm).

Table 4-1 Deposition parameters for thin film on silica substrate using different laser fluence

Laser fluence (J/cm ²)	O ₂ pressure (mTorr)	Temperature (°C)	Distance (mm)	Frequency (Hz)	Duration (h)
2.6	165	300	55	10	3
2.3	165	300	55	10	3
2.1	165	300	55	10	3
1.8	165	300	55	10	3
1.3	165	300	55	10	3

Note: laser fluence was calculated using the real laser energy (measured using power meter) incident on target /area of laser spot on the target.

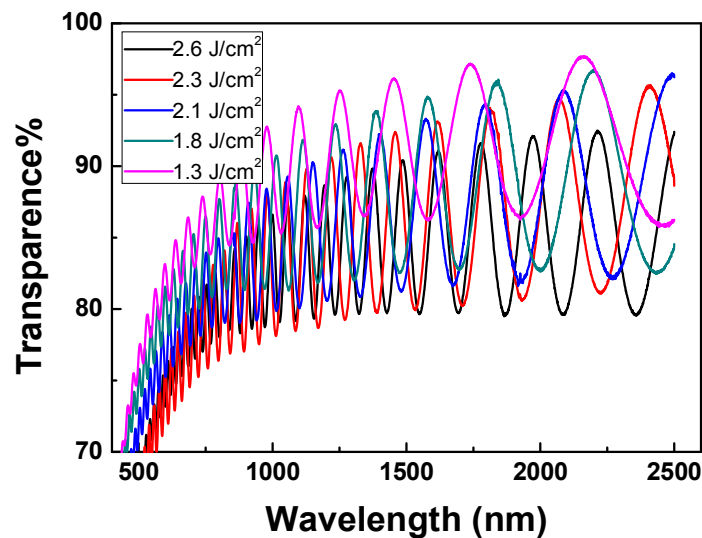


Figure 4-4 The transparencies of the thin films on silica substrate prepared using different laser energy

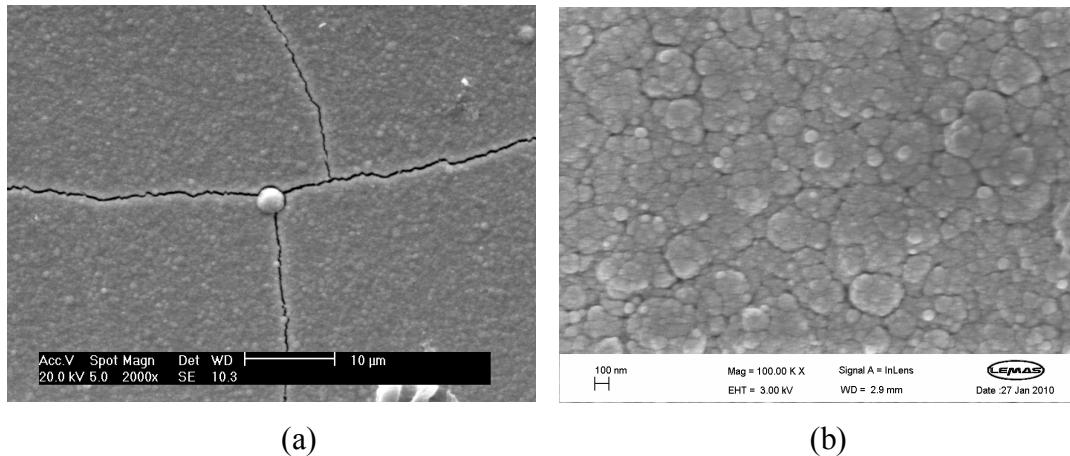


Figure 4-5 Images of thin films on silica substrate deposited at 300 °C (a) the images at low magnification (b) image of the area between the cracks at high magnification

4.2.2 Optimization of the O₂ pressure

As discussed in Section 4.2.1, if the large cracks are caused by the fast cooling down rate and the differential stress near large particles, then at least one of the factors influencing the crack will be managed better by carrying out the deposition of films at RT. Based on this assumption, a series of glass films were prepared at RT under O₂ pressure in a range of 120 mTorr to 160 mTorr, and all the other parameters, like repetition rate, distance between substrate and targets were unchanged as in the deposition of the first series of thin films. In addition, laser fluence was set as 1.3 J/cm² based on the results in section 4.2.1. The deposition parameters used here are listed in Table 4-2.

Large cracks were removed as we expected, when these thin films were investigated using the optical microscope. For further confirmation, one of the thin films was investigated using SEM, and the image is shown in Figure 4-6. Unfortunately, even though the large cracks are removed, there are many micrometer level cracks on the surface of the film, which can be seen clearly from the image at high resolution. It is worth noticing that these micrometer level cracks are quite different from the large cracks shown in Figure 4-5. Since cracks can be caused by both external load and residual stress [266], it is believed that the large cracks were caused by the thermal stress which can be removed by changing the cooling down rate while the micrometer cracks were produced due to the CTE mismatch between tellurite glass and silica substrate. Therefore, it may be possible to remove or reduce these micrometer cracks by using proper substrate temperature.

The transmittance of these films are shown in Figure 4-7, and it is obvious that thin film deposited under 135 mTorr has the highest transparenance than other films. As a result, O₂ pressure was decided to be 135 mTorr in future deposition.

Table 4-2. Deposition parameters of thin films on silica substrate prepared at room temperature under different O₂ pressures.

O ₂ pressure (mTorr)	Energy (mJ/cm ²)	Temperature (°C)	Distance (mm)	Repetition rate(Hz)	Duration (h)
165	1.3	RT	55	10	3
150	1.3	RT	55	10	3
135	1.3	RT	55	10	3
120	1.3	RT	55	10	3

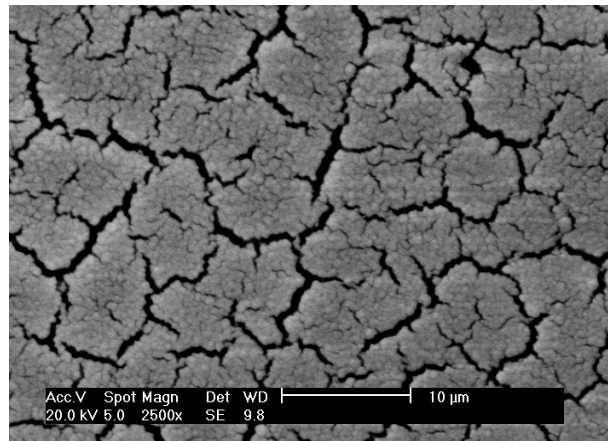


Figure 4-6 SEM images of the samples deposited using various O₂ pressure in the range of 120-160 mTorr

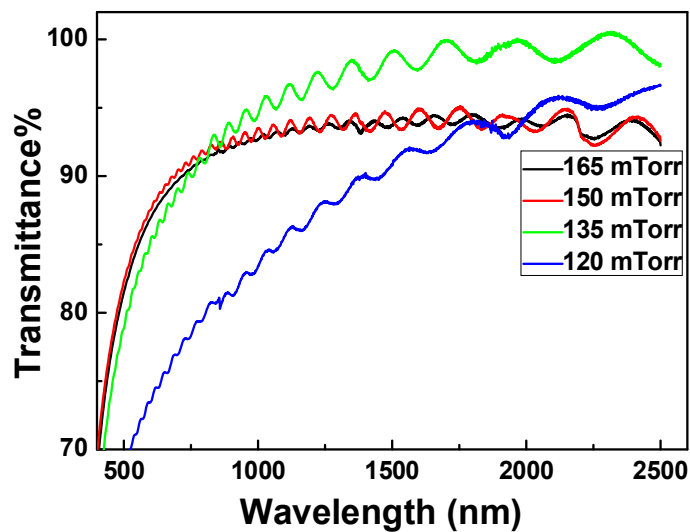


Figure 4-7 Transparenances of thin films deposited on silica substrate using various O₂ pressures in the range of 120-160 mTorr

4.2.3 Temperature optimization

Based on the results of Section 4.2.2, a series of samples were prepared using different temperatures to try to remove the micrometer scale cracks on the surface of the film. The parameters used for this series of thin films are listed in Table 4-3.

Films obtained at different temperatures were, first of all, examined using the optical microscope, and no cracks for samples deposited at 100 °C and 150 °C were observed. These two samples were measured using SEM to further study the topographies and images obtained are shown in Figure 4-8. It is shown that the thin film deposited at 100 °C has a relatively better surface compared to that of films deposited at 50 °C and 150 °C. Additionally, with the increase of the temperature from RT to 300 °C, the dimension of the cracks reduced and reached minimum at around 100 °C, and then increased again. Based on this result, one more thin film was prepared at 120 °C, and there is no further improvement of the films topography.

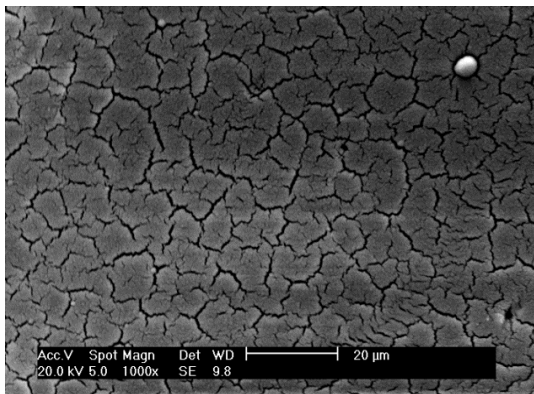
To summarize the results, the cracks on the films obtained at RT and any other temperatures from 50 °C to 150 °C are quite different from the cracks on the surface of the sample deposited at 300 °C as shown in Figure 4-5. It is assumed that the cracks produced at the temperature lower than 300 °C are due to the huge discrepancies between the CTE of the substrate and the glass film, while the cracks on the film obtained at 300 °C is attributed to the fast cooling down rate (50 °C/min). As can be seen from Figure 4-5 (b), areas between the cracks on the surface of the film deposited at 300 °C is better than the surface of films deposited at 100 °C as shown using the images of high resolution. Therefore, if the thin film is deposited at 300 °C with a slow cooling down rate, thin films may be crackfree or with little small cracks. Based on this assumption, a thin film was grown at 300 °C with a slow cooling rate of 0.5 °C/min after the deposition was completed. The SEM images of this film are shown in Figure 4-9. It is exciting to find that there are no large cracks on the film as expected.

When comparing SEM images of film deposited at 100 °C in Figure 4-8 (b) and SEM images of films prepared at 300 °C with a slow cooling rate in Figure 4-9, it is evident that uniformity of particles on the surface of film deposited at 100 °C is

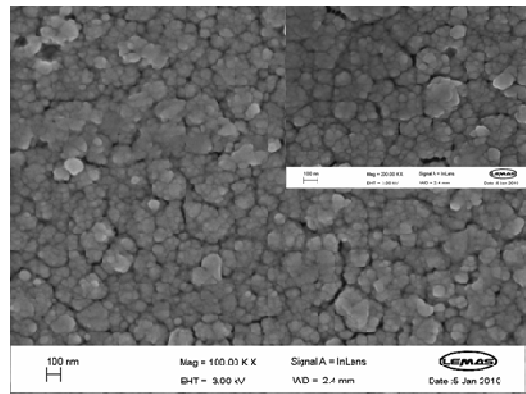
better than that of film prepared at 300 °C in Figure 4-9 (b). However, the microstructures in Figure 4-8 (b) shows a large number of uniformly distributed nanometer-scale cracks, which are evident from the high magnification image analysis. The nano-scale cracks on the film prepared at 100 °C have little influence on the application of fabricating micrometer scale devices.

Table 4-3 Deposition parameters for films using different temperatures

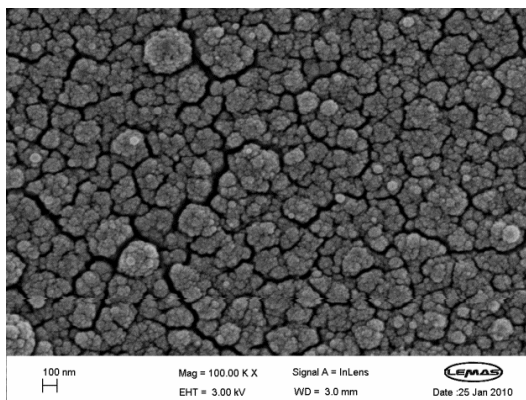
Temperature (°C)	O ₂ pressure (mTorr)	Energy (mJ)	Distance (mm)	Repetition rate(Hz)	Duration (h)
150	135	1.36	55	10	3
120	135	1.36	55	10	3
100	135	1.36	55	10	3
50	135	1.3	55	10	3



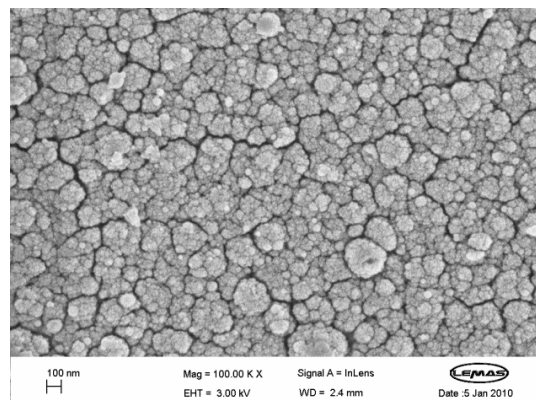
(a)



(b)



(c)



(d)

Figure 4-8 SEM images of films deposited at different substrate temperatures, and other conditions are shown in Table 4-3. Inset image in right top picture is the same sample at higher magnification. (a) 50 °C, (b) 100 °C, (c) 120 °C. (d) 300 °C

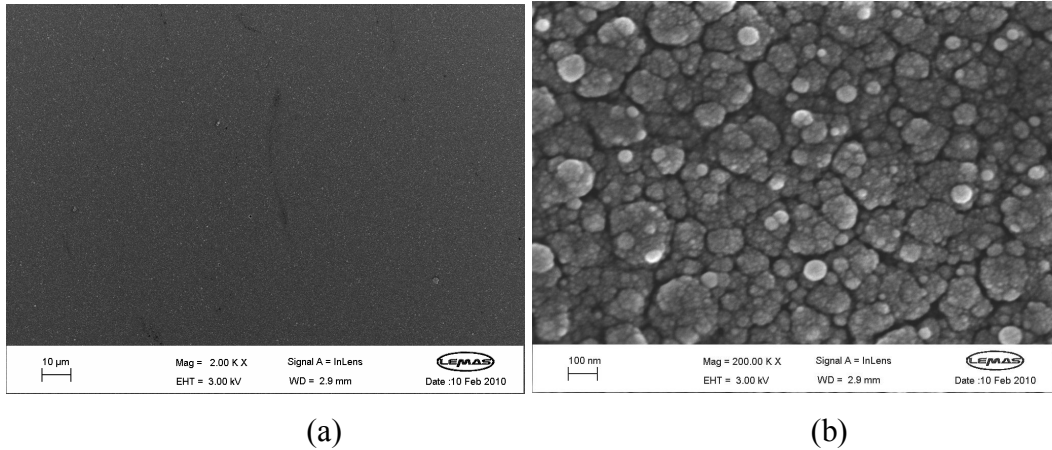


Figure 4-9. SEM images of film prepared at 300 °C and cooling down with rate of 0.5 °C/min when deposition finished, other deposition conditions are shown in Table 4-3, (a) low magnification, (b) high magnification

The transparencies of the samples deposited at different temperature are shown in Figure 4-10. It is clear that these films are uniform, and have high transparencies.

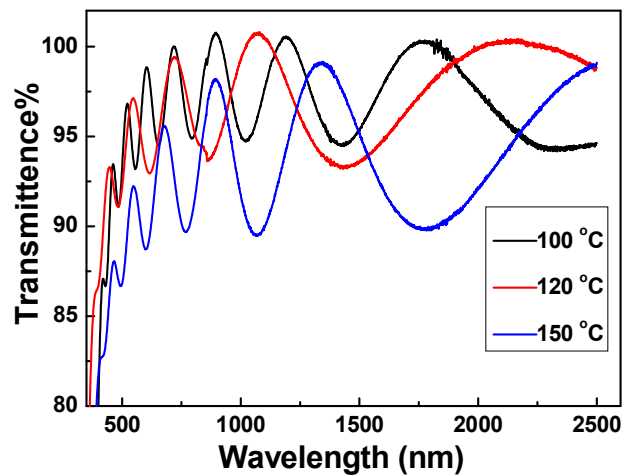


Figure 4-10 Transmittences of films deposited on silica substrate at different temperatures with other deposition conditions shown in Table 4-3.

In summary, to obtain a high quality film with good optical properties and surface condition, targets were prepared using the same recipe as glass TWL1 and series of optimization experiments were carried out. It can be concluded that excellent films can be obtained using an Excimer laser with a wavelength of 193 nm (pulse duration 20 ns) and a repetition rate of 10 Hz. The substrate is placed vertically above the target at a distance of 55 mm. The laser beam is incident on the target with a fluence of 1.3 J/cm². Prior to deposition, the PLD chamber needs to be pumped down to less than 10⁻⁶ mTorr to avoid contamination, and then filled with high purity processing gases at a flow rate of 20 sccm, whilst continuing to pump in order to maintain a

residual pressure of 135 mTorr. The substrate temperature can be set at both 100 °C and 300 °C with a cooling rate of 50 °C/min or 0.5 °C/min, respectively.

Thin films obtained using these parameters at these two different deposition temperatures were fully characterized and compared utilizing UV/VIS/IR spectrometer, FTIR spectrometer, prism coupler, fluorescence spectrometer, SEM-EDX, and XRD in the following section.

4.3 Results and discussions of the thin films obtained at optimal conditions

4.3.1 Optical properties

The optical properties, namely transmittance, refractive indices, fluorescence spectra and lifetimes, of the two films deposited at 100 °C and 300 °C were investigated and compared in this section.

The transmittance of these two films are shown in Figure 4-11. It can be seen that the transmittance of the thin film deposited at 100 °C on the silica substrate is as high as 95%, over the range of 650 nm to 2500 nm. By comparison, the transmittance of the thin films deposited at 300 °C is seen to be fractionally lower than those for 100°C, which is the result of larger particle clusters constituting the film at higher substrate temperature (see Figure 4-9 (b)). The interference fringe patterns shown in the figure are an indication of thickness uniformity of the films in the measured area.

The refractive index and propagation loss of the thin films deposited at 100°C on silica substrates were measured at 633 nm using the prism coupler, and were found to be 1.80 and 0.2 dB/cm, respectively. While the thin films deposited at 300°C have a higher refractive index of 1.92 and an optical loss of 0.71 dB/cm. The distinction of the refractive indices between these two thin films indicates differences in density of the thin films [28]. While the difference in loss values observed for the two films can be justified by the different refractive index contrast between the thin film and the adjoining silica substrate, and the nanoscale defects on the surface shown in Figure 4-8 (b), that affect the Rayleigh scattering losses [267-269].

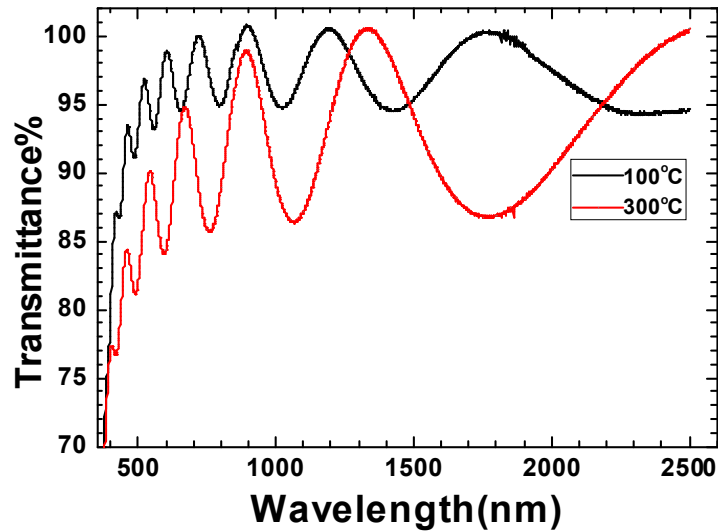


Figure 4-11 Optical transmittance spectra of the TWL glass thin films deposited using 193 nm laser on silica substrates at 100 °C and 300 °C in the range of 350 nm to 2500 nm.

In Figure 4-12, the room temperature fluorescence in the Er^{3+} -ion doped TWL glass thin films deposited on the silica substrate at 100 °C and 300 °C are compared. The spectra were measured using a 980 nm semiconductor diode laser. The pumping at 980 nm excites the $\text{Er}^{3+} : ^4\text{I}_{15/2}$ states to a metastable $^4\text{I}_{11/2}$ state, from which the non-radiative decay occurs and populates the lasing level at $^4\text{I}_{13/2}$. The line-widths of the $^4\text{I}_{13/2} \rightarrow ^4\text{I}_{15/2}$ transition in TWL thin films deposited on silica substrates at 100 °C and 300 °C have similar shape, but no significant difference in the peak position. The small blue shift (~ 3 nm) of the peak of the spectrum of high temperature deposited film compared to that of the film deposited at 100 °C is within experimental error.

The values of the fluorescence bandwidth ($\Delta\lambda = \int I d\lambda / I_{\text{max}}$) of these two fluorescence spectra are reported in Table 4-4, and the bandwidth of the films deposited at 100 °C and 300 °C are the same at 72 nm. The lifetimes of the $^4\text{I}_{13/2} \rightarrow ^4\text{I}_{15/2}$ transition in addition to the experimental data of the propagation loss, refractive index (at 633 nm) and thickness of the films are listed in Table 4-4 as well. And it can be observed that the fluorescence lifetime of the films deposited on silica is lower compared to that of the target. As discussed in Section 3.2.2.2 of Chapter 3, the longer measured lifetime of the bulk glass is caused by the radiative trapping due to the large thickness of the glass (around 4.5 mm). The theoretical lifetime of Er^{3+} doped glass TWL, as a target for thin film deposition here, was determined to be around 2.44 ms in Chapter 3.

The measured lifetime (2.28 ms and 2.0 ms for thin films deposited at 100 and 300 °C, respectively) of the TWL thin film is similar to the theoretical lifetime of the target glass 2.44 ms. The reduction of the lifetime compared to the theoretical lifetime of the target can be attributed to the free OH absorption in the thin film as shown in Figure 4-13 which resulting in an increase of the nonradiative relaxation from $^4I_{13/2}$ level. These hydroxyl groups may be from the moisture present in the process and gas used during the deposition. In addition, the presence of nanoscale grain boundaries also favours moisture adsorption from the atmosphere.

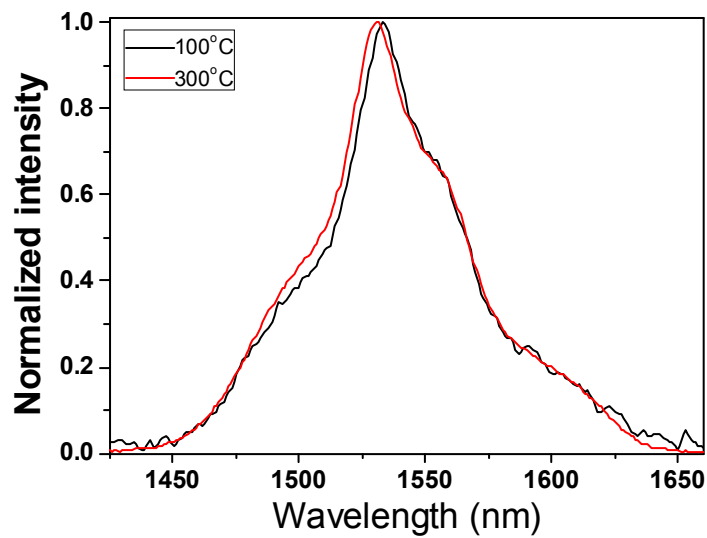


Figure 4-12 The room temperature PL spectra of the TWL thin films deposited on silica substrate using 193 nm laser at 100 °C (solid) and 300 °C (dashed), all the other deposition conditions are listed in Table 4-3

Table 4-4 Optical and spectroscopic properties of TWL bulk glass and thin films deposited on plain and polymer-coated silica substrates

Glass films deposited on	Gas atmosphere for deposition @ 135 mTorr	Refractive index at 633 nm	Loss at 633 nm (dB cm ⁻¹)	Fluorescence bandwidth (nm)	Lifetimes (ms) $^4I_{13/2} \rightarrow ^4I_{15/2}$	Thickness (nm)
Silica substrate at 100 °C	O ₂	1.82	0.20	72	2.28	1073
Silica substrate at 300 °C	O ₂	1.92	0.71	72	2.00	983
Bulk glass		2.11		77	5.30	

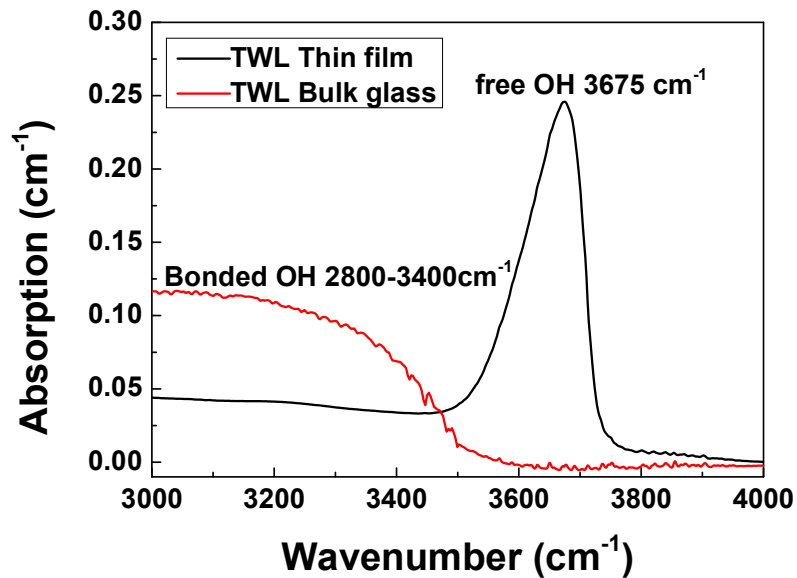


Figure 4-13 The OH absorption peak in the TWL thin film deposited using PLD and bulk glass

4.3.2 Topography

Topographies of thin films were investigated using SEM technique in this section.

Figure 4-14 (a) and (b) show the SEM images of the surface of the films deposited at 100 °C and 300 °C respectively. It is apparent that there is no much difference in the film structure, except the nano-scale grain boundaries (dark appearance in the image) per unit area. The particle size on average is much smaller and there is no large cracks shown for the 300 °C deposition while at 100 °C there is better agglomeration of particles of relatively larger size and fewer cracks at the nanoscale. The comparison of microstructure also confirms the reformation and growth of particulates in the post-plasma plume, which carries a majority of ablated materials through kinetic energy exchange with the gas molecules to the substrate.

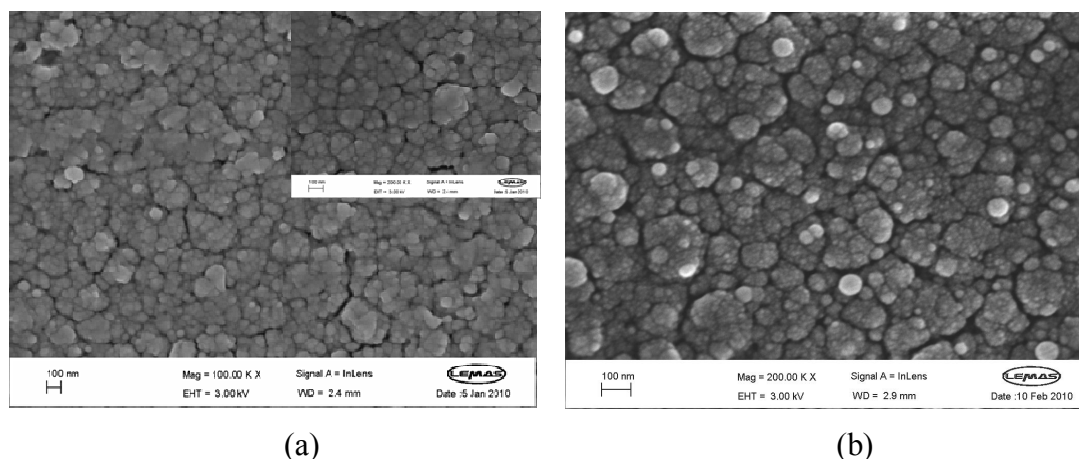


Figure 4-14 SEM images of thin films deposited on silica substrate using 193 nm laser at (a) 100 °C, (b) 300 °C

4.3.3 Structure and composition analysis

As mentioned in Chapter 2, section 2.5.7, PLD is an excellent thin film deposition technique, and has a number of advantages over other thin film growth techniques. One of the primary advantages is PLD could transfer the composition truthfully from targets to thin films. In this section, the target and thin films obtained were investigated and compared using Raman, EDX and XRD to study the structure and composition of these films and composition conservation capability of the PLD processes.

Since the inVia Raman microscope uses laser of 514 nm which then causes fluorescence of Er-ion present, an undoped glass thin film was grown using optimal conditions (at 100 °C) that was obtained in Section 4.2. Raman spectra of the undoped glass and thin film are plotted in Figure 4-15 and the assignments of the peaks are listed in Table 3-18. The intensities are normalized to remove the effect that involved by differences of the measurement condition. It can be seen that all the peaks and the peak positions in the Raman spectra of the undoped thin film are quite close to that in the Raman spectra of the undoped glass, which indicates that the undoped film has a similar structure to that of undoped glass with a little change of the ratio between different unit groups.

As explained in Section 3.2.4 in Table 3-18, the peak at around 279 cm^{-1} is attributed to the vibration of bond W-O-W in unit group WO_6 , while the peaks around 652 cm^{-1} and 758 cm^{-1} are believed to be due to the stretching vibrations of Te-O-Te between

two TeO_4 groups and stretching vibrations of TeO_3 , respectively. Therefore, the intensities of peaks 279 cm^{-1} , 652 cm^{-1} and 758 cm^{-1} can be used to represent the amount of unit groups WO_6 , TeO_4 and TeO_3 , respectively, and $I_{652} + I_{758} / I_{279}$ can be used to characterize the ratio between W and Te atoms as Himei did in his paper[262]. These intensities of the peaks and peak ratio are listed in Table 4-5. It can be seen that the ratio $I_{652} + I_{758} / I_{279}$ for the thin film can be considered to be the same as that for the bulk glass, which indicates that the ratio fraction of Te and W atoms has little changes in the thin film compared to that in the bulk glass.

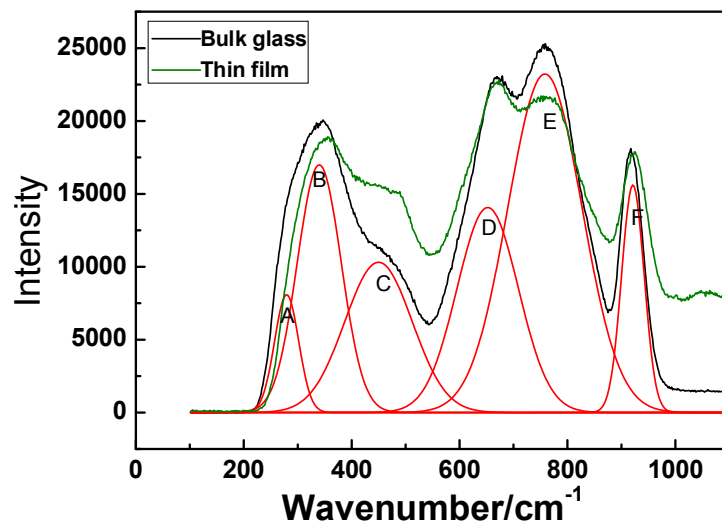


Figure 4-15 Comparison of the Raman spectra of undoped TWL glass and undoped TWL glass film deposited on silica substrate at $100\text{ }^\circ\text{C}$, red lines are deconvolution peaks based on Raman spectrum of TWL glass

Table 4-5 The intensity of peak 279 cm^{-1} , 652 cm^{-1} and 758 cm^{-1} of TWL thin film and bulk glass

Samples	I_{279}	I_{652}	I_{758}	$I_{652} + I_{758} / I_{279}$
Thin film	0.824	0.992	0.947	2.4
Bulk glass	0.789	0.905	0.992	2.4

The compositions of the target glass and the thin films obtained using EDX are listed in Table 4-6 in atomic%. The EDX data of the samples show 2.71 atomic% aluminum ($\sim 0.7\text{ mol}\% \text{ Al}_2\text{O}_3$) introduced in the target glass due to the use of an alumina crucible for glass melting. Varying concentrations of Al are present in the thin films reported in the table. Bai et al.[270] found that codoping with a small amount of Al_2O_3 (0-4 wt%) in the ZnO thin films can improve the transmittance of

the thin film and also reduce the size of the particles on the surface of the thin film. Therefore, it is assumed that the presence of Al_2O_3 in such small concentrations will not detrimentally affect the optical and spectroscopic properties of the glass. In addition, it can also be seen that, in both thin films, concentration of O atoms increased compared to that in the target, which may be due to the loss of Te and W atoms or the existence of pure O_2 in the chamber during the deposition process. The amount of Te atoms in the thin films fabricated at 100 and 300 °C became smaller compared to that in the bulk glass. In addition, the amount of W atoms in thin films fabricated at temperature of 300 °C increased compared to that in the bulk glass while in the one fabricated at temperature of 100 °C, the amount of W has a similar value compared to that in the bulk glass. These results are consistent with that obtained from Raman spectra.

To study the compositions changes further, data of atomic percentages were converted into the molar percentages of each compound in the samples, and the results are listed in

Table 4-7. It can be seen that the ratio of WO_3 increased significantly compared to that in the bulk glass, while the ratio of TeO_2 reduced on the contrary. This conclusion is in agreement with the above discussion.

Table 4-6 Compositions of target and thin films in atomic% measured using EDX

Element/Glass thin films deposited on	O	Te	W	La	Er	Al
Silica substrate at 100 °C in O_2	87.3	6.0	3.4	1.4	0.2	1.7
Silica substrate at 300 °C in O_2	80.2	7.5	8.1	2.7	0.1	1.4
Bulk glass	78.4	11.73	3.72	3.14	0.31	2.71

Table 4-7 Compositions of target and thin films in mol% converted using the data in above table, ignoring the existence of Al_2O_3 in the samples

Compositions/Glass thin films deposited on	TeO_2	WO_3	La_2O_3	Er_2O_3
Silica substrate at 100 °C in O_2	59%	33%	7%	1%
Silica substrate at 300 °C in O_2	44%	48%	8%	0.03%
Bulk glass	70%	22%	9.3%	0.09%

The XRD of the target glass and thin films prepared under different conditions are reported in Figure 4-16. It is evident that there is no sharp peaks resulting from crystalline phase in all the XRD curves which suggested that both target glass and thin films obtained are amorphous materials.

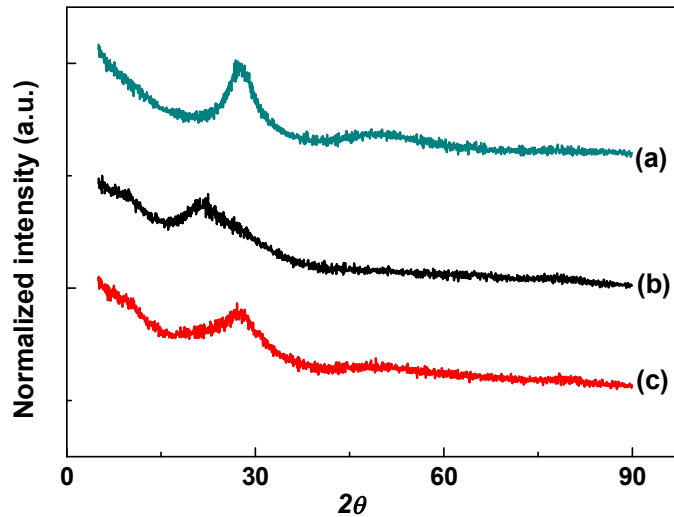


Figure 4-16 XRD of samples: (a) target glass, (b) glass film on silica deposited at 100 °C, (c) glass film on silica deposited at 300 °C

4.4 Conclusions

1. High quality tellurite glass thin films were obtained using 193 nm excimer laser (pulse duration: 20 ns) at 10 Hz. The laser fluence is around 1.3 J/cm² and O₂ pressure in the chamber during the deposition is around 135 mTorr and distance between targets and substrate is 55 mm. The substrate temperature could be 100 °C or 300 °C.
2. The thin films obtained at 100 °C have higher transparence, lower propagation loss than that of thin films deposited at 300 °C. In addition, the thin film prepared at 100 °C has a more uniform surface than the thin films grown at 300 °C. However, when deposited at 100 °C, the thin films still have nano meter cracks.
3. The measured lifetime of the thin films are similar to the calculated radiative lifetime of the bulk glass which indicates that the radiative trapping effects

that affect the measured lifetime of the bulk glass have been reduced for lifetime measurement of the thin films.

Chapter 5 Fabrication and characterisation of composite thin films

As mentioned in Section 2.4.2 of Chapter 2, composite materials have been studied extensively as they could improve the properties of materials, and even behave like novel materials that cannot be fabricated using traditional techniques. Glass and polymer are two of the critical materials for fabrication of optical devices nowadays, both of which have excellent optical properties, such as low loss, high transparency and good mechanical and thermal properties. The main purpose of engineering a composite is to combine the advantages of the source materials and improve or remove their deficiencies for device application. The resulting glass-polymer composite fabricated using PLD in this work is expected to have tremendous application in the optical communication system in the future, such as optical amplifiers, optical sensors, and optical switches. The efforts of fabricating multilayer composites using PLD has opened a door of fabricating composite thin films for not only glass and polymer, but also many other materials, such as semiconductors and ceramics.

Two different ways have been used to prepare glass-polymer composites, one of which is to deposit TWL glass films on polymer coated silica substrates, and the other is to deposit multilayer glass-polymer composite film with periodic phosphate modified tellurite (PT) glass and PDMS bilayers on silica substrates. To engineer the multilayer composite films, PT glass was chosen for the sake of comparable refractive index with polymer in addition to the broad fluorescence bandwidth and high rare earth solubility which are critical factors for short compact waveguide amplifier [271].

A variety of analysis techniques namely, FEG-TEM, SEM-EDX, UV/VIS/IR spectrometer, FTIR, fluorescence spectrometer, M-line spectrometer and XRD were employed to investigate the layers structure, topography, absorption, fluorescence, refractive index and loss of the films, respectively. These results obtained are discussed in detail.

5.1 Transmission electron microscopy (TEM)

The TEM is used to investigate the structure inside the specimen as well as the crystalline orientation. In this work, TEM is employed to examine the layer structure inside the composite thin films. The TEM is also a microscopy technique like SEM using electron beam, except in this case the sample is extremely thin (of the order of sub-micrometer), allowing electron beams to pass through and interact with the materials for producing a diffraction contrast[272, 273].

5.1.1 Sample preparation

TEM measurement requires an ultra thin specimen to allow transmission of electrons and produce high quality images. This limitation indicates that TEM sample preparation needs some special techniques.

There are many TEM sample preparation techniques, for example, electropolishing with a mixed nitric acid and methanol solution, mechanical milling, and focused ion beam etching (FIB). FIB is quite a new method for TEM sample preparation which is still in its infancy. This technique can be used to prepare semiconductor, metals, polymers, biologic materials and tissues samples [274]. In this work, FIB is used to prepare the TEM sample and is discussed in detail.

FIB uses a similar working principle to SEM, and it uses an ion beam instead of an electron beam, to focus on a specimen. Basically, there is a liquid metal ions source (LMIS) positioned with a sharp tungsten needle which can produce an ion beam using a high accelerated voltage. The LMIS and FIB setup are schematically shown in Figure 5-1.

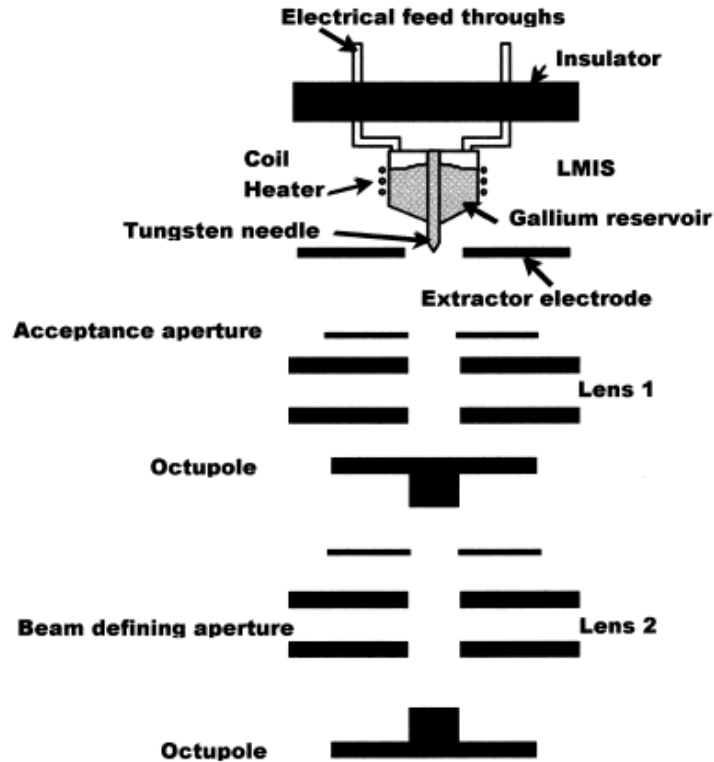


Figure 5-1 Schematic of LMIS and FIB setup[274]

Generally, gallium (Ga) is used as the ion source in FIB due to its low melting point and capability of being focused to a tiny beam spot (< 10 nm in diameter) [274]. In the process of TEM preparation, another feature of FIB that needs to be used is the ion beam assisted chemical vapour deposition. For the dielectric materials used in this work, platinum (Pt) was deposited on areas of interest to prevent damage and spurious sputtering by Pt gun beam.

As shown in Figure 5-2, the area to be analysed is chosen and then covered by a Pt thin layer. A thin slice (< 50 μm) is produced using the ion beam by removing the materials around it as shown in Figure 5-2 (a). The thin slice is cut around to make sure it could be lifted out easily, and it is then moved by a micromanipulation with a tungsten needle which is connected to it by the Pt welding technique (Figure 5-2 (b)). After that, the thin slice is lifted out and put into the sample grid as shown in Figure 5-2 (c). The thin slice on the sample grid is sliced into a much thinner layer using ion beam and then polished finely. The final thin layer shown in Figure 5-2 (d) has a thickness of ≤ 100 nm.

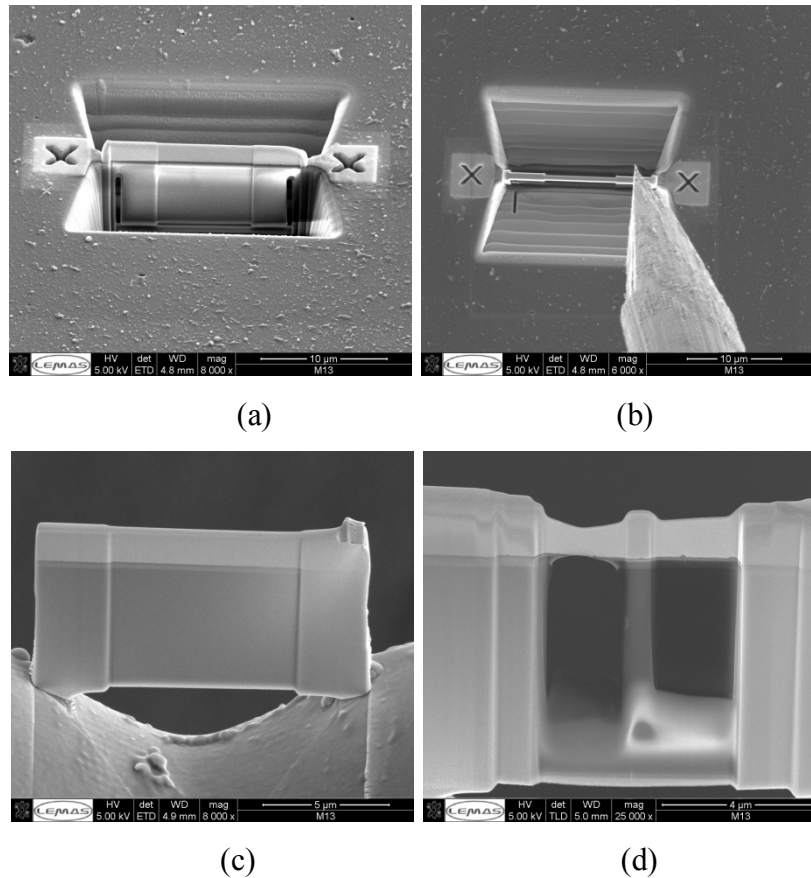


Figure 5-2 TEM Sample preparation process using FIB. (a) choose a thin slice by removing the material around it, (b) take the thin slice out using the micromanipulation, (c) the thin slice on the sample grid (d) the final thin sample

5.1.2 FEG-TEM measurement

In the FEG-TEM system, there is an electron beam accelerated by a field emission gun and then the beam is focused on the specimen by a condenser lenses system. The electron beam interacts with the materials and electron scattering happen, subsequently. TEM can provide a high resolution for imaging and also offers diffraction information of specimens. If the electrons are diffracted without any energy loss, it is known as elastic scattering and the diffraction pattern can be obtained. Whilst, most of the electrons will lose energy through absorption, scattering effects, known as inelastic scattering, and these electrons can be used to produce images of TEM [272, 273].

Electrons can be scattered at different angles, and the scatterings are named as back scattering and forward scattering based on their angular distribution. Forward scattering electrons are the main source of TEM images while backscattering electrons are the main signal for certain SEM images. Electrons in the solids can be

scattered once or more than once. In the case of single scattering, it is easy to predict the path which correlated with the structure of the material. Multiple scattering is too complicated and has no meaning with the analysis of images. In an ultra thin specimen, it is reasonable to assume that electrons only experienced single scattering. And this is another reason why ultra thin specimens need to be prepared when using TEM [272, 273].

A TEM system comprises of a condenser lens system, objective lens, intermediate lens, and detectors as shown in Figure 5-3. The electron beam is produced by the anode under a high voltage, and then it is focused on the sample with the help of condenser lenses 1 and 2. The electrons pass through the ultrathin specimen by diffraction process and the signal is recorded on the final screen after a series of lenses magnify it. The condenser lens system is used to focus the beam on the specimen, while the objective lens is used to form diffraction pattern on the back focal plane and images on the image plane. Intermediate lens magnify the signals for diffraction pattern or images [275]. As TEM specimen is ultra thin (<100 nm), the contrast is low even when it is focused. Therefore, an objective diaphragm is inserted in the back focal plane to obtain better contrast by selecting the transmitted signal. The crystal part with the Bragg orientation shows dark while amorphous or crystal not in Bragg orientation appears bright [276]. This mode is known as bright field mode and is used to take images.

To measure diffraction scattering of the specimen, dark field mode is required. There are two methods to form a dark field image. One is to place the objective diaphragm in a centre of diffraction spot instead of placing it in the centre of the back focal plane in the bright field mode. This is called off-axis dark field imaging. In the other method, the objective diaphragm is kept in the center of the back focal plane, while coils tilt the electron beam to obtain a diffraction spot in the centre of the column axis to allow the diffraction to pass the objective diaphragm. This is named as on-axis dark field imaging. These dark field images contain the information of size and shape of diffracting crystallites in a particle. The crystallites have strong diffraction compared to amorphous or crystallites not in Bragg orientation, therefore they appear

much brighter under dark field mode due to the fact that objective diaphragm blocks out the transmitted signals, and no diffracted scattering happens [276]

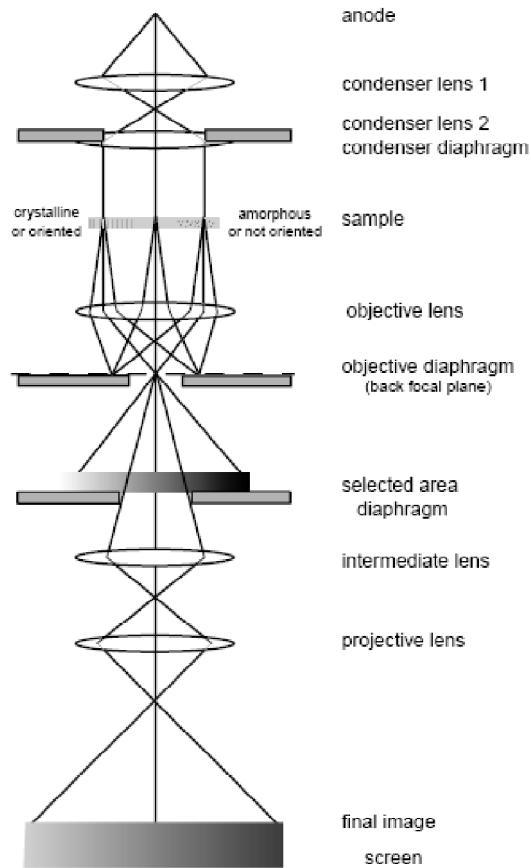


Figure 5-3 Schematic of TEM system [275]

In this work, a cross-sectional lamella of the composite film with a thickness of <100 nm, was prepared using an in-situ lift out procedure by FIB (FEI Nova 200 Nano Lab) for TEM (FEI Tecnai TF20). The cross-sectional images of the composite thin film were acquired at 200 kV using the bright field imaging mode in TEM, while the diffraction profile was investigated using dark field imaging mode.

5.2 Fabrication and characterisation of tellurite glass thin films on polymer coated silica substrates

This section discusses the fabrication and characterisation of tellurite glass thin films on a siloxane polymer coated silica substrates. The siloxane polymer coated silica substrates were fabricated utilizing spinning coating technique by Dr. Nikos Bamiedakis at the Electrical Division at the University of Cambridge, with whom the University of Leeds had the formal academic collaboration in the Basic Technology

project sponsored by the RCUK. The thickness of the polymer layer on the silica substrate is around 25 μm with the refractive index of about 1.51.

5.2.1 Fabrication of tellurite glass thin films on polymer coated silica substrates

The optimized deposition parameters of tellurite glass thin film on polymer coated silica substrates were determined based on the optimized conditions obtained for the tellurite glass thin films on silica substrates as concluded in Chapter 4. Tellurite glass thin films were deposited at 100 °C and 300 °C respectively, as shown in Section 4.2 of Chapter 4. However, siloxane polymer degradation due to thermal decomposition becomes significant at 300 °C. Therefore, 100 °C was chosen for the deposition of the tellurite glass thin film on polymer coated silica substrate.

Thin films were deposited on polymer coated silica substrates using the same optimized parameters as the glass thin films on silica substrates except that two different filled gases were used: high pure oxygen and mixture of 96% (volume fraction) oxygen and 4% (volume fraction) helium. The reason for introducing helium (He) with O_2 into the chamber at a comparable partial pressure is that the ionization energy of He is higher than that of O_2 (He: 24.59 eV and O_2 : 13.62 eV). The high energetic He species (He radicals and He ions) impinging on the thin film that results in a large number of nucleations sites and produce smaller particles[277]. The dual layer glass and polymer films acquired in two different background gases were compared and analysed to understand the difference of their properties.

5.2.2. Results and discussions of tellurite glass thin film on polymer coated silica substrate

To confirm the assumption of the influence of the He gas addition, the surface of thin films deposited in different gas atmosphere were investigated using SEM. As can be seen that the surface of thin film prepared in O_2 -He atmosphere, shown in Figure 5-4 (b) appears to have much denser and finer structures than that deposited in O_2 atmosphere, as shown in Figure 5-4 (a).

The microstructures observed in the SEM images in Figure 5-4 significantly differ from those shown in Figure 4-14 in terms of number of cracks per unit area. The cracks seen in Figure 5-4 appear to have a width below 50 nm but are interconnected

to a scale of few hundreds of nanometers. It can be concluded from the deposition experiments that the cracking tendency in TWL glass films on silica and PDMS-coated silica is strongly dependent on the thermal expansion coefficient of the substrate and less on the substrate temperatures and the types of gases used in the deposition process.

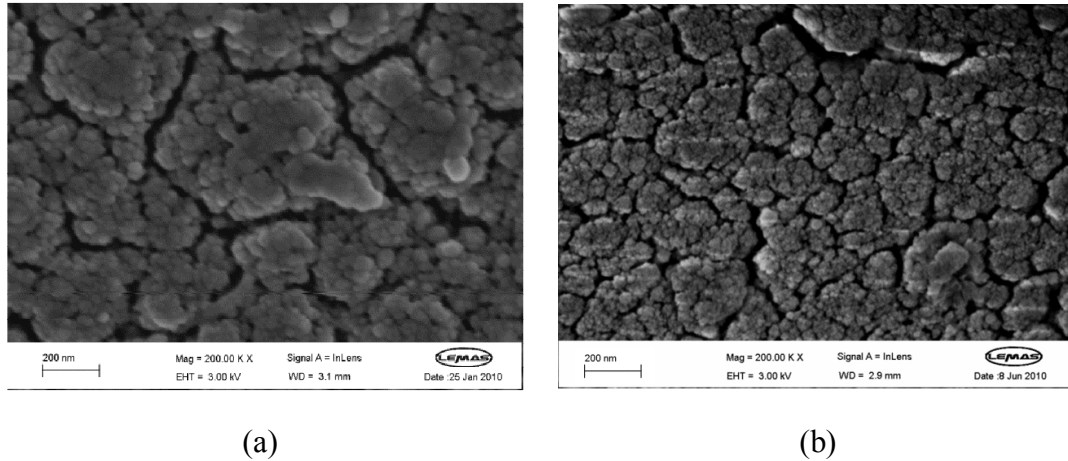


Figure 5-4 SEM images of TWL glass thin films on polymer substrates: a) at 100 °C in O₂ gas, b) at 100 °C in a gas mixture of 96 vol% O₂ and 4 vol% He.

The transmission spectra of TWL glass films on PDMS, formed at 100 °C in a residual gas of pure oxygen and a mixture of 96 vol% O₂ mixed with 4 vol% He are compared in Figure 5-5. The two films exhibit transmittance of better than 90% between 800 nm and 1600 nm. However, the film deposited with He/O₂ mixture shows marginally better transmission at shorter wavelengths below 800 nm.

The measured refractive index and propagation loss at 633 nm for these two films on PDMS-coated silica substrates are compared in Table 5-1. The TWL film deposited on PDMS-coated silica has higher refractive index at 1.89 than that of the film deposited on plain silica substrate alone at 1.82. Since the index of refraction depends significantly on the material density, the comparison of measured refractive indices of the TWL films with bulk glass indicates a lower density for the TWL glass films which can be attributed to the fractional porosity in the film due to the presence of nano-scale cracks, shown in Figure 4-14 and Figure 5-4.

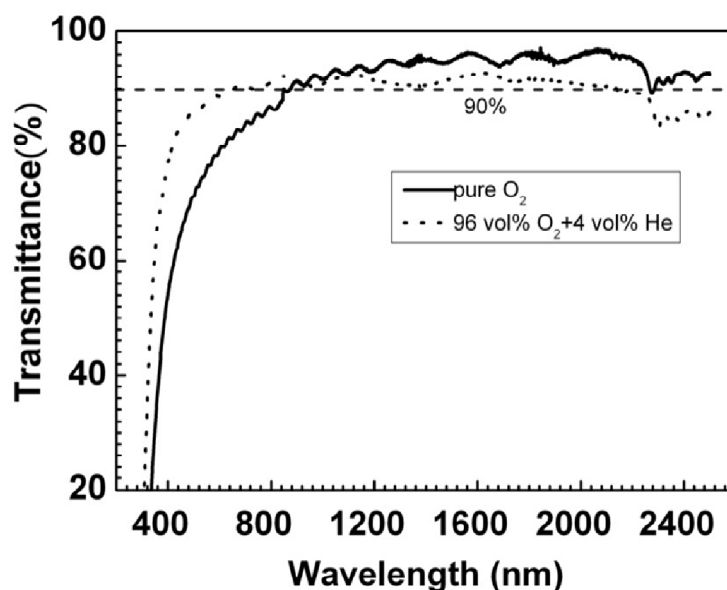


Figure 5-5 UV-visible-NIR transmittance spectra of the TWL glass thin films deposited in pure oxygen and oxygen/He mixtures on PDMS coated silica substrates

The room temperature photoluminescence spectra of the TWL glass thin films, deposited in oxygen and oxygen-helium mixture are compared in Figure 5-6. The PL spectra, corresponding to the ${}^4I_{13/2} \rightarrow {}^4I_{15/2}$ transition for Er^{3+} -ions present in the TWL glass, indicate that Er^{3+} ions in these two films have similar environment. The deposited film in the presence of O_2/He gas, exhibits comparable PL bandwidth with the film deposited in O_2 atmosphere, which are 71 nm and 69 nm, respectively and there is no apparent shift in the peak positions.

As shown in Table 5-1, the fluorescence lifetime of films on PDMS-coated silica has a further reduction in the lifetime compared to that of the thin film on silica shown in Table 4-4, and this may be due to the formation of polymer-rare earth complexes at the polymer-glass interfaces (C-H absorption) and the OH absorption resulting in a nonradiative relaxation from ${}^4I_{13/2}$ level.

The EDX data of these two thin films were measured using SEM-EDX instruments. As shown in Table 5-2, elemental changes in both films are close to each other indicating the gas used in the chamber during the deposition process has little influence on the composition transfer. The concentration of Er-ions has changed from 0.31 atomic% to 0.24 atomic % due to the ablation process, which has also been reported by Irranejad in the PT glass thin films deposition process[278].

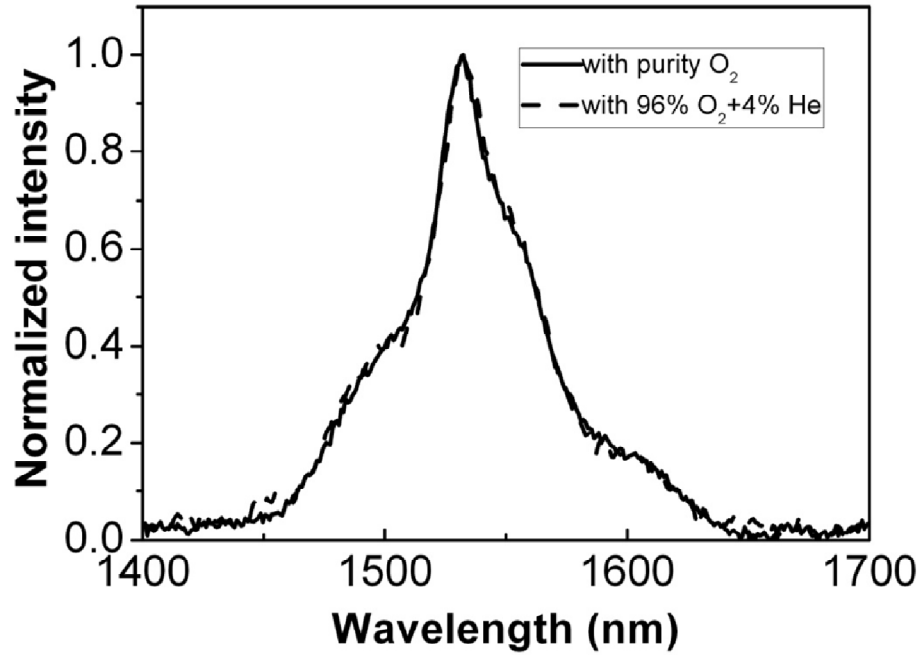


Figure 5-6 Room temperature PL spectra of TWL glass films, deposited at 100 °C on PDMS coated silica substrates in O₂ and O₂/He atmospheres.

Table 5-1 Refractive indices, thickness and fluorescence decay and lifetime of transition $^4I_{13/2} \rightarrow ^4I_{15/2}$ in Er³⁺ ions

Glass films deposited on	Gas atmosphere for deposition @ 135 mTorr	Refractive index at 633 nm (± 0.002)	Loss at 633 nm ($\text{dB cm}^{-1} \pm 0.2$)	Fluorescence bandwidth (nm)	Lifetimes (ms) $^4I_{13/2} \rightarrow ^4I_{15/2}$	Thickness (μm) (0.001)
PDMS on silica at 100 °C	O ₂	1.65	1.1	69	1.24	1.698
PDMS on silica at 100 °C	96 vol%O ₂ -4 vol% He	1.89	0.1	71	1.22	0.784
Bulk glass		2.11	-	77	5.30	

Table 5-2 Composition (in atomic %) of target and glass thin films on polymer coated silica substrates under different gas environments measured using EDX

Element/Glass thin films deposited on	O	Te	W	La	Er	Al
PDMS on silica substrate at 100 °C in O ₂	83.76	7.62	5.81	2.27	0.24	0.3
PDMS on silica substrate at 100 °C in 96vol%O ₂ /4vol%He	81.62	7.71	6.22	2.36	0.24	1.85
Bulk glass	78.4	11.73	3.72	3.14	0.31	2.71

5.3 Fabrication and characterisation of PT glass and polymer composite thin film on silica

In this section, both PT glass and polymer layers in composite thin films were deposited using PLD, which are different from the TWL glass thin film on polymer

substrates in the above section. The quality of the TWL glass and polymer composite thin film with multilayer structure prepared using the PLD was low transparence due to the large refractive index differences between the source materials. PT glass and siloxane polymer used here have similar refractive indices, which implies that the composites will exhibit high transparence as required. As a result, these two materials can be ablated alternatively to produce a layer-by-layer periodic structure using PLD. The propreties of the PT glass and siloxane polymer are listed in Table 5-3.

Table 5-3 The properties of PT glass and siloxane polymer

Materials	Refractive index	Propagation loss (dB/cm)@633 nm	CTE (ppm)
PT glass	1.666	0.35	11.6
Siloxane polymer[105]	1.40-1.55	<0.01	310

5.3.1 Fabrication of PT glass and polymer composite thin film on silica

In this section, nano-scale multi-layer glass-polymer composite thin films were fabricated using PT glass and a siloxane polymer as targets. Siloxane polymer was prepared by mixing the base agent and cure agent (10:1) in a siloxane polymer set Sylgard 184 from Dow Corning at room temperature. The PT glass with a composition (mol%) of 46.5TeO₂-20Na₂O-20P₂O₅-10ZnF₂-1.1Er₂O₃-1.5Yb₂O₃-0.9CeO₂ were prepared by Mr Mehrdad Irannejad utilizing the traditional melting and quenching technique. The details of the glass preparation have been discussed in his paper [271]. The erbium ions were chosen as the main doping element which in conjunction with the Ce³⁺ and Yb³⁺ are quite efficient in enhancing the population inversion at the ⁴I_{13/2} level of Er³⁺ state, from which the lasing transition to the ground state, ⁴I_{15/2} level takes place, resulting into the emission of photons in the range of 1520-1570 nm, which can be used for lasers and amplifiers [87, 279]. The silica substrate for deposition of glass-polymer composite was cleaned with hydrofluoric acid, followed by deionized water, and then baked inside the deposition chamber of the PLD system (PVD Products, USA) during the degassing phase at the start of the deposition process. The chamber was kept at 5 mTorr using mixed gas of 96 vol%O₂ and 4 vol% He, for minimizing the particle size in the film to achieve atomic layer growth. The method for thin film deposition was optimized using 193 nm excimer laser with pulse duration of 20 ns and a repetition rate of 20 Hz. The

optimized ablation fluence of $\sim 0.4 \text{ J/cm}^2$ used in this paper, is below the upper fluence limit of 1 J/cm^2 required to maintain the structure of the siloxane polymer [280]. The substrate was kept at $100 \text{ }^\circ\text{C}$ with a separation of 55 mm away from targets during the deposition. The glass and polymer films were formed separately using the above deposition conditions to establish the growth rate for each material, which is determined to be 0.3 nm/s and 0.1 nm/s , respectively. These rates were used to decide the deposition times for glass and polymer layers at required thicknesses in the composite thin film. The laser ablation was carried out using pre-programmed parameter controlled software of the PLD system that maintains precise changeover between the two targets. Samples were cooled down to RT at the rate of $50 \text{ }^\circ\text{C/min}$ after the deposition of the final layer. The topography, structural and optical properties of the multilayer composite thin films will be investigated in the following section.

Different samples with various glass and polymer ratio were tried for PLD, and the one with ablations periods of 100 s for glass and 10 s for polymer showed the better quality. As a result, it was this sample which was chosen for characterisation.

5.3.2 Results and discussions of composite thin film

Figure 5-7 shows images of the cross-section of a composite thin film with superlattice structure acquired using TEM at different magnification. This superlattice was prepared using alternating polymer and glass targets for ablation with durations of 10 and 100 seconds in each cycle, respectively. A total of 96 such cycles were used overall to grow a film of $\sim 1\mu\text{m}$ thickness. The very first layer on the silica glass substrate was formed using the glass target, whereas the final layer was polymer.

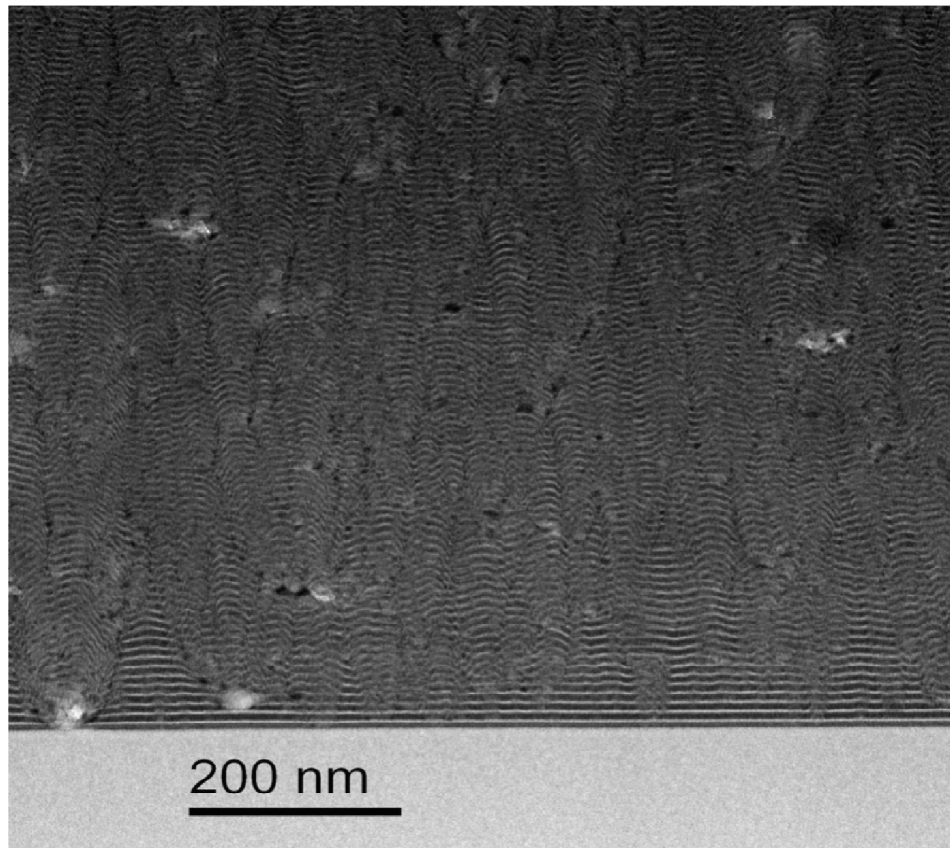
All images in Figure 5-7 show that the interfaces between the two dissimilar materials layers are well defined on a nanometer scale. The higher atomic mass of the glass layer means that it scatters electron more effectively and thus appears darker. The interlayer intensity profile simulation in Figure 5-8 demonstrates that the average thicknesses of the glass and polymer layers were in the vicinity of 7 nm and 4 nm respectively. However, at this point the details of interfacial chemistry remain unknown, which will be the subject of a further detailed analysis including an

investigation into the link between the interface and the surface energy corresponding to the formation of such interfaces during the ns-PLD process. The glass-polymer interfaces also appear to be largely defect free, except when a glass (dark) or polymer (light) particle impacts upon and is then buried within the layers, disrupting continuity of the layers and creating ripples as shown in Figure 5-7 (c). It has been observed that the presence of helium gas in the chamber helps to reduce the average size and the distribution of the particulates[127], however the deposition regime used in the formation of this sample, which is not yet fully optimized for the polymer, appears to generate some particles of size less than 50 nm.

Moreover, Figure 5-7 (a) shows that more polymer particulates exist in the superlattice than glass ones, and their projectile dynamics in a superlattice amorphous medium may be assessed using the Stoke-Einstein type approximation, in which the terminal velocity or diffusion in a viscous fluid medium is inversely proportional to the diameter of the particle. The particles which are typically several nanometers in size mostly result from the polymer material deposition phase and appear to perturb the already formed layers, depending on the particle's size and kinetic energy. These particles are responsible for the ripples in successive layers due to fluid like behavior of the deposited materials, which flows under the influence of hot plasma at the top of the film (Figure 5-7 (c)). As we are only able to analyse the film in a two-dimensional slice at present, in reality the ripples may be cone-shape and propagate outward as well as upwards. This certainly disrupts the superlattice growth and limits the high integrity layers to a limited level. The particles embedded in the intermediate layers as shown in Figure 5-7 (c) promote the growth of convex surfaces which lead to larger surface roughness than expected as the thickness increases. This is clearly evident from the investigation of topography of the last deposited polymer layer of the thin film carried out using high resolution SEM. It is obvious that the surface of the composite thin film is largely covered by relatively uniform particles of diameter less than 20 nm and few agglomerated particles with diameters of around 100 nm.

The repetitive pulsed laser deposition process generates plasma, and the thermal energy of the plasma plume, in the wake of electron-hole recombination, is partly

controlled by the presence of the O_2/He gas molecules which exchange energy with the ablated materials. The residual thermal energy of the gas mixture and the post-plasma condensate is thought to maintain a rapidly cooling liquid-like flat interface for each layer of the superlattice during the process of deposition. We can clearly see that the inter layer diffusion is only of the order of one or two nanometer, which might suggest that the glass and polymer are immiscible under the deposition conditions. However, there are large particles on the top layer of the thin films as shown in Figure 5-9. This may take place because when the ablation stops, then the thermal energy of the gas mixture and the post-plasma condensate drops dramatically, allowing the formation of larger particles without the help of large surface energy.



(a)

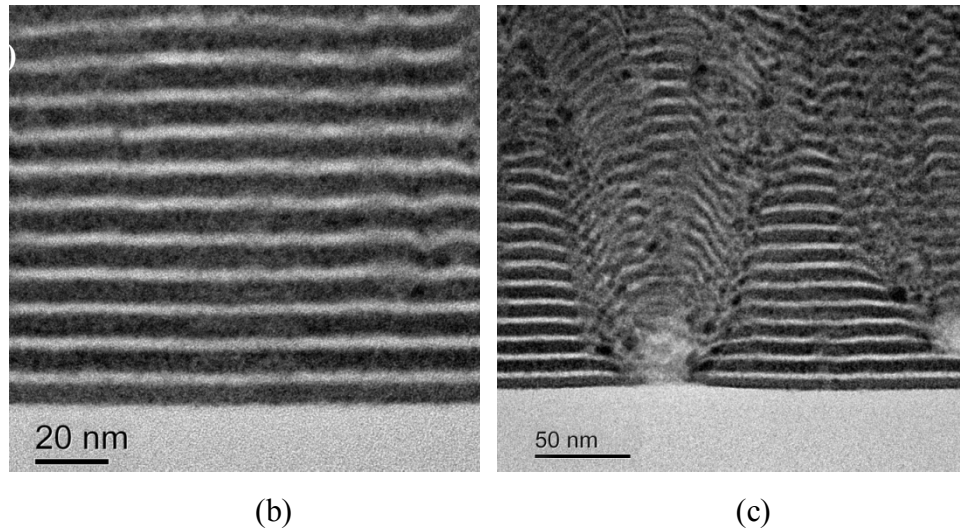


Figure 5-7 TEM images of a cross section of the superlattice thin film fabricated using at, a) lower magnification and b) higher magnification. (c) image showing particle diffusion between layers, deposition conditions: laser fluence 0.4 J/cm^2 , substrate temperature $100 \text{ }^\circ\text{C}$, background gas pressure 5 mTorr , laser repetition rate 20 Hz

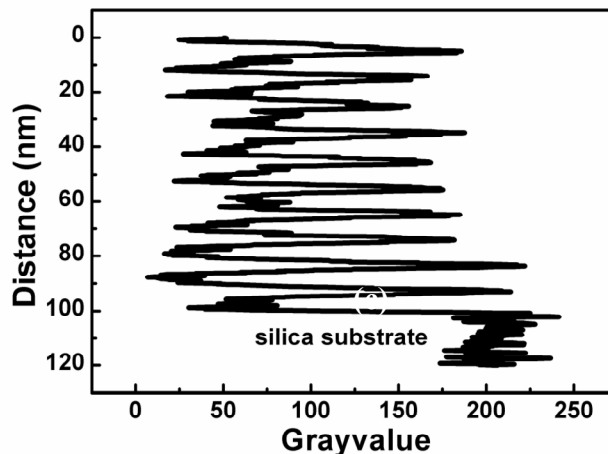


Figure 5-8 Interlayer intensity profile of composite thin film layers thick extracted using Image J software. It is worth noticing that when depositing TWL glass thin films on silica substrate or polymer coated silica substrate and cooling down at the rate of $50 \text{ }^\circ\text{C/min}$ after the deposition, there are large cracks on the surface of the thin films as mentioned in the Chapter 4 and Chapter 5. However, as shown in Figure 5-9, there is no crack on the surface of the superlattice thin films even though the cooling rate is also $50 \text{ }^\circ\text{C/min}$. This, first of all, may be due to that the sublayers in the superlattice thin film is ultra thin (in the order of nanometer level), and secondly, the fluid like materials with the help of hot plasma has no chance to form cracks before the growth of new layers. Thirdly, the multilayers might be able to inhibit crack propagation.

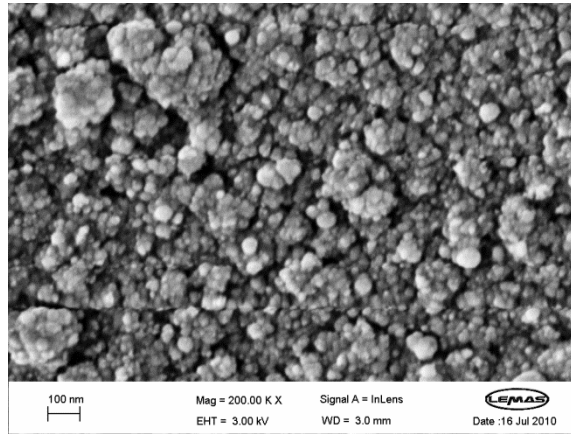


Figure 5-9 High resolution SEM image of the surface of the PT glass-polymer composite thin film

To further investigate the layers and interfaces, we performed X-Ray reflectometry (XRR) experiments on a PANalytical MPD system with Cu K_{α} radiation using a hybrid incident monochromator to obtain pure Cu $K_{\alpha 1}$ radiation with $\lambda=0.15406$ nm. All the XRR experiments were performed by Dr. Timothy Comyn. Due to the high surface roughness and non planarity of the terminating layers of the $1\mu\text{m}$ thick samples the signal to noise ratio was too low in the XRR data. We therefore prepared a thinner film using only 10 cycles with identical deposition parameters as the sample shown in Figure 5-7, except with a somewhat higher laser fluence of 0.54 J/cm^2 compared with 0.4 J/cm^2 which was used for the composite thin films shown in Figure 5-7. For composite thin films, data was collected in the range of 0.05 to 2 degrees, with step size 0.002 degrees, for a total collection time of 560 mins. The reflectivity curves in Figure 5-10 (a) were used to investigate the thickness of the repeat unit, roughness of the interface, and the density of the materials. The cut-off edge of the composite thin film, compared in the inset of Figure 5-10 (a), is between that of the polymer film and PT glass thin film which indicates that the density of the composite thin film is between densities of glass and siloxane polymer as expected. The visibility of the Kiessig fringes [281] of the reflectivity curve in Figure 5-10 (a) implies that the layers in the thin films obtained are uniform throughout a sample area of 1×2 cm^2 . Six out of 10 repeat units are clearly visible from the interference fringes in the figure. The X-ray absorption and scattering due to particulate growth described before reduced the visibility of the higher order fringes. The thickness of the repeat unit in the composite thin films can be calculated according to Bragg's law with the formula $n\lambda=2d\sin\theta$, yielding a value of ~ 25 nm for the composite thin film. This thickness is comparable to the repeat unit obtained from TEM results shown in

Figure 5-10 (b) and larger than that of the sample used in Figure 5-7. This apparent difference in the thickness of the repeat unit can be attributed to the different laser fluence used for the fabrication of the samples. The roughness of the interfaces estimated by the theoretical fitting of the XRR data is less than 1 nm.

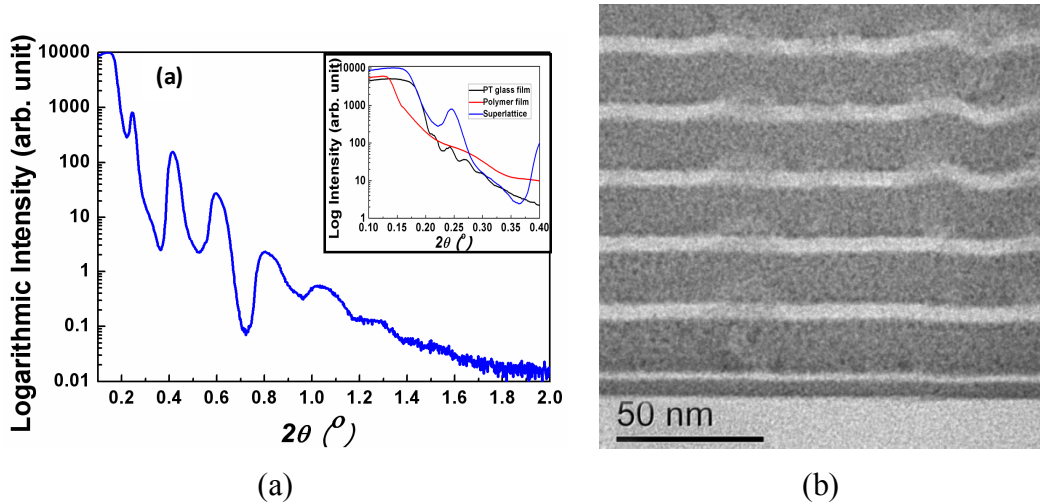


Figure 5-10(a) The X-ray reflectivity (XRR) curve of the superlattice thin film, (inset: the XRR curves for polymer film (black), PT glass film (red) and composite film with 10 deposition cycles (blue) depicting the shift in the absorption edge), (b) the TEM images of the cross-section of the same film

PT glass polymer layer by layer structures were confirmed by element mapping as well. Element mapping was measured using EDX equipped in the TEM system. Figure 5-11 (a) shows the high angle annular dark field (HAADF) image of the composite thin films (the one with 10 periodic cycles) and silicon (Si) mapping image in the thin films. Layers of Si elements are clear as shown in the figure which implies that there is little diffusion of Si elements between glass and polymer layers. Consequently, it can be concluded that the boundaries between glass and polymer layers are defined well.

To further examine the composite thin films, a diffraction pattern profile was measured using diffraction mode in TEM. The diffraction pattern obtained is shown in Figure 5-12. It is clear that no crystalline structures can be recognized in the image which indicates that the composite thin films are amorphous only.

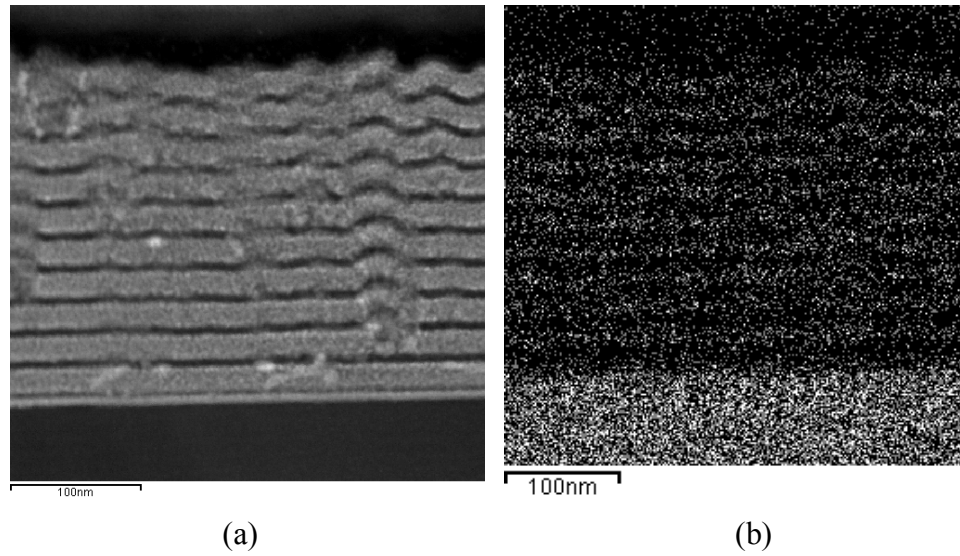


Figure 5-11 (a) HAADF images of thin films (b) Si X-ray mapping images in the composite thin film, white dots

represent Si rich atoms



Figure 5-12 Diffraction pattern of PT glass-polymer composite thin films measured using TEM

XRD was employed to further confirm the amorphous structure of the PT glass polymer composite, and the curve is shown in Figure 5-13. There is no sharp peak in the pattern which also implies that the composite thin films obtained using PLD is are amorphous.

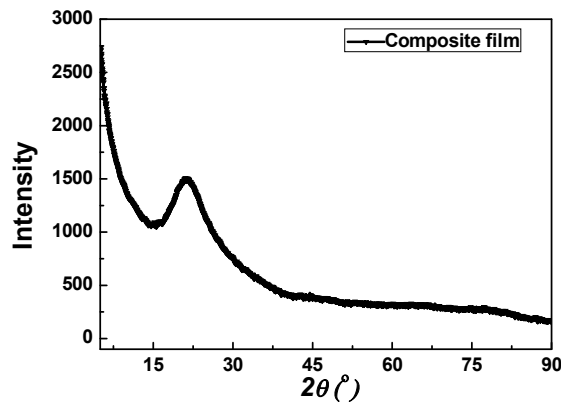


Figure 5-13 XRD curve of PT glass and polymer composite thin film

Though TEM diffraction pattern and XRD results prove that the composite thin films are amorphous, there are still some short order structures in both the glass and polymer layers of the composite films. In addition to confirm that the glass and polymer layers preserve their characteristic structural properties, we analysed the absorption spectra of the bulk glass, the bulk polymer, and the composite film using FTIR. The spectra have been measured using the reflection mode and are reported in Figure 5-14. The absorption peaks around 2900 cm^{-1} that can be attributed to the C-H stretching vibration in CH_3 and CH_2 groups in the polymer, are also present in the PLD-formed composite thin film. A broad peak around 1360 cm^{-1} in the curve of the composite film is the contribution of the absorption of P=O stretching mode in PT glass layer and is observed in bulk PT glass as well [282, 283]. The Si-C bond stretching resonance in the bulk polymer is also observed in the same wavenumber region (1360 cm^{-1}) [284]. Therefore the resonance absorption band at this wavenumber in the composite thin film can be attributed to the superposition of P=O and Si-C vibrational modes of the composite film. These two absorption bands clearly indicate that the polymer structure is maintained in the composite films. The peak around 1190 cm^{-1} in the composite thin film is attributed to the resonant absorption of P=O in the PT glass layer, and the absorption of the Si-O bond stretching in the polymer layers [285, 286]. The broad peak at $780\text{-}950\text{ cm}^{-1}$ in the composite may include the absorption of Te=O, P-O-P bond vibrations in the glass layer and the Si-O in the polymer layers [80, 287, 288]. The strong peak located at $470\text{-}600\text{ cm}^{-1}$ is the contribution of the O=P-O bond stretching of the glass [285]. Analysis of the FTIR results clearly demonstrates that the structural integrity of the polymer and glass in the composite thin film is well preserved.

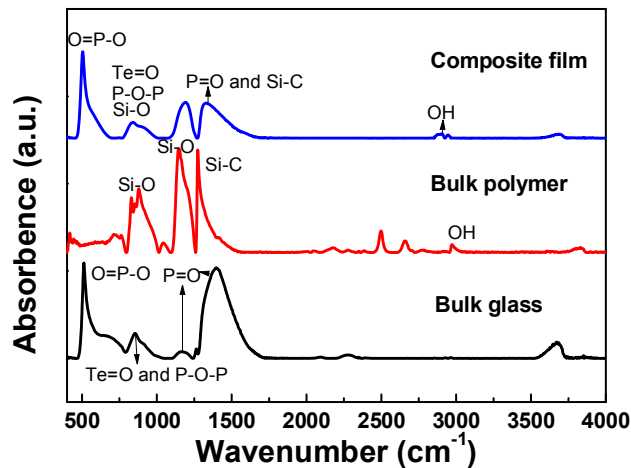


Figure 5-14 FTIR spectra of bulk polymer (black), target glass (red), glass-polymer composite thin film (blue) recorded using the reflection mode.

The optical properties of the composite thin films were characterized using UV/VIS/NIR, M-line and photoluminescence spectroscopic techniques, for the film transmittance, the effective refractive indices and propagation loss, and the fluorescence spectra and fluorescence decay lifetimes, respectively. As shown in Figure 5-15, the transmittance of the multilayer thin film is higher than 93% in the range of 750-2000 nm and larger than that of the glass only film on silica substrate. In XRR curves the interference patterns result from the Bragg reflections of different layers with few nanometer thicknesses, while the optical transmission, in the visible and infrared wavelengths shown in Figure 5-15, confirms that the individual layers are indistinguishable at these wavelengths and the whole structure behaves like a homogeneous film. The smooth interference patterns are further evidence of the uniformity of the composite thin film and hence its suitability for photonic device engineering. This is again supported by the waveguide propagation measurements carried out using an M-line spectrometer with 633 nm laser.

Figure 5-16 shows two transverse electric (TE) modes coupled into the films and their effective refractive indices. The refractive index of the composite thin film obtained from this measurement is 1.635 at 633 nm and lies between that of the glass (1.666) and polymer (1.4-1.55)[289]. The larger volume fraction of the glass layers in the superlattice causes the average refractive index to be closer to the glass rather than the polymer. The propagation loss of the films was measured to be around 1 dB/cm using the same technique at 633 nm. The top layer roughness greatly

contributes to this loss value and consists of an important loss component in the formed composite films.

Figure 5-17 compares the normalized fluorescence spectrum for the transition ${}^4I_{13/2} \rightarrow {}^4I_{15/2}$ in the Er^{3+} doped composite glass thin film with superlattice structure to that in a PT target glass and PT glass thin film. The comparison of the fluorescence data clearly shows that the superlattice structure has little influence on the shape and the peak position of the spectrum suggesting that the Er-ion environment has been preserved. This is apparent from the similar bandwidths of 64 nm in the superlattice and of 67 nm in the bulk glass. However, the measurements of the lifetimes of the ${}^4I_{13/2}$ level of Er^{3+} ions, for the composite film is only 1.5 ms compared to a 9.3 ms for the bulk glass. This indicates that there may be strong quenching of the ${}^4I_{13/2}$ states in the composite film as was observed with the PT glass films [271]. The presence of high energy phonon bands at $\sim 1350 \text{ cm}^{-1}$ in the glass films, shown by peaks in FTIR (Figure 5-14) are also present in the composite film leading to a fast non radiative relaxation by multiphonon decay of Er^{3+} ions.

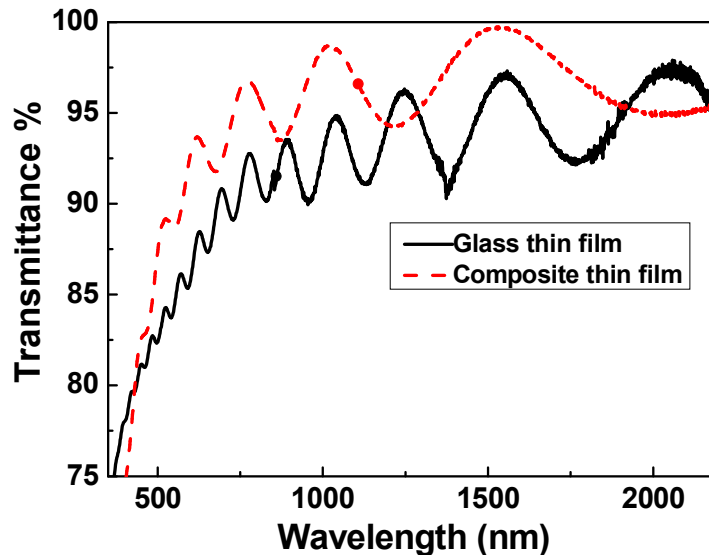


Figure 5-15 The optical transmittance of the glass only (black) and composite (red) thin film from 350 nm to 2200 nm

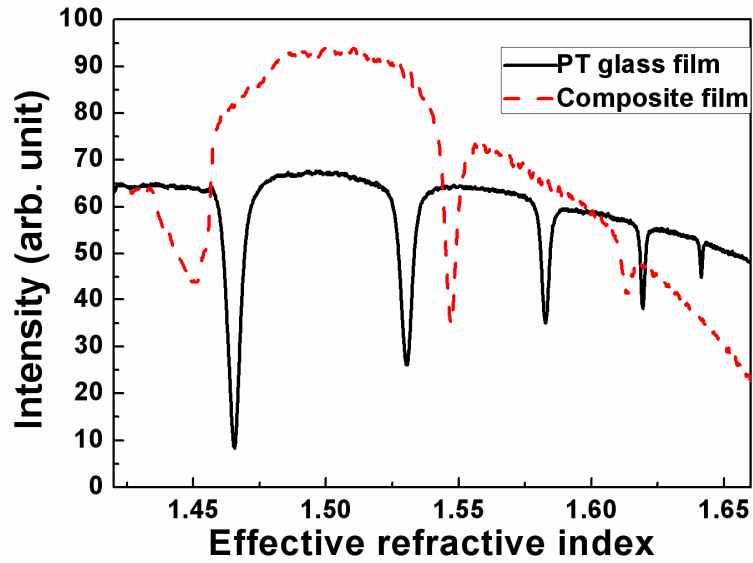


Figure 5-16 M-line spectra of the glass only and composite thin film on silicate substrate

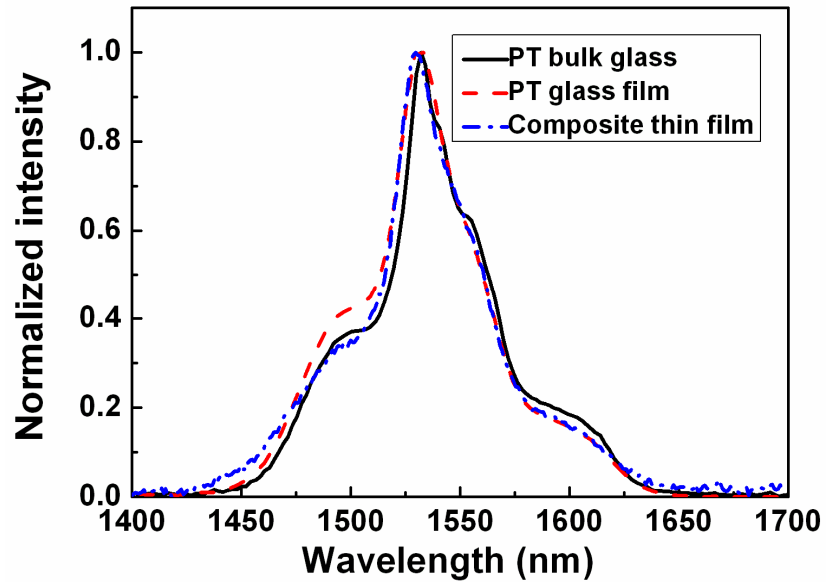


Figure 5-17 The fluorescence spectra of the $\text{Er}^{3+}: {}^4\text{I}_{13/2} \rightarrow {}^4\text{I}_{15/2}$ transition in the PT glass, glass film and composite films

5.4 Conclusions

1. TWL glass thin films deposited on PDMS-coated silica substrates were reported in this chapter. To study the influence of the background gas on the surface smoothness of thin films, two different background gases were used, and thin films prepared under these two gases were characterized in detail.

2. Thin film deposited in the O₂ environment has higher surface roughness and propagation loss but lower density, and consequently lower refractive indices compared to the thin film deposited in O₂ and He mixture.
3. Thin film fabricated under O₂ background has a higher transmittance compared to that of the film obtained under the O₂ and He mixture. While the shape and peak position of fluorescence spectra of both films are similar to that of the target glasses. However, the lifetimes of transition ${}^4I_{13/4} \rightarrow {}^4I_{15/4}$ in Er³⁺ ions in thin films are much lower than that of the target glass which might be due to the quenching effect in the films.
4. EDX results of both thin films show that thin films obtained in different gas background have similar composition compared to that of the target glass.
5. PT glass and polymer composite thin film with periodic layer-by-layer structure fabricated by PLD was discussed as well. The total thickness of the composite thin films is around 1 μm, while the thicknesses of the sublayers (both glass layer and polymer layer) are less than 10 nm which can be seen as a kind of superlattice structure.
6. The layer boundaries between glass and polymer layers are defined clearly with some particles implanted inside the thin films. In addition, some polymer particles diffuse and damage several layers which may cause by the un-optimized deposition parameters of polymer.
7. Heat energy in the plasma plays a critical role during the deposition of the composite, which reduce the size and amount of particles inside the composite thin films. While the top layer of the composite thin film (final layer) has rougher surface because of the absence of thermal energy coming from plasma.
8. Electron diffraction pattern and XRD data show that the composite thin films are total amorphous materials.

9. FTIR results indicate that both glass and polymer structures are conserved during the PLD process.

10. Excellent optical properties imply that composite thin films behave like a single material thin film without any influence coming from the layer structures. Compared to the target glass, composite thin films have a lower lifetime of transition ${}^4I_{13/4} \rightarrow {}^4I_{15/4}$ in Er^{3+} ions which may be due to the fast non-radiative relaxation of state ${}^4I_{13/4}$ in Er^{3+} ions caused by C-H and OH absorptions in the composites.

Chapter 6 Fabrication of ridge waveguides

Channel waveguide is a two dimensionally confined region where electromagnetic waves can be propagated efficiently. As discussed in Chapter 2, there are many kinds of techniques for waveguide structural engineering. In this work, two of the most extensively used techniques, namely RIE and laser micromaching, were used to fabricate waveguide structures on the thin films.

Tellurite glass channel waveguides are at an early stage of development and are quite popular topic at present due to their potential in engineering high and flat gain optical amplifiers [6]. Chierici et al.[209] in 2002, demonstrated a channel waveguide structure inside a bulk tellurite glass with the composition of $\text{TeO}_2\text{-ZnO-Na}_2\text{O-GeO}_2$, and this channel waveguide structure was written by a continuous wave (CW) UV laser beam. The energy of the laser beam could modify the refractive indices of the glass and consequently channel waveguides were formed inside the glass. Nandi and his colleagues[290] demonstrated 2D channel waveguides inside the Er^{3+} doped PT using fs laser direct writing, in which the channel waveguide could guide 1310 nm light with a propagation loss of lower than 2 dB/cm. Berneschi and coworkers tried two techniques, ion exchange and fs laser micromachining, to fabricate waveguides inside the tellurite glasses, and found that the former technique caused serious damage on the surface of the tellurite glass, while the latter could only obtain negative refractive index changes. As a result, they transferred to ion beam irradiation to fabricate channel waveguide structure inside the Er^{3+} doped $\text{TeO}_2\text{-ZnO-Na}_2\text{O}$ (TZN) bulk glass[291]. However, all the results of the research work that discussed above have not shown optical gain obtained from the channel waveguide of tellurite glasses.

Fernandez et al. [292] demonstrated active channel waveguides in an erbium doped PT glass by fs laser micromachining. And for the first time, they obtained gain from this channel waveguide structure. Lanata and his colleagues [293] showed channel waveguide structures on sputtered tellurite glass thin films on silicon fabricated by RIE, which has a rough surface and contamination that may be due to the nonvolatile products yielded in the etching process. Subsequently, the same group reported the

propagation loss and discussed the cause of the high loss of this channel waveguide, and they reported the propagation loss for fundamental TE mode to be 6.3 dB/cm at 1.5 μm [294]. In 2009, Madden and his colleagues [295] reported a very low loss channel waveguide on Er^{3+} doped tellurium oxide glass films prepared using RIE technique, and the propagation loss they reported was as low as 0.1 dB/cm. In the following year, they obtained the internal gain using a single mode channel waveguide on Er^{3+} doped tellurite glass thin films for the first time which is about 2.8 dB/cm [296]. It is the best result that has been achieved till now using Er^{3+} doped tellurite glass. Similar result has been recently reported by Irranejad and his colleagues[278]. They fabricated a waveguide amplifier using fs laser micromachining on PT glass thin films with length of 11 mm, and obtained an internal gain of 2.5 dB at 1565 nm pumped using 1480 nm laser at power of 150 mW. However, more research needs to be done to increase the internal gain for this kind of channel waveguide to meet the requirement of the optical communication system.

As we discussed in Chapter 2, planar waveguides have three layers: top cladding layer (usually air), waveguiding layer, and substrate layer. The refractive indices of these three layers are n_1 , n_2 , n_3 , respectively. An optical mode is a spatial distribution of optical energy in one or more dimensions as shown in Figure 6-1[297].

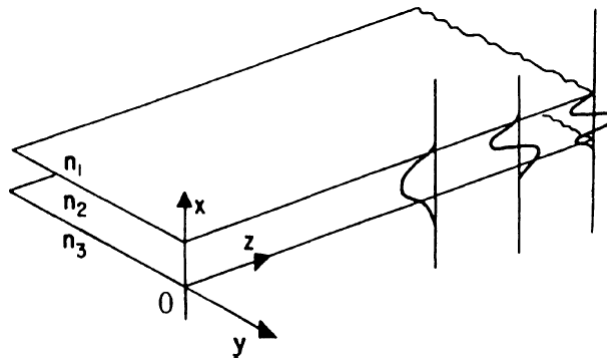


Figure 6-1 The schematic of three layer planar waveguides[297]

The number of modes is related to the thickness of the waveguiding layer, ω (the frequency of signal that passes through the waveguide), n_1 , n_2 , and n_3 . To form a well confined waveguiding layer, the change of refractive indices Δn should satisfied the following equation[297]:

$$\Delta n = n_2 - n_3 = (2m + 1)^2 \lambda_0^2 / (32n_2 t^2)$$

where $m=0, 1, 2, \dots$ is the number of modes, and λ_0 is the vacuum wavelength.

The mode profile which can be used to decide the number of modes is an important factor for channel waveguide. The optical mode profiles for TE_0 (single mode) and TE_1 (double modes) which can be measured using the experimental apparatus are shown in Figure 6-2[298].

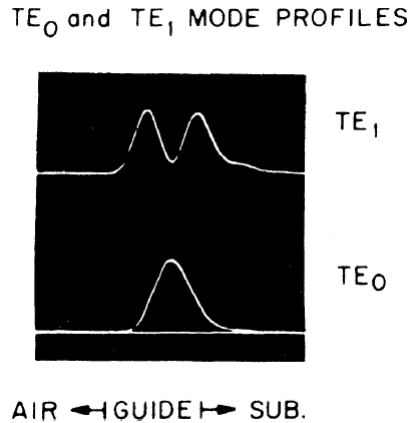


Figure 6-2 The mode profiles for TE₀ (single mode) and TE₁ (double modes) [298]

In this chapter, the fabrication of channel waveguide structures on the tellurite glass thin films using RIE, and the fabrication of channel waveguide structures on the glass-polymer composite thin films using laser micromachining have been demonstrated. The structures that are obtained on these two kinds of thin films have been shown. In addition, loss and mode profile of the waveguide structure on glass and polymer composite thin film have been performed.

6.1 Fabrication of ridge waveguides on tellurite thin films on silica

It is known that tellurite glass thin films can be dissolved in both acid and alkaline aqueous solution. As a result, dry etching tends to be the only choice for this kind of glass. In this section, RIE was utilized to fabricate channel waveguide structures on the tellurite glass thin films. Before etching, thin films should be prepared using photolithography process, and the steps of this process are similar to that shown in Figure 2-1. All the operations were finished in a cleanroom environment at RT.

Tellurite glass thin films on silica prepared using the optimal deposition parameters by PLD were chosen to etch. The deposition details have been discussed in Chapter

4. The thicknesses of the thin films are around 1-2 μm . Before spin coating, the substrates needed to be cleaned carefully with acetone and (isopropyl alcohol) (IPA), and then dried with high purity Nitrogen (N_2). After that, the thin film was stuck onto the spin coating chuck by the vacuum. Subsequently, the resist was dropped carefully onto the thin film until the film was fully covered by the resist. Waiting for a while, and let the gas inside the resist remove to obtain a uniform resist layer. Generally, the spinning speed was set as 5000 rpm/s which could produce a resist layer of around 1200 nm. Afterwards, the thin film with resist layer was put onto the hot plate at 115 $^\circ\text{C}$ to bake for about 2 mins. Later on, the thin film with resist was patterned using aligner (Kurl Suss company) with the help of a chrome copy mask (compugraphics), and then put into MF 319 developer (Rohm and Haas Materials Europe Company) for a period of time to develop.

To remove the resist in the exposure area completely, the spinning speed and duration, thickness of the resist, power of aligner, exposure time, and developing duration are required to match with each other. Values used for these parameters during the experiments are listed in Table 6-1.

After developing, the thin film was washed with dilute water and dried with high purity N_2 , and then was put into a chamber at the temperature of 120 $^\circ\text{C}$ for half an hour to avoid the resist lifting off during the etching process. After half an hour, the film with pattern was investigated under the optical microscope to make sure that the patterns were uniform without any damages.

Films with uniform pattern were put into the etcher (RIE-80) to obtain ridge waveguide structures on the thin film. To understand the etching process, the thicknesses of the depth of the obtained channel waveguides need to be measured before the etching process, right after the etching process, and after removed of the resist for each etching samples.

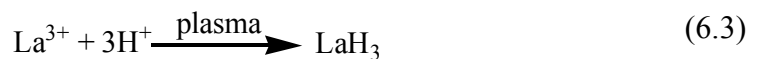
Four series of samples were fabricated using different gas pressure, etching duration and power to obtain optimal etching conditions. The etching parameters are shown in Table 6-2.

Table 6-1 List of the conditions used during the photolithography process

Spinning coating rotation speed(rpm)	Duration(s)	Thickness of the resist (nm)	Power of the aligner (mw/cm ²)	Exposure time(s)	Developing duration(s)
5000	30	1200	1.5	20	30
3000	30	1600	1.4	21	40
3000	30	1600	1.3	23	40
3000	30	2900	1.4	50	40
3000	30	2100	1.1	77	40

In the first series, gas pressures in the range of 36 mTorr and 60 mTorr were used to pattern on the film deposited at 100 °C. Here, the etching rate was employed as the first criterion. It could be concluded that, the etching rate was as high as 100 nm/min when the gas pressure was 48 mTorr. However, the total depth of the channel waveguides (513 nm) was not high enough for light propagation in the next characterisation step. Therefore, using the same etching parameters, a thin film with thickness of around 2 µm were etched for 30 min to try to obtain a channel waveguide more than 1 µm deep.

Unfortunately, at this time, the etching rate was reduced to 30 nm/min and the surface of the channel waveguides achieved was not flat. In the etching process, there are some byproducts produced, some of which can be pumped away by the gas flow while others which are nonvolatile will be adsorped on the surface of the waveguide. The reaction processes of byproducts production are shown below:



Erbium hydride [296] and lanthanum hydride compounds are known as low volatility compounds, as a result, it is easy to redeposit on the surface of the waveguide. Therefore, the uneven surface of the waveguide discussed above may be caused by the redeposition of the nonvolatile products after a long etching period. The redeposition problem was too dreadful to acquire high quality channel waveguides at this etching condition.

For the second series of etching experiments, thin films deposited at 300 °C were used, it was unexpected that even though experiments 1-1 and 2-1 used exactly the same parameters, the etching rates were significantly different. It may be due to thin films obtained at 300 °C being denser (discussed in Chapter 4) and consequently harder to etch. When tried to increase the etching duration, the nonvolatile byproducts erbium hydride and lanthanum hydride growth on the surface of the waveguide as happened in the first series of etching experiments.

After optimized the etching power using the third series, it is shown that when the etching power was 150 W, the redeposition problem was diminished. However, the etching rate was not satisfied. The etching rate of the resist is fast and will be etched completely when increasing the etching duration. This restricted the total depth of channel that could be achieved.

Table 6-2 RIE parameters used for thin films patterning

Process number	Gas	Gas flow rate (sccm)	Power (W)	Pressure (mTorr)	DC Bias (V)	Duration	Etching rate (nm/min)	Depth of the channel waveguide(nm)
1-1	CHF ₃	2	200	36	585-600	10	68	680
1-2	CHF ₃	2	200	48	440-460	5	102	513
1-3	CHF ₃	2	200	60	420-500	8	60	240
1-4	CHF ₃	2	200	48	440-468	30	30	891
2-1	CHF ₃	2	200	36	540-560	10	16.5	165
2-2	CHF ₃	2	200	36	560-645	30	6	244
2-3	CHF ₃	2	200	36	530-580	60	14	856
3-1	CHF ₃	2	200	60	420-500	8	30	240
3-2	CHF ₃	2	150	60	425-460	100	6	623

In all these etching results, the thin film etched in the process of experiments 1-1 has relatively good channels with thickness of 680 nm to 813 nm. The width of the channel is around 3 μm. The SEM image of the channel waveguides is shown in Figure 6-3. It can be seen that the surfaces of the channel waveguides are smooth with sharp vertical edges. The propagation experiment was tried using the channel on this thin film, however it tends to be difficult to couple light into it. That might be due to the small dimension of the channel and especially the low depth.

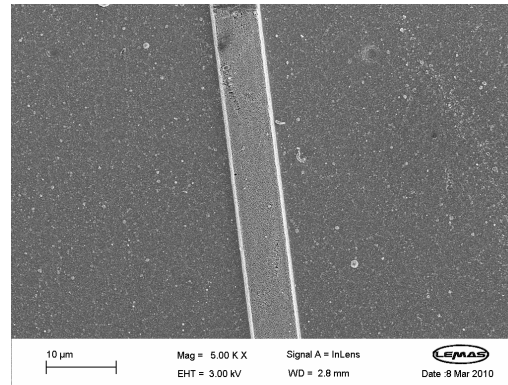


Figure 6-3 SEM images of channel waveguide on the tellurite glass thin film fabricated using RIE. Etching conditions are listed as 1-1 in Table 6-2.

After three series of etching experiments, it was difficult to acquire a high quality channel waveguide with a depth of more than 1 μm using RIE system due to yielding of weak volatile byproducts. Therefore, laser micromachining were used to fabricate ridge waveguides on composite thin films in the next section.

6.2 Fabrication of ridge waveguides on composite thin films

Since the results of the channel waveguides fabricated using RIE were not promising, fs laser micromachining was used to engineer the channel waveguide structure on the glass and polymer composite thin films. In this section, channel waveguides on composite thin films with superlattice structure (discussed in Chapter 5) were prepared using an amplified, fs- Ti:Sapphire laser (Coherent Libra) operating at a wavelength of 800 nm with a pulse duration of 100 fs and a maximum repetition rate of 1 kHz (variable). To acquire high quality channel waveguides, there are many parameters, namely pulse energy, repetition rate, writing speeds that need to be optimized. This section will demonstrate the optimization process of the waveguide preparation, and the channel waveguide obtained using optimal writing parameters. All the strip waveguides were etched by Dr. Toney T. Fernandez using fs laser micromachining. Dr. Toney T. Fernandez and the author of the thesis measured the SEM images of these channels together.

Fs-laser writing system includes fs laser source, half wave plate, polarizer, several control optics, high precision 5-axis translational stages and focusing objective. The combination of a half wave plate and polarizer is used to precisely adjust the power delivered at the sample stages. An aspheric lens objective is used to focus the laser

beam on the sample. Here an aspheric lens is used so as to reduce spherical aberrations and render a clean laser spot. Numerical aperture (NA) of the objective is a crucial parameter for the laser writing system which influences the quality of the structures. The samples are translated at various speeds to deliver the right fluence to find the optimum parameter for material processing. The picture of the fs laser writing system is shown in Figure 6-4.

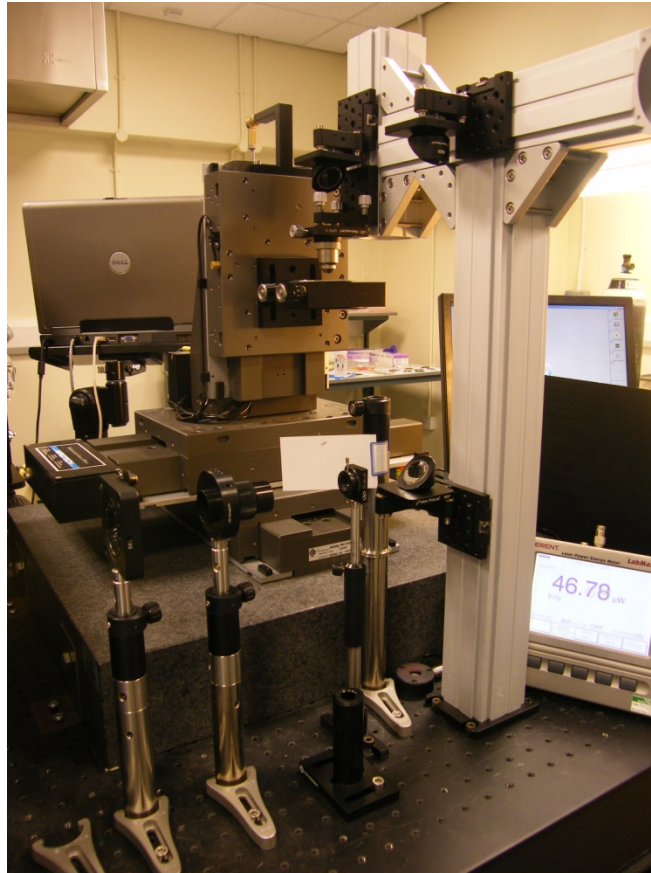


Figure 6-4 The picture of fs laser writing system.

Basically, NA of the objective is a parameter that needs to be optimized for nanostructure writing on different materials. In this work, the NA of the objective 0.4 was chosen as the best based on a few trials. And the results obtained proved that high quality channel waveguide structures could be obtained using this objective. The polarization of the laser beam was set along the writing direction to achieve better side wall channels for the waveguide [299]. The writing parameters used during the optimization process are listed in Table 6-3.

As shown in Table 6-3, laser powers used for waveguide fabrication in the first series (No. 1) experiment were between 1 μ J to 10 μ J. For each laser power,

different scan speeds, 0.1 mm/s, 0.5 mm/s, 1 m/s, 1.5 mm/s, 2 mm/s, and 4 mm/s, were used to deliver various fluences. The SEM images of this series of channel waveguides are shown in Figure 6-5. Figure 6-5 (a) shows the image of structures obtained using the laser energy at just around the damage threshold (4 μ J, 4mm/s). It is evident that there was a substantial increase in the porosity when the fluence increased as shown in Figure 6-6 and also it was found that the pore size distribution and density could be tailored simply by changing the fluence. This highly localized sub-micron sized pore production might be due to the micro bursts from the first few (near surface) polymer interlayers which are embedded between the glass. This is interesting en route for the material being used as a sensor or any receptive elements as it could increase the surface area, and is also well known that an increase in porosity could tailor the hydrophilicity of the thin films. Hence basically, porosity tuning or site selective porosity could be possible with laser structuring in such films.

Table 6-3 Writing parameters used during channel waveguide structure writing process on the composite thin films.

No. 1	Single scan	Power (μ J)	1	3	5	6	7	8	10
		Scan Speed(mm/s)	0.1	0.5	1	1.5	2	4	
No.2	Double scan	Power (μ J)	7	8					
		Scan Speed(mm/s)	3	3.5	4	4.5			
No. 3	Double scan	Power (μ J)	7	7.5	8				
		Scan Speed(mm/s)	3	4	5				

From comparison of images of (b), (c) and (d) in Figure 6-5, it can be seen that, the side wall of the channel waveguide structures written using powers of 7 μ J and 8 μ J are much better than that written at other powers. Based on these results, further optimization experiments No.2 and No.3 were carried out as shown in Table 6-3. SEM images of better channel waveguide structures obtained using 7 μ J and 8 μ J at both 3 mm/s and 4 mm/s in experiments No.2 are shown in Figure 6-7. It can be seen that these channel waveguides have smooth side walls.

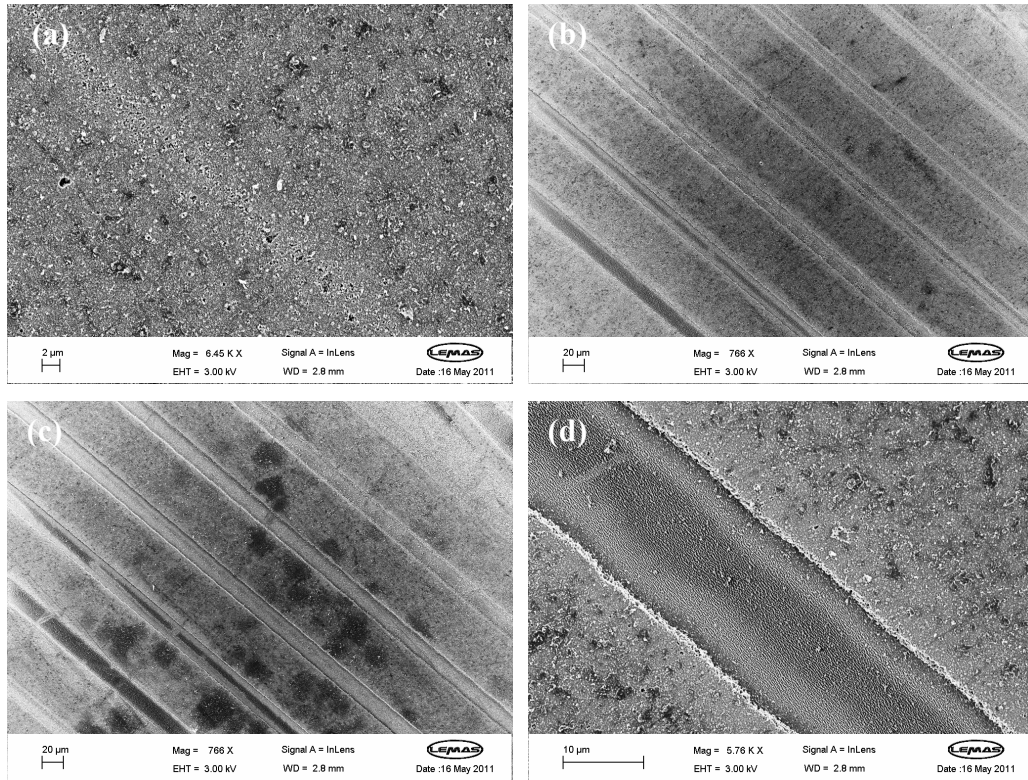


Figure 6-5 SEM images of channel waveguide structures on the composite thin film obtained in No.1 experiments (a) 4 μ J, 4 mm/s (b) 5 μ J from left to right: 0.1 mm/s, 0.5, 1, 1.5, 2, 4 mm/s, (c) 7 μ J, from the second one left to right: 0.1 mm/s, 0.5, 1, 1.5, 2, 4 mm/s, (d) 8 μ J 1mm/s

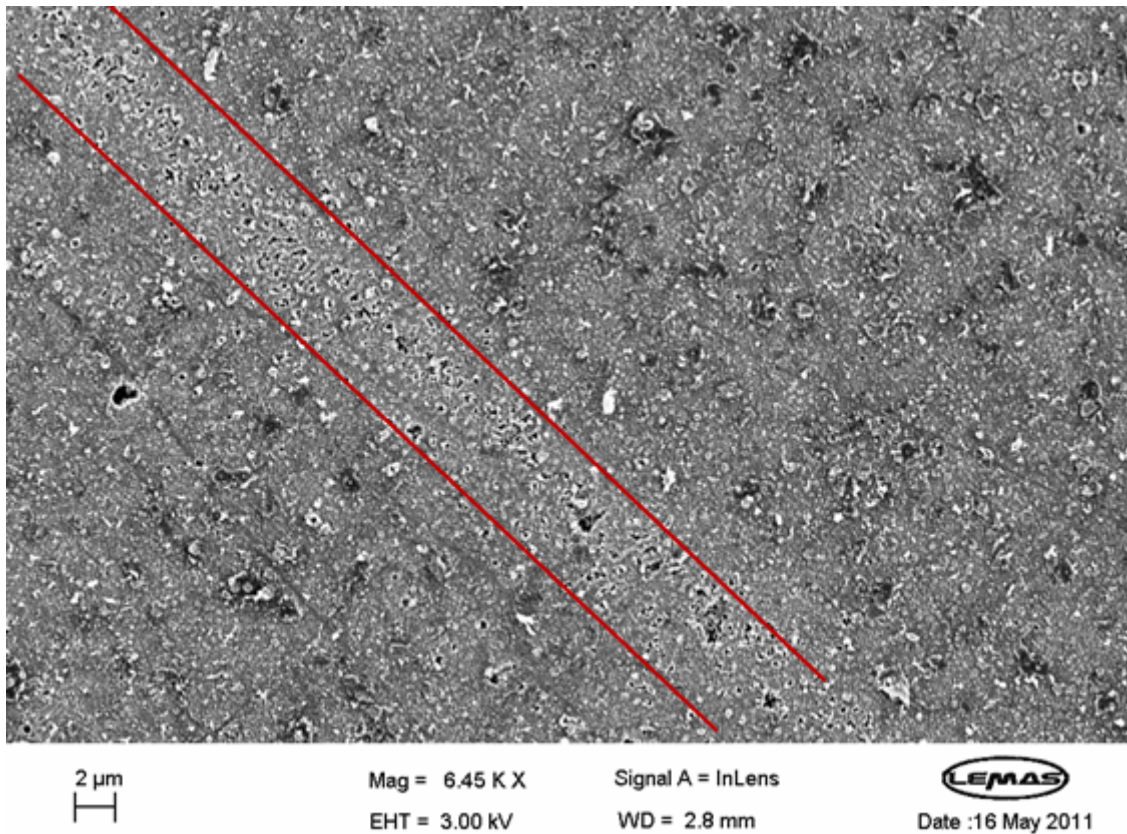


Figure 6-6 Localized pore formation along the laser beam scan direction

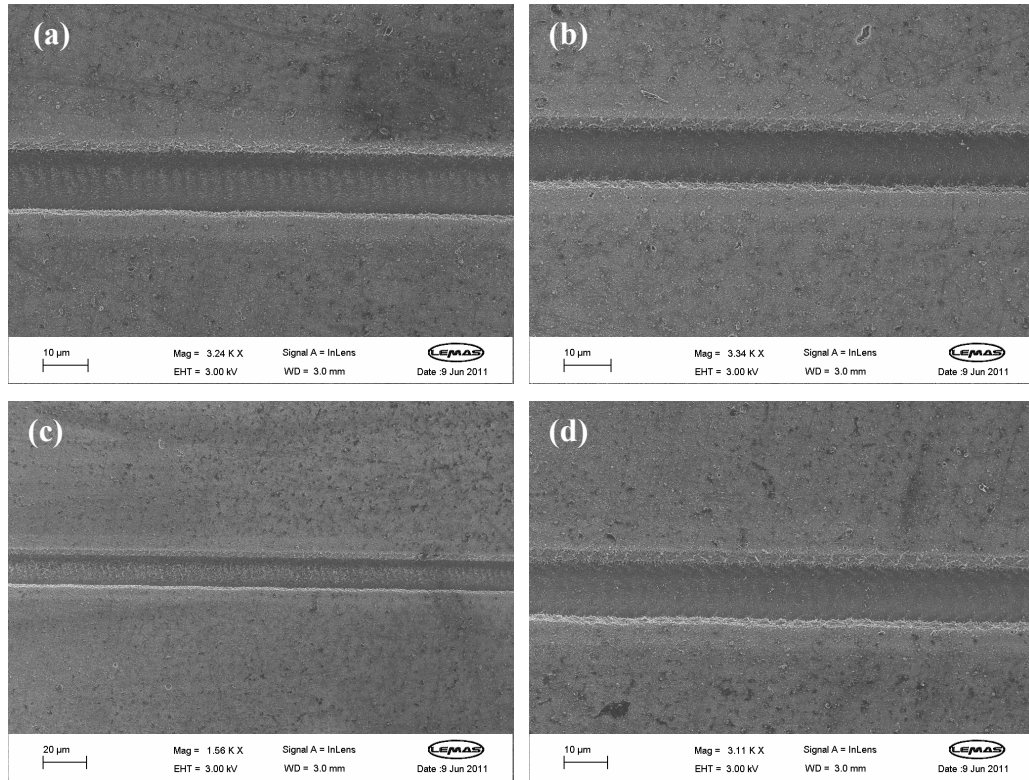


Figure 6-7 SEM images of waveguide structure on composite thin film obtained in No. 2 experiments. (a) 7 uJ 3 mm/s, (b) 7 uJ 4 mm/s, (c) 8 uJ 3 mm/s, (d) 8 uJ 4 mm/s

As shown in Figure 6-8, the Raman spectra of the trench area in the etched film are exactly the same as that of the SiO₂ substrate which indicates that all the composite materials in the trench area are ablated away, and the depth of the waveguide structure is around 1 µm (the same as the thickness of the composite thin film).

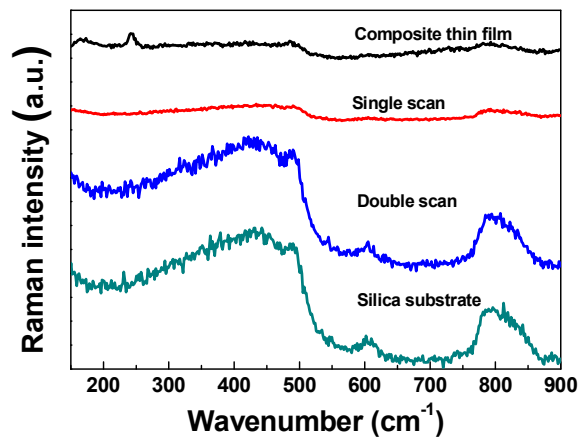


Figure 6-8 Raman spectra of composite thin film trench of ablated area with double scan of fs laser and silica substrate

From all the results discussed above, the optimal channel waveguide structures can be achieved using double laser scan at powers of 7 μJ to 8 μJ with a translational speed of 3 mm/s or 4 mm/s.

Through the results of experiments No. 2, the relationship between the width of the trench area and waveguide writing parameters (laser power and writing speed) is acquired and shown in Figure 6-9. Based on this correlation, the width of the expected waveguide structure could be calculated. In experiment No.3, channel waveguides with a width of 18 μm and 25 μm were fabricated using optimized parameters aforementioned. The SEM image of the two waveguide channels is shown in Figure 6-10.

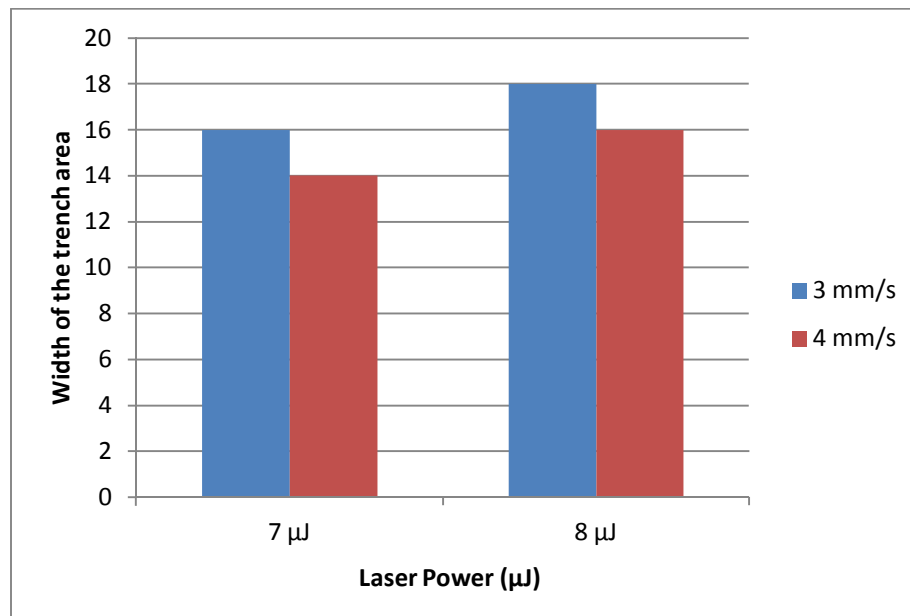


Figure 6-9 Correlation between width of trench area and writing parameters, blue bars represent

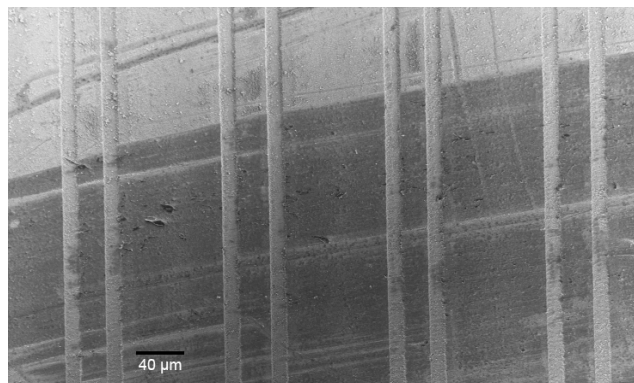


Figure 6-10 SEM image of waveguides used for light propagation

A 1480 nm laser was propagated through one of the channels with 18 μm width and 10 mm length. The mode profile of this channel obtained is shown in Figure 6-11. It is evident that only TE₀ and TM₀ are shown, which indicates that this waveguide is a single mode channel. The curves of the mode simulation in vertical and landscape direction illustrated in Figure 6-11 is Gaussian profile which imply that the channel waveguide is of good quality. The loss of this channel was measured to be 1.5 dB/cm at the wavelength of 1600 nm.

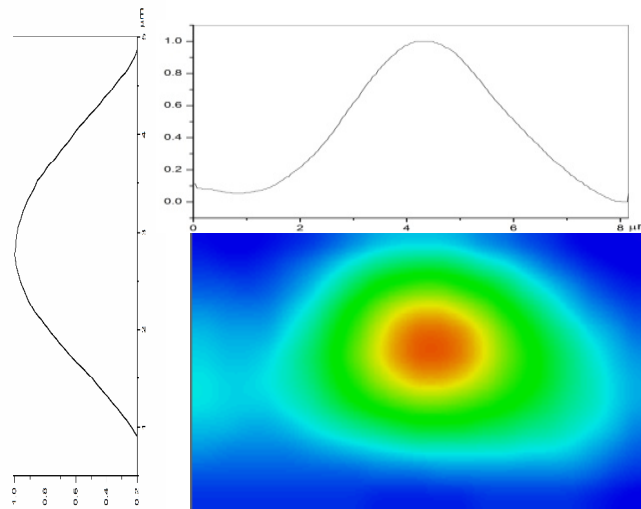


Figure 6-11 Mode profile of channel waveguides with 18 μm width and 11 mm length

6.3 Conclusions

1. This chapter discussed the tellurite glass thin films on silica substrates that are patterned using the RIE technique. After a series of experiments, it illustrated that due to the redeposition of the non-volatile byproducts, it is difficult to obtain a high quality channel waveguides with a depth of $\geq 1 \mu\text{m}$.
2. A relatively good channel waveguide structure was achieved using CHF_3 gas (flow rate of 2 sccm) at an etching power of 200 W and pressure of around 36 mTorr in the chamber. The DC Bias was fluctuated in the range of 585 V to 600 V. The final etching rate of this experiment was calculated to be 68 nm/min.

3. The channel waveguides obtained on the tellurite glass thin film has a width of 3 μm and total thickness of 0.68 μm . It is believed that thicker channel waveguide is required to couple the laser (diameter of fiber is around 9 μm) into the channel.
4. Channel waveguide structures were achieved using fs laser micromachining (1 kHz, pulse duration: 100 fs) with a wavelength of 800 nm. An objective lens with a numerical aperture of 0.4 was used based on the experience.
5. After a series of optimized experiments, it is believed that high quality channel waveguides could be attained when the laser power is in the range of 7 μJ to 8 μJ with double scan and a translational writing speed of 3 mm/s or 4 mm/s.
6. A 1480 nm laser was used to propagate through a channel waveguide structure obtained using 7 μJ with a translational speed of 3 mm/s. The results showed that this channel waveguide (18 μm width and 11 mm) tended to be a single mode waveguide with a loss of 1.5 dB/cm at 1600 nm.

Chapter 7 Conclusions and future work

In this work, tellurite bulk glass, glass thin film on silica and polymer coated silica substrates, PT glass and siloxane polymer composite thin films have been fabricated and characterized for optical applications, especially waveguide amplifiers. In addition, channel waveguide structures on the thin films produced here have been etched using RIE and fs laser micromachining to investigate its feasibility of fabricating waveguide amplifiers. The following conclusions are drawn from this study.

7.1 Conclusions

7.1.1 Tellurite glasses

TWL glasses with different dopants have been demonstrated. To investigate the influence of rare earth ions on the properties of TWL glasses, the thermal, optical and structural properties of Er^{3+} doped, $\text{Er}^{3+}/\text{Yb}^{3+}$ and $\text{Er}^{3+}/\text{Ce}^{3+}$ codoped and $\text{Er}^{3+}/\text{Yb}^{3+}/\text{Ce}^{3+}$ codoped tellurite glasses were compared respectively.

The thermal properties of TWL glasses were studied using the DTA technique. The results obtained show that Er^{3+} doped glass has higher thermal stability. T_g of TWL glasses with different rare earth ions are close to each other (around 430 °C (Table 3-3)), while the glass crystallisation temperatures have significant differences. Er^{3+} doped TWL glass has only one crystallisation temperature which is around 615 °C (Table 3-3), while there is no crystallisation peaks observed in $\text{Er}^{3+}/\text{Yb}^{3+}$ and $\text{Er}^{3+}/\text{Ce}^{3+}$ codoped glasses, and there are one crystallisation peaks and two melting peaks in the DTA traces of $\text{Er}^{3+}/\text{Yb}^{3+}/\text{Ce}^{3+}$ codoped TWL glasses .

Optical properties including UV and IR absorption and optical energy gap, refractive indices as well as fluorescence spectra and the decay lifetime of transition $^4\text{I}_{13/4} \rightarrow ^4\text{I}_{15/4}$ in Er^{3+} ions were investigated using spectrometers, M-line technique and fluorescence spectrometer, respectively. The results illustrate that Ce^{3+} codoping can shift the UV cutoff edge to longer wavelength and reduce the optical energy gap consequently. This may be due to the fact that Ce^{3+} could absorb UV light through the interconfiguration transition of the electrons.

In addition, $\text{Er}^{3+}/\text{Yb}^{3+}/\text{Ce}^{3+}$ codoping may increase the bandwidth of the fluorescence at around 1535 nm. To further study the fluorescence properties of the TWL glasses, Judd-Ofelt parameters were calculated. The results indicate that the $\text{Er}^{3+}/\text{Yb}^{3+}/\text{Ce}^{3+}$ codoping can reduce the covalency of Er-O bonds which caused the reduction of Ω_2 . The calculated radiative lifetimes obtained using the Judd-Ofelt parameters are much shorter than the corresponding measured lifetime, which implies that there are radiative trapping effects in the TWL glass studied in this thesis. Moreover, Yb^{3+} codoping can increase the emission efficiency of transition ${}^4\text{I}_{13/4} \rightarrow {}^4\text{I}_{15/4}$ through an energy transfer process. It also increases the upconversion process which is undesirable for optical amplifiers, however.

From the analysis of Raman spectra and FTIR absorption spectra obtained using reflection mode, it is believed that TWL glasses prepared in this work contain WO_6 , TeO_4 , TeO_3 and also double pairs of $[\text{TeO}_6]$ and $[\text{WO}_6]_2$. The structure of the TWL glasses in this thesis also has been shown schematically according to the results and some references.

7.1.2 Tellurite glass thin films

TWL glass thin films on silica substrates were fabricated using PLD technique.

After series of experiments, optimal deposition parameters were obtained for TWL glass thin film deposited on silica using a 193 nm laser (pulsed duration 20 ns) with a repetition rate of 10 Hz and laser fluence of 1.3 J/cm^2 . The pressure in the chamber was 135 mTorr during the deposition process. Target and substrates were separated by 55 mm while substrates were kept at either $100 \text{ }^\circ\text{C}$ or $300 \text{ }^\circ\text{C}$.

Properties of thin films fabricated at $100 \text{ }^\circ\text{C}$ or $300 \text{ }^\circ\text{C}$ were compared. The results show that there is nano-meter level crack on thin films obtained at $100 \text{ }^\circ\text{C}$, while the size of the particulate on the surface of thin films at this temperature are smaller than these on the surface of the large crack-free thin films obtained at $300 \text{ }^\circ\text{C}$ (Figure 4-14). Thin films prepared at $100 \text{ }^\circ\text{C}$ have relatively higher transmittance when measured using a UV spectrometer (Figure 4-10). EDX and Raman spectra reveal that the composition and structure of thin films deposited by PLD are in good

agreement with that of the target glass used (Table 4-6 and Figure 4-16). Moreover, the target glass and thin films obtained are both amorphous materials as shown by XRD (Figure 4-16).

Decay lifetime of transition ${}^4I_{13/4} \rightarrow {}^4I_{15/4}$ in Er^{3+} ions of thin films grown is comparable with the calculated radiative lifetime of the same transition of bulk glass, which means the radiative trapping effects are reduced for the thin films. The small discrepancy between the measured lifetime of thin film and the calculated radiative lifetime might be due to the OH absorption quenching.

7.1.3 Glass and polymer composite thin films

Two types of glass and siloxane polymer composite thin films were fabricated using PLD. One was obtained by depositing TWL glass thin film onto polymer coated silica and the other was produced by depositing both PT glass and polymer with layer by layer periodic structure.

The deposition parameters of TWL glass and polymer composite thin films are similar to that used for TWL glass thin films on silica. Two kinds of background gas have been used to study its influence on the quality of the TWL glass and polymer composite thin film. The characterisation this thin film illustrates that there are nanometer cracks on the surface of thin films no matter which gas is used in the chamber during deposition. However, thin films prepared in the 96% O_2 /He have a smoother surface than that of thin films deposited in pure O_2 , while all the other properties of these two kinds of thin films are similar to each other.

The refractive index of PT glass is close to that of siloxane polymer, therefore, these two materials could be deposited alternatively to grow layer by layer structure using PLD. A composite thin film was deposited using PLD by ablating a glass target for 100 s and polymer target for 10 s as a cycle, and after 96 such cycles, a thin film with thickness of around 1 μm was obtained.

TEM images confirmed that the glass and polymer composite thin film has the layer by layer structure with clearly defined boundaries between these two materials. The thickness of both glass and polymer layers can be prepared lower than 10 nm to

grow a superlattice structure using this technique. And the thicknesses of each layer can be well controlled by adjusting the deposition parameters.

Inside the superlattice composite thin film, there are some polymer particles implanted across several layers (Figure 5-7 (c)), and there are also some wave like structures yielded with these particles causing the increase of the roughness of the glass and polymer interface.

SEM images demonstrate that the top layer of this composite thin film is covered by uniform particles in a dimension of around 50 μm (Figure 5-9). The quantity of particles is much larger than that inside the composite thin films. This may be due to the thermal energy of plasma helps to melt and remove most of the particles inside the thin films during deposition process. When the set pulses finish, the plasma stops before the growth of the top layer. As a result, particles are left on the top of the thin film and attributed uniformly on the surface of the thin film.

XRR and element mapping results confirm the layer structures of the composite thin films (Figure 5-10 and Figure 5-11). XRD and electron diffraction patterns also reveal that this composite thin film is completely amorphous.

Even though two materials were grown alternatively with a layer by layer structure in the PT-polymer composite thin film, the results of the optical properties show that this thin film behaves like a single composite material. In addition, there are no optical properties sacrificed in this layer by layer structure. The lifetime of transition ${}^4\text{I}_{13/4} \rightarrow {}^4\text{I}_{15/4}$ of Er^{3+} in PT-polymer composite and the PT thin film is much lower than that of the bulk glass, which may be due to the OH absorption causing the nonradiative transition of Er^{3+} ions.

7.1.4 Channel waveguides on composite thin films

A channel waveguide structure was obtained using a power of 200 W in CHF_3 environment with a gas flow rate of 2 sccm and pressure inside the chamber of 36 mTorr. The total thickness of the channel waveguide is about 680 nm which produced within 10 min.

Fs laser micromachining was used to pattern PT-polymer composite thin films. The wavelength of the laser is 800 nm at a fixed repetition rate of 1 kHz. After a series of writing experiments, optimized conditions were obtained, which was NA of 0.4, a power of the laser in the range of 7-8 μJ with a translational scan speed of 3 mm/s or 4 mm/s using a double scan. The threshold of damage this composite material was measured to be 4 μJ .

A series of waveguide structures with widths of 18 and 25 μm were obtained using the optimal writing conditions. One of these channels with width of 18 μm and length of 10 mm was chosen to propagate light using a 1480 nm laser. A single mode profile was obtained and the loss of this channel is around 1.5 dB/cm at wavelength of 1600 nm.

7.2 Future work

The main aim of this thesis is to study the fabrication and characterisation of tellurite glass, glass and polymer composite thin films as optical materials. These optical materials have potential to fabricate various optical devices, like planar optical amplifiers and sensors. To fully explore their application, several directions have been identified for future work.

7.2.1 $\text{Er}^{3+}/\text{Yb}^{3+}/\text{Ce}^{3+}$ triply doped TWL glasses

$\text{Er}^{3+}/\text{Yb}^{3+}/\text{Ce}^{3+}$ triply doped TWL glasses have excellent green and red upconversion, therefore, their potential applications as optical sensor are interesting to be studied using fluorescence intensity ratio (FIR) technique. To study the possibility of fabricate optical temperature sensors using these glasses, the upconversion spectra of the glasses in the range of 500 to 700 nm at different temperatures can be investigated using a 980 nm laser diode as an excitation source. It is also possible to write array waveguide in the TWL bulk glass using fs laser micromachining through changing the refractive index of the material, which has already been done. The propagation loss, gain, and mode profile need to be measured to study their feasibility as laser in the visible wavelength region.

7.2.2 TWL glass thin film on silica substrate and polymer coated silica substrate

The channel waveguide written using RIE technique as discussed in Section 6.1, Chapter 6 can be further investigated. Previously, to characterise the property of the channel waveguide obtained using RIE, a fibre with a diameter of 9 μm was used to couple the laser beam into the channel waveguide, which was failed due to the small dimension of the channel waveguide. A solution to this problem is to use a fibre with a smaller diameter (e.g. 3 μm) to couple the laser beam into the channel waveguide. An alternative solution is to use free space technique, which employs two spot-focusing horn lenses to reduce the dimension of the laser beam, and help to couple into the channel waveguide more easily. The horn lens also can help to receive the signal from the channel waveguide. It is worth to try these two solutions, and study the properties of the channel waveguide, for example, measure the optical loss, gain, mode profile and noise figure.

The feasibility of writing channel waveguides on Er^{3+} doped TWL glass thin film using fs laser micromachining is also of interest. The optimal writing parameters including the NA, writing speed, laser power and the repetition rate need to be sorted out. The high quality channel waveguides on the thin film obtained at optimal writing condition should be characterized, including the measurements of loss, gain, mode profile, and noise figure etc.

7.2.3 Channel waveguides on glass-polymer composite thin films

The channel waveguide shown in Section 6.2, Chapter 6 has not been fully investigated. As a result of the high loss of the waveguides, gain has not been shown in this channel waveguide. Therefore, to reduce the loss, the quantity and dimension of the particulates on the glass-polymer composite thin film should be reduced. One solution for this problem is to install a high speed microfilter on the PLD system to filter the large particles. The other solution is to try the fs laser PLD which is known to be able to produce smaller and uniform particulates on the thin film compared with nano second Excimer laser. Once the composite thin film with small uniform particulates is obtained, channel waveguides can be written on using fs laser micromachining at the optimal conditions discussed in Chapter 6. The loss, gain, mode profile and noise figure need to be investigated as well.

Chapter 8 Appendix

8.1 Optical gain

The electrons in rare earth ions can be excited within the 4f energy states and inversion population formed. When the light signals come through a medium with electrons in the population inversion state, the electrons at the excited level will release photons in form of light with the same wavelength of the passing signal. The signal is amplified in this process as shown in Figure 2-3.

The optical gain G_o of an amplifier which is defined as the ratio between the input signal and the output signal is typically described in dB as follows[38]:

$$G_o(dB) = 10\log_{10}\left(\frac{P_{signal-out}}{P_{signal-in}}\right) \quad (8.1)$$

However, there are also polarization-dependent effects and broadband optical noise (amplified spontaneous emission, ASE) signals in the output signal, which makes the measurements of output signal complicated. Therefore, people defined other two kinds of gains, relative gain G_R and internal gain G_{INT} which are expressed as[300]:

$$G_R(dB) = 10\log_{10}\left(\frac{P_{signal-out} - P_{ASE}}{P_{signal-in}}\right) \quad (8.2)$$

and

$$G_{INT} = G_R - \alpha_P \quad (8.3)$$

where P_{ASE} represents the amplified spontaneous emission power, and α_P is the propagation loss. To study the external amplification for a real optical amplifier, net gain G_{NET} which is considered to be a crucial parameter is defined as[300]:

$$G_{NET} = G_{INT} - 2\alpha_{coup} \quad (8.4)$$

where α_{coup} is the fiber-waveguide coupling loss.

To measure the relative gain G_R , an optical spectrum analyzer is used to filter the output signal and distinguish the signal from noise at the output[38]. The schematic experimental setup is shown in Figure 8-1.

In this setup, attenuators, taps, and power meters are used to control and monitor the counterpropagating pump power and input signal levels, and an optical spectrum analyzer is used to detect the output signal and noise components. An isolator after the signal laser is used to reduce backward-propagating light which can destabilize the signal laser. A bandpass filter is used to filter out the signal laser spontaneous emission. An attenuator is used to control the input signal level. A 1% tap is used to monitor the input signal level. A WDM is used to combine the signal and pump. An isolator after the WDM is used to reduce backward-propagating light which can destabilize the signal laser. A 1% tap is used to monitor the pump power level. An attenuator is used to control the pump power level. An OSA is used to detect the output signal and noise components.

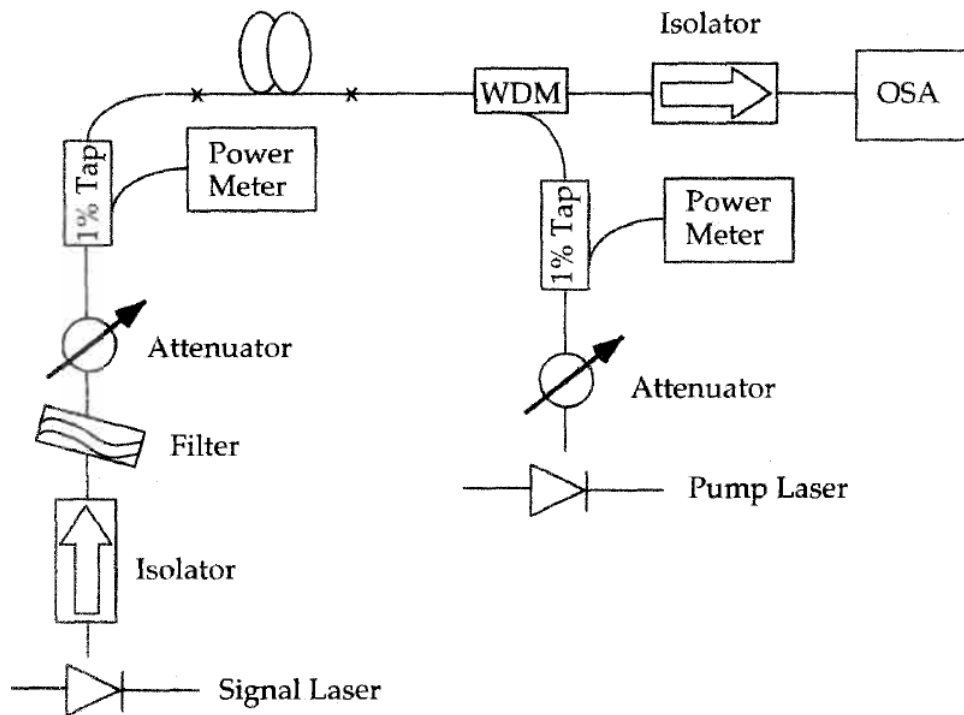


Figure 8-1 The schematic of the experimental setup of the gain measurement with an optical spectrum analyzer[38]

8.2 Judd-Ofelt theory

The absorption intensity obtained using UV spectrometer can be used to calculate the absorption coefficient:

$$a(\lambda) = \frac{-Ln(I/I_0)}{t} = \frac{2.303 (-\log_{10} (I/I_0))}{t} \quad (8.5)$$

where t is the thickness of the glass

The absorption coefficient α is used to calculate the experimental oscillator strength of transition a $\{L, S, J\} \rightarrow b \{L', S', J'\}$:

$$f_{exp(a \rightarrow b)} = \frac{4\varepsilon_0 mc^2}{Ne^2 \bar{\lambda}^2} \int \alpha(\lambda) d\lambda \quad (8.6)$$

where ε_0 is the permittivity of free space, c is the light velocity (2.998×10^8 m/s), N is the rare earth ion concentration (ion/m³), e (1.609×10^{-19} C) and m (9.11×10^{-31} kg) are the charge and mass of electron, and $\alpha(\lambda)$ is the absorption coefficient at a wavelength of λ , average wavelength $\bar{\lambda} = \int \lambda \alpha(\lambda) / \int \alpha(\lambda)$. The rare earth ion concentration can be calculated by the weight of rare earth oxide (Er₂O₃ here) in the glass and the density of the glass ρ .

$$N = \frac{\left(\frac{m_{Er_2O_3}}{M_{Er_2O_3}}\right) \times 2 \times 6.02 \times 10^{23}}{\frac{m_{glass}}{\rho_{glass}}} \quad (8.7)$$

where m_{glass} is 20 g, and $m_{Er_2O_3}$ can be calculated using the weight of glass, and the concentration of the rare earth ions, $M_{Er_2O_3}$ is the molecular weight 382.56 g/mol, and ρ_{glass} is listed in Table 3-2. Actually, the weight of glass obtained is smaller than 20 g powder after melting, and the concentration of rare earth ions in resultant glass is different from the theory value because the weight loss for different compounds are different in the glass melting process. Therefore, the weight of both glass and rare earth ions in the glass used for this calculation are estimated.

According to the Judd-Ofelt theory, theory oscillator strength of transition a $\{L, S, J\} \rightarrow b \{L', S', J'\}$ can be expressed as follow:

$$f_{cal(a \rightarrow b)} = \frac{8\pi^2 mc}{3h(2J_a + 1)\lambda n^2 e^2} (\chi_{ed} S_{ed} + \chi_{md} S_{md}) \quad (8.8)$$

where S_{ed} and S_{md} are line strength of the electric dipole and magnetic dipole transitions, respectively, which are defined as

$$S_{ed} = e^2 \sum_{t=2,4,6} \Omega_t |\langle a || U^{(t)} || b \rangle|^2 \quad (8.9)$$

$$S_{md} = \left(\frac{eh}{4\pi mc}\right)^2 |\langle a || L + 2S || b \rangle|^2 \quad (8.10)$$

where $\chi_{ed} = n(n^2 + 2)^2 / 9$ and $\chi_{md} = n^3$ are the correction terms of the local field which stand for the increase of the electric field around the rare earth ions due to the

polarizability of the host medium, J is the total angular quantum number for this transition, n is the refractive index of the host medium at the average wavelength, h is the Planck constant, the reduced matrix $|\langle a \| U^{(t)} \| b \rangle|^2$ was tabulated by Weber [44] and $|\langle a \| L + 2s \| b \rangle|^2$ can be calculated using the equation offered by Carnall [45].

Based on the above equations, the experimental oscillator strength can be calculated. In the equation of the theory oscillator strength, only $\sum_{t=2,4,6} \Omega_t |\langle a \| U^{(t)} \| b \rangle|^2$ is unknown. Theoretically, experimental oscillator strength and theory oscillator strength should be equal to each other:

$$f_{\text{exp}} = f_{\text{cal}} \quad (8.11)$$

Then the Judd-Ofelt parameters Ω_2 , Ω_4 , Ω_6 can be obtained by fitting this equation using least square method in Matlab software.

Once the Judd-Ofelt parameters obtained, they can be used to calculate the oscillator strength of the unreachable absorption transitions ($a \rightarrow b$), the transition rate, lifetime and the branching ratio of emission transition ($b \rightarrow a$).

References

1. Bamiedakis, N., et al., *Cost-effective multimode polymer waveguides for high-speed on-board optical interconnects*. Ieee Journal of Quantum Electronics, 2009. **45**(4): p. 415-424.
2. Beals, J., et al., *A terabit capacity passive polymer optical backplane based on a novel meshed waveguide architecture*. Applied Physics a-Materials Science & Processing, 2009. **95**(4): p. 983-988.
3. Polman, A. and Van Veggel, F.C.J.M., *Broadband sensitizers for erbium-doped planar optical amplifiers: review*. Journal of the Optical Society of America. B, 2004. **21**(5): p. 871-892.
4. Sudo, S., *Current trends in optical amplifiers and their applications*, in *Progress in optical fiber amplifiers*, T.P. Lee, Editor 1996, World scientific publishing.
5. Polman, A., *Exciting erbium-doped planar optical amplifier materials*, in *Thin Films for Optical Waveguide Devices and Materials for Optical Limiting*, K.P.R.W.B.W.S.J.J.A.K.Y.L. Nashimoto and R.P.J.W. K; Sutherland, Editors. 2000. p. 3-14.
6. Chryssou, C.E., Di Pasquale, F., and Pitt, C.W., *Er³⁺-doped channel optical waveguide amplifiers for WDM systems: a comparison of tellurite, alumina and Al/P silicate materials*. Selected Topics in Quantum Electronics, IEEE Journal of, 2000. **6**(1): p. 114-121.
7. Hattori, K., et al., *Erbium-doped silica-based planar waveguide amplifier pumped by 0.98 μm laser diodes*. Electronics Letters, 1993. **29**(4): p. 357-359.
8. Liu, K., et al., *Erbium-doped waveguide amplifiers fabricated using focused proton beam writing*. Applied Physics Letters, 2004. **84**(5): p. 684-686.
9. Lallier, E., *Rare-earth-doped glass and LiNbO₃ waveguide lasers and optical amplifiers*. Applied Optics, 1992. **31**(25): p. 5276-5282.
10. Palm, J., et al., *Electroluminescence of erbium-doped silicon*. Physical Review B, 1996. **54**(24): p. 17603-17615.
11. Miniscalco, W.J., *Erbium-doped glasses for fiber amplifiers at 1500 nm*. Journal of Lightwave Technology, 1991. **9**(2): p. 234-250.
12. Slooff, L.H., et al., *Rare-earth doped polymers for planar optical amplifiers*. Journal of Applied Physics, 2002. **91**(7): p. 3955-3980.
13. Rehouma, F., Aiadi, K.E. , *Glasses for ion-exchange technology*. International journal of communications, 2008. **1**(4): p. 148-155.
14. Wong, W.H., Pun, E.Y.B., and Chan, K.S., *Er³⁺-Yb³⁺ codoped polymeric optical waveguide amplifiers*. Applied Physics Letters, 2004. **84**(2): p. 176-178.
15. Barber, D.B., et al., *Amplification by optical composites*. Optics Letters, 1997. **22**(16): p. 1247-1249.
16. Novak, B.M., *Hybrid nanocomposite materials - between inorganic glasses and organic polymers*. Advanced Materials, 1993. **5**(6): p. 422-433.
17. Beecroft, L.L. and Ober, C.K., *Nanocomposite materials for optical applications*. Chemistry of Materials, 1997. **9**(6): p. 1302-1317.
18. Mears, R.J., et al., *Low-noise erbium-doped fibre amplifier operating at 1.54 μm* . Electronics Letters, 1987. **23**(19): p. 1026-1028.

19. Miller, S.E., *Integrated optics-an introduction*. Bell System Technical Journal, 1969. **48**(7): p. 2059-2069.
20. Yajima, H., Sekimoto, Y., and Kawase, S., *Amplification at 1.06 μm using a Nd-glass thin-film waveguide*. Applied Physics Letters, 1972. **21**(9): p. 407-409.
21. Kitagawa, T., et al., *Guided-wave laser based on erbium-doped silica planar lightwave circuit*. Electronics Letters, 1991. **27**(4): p. 334-335.
22. Kitagawa, T., et al., *Amplification in erbium-doped silica-based planar lightwave circuits*. Electronics Letters, 1992. **28**(19): p. 1818-1819.
23. Shmulovich, J., et al., *Er^{3+} glass waveguide amplifier at 1.5 μm on silicon*. Electronics Letters, 1992. **28**(13): p. 1181-1182.
24. Shuto, K., et al., *Erbium-doped phosphosilicate glass waveguide amplifier fabricated by PECVD*. Electronics Letters, 1993. **29**(2): p. 139-141.
25. Han, H.-S., Seo, S.-Y., and Shin, J.H., *Optical gain at 1.54 μm in erbium-doped silicon nanocluster sensitized waveguide*. Applied Physics Letters, 2001. **79**(27): p. 4568-4570.
26. Nazabal, V., et al., *Optical waveguide based on amorphous Er^{3+} -doped Ga-Ge-Sb-S(Se) pulsed laser deposited thin films*. Thin Solid Films. **518**(17): p. 4941-4947.
27. Caricato, A.P., et al., *Er^{3+} -doped tellurite waveguides deposited by excimer laser ablation*. Materials Science and Engineering B-Solid State Materials for Advanced Technology, 2003. **105**(1-3): p. 65-69.
28. Caricato, A.P., et al., *Er-doped oxyfluoride silicate thin films prepared by pulsed laser deposition*. Optical Materials, 2007. **29**(9): p. 1166-1170.
29. Mori, A., Ohishi, Y., and Sudo, S., *Erbium-doped tellurite glass fibre laser and amplifier*. Electronics Letters, 1997. **33**(10): p. 863-864.
30. Chen, Y., et al., *Stimulated emission and optical gain in ZnO epilayers grown by plasma-assisted molecular-beam epitaxy with buffers*. Applied Physics Letters, 2001. **78**(11): p. 1469-1471.
31. Mais, N., et al., *Er doped nanocrystalline ZnO planar waveguide structures for 1.55 μm amplifier applications*. Applied Physics Letters, 1999. **75**(14): p. 2005-2007.
32. Lawrence, J.R., Turnbull, G.A., and Samuel, I.D.W., *Broadband optical amplifier based on a conjugated polymer*. Applied Physics Letters, 2002. **80**(17): p. 3036-3038.
33. Kamalasanan, M.N. and Chandra, S., *Sol-gel synthesis of ZnO thin films*. Thin Solid Films, 1996. **288**(1-2): p. 112-115.
34. Bahtat, A., et al., *Fluorescence of Er^{3+} ions in TiO_2 planar waveguides prepared by a sol-gel process*. Optics Communications, 1994. **111**(1-2): p. 55-60.
35. Neufeld, E., et al., *Influence of germanium content on the photoluminescence of erbium- and oxygen-doped SiGe grown by molecular beam epitaxy*. Applied Physics Letters, 1997. **71**(21): p. 3129-3131.
36. Serna, R. and Afonso, C.N., *In situ growth of optically active erbium doped Al_2O_3 thin films by pulsed laser deposition*. Applied Physics Letters, 1996. **69**(11): p. 1541-1543.
37. Dutton, H.J.R., *Understanding optical communications*, 1998, IBM.
38. Becker, P., Olsson, A., and Simpson, J., *Erbium-doped fiber amplifiers*: Elsevier Academic Press. 1999

39. Miniscalco, W., *Optical and Electronic Properties of Rare Earth Ions in Glasses*, in *Rare-Earth-Doped Fiber Lasers and Amplifiers, Revised and Expanded* 2001, CRC Press.
40. Shen, S. *New rare earth ion-doped hosts for broadband fibre amplifier*: University of Leeds, Institute for materials research. 2000
41. Schweizer, T. *Rare-earth-doped gallium lanthanum sulphide glasses for mid-infrared fiber lasers*: University of Southampton, Optoelectronics Research Centre, University of Southampton and Institut für Laser-Physik, University of Hamburg. 1998
42. Judd, B.R., *Optical absorption intensities of rare-earth ions*. Physical Review, 1962. **127**(3): p. 750-761.
43. Ofelt, G.S., *Intensities of crystal spectra of rare-earth ions*. The Journal of Chemical Physics, 1962. **37**(3): p. 511-520.
44. Weber, M.J., *Probabilities for radiative and nonradiative decay of Er^{3+} in LaF_3* . Physical Review, 1967. **157**(2): p. 262-272.
45. Carnall, W.T., Fields, P.R., and Rajnak, K., *Electronic energy levels in the trivalent lanthanide aquo ions. I. Pr^{3+} , Nd^{3+} , Sm^{3+} , Dy^{3+} , Ho^{3+} , Er^{3+} , and Tm^{3+}* . Journal of chemical physics, 1968. **49**: p. 4424-4442.
46. Xu, T., et al., *Spectral properties and thermal stability of Er^{3+}/Yb^{3+} codoped tungsten-tellurite glasses*. Optical Materials, 2006. **28**(3): p. 241-245.
47. Yamauchi, H., Murugan, G.S., and Ohishi, Y., *Optical properties of Er^{3+} and Tm^{3+} ions in a tellurite glass*. Journal of Applied Physics, 2005. **97**(4).
48. Pradeesh, K., et al., *Optical properties of Er^{3+} doped alkali chlorophosphate glasses for optical amplifiers*. Optical Materials, 2008. **31**(2): p. 155-160.
49. Sun, H., et al., *Host dependent frequency upconversion of Er^{3+} -doped oxyfluoride germanate glasses*. Journal of Luminescence, 2006. **117**(2): p. 179-186.
50. Florez, A., et al., *Optical transition probabilities and compositional dependence of Judd-Ofelt parameters of Er^{3+} ions in fluoroindate glass*. Journal of Alloys and Compounds, 1995. **227**(2): p. 135-140.
51. Qian, Q., et al., *Thermal stability and spectroscopic properties of Er^{3+} -doped antimony-borosilicate glasses*. Spectrochimica Acta Part a-Molecular and Biomolecular Spectroscopy, 2008. **71**(1): p. 280-285.
52. Yang, J., et al., *Spectroscopic properties and thermal stability of erbium-doped bismuth-based glass for optical amplifier*. Journal of Applied Physics, 2003. **93**(2): p. 977-983.
53. Kiel, A. *Multi phonon spontaneous emission in paramagnetic crystals*. in *Quantum Electronics; proceedings of the third international congress*. 1964. Dunod Éditeur, Paris, and Columbia University Press, New York.
54. Riseberg, L.A. and Moos, H.W., *Multiphonon orbit-lattice relaxation of excited states of rare earth ions in crystals*. Physical Review, 1968. **174**(2): p. 429-438.
55. Layne, C.B., Lowdermilk, W.H., and Weber, M.J., *Multiphonon relaxation of rare-earth ions in oxide glasses*. Physical Review B, 1977. **16**(1): p. 10-20.
56. Wang, J.S., Vogel, E.M., and Snitzer, E., *Tellurite glass: a new candidate for fiber devices*. Optical Materials, 1994. **3**(3): p. 187-203.
57. Shen, S., et al., *Compositional effects and spectroscopy of rare earths (Er^{3+} , Tm^{3+} , and Nd^{3+}) in tellurite glasses*. Comptes Rendus Chimie, 2002. **5**(12): p. 921-938.

58. Jha, A., Shen, S., and Naftaly, M., *Structural origin of spectral broadening of 1.5- μm emission in Er^{3+} -doped tellurite glasses*. *Physical Review B*, 2000. **62**(10): p. 6215.
59. El-Hagary, M., et al., *Optical properties of glasses ($\text{TeO}_2\text{-GeO}_2\text{-K}_2\text{O}$) thin films co-doped with rare earth oxides $\text{Sm}_2\text{O}_3/\text{Yb}_2\text{O}_3$* . *Journal of Alloys and Compounds*, 2009. **485**(1-2): p. 519-523.
60. Conti, G.N., et al., *Rare-earth doped tungsten tellurite glasses and waveguides: fabrication and characterization*. *Journal of Non-Crystalline Solids*, 2004. **345**: p. 343-348.
61. Churbanov, M.F., et al., *Glasses of $\text{TeO}_2\text{-WO}_3$ and $\text{TeO}_2\text{-WO}_3\text{-La}_2\text{O}_3$ systems for fiber optics*. *Journal of Optoelectronics and Advanced Materials*, 2005. **7**(4): p. 1765-1772.
62. Nandi, P. and Jose, G., *Erbium doped phospho-tellurite glasses for 1.5 μm optical amplifiers*. *Optics Communications*, 2006. **265**(2): p. 588-593.
63. Stanworth, J.E., *Tellurite glasses*. *Nature*, 1952. **169**(4301): p. 581-582.
64. Pauling, L., *The nature of the chemical bond*. 2nd ed: Cornell University Press, Oxford University press. 1940
65. Brady, G.W., *X-ray study of tellurium oxide glass*. *Journal of Chemical Physics*, 1956. **24**(2): p. 477-477.
66. Brady, G.W., *Structure of tellurium oxide glass*. *Journal of Chemical Physics*, 1957. **27**(1): p. 300-303.
67. Koen, J.G., et al., *Investigation of photochromic effect in erbium-doped tellurite glasses*. *Journal of Physics D-Applied Physics*, 1976. **9**(1): p. L13-L16.
68. Le Neindre, L., et al., *Effect of relative alkali content on absorption linewidth in erbium-doped tellurite glasses*. *Journal of Non-Crystalline Solids*, 1999. **255**(1): p. 97-102.
69. Marinov, M.R., et al., *Phase-equilibrium in system $\text{TeO}_2\text{-PbO}$* . *Dokladi Na Bolgarskata Akademiya Na Naukite*, 1974. **27**(11): p. 1533-1536.
70. Dimitriev, Y., Kaschieva, E., and Gurov, E., *Phase diagram of the $\text{TeO}_2\text{-GeO}_2$ system*. *Materials Research Bulletin*, 1976. **11**(11): p. 1397-1403.
71. Dimitriev, Y.B., Ivanova, Y.Y., and Stavrakeva, D.A., *Phase equilibrium in $\text{Ag}_2\text{O} - \text{TeO}_2$ system*. *Dokladi Na Bolgarskata Akademiya Na Naukite*, 1976. **29**(12): p. 1783-1786.
72. Dimitriev, Y.B., Ivanova, Y.Y., and Marinov, M.R., *Phase equilibria in the $\text{CuO-TeO}_2\text{-V}_2\text{O}_5$ system*. *Acad. Bu:g.Sci.*, 1974. **27**(9).
73. Ivanova, Y.Y. and Dimitriev, Y.B., *Phase equilibria of the $\text{Ag}_2\text{O-TeO}_2\text{-V}_2\text{O}_5$ system*. *Materials Chemistry*, 1981. **6**(4-5): p. 287-297.
74. Ivanova, Y.Y. and Dimitriev, J.B., *Phase-equilibrium in the $\text{TeO}_2\text{-B}_2\text{O}_3\text{-V}_2\text{O}_5$ system*. *Journal of Materials Science Letters*, 1989. **8**(9): p. 1006-1008.
75. Dimitriev, J., Dimitrov, V., and Arnaudov, M., *Structure of glasses from $\text{TeO}_2\text{-VO}_2$ system*. *Monatshefte Fur Chemie*, 1978. **109**(4): p. 791-797.
76. Dimitriev, Y., et al., *Structure of Glasses of the $\text{TeO}_2\text{-MoO}_3$ System*. *Zeitschrift für anorganische und allgemeine Chemie*, 1981. **479**(8): p. 229-240.
77. Dimitrov, V., Arnaudov, M., and Dimitriev, Y., *IR-spectral study of the effect of WO_3 on the structure of tellurite glasses*. *Monatshefte Fur Chemie*, 1984. **115**(8-9): p. 987-991.
78. Kozhukharov, V., et al., *Neutron diffraction investigation of a tellurite-tungstate glass*. *Journal of Materials Science*, 1986. **21**(5): p. 1707-1714.

79. Sekiya, T., Mochida, N., and Ogawa, S., *Structural study of WO₃-TeO₂ glasses* Journal of Non-Crystalline Solids, 1994. **176**(2-3): p. 105-115.
80. Sokolov, V.O., et al., *On the structure of tungstate-tellurite glasses*. Journal of Non-Crystalline Solids, 2006. **352**(52-54): p. 5618-5632.
81. Blanchandin, S., et al., *New investigations within the TeO₂-WO₃ system: phase equilibrium diagram and glass crystallization*. Journal of Materials Science, 1999. **34**(17): p. 4285-4292.
82. Kosuge, T., et al., *Thermal stability and heat capacity changes at the glass transition in K₂O-WO₃-TeO₂ glasses*. Journal of Non-Crystalline Solids, 1998. **242**(2-3): p. 154-164.
83. Feng, X., et al. *Tungsten-tellurite glass: a new candidate medium for Yb³⁺-doping*. in *11th International Symposium on Non-Oxide and New Optical Glasses*. 1998. Sheffield, England: Elsevier Science Bv.
84. Wang, X.M., *Investigation of thermal stability and spectroscopic properties in Er³⁺/Yb³⁺ co-doped niobic tungsten tellurite glasses*. Spectrochimica Acta Part a-Molecular and Biomolecular Spectroscopy, 2008. **70**(1): p. 99-103.
85. Shen, S.X., Naftaly, M., and Jha, A., *Tungsten-tellurite - a host glass for broadband EDFA*. Optics Communications, 2002. **205**(1-3): p. 101-105.
86. Xu, T.F., et al., *Study of upconversion fluorescence property of novel Er³⁺/Yb³⁺ co-doped tellurite glasses*. Spectrochimica Acta Part a-Molecular and Biomolecular Spectroscopy, 2006. **64**(3): p. 560-563.
87. Shen, S., Richards, B., and Jha, A., *Enhancement in pump inversion efficiency at 980 nm in Er³⁺, Er³⁺/Eu³⁺ and Er³⁺/Ce³⁺ doped tellurite glass fibers*. Optical Express, 2006. **14**(12): p. 5050-5054.
88. Nayak, R., et al., *Optical waveguiding in amorphous tellurium oxide thin films*. Thin Solid Films, 2003. **445**(1): p. 118-126.
89. Miniscalco, W.J. and Quimby, R.S., *General procedure for the analysis of Er³⁺ cross-sections*. Optics Letters, 1991. **16**(4): p. 258-260.
90. Jiang, S., et al., *Er³⁺-doped phosphate glasses for fiber amplifiers with high gain per unit length*. Journal of Non-Crystalline Solids, 2000. **263-264**(0): p. 364-368.
91. Intyushin, E.B. and Novikov, V.A., *Tungsten-tellurite glasses and thin films doped with rare-earth elements produced by radio frequency magnetron deposition*. Thin Solid Films, 2008. **516**(12): p. 4194-4200.
92. Lecomte, A., et al., *Sol-gel processing of TeO₂ thin films from citric acid stabilised tellurium isopropoxide precursor*. Journal of the European Ceramic Society, 2007. **27**(2-3): p. 1151-1158.
93. Craciun, V., et al., *Effects of Laser Wavelength and Fluence on the Growth of ZnO Thin-Films by Pulsed-Laser Deposition*. Applied Surface Science, 1995. **86**(1-4): p. 99-106.
94. King, S.L., Gardeniers, J.G.E., and Boyd, I.W., *Pulsed-laser deposited ZnO for device applications*. Applied Surface Science, 1996. **96-98**(0): p. 811-818.
95. Vispute, R.D., et al., *Heteroepitaxial growth of ZnO films by PLD*, in *Epitaxial Oxide Thin Films Iii*, D.G.E.C.B.H.M.E.F.C.M.S.J.S. Schlom, Editor 1997. p. 383-388.
96. Ryu, Y.R., et al., *ZnSe and ZnO film growth by pulsed-laser deposition*. Applied Surface Science, 1998. **127**: p. 496-499.
97. Wang, W., et al., *Optical Characteristics of ZnTeO Thin Films Synthesized by Pulsed Laser Deposition and Molecular Beam Epitaxy*. Journal of Electronic Materials, 2009. **38**(1): p. 119-125.

98. Martino, M., et al., *Pulsed laser deposition of active waveguides*. Thin Solid Films, 2003. **433**(1-2): p. 39-44.
99. Eldada, L. *Advances in polymer optical interconnects*. in *Lasers and Electro-Optics Society, 2005. LEOS 2005. The 18th Annual Meeting of the IEEE*. 2005.
100. Sullivan, C.T., Booth, B.L., and Husain, A., *Polymeric waveguides*. Circuits and Devices Magazine, IEEE, 1992. **8**(1): p. 27-31.
101. Dangel, R., et al. *Development of a low-cost low-loss polymer waveguide technology for parallel optical interconnect applications*. in *Biophotonics/Optical Interconnects and VLSI Photonics/WBM Microcavities, 2004 Digest of the LEOS Summer Topical Meetings*. 2004.
102. Mendez, A. and Morse, T.F., *Specialty Optical Fibers Handbook*: Academic Press. 1. 2007
103. Koike, Y., et al., *High-speed photonics polymer and its application*. Pure and Applied Optics, 1998. **7**(2): p. 201-210.
104. Tanaka, A., et al. *New plastic optical fiber with polycarbonate core and fluorescence-doped fiber for high temperature use*. in *Fiber optic systems for mobile platforms*. 1987. San Diego, CA: Society of Photo-Optical Instrumentation Engineers.
105. DeGroot, J.V., et al., *Highly transparent silicone materials*. Linear and Nonlinear Optics of Organic Materials, 2004. **5517**: p. 116-123.
106. Brunchi, C.E., et al., *Properties of some poly(siloxane)s for optical applications*. High Performance Polymers, 2009. **21**(1): p. 31-47.
107. Sankar, V., Kumar, S.T., and Rao, P.K., *Preparation, characterization and fabrication of intraocular lenses from photo initiated polymerized PMMA*. Trends biomater. Artif. Organs, 2004. **17**(2): p. 24-30.
108. Garvey, D.W., et al., *Single-mode nonlinear-optical polymer fibers*. J. Opt. Soc. Am. B, 1996. **13**(9): p. 2017-2023.
109. Chen, J.-g., et al., *Low-loss planar optical waveguides fabricated from polycarbonate*. Polymer Engineering & Science, 2009. **49**(10): p. 2015-2019.
110. Sakaguchi, S., et al. *Fluorinated polyimide for low-loss optical waveguides at 1.55 μm* . in *WDM and photonic switching devices for network applications III*. 2002.
111. Brown, K.S., et al., *Characterization of poly(phenylsilsesquioxane) thin-film planar optical waveguides*. Ieee Photonics Technology Letters, 1997. **9**(6): p. 791-793.
112. Watanabe, T., et al., *Polymeric optical waveguide circuits formed using silicone resin*. Journal of Lightwave Technology, 1998. **16**(6): p. 1049-1055.
113. Ingham, J.D., et al. *Multimode siloxane polymer waveguides for robust high-speed interconnects*. in *Lasers and Electro-Optics, 2006 and 2006 Quantum Electronics and Laser Science Conference. CLEO/QELS 2006. Conference on*. 2006.
114. Dangel, R., et al., *Polymer-waveguide-based board-level optical interconnect technology for datacom applications*. Ieee Transactions on Advanced Packaging, 2008. **31**(4): p. 759-767.
115. Dire, S., et al., *Sol-gel synthesis of siloxane-oxide hybrid coatings $[\text{Si}(\text{CH}_3)_2\text{O}\cdot\text{MO}_x]$: $M = \text{Si, Ti, Zr, Al}$ with luminescent properties* Journal of Materials Chemistry, 1992. **2**(2): p. 239-244.

116. Viana, B., et al., *Optical-properties of neodymium and dysprosium doped hybrid siloxane-oxide coatings*. Journal of Materials Chemistry, 1995. **5**(5): p. 719-724.
117. Koslova, N.I., Viana, B., and Sanchez, C., *Rare-earth doped hybrid siloxane oxide coatings with luminescent properties*. Journal of Materials Chemistry, 1993. **3**(1): p. 111-112.
118. Kreiter, M., et al., *Orientation dependence of fluorescence lifetimes near an interface*, 2002.
119. Miya, T., *Silica-based planar lightwave circuits: passive and thermally active devices*. Selected Topics in Quantum Electronics, IEEE Journal of, 2000. **6**(1): p. 38-45.
120. Yang, J., et al., *Nd-doped polymer waveguide amplifiers*. Ieee Journal of Quantum Electronics. **46**(7): p. 1043-1050.
121. O'Brien, D.J., Juliano, Thomas F. , Patel, Parimal J. and Mcknight, Steven H., *Transparent nanoporous glass-polymer composite for U.S. army applications*, 2006, U.S. Army Research Laboratory. p. 22.
122. Cho, J.P. and Liu, M.L., *Preparation and electrochemical properties of glass-polymer composite electrolytes for lithium batteries*. Electrochimica Acta, 1997. **42**(10): p. 1481-1488.
123. Lu, H.H., et al., *Three-dimensional, bioactive, biodegradable, polymer-bioactive glass composite scaffolds with improved mechanical properties support collagen synthesis and mineralization of human osteoblast-like cells in vitro*. Journal of Biomedical Materials Research Part A, 2003. **64A**(3): p. 465-474.
124. Iba, H., Chang, T., and Kagawa, Y., *Optically transparent continuous glass fibre-reinforced epoxy matrix composite: fabrication, optical and mechanical properties*. Composites Science and Technology, 2002. **62**(15): p. 2043-2052.
125. Julian, B., et al., *Synthesis and optical properties of Eu³⁺-doped inorganic-organic hybrid materials based on siloxane networks*. Journal of Materials Chemistry, 2004. **14**(22): p. 3337-3343.
126. Cordoncillo, E., et al., *Blue emitting hybrid organic-inorganic materials*. Optical Materials, 2001. **18**(3): p. 309-320.
127. Zhao, Z., et al., *Tellurite glass thin films on silica and polymer using UV (193 nm) pulsed laser ablation*. Journal of Physics D-Applied Physics, 2011. **44**(9): p. 095501.
128. Mazurczyk, R., *Semiconductor Superlattices*. Chaos, Solitons & Fractals, 1999. **10**(12): p. 1971-1982.
129. Schuller, I.K., *New class of layered materials*. Physical Review Letters, 1980. **44**(24): p. 1597-1600.
130. Arthur, J.R., *Molecular beam epitaxy*. Surface Science, 2002. **500**(1-3): p. 189-217.
131. Wanke, M.C., et al., *Monolithically integrated solid-state terahertz transceivers*. Nature Photonics. **4**(8): p. 565-569.
132. Kakalios, J., et al., *Properties of amorphous semiconducting multilayer films* Journal of Non-Crystalline Solids, 1984. **66**(1-2): p. 339-344.
133. Kotov, N.A., et al., *Mechanism of and defect formation in the self-assembly of polymeric polycationâ€™montmorillonite ultrathin films*. Journal of the American Chemical Society, 1997. **119**(29): p. 6821-6832.

134. Haugan, T., et al., *Addition of nanoparticle dispersions to enhance flux pinning of the $YBa_2Cu_3O_{7-x}$ superconductor*. Nature, 2004. **430**(7002): p. 867-870.
135. Sloyan, K.A., et al., *Growth of crystalline garnet mixed films, superlattices and multilayers for optical applications via shuttered Combinatorial Pulsed Laser Deposition*. Opt. Express, 2010. **18**(24): p. 24679-24687.
136. Olek, M., et al., *Layer-by-layer assembled composites from multiwall carbon nanotubes with different morphologies*. Nano Letters, 2004. **4**(10): p. 1889-1895.
137. Watcharotone, S., et al., *Graphene-silica composite thin films as transparent conductors*. Nano Letters, 2007. **7**(7): p. 1888-1892.
138. Ray, S.S. and Okamoto, M., *Polymer/layered silicate nanocomposites: a review from preparation to processing*. Progress in Polymer Science, 2003. **28**(11): p. 1539-1641.
139. Wasa, K. and Hayakawa, S., *Handbook of sputter deposition technology: principles, technology and application*. New Jersey: Noyes Publication. 1991
140. Sherman, A., *Chemical vapor deposition for microelectronics: principle, technology and application*. New Jersey: Noyes publication. 1987
141. Elshabini-Riad, A. and Barlow, F.D., *Thin film technology handbook*, C.A. Harper, Editor 1997, McGraw Hill: New York.
142. Wasa, K., Kitabatake, M., and Adachi, H., *Thin films materials technology: sputtering of compound materials*: William Andrew, Inc. and Springer-Verlag GabH&co.KG. 2004
143. Creighton, J.R. and Ho, P., *Introduction to chemical vapor deposition*, in *Chemical vapor deposition*, J.-H.P. T.S.Sudarshan, Editor 2001, ASM International.
144. Bartl, A., et al., *A comparison of low-pressure CVD synthesis of diamond and c-BN*. International Journal of Refractory Metals and Hard Materials, 1996. **14**(1-3): p. 145-157.
145. Ohguro, T., et al. *Tenth micron p-MOSFET's with ultra-thin epitaxial channel layer grown by ultra-high-vacuum CVD*. in *Electron Devices Meeting, 1993. IEDM '93. Technical Digest., International*. 1993.
146. Lee, S.N., et al., *Investigation of optical and electrical properties of Mg-doped p-InxGal-xN, p-GaN and p-AlxGayN grown by MOCVD*. Journal of Crystal Growth, 2004. **272**(1-4): p. 455- 459.
147. Chhowalla, M., et al., *Growth process conditions of vertically aligned carbon nanotubes using plasma enhanced chemical vapor deposition*. Journal of Applied Physics, 2001. **90**(10): p. 5308-5317.
148. Tsai, C.L., Chen, C.F., and Wu, L.K., *Bias effect on the growth of carbon nanotips using microwave plasma chemical vapor deposition*. Applied Physics Letters, 2002. **81**(4): p. 721-723.
149. Colomer, J.F., et al., *Large-scale synthesis of single-wall carbon nanotubes by catalytic chemical vapor deposition (CCVD) method*. Chemical Physics Letters, 2000. **317**(1-2): p. 83-89.
150. Perkins, C.M., et al., *Electrical and materials properties of ZrO_2 gate dielectrics grown by atomic layer chemical vapor deposition*. Applied Physics Letters, 2001. **78**(16): p. 2357-2359.
151. Che, G., et al., *Chemical vapor deposition based synthesis of carbon nanotubes and nanofibers using a template method*. Chemistry of Materials, 1998. **10**(1): p. 260-267.

152. Tatebayashi, J., Nishioka, M., and Arakawa, Y., *Over 1.5 μm light emission from InAs quantum dots embedded in InGaAs strain-reducing layer grown by metalorganic chemical vapor deposition*. Applied Physics Letters, 2001. **78**(22): p. 3469-3471.
153. Kobashi, K., et al., *Synthesis of diamonds by use of microwave plasma chemical-vapor deposition-morphology and growth of diamond films*. Physical Review B, 1988. **38**(6): p. 4067-4084.
154. Xu, W.Z., et al., *ZnO light-emitting diode grown by plasma-assisted metal organic chemical vapor deposition*. Applied Physics Letters, 2006. **88**.
155. Klein, L.C., *Sol-Gel Technology for Thin Films, Fibers, Preforms, Electronics and Specialty Shapes*, 1988, William Andrew Publishing/Noyes. p. 49.
156. Jeffrey Brinker and Sherer, G.W., *Sol-gel science: the physics and chemistry of sol-gel processing*. San Diego: Academic press Inc. 1990
157. Almeida, R.M. and Xu, J., *Sol-gel processing of sulfide materials*, in *Handbook of sol-gel science and technology: processing, characterization and applications*, S. Sukka, Editor 2005, Kluwer Academic publisher: New York.
158. Petty, M.C., *Molecular electronics: from principles to practices*. Chichester: John wiley&son ltd. 2007
159. Yao, B.D., Chan, Y.F., and Wang, N., *Formation of ZnO nanostructures by a simple way of thermal evaporation*. Applied Physics Letters, 2002. **81**(4): p. 757-759.
160. Cantalini, C., et al., *Investigation on the O₃ sensitivity properties of WO₃ thin films prepared by sol-gel, thermal evaporation and r.f. sputtering techniques*. Sensors and Actuators B: Chemical, 2000. **64**(1-3): p. 182-188.
161. Kaur, M., et al., *Growth of nanostructures of Zn/ZnO by thermal evaporation and their application for room-temperature sensing of H₂S gas*. Applied Physics A: Materials Science & Processing, 2007. **87**(1): p. 91-96.
162. Dai, Z.R., Pan, Z.W., and Wang, Z.L., *Novel nanostructures of functional oxides synthesized by thermal evaporation*, 2003, WILEY-VCH Verlag. p. 9-24.
163. Cho, A.Y., *Morphology of epitaxial growth of GaAs by a molecular beam method-observation of surface structures*. Journal of Applied Physics, 1970. **41**(7): p. 2780-2786.
164. Chow, P.P., *Molecular beam epitaxy*, in *Thin film processes II*, W.K. John L.Vossen, Editor 1991, Academic Press Limited: New Mexico.
165. Look, D.C., et al., *Characterization of homoepitaxial p-type ZnO grown by molecular beam epitaxy*. Applied Physics Letters, 2002. **81**(10): p. 1830-1832.
166. Ueda, K. and Naito, M., *As-grown superconducting MgB₂ thin films prepared by molecular beam epitaxy*. Applied Physics Letters, 2001. **79**(13): p. 2046-2048.
167. VanHove, J.M., et al., *Ultraviolet-sensitive, visible-blind GaN photodiodes fabricated by molecular beam epitaxy*. Applied Physics Letters, 1997. **70**(17): p. 2282-2284.
168. Stimmer, J., et al., *Electroluminescence of erbium-oxygen-doped silicon diodes grown by molecular beam epitaxy*. Applied Physics Letters, 1996. **68**(23): p. 3290-3292.

169. Hooper, S.E., et al., *InGaN multiple quantum well laser diodes grown by molecular beam epitaxy*. Electronics Letters, 2004. **40**(1): p. 33-34.
170. Barnat, E.V. and Lu, T.-M., *Pulsed and pulsed bias sputtering: principles and applications*. Massachusetts: Kluwer Academic Publishers. 2003
171. Inoue, S., et al., *Shape memory behavior of Fe-Pd alloy thin films prepared by dc magnetron sputtering*. Materials Science and Engineering a-Structural Materials Properties Microstructure and Processing, 2003. **339**(1-2): p. 29-34.
172. Vaglio, R., Maglione, M.G., and Di Capua, R., *High-quality MgB₂ thin films in situ grown by dc magnetron sputtering*. Superconductor Science & Technology, 2002. **15**(8): p. 1236-1239.
173. Chrisey, D.B. and Hubler, G.K., eds. *Pulsed laser deposition of thin film*. 1 ed. 1994, John Wiley& Son Canada.
174. Smith, H.M. and Turner, A.F., *Vacuum deposited thin films using a ruby laser*. Applied Optics, 1965. **4**(1): p. 147-148.
175. Kokai, F., et al., *Effect of laser fluence on the deposition and hardness of boron carbide thin films*. Applied Physics A: Materials Science & Processing, 2002. **74**(4): p. 533-536.
176. Kim, J.H., et al., *Laser wavelength effect on the light emission properties of nanocrystalline Si on Si substrate fabricated by pulsed laser deposition*. Materials Science and Engineering: B, 2002. **89**(1-3): p. 70-72.
177. Suche, M., et al., *Substrate temperature influence on the properties of nanostructured ZnO transparent ultrathin films grown by PLD*. Applied Surface Science, 2007. **253**(19): p. 8141-8145.
178. Zhao, Y., Jiang, Y., and Fang, Y., *The influence of substrate temperature on ZnO thin films prepared by PLD technique*. Journal of Crystal Growth, 2007. **307**(2): p. 278-282.
179. Munoz-Martin, D.e.a., *Compositional structural and optical properties of tellurite thin film glasses deposited by PLD*. Thin Solid Films, 2011. **520**(1): p. 131-137.
180. Zeng, J.N., et al., *Effect of deposition conditions on optical and electrical properties of ZnO films prepared by pulsed laser deposition*. Applied Surface Science, 2002. **197-198**(0): p. 362-367.
181. Kim, S.S. and Lee, B.-T., *Effects of oxygen pressure on the growth of pulsed laser deposited ZnO films on Si(0 0 1)*. Thin Solid Films, 2004. **446**(2): p. 307-312.
182. Haugan, T., et al., *Effect of O₂ partial pressure on YBa₂Cu₃O_{7-δ} thin film growth by pulsed laser deposition*. Physica C: Superconductivity, 2003. **397**(1-2): p. 47-57.
183. Nishikawa, Y., Tanaka, K., and Yoshida, Y., *Morphology of particles generated from thin film by excimer laser ablation*. Journal of the Japan Institute of Metals, 1991. **55**(5): p. 581-587.
184. Yoshitake, T., Hara, T., and Nagayama, K., *The influence of the repetition rate of laser pulses on the growth of diamond thin films by pulsed laser ablation of graphite*. Diamond and Related Materials, 2003. **12**(3-7): p. 306-309.
185. Tamir, S. and Drezner, Y., *New aspects on pulsed laser deposition of aligned carbon nanotubes*. Applied Surface Science, 2006. **252**(13): p. 4819-4823.
186. Jones, S.W., *Photolithography*, 2008.
187. Cui, Z., *Nanofabrication: principle, capabilities and limits*. Didcot: Springer Science+Business media, LLC. 2008

188. Zhuang, D. and Edgar, J.H., *Wet etching of GaN, AlN, and SiC: a review*. Materials Science and Engineering: R: Reports, 2005. **48**(1): p. 1-46.
189. Lee, M.B., Kim, H.S., and Sohn, J.S., *Polymer-coated silicon micromirror array for integrated optical pickup application*. Japanese Journal of Applied Physics Part 2-Letters & Express Letters, 2005. **44**(33-36): p. L1119-L1121.
190. Ulrich, R., et al., *Embossed optical waveguides*. Applied Physics Letters, 1972. **20**(6): p. 213-&.
191. Lukosz, W. and Tiefenthaler, K., *Embossing technique for fabricating integrated optical components in hard inorganic waveguiding materials*. Opt. Lett., 1983. **8**(10): p. 537-539.
192. Becker, H. and Heim, U., *Hot embossing as a method for the fabrication of polymer high aspect ratio structures*. Sensors and Actuators A: Physical, 2000. **83**(1-3): p. 130-135.
193. Hecke, M., Bacher, W., and Müller, K.D., *Hot embossing - The molding technique for plastic microstructures*. Microsystem Technologies, 1998. **4**(3): p. 122-124.
194. Fontana, R.E., et al., *E-beam writing: a next-generation lithography approach for thin-film head critical features*. Magnetics, IEEE Transactions on, 2002. **38**(1): p. 95-100.
195. Yamazaki, K., *Electron beam direct writing*, in *Nanofabrication: fundamentals and application*, A.A. Tseng, Editor 2008, World Scientific Publishing Co.Pte.ltd.
196. Wong, W.H., Zhou, J., and Pun, E.Y.B., *Low-loss polymeric optical waveguides using electron-beam direct writing*. Applied Physics Letters, 2001. **78**(15): p. 2110-2112.
197. Matsui, S. and Mori, K., *Direct writing onto Si by electron-beam stimulated etching*. Applied Physics Letters, 1987. **51**(19): p. 1498-1499.
198. Yu, W. and Yuan, X., *Fabrication of refractive microlens in hybrid SiO₂/TiO₂ sol-gel glass by electron beam lithography*. Opt. Express, 2003. **11**(8): p. 899-903.
199. Lee, S.-J.J. and Sundararajan, N., *Microfabrication for microfluidics*. Norwood: Artech House INC. 2010
200. Albert G. Baca, C.I.H.A., ed. *Fabrication of GaAs devices*. EMIS Processing series 62005, The institute of electrical engineers: London.
201. Oehrlein, G.S., *Reactive ion etching*, in *Handbook of plasma processing technology: fundamentals, etching, deposition and surface interaction*, J.J.C. Stephen M. Rosssnagel, William Dickson Westwood, Editor 1990, Noyes Publication: Norwich.
202. Lieberman, M.A.a.L., Allan J., *Principle of plasma discharges and materials processing*. 2 ed. Canada: John Wiley&Son , Inc. . 2005
203. Jackel, J.L., et al., *Reactive ion etching of LiNbO₃*. Applied Physics Letters, 1981. **38**(11): p. 907-909.
204. Werking, J., et al., *Methane hydrogen-based reactive ion etching of InAs, InP, InAs, InP, GaAs, and GaSb*. Applied Physics Letters, 1991. **58**(18): p. 2003-2005.
205. Shen, R. and Righini, G.C., *Characterization of reactive ion etching of glass and its applications in integrated optics*. Journal of Vacuum Science & Technology A: Vacuum, Surfaces, and Films, 1991. **9**(5): p. 2709-2712.

206. Rangelow, I.W. and Loschner, H., *Reactive ion etching for microelectrical mechanical system fabrication*. Journal of Vacuum Science & Technology B, 1995. **13**(6): p. 2394-2399.
207. Henry, L. and Granjoux, P., *Novel process for integration of optoelectronic devices using reactive ion etching without chlorinated gas*. Electronics Letters, 1987. **23**(24): p. 1253.
208. Osgood, R.M. and Gilgen, H.H., *Laser direct writing of materials*. Annual Review of Materials Science, 1985. **15**: p. 549-576.
209. Chierici, E., et al., *Direct writing of channel waveguide on a tellurite glass using a focused ultraviolet laser beam*. Proceedings of 2002 Ieee/Leos Workshop on Fibre and Optical Passive Components, 2002: p. 24-28.
210. Jiang, J., et al., *All-polymer photonic devices using excimer laser micromachining*. Photonics Technology Letters, IEEE, 2004. **16**(2): p. 509-511.
211. Dyer, P.E., *Excimer laser polymer ablation: twenty years on*. Applied Physics a-Materials Science & Processing, 2003. **77**(2): p. 167-173.
212. Naessens, K., et al., *Flexible fabrication of microlenses in polymer layers with excimer laser ablation*. Applied Surface Science, 2003. **208**: p. 159-164.
213. Ihlemann, J. and Wolff-Rottke, B., *Excimer laser micro machining of inorganic dielectrics*. Applied Surface Science, 1996. **106**: p. 282-286.
214. Perry, M.D., et al., *Ultrashort-pulse laser machining of dielectric materials*. Journal of Applied Physics, 1999. **85**(9): p. 6803-6810.
215. Chichkov, B.N., et al., *Femtosecond, picosecond and nanosecond laser ablation of solids*. Applied Physics a-Materials Science & Processing, 1996. **63**(2): p. 109-115.
216. Rizi, N.H., *Femtosecond laser micromachining current status and application*, 2002, Exitech Limited: Oxford.
217. Schaffer, C.B., Garcia, J.F., and Mazur, E., *Bulk heating of transparent materials using a high-repetition-rate femtosecond laser*. Applied Physics a-Materials Science & Processing, 2003. **76**(3): p. 351-354.
218. Schaffer, C.B., et al., *Micromachining bulk glass by use of femtosecond laser pulses with nanojoule energy*. Opt. Lett., 2001. **26**(2): p. 93-95.
219. Minoshima, K., et al., *Photonic device fabrication in glass by use of nonlinear materials processing with a femtosecond laser oscillator*. Optics Letters, 2001. **26**(19): p. 1516-1518.
220. Shah, L., et al., *Waveguide writing in fused silica with a femtosecond fiber laser at 522 nm and 1 MHz repetition rate*. Optics Express, 2005. **13**(6): p. 1999-2006.
221. Della Valle, G., Osellame, R., and Laporta, P., *Micromachining of photonic devices by femtosecond laser pulses*. Journal of Optics a-Pure and Applied Optics, 2009. **11**(1).
222. Streltsov, A.M. and Borrelli, N.F., *Study of femtosecond-laser-written waveguides in glasses*. J. Opt. Soc. Am. B, 2002. **19**(10): p. 2496-2504.
223. Chan, J.W., et al., *Structural changes in fused silica after exposure to focused femtosecond laser pulses*. Opt. Lett., 2001. **26**(21): p. 1726-1728.
224. Baum, A., et al., *Photochemistry of refractive index structures in poly(methyl methacrylate) by femtosecond laser irradiation*. Optics Letters, 2007. **32**(2): p. 190-192.
225. Gattass, R.R. and Mazur, E., *Femtosecond laser micromachining in transparent materials*. Nature Photonics, 2008. **2**(4): p. 219-225.

226. Glezer, E.N. and Mazur, E., *Ultrafast-laser driven micro-explosions in transparent materials*. Applied Physics Letters, 1997. **71**(7): p. 882-884.
227. Beinhorn, F., et al., *Sub-micron grating formation in Ta₂O₅-waveguides by femtosecond UV-laser ablation*. Applied Surface Science, 1999. **138-139**: p. 107-110.
228. Kawamura, K.-i., et al., *Holographic encoding of fine-pitched micrograting structures in amorphous SiO₂ thin films on silicon by a single femtosecond laser pulse*. Applied Physics Letters, 2001. **78**(8): p. 1038-1040.
229. Miyaji, G. and Miyazaki, K., *Origin of periodicity in nanostructuring on thin film surfaces ablated with femtosecond laser pulses*. Opt. Express, 2008. **16**(20): p. 16265-16271.
230. Narendra, B.D. and Sandip, P.H., *Laser fabrication and machining of materials*. New York: Springer Science+Business Media, LLC. 2008
231. Zhu, L., et al., *Spectral properties and thermal stability of erbium-doped TeO₂-WO₃-La₂O₃ glass*. Journal of Inorganic Materials, 2006. **21**(2): p. 351-356.
232. Shelby, J.E., *Introduction to glass science and technology*. The Royal society of chemistry. 2005
233. Dorofeev, V.V., et al., *Production and properties of high purity TeO₂-WO₃-(La₂O₃, Bi₂O₃) and TeO₂-ZnO-Na₂O-Bi₂O₃ glasses*. Journal of Non-Crystalline Solids, 2011. **357**(11-13): p. 2366-2370.
234. Paul, A., *Chemistry of glasses*. London&New York: Chapman and Hall. 1982
235. Parikh, V.M., *Absorption spectroscopy of organic molecules*. London: Addison-Wesley Publishing company. 1973
236. Gauglitz, G. and Vo-Dinh, T., eds. *Handbook of spectroscopy*. Vol. 1. 2003, WILEY-VCH GmbH&Co.KGaA: Weinheim.
237. Tien, P.K., Ulrich, R., and Martin, R.J., *Modes of propagating light waves in thin deposited semiconductor films*. Applied Physics Letters, 1969. **14**(9): p. 291-294.
238. Ulrich, R. and Torge, R., *Measurement of thin film parameters with a prism coupler*. Applied Optics, 1973. **12**(12): p. 2901-2908.
239. Jiang, X. *Engineering of novel single- and multi-mode infrared optical fibers for device applications* University of Leeds, Institute for Materials Research. 2009
240. Deutsch, T.F., *Absorption -coefficient of infrared -laser window materials*. Journal of Physics and Chemistry of Solids, 1973. **34**(12): p. 2091-2104.
241. McGill, T.C., et al., *Infrared absorption in ionic insulators due to multiphonon processes*. Journal of Physics and Chemistry of Solids, 1973. **34**(12): p. 2105-2115.
242. Dai, N., et al., *The spectroscopic properties of Er³⁺ single doped and Er³⁺/Yb³⁺ co-doped SiO₂-Al₂O₃-La₂O₃ glasses* Acta Photonica Sinica, 2003. **32**(1): p. 112-116.
243. Alani, S.K.J., Hogarth, C.A., and Elmalawany, R.A., *A study of optical-absorption in tellurite and tungsten tellurite glasses*. Journal of Materials Science, 1985. **20**(2): p. 661-667.
244. El-Mallawany, R.A.H., *Optical Properties of Tellurite Glasses in the Ultraviolet Region*, in *Tellurite Glasses Handbook*2001, CRC Press.
245. Binet, C., Badri, A., and Lavalley, J.-C., *A spectroscopic characterization of the reduction of ceria from electronic transitions of intrinsic point defects*. The Journal of Physical Chemistry, 1994. **98**(25): p. 6392-6398.

246. El-Deen, L.M.S., Al Salhi, M.S., and Elkholy, M.M., *IR and UV spectral studies for rare earths-doped tellurite glasses*. Journal of Alloys and Compounds, 2008. **465**(1-2): p. 333-339.
247. Davis, K.M., et al., *Writing waveguides in glass with a femtosecond laser*. Opt. Lett., 1996. **21**(21): p. 1729-1731.
248. Ghosh, G., *Sellmeier coefficients and chromatic dispersions for some tellurite glasses*. Journal of the American Ceramic Society, 1995. **78**(10): p. 2828-2830.
249. Nagamatsu, K., et al., *Influence of Yb³⁺ and Ce³⁺ codoping on fluorescence characteristics of Er³⁺-doped fluoride glass under 980 nm excitation*. Optical Materials, 2004. **27**(2): p. 337-342.
250. Choi, Y.G., et al., *Comparative study of energy transfers from Er³⁺ to Ce³⁺ in tellurite and sulfide glasses under 980 nm excitation*. Journal of Applied Physics, 2000. **88**(7): p. 3832-3839.
251. Ebendorff-Heidepriem, H. and Ehrhart, D., *Spectroscopic properties of Eu³⁺ and Tb³⁺ ions for local structure investigations of fluoride phosphate and phosphate glasses*. Journal of Non-Crystalline Solids, 1996. **208**(3): p. 205-216.
252. Jørgensen, C.K. and Reisfeld, R., *Judd-Ofelt parameters and chemical bonding*. Journal of the Less Common Metals, 1983. **93**(1): p. 107-112.
253. Dai, S., et al., *Effect of radiative trapping on measurement of the spectroscopic properties of Yb³⁺:phosphate glasses*. Journal of Luminescence, 2003. **104**(1-2): p. 55-63.
254. Vetrone, F., et al., *Effect of Yb³⁺ codoping on the upconversion emission in nanocrystalline Y₂O₃:Er³⁺*. Journal of Physical Chemistry B, 2003. **107**(5): p. 1107-1112.
255. Ferraro, J.R., Nakamoto, K., and Brown, C.W., *Introductory Raman Spectroscopy*. 2nd Edition, ed: Elsevier Science. 2003
256. Sekiya, T., Mochida, N., and Soejima, A., *Raman-spectra of binary tellurite glasses containing tri-valent or tetra-valent cations*. Journal of Non-Crystalline Solids, 1995. **191**(1-2): p. 115-123.
257. O'Donnell, M.D., et al., *Fluorotellurite glasses with improved mid-infrared transmission*. Journal of Non-Crystalline Solids, 2003. **331**(1-3): p. 48-57.
258. Dorofeev, V.V., et al., *High-purity TeO₂-WO₃-(La₂O₃, Bi₂O₃) glasses for fiber-optics*. Optical Materials, 2011. **33**(12): p. 1911-1915.
259. Daniel, M.F., et al., *Infrared and Raman study of WO₃ tungsten trioxides and WO₃, xH₂O tungsten trioxide hydrates*. Journal of Solid State Chemistry, 1987. **67**(2): p. 235-247.
260. Cozar, O., et al., *Raman spectroscopic study of some lead phosphate glasses with tungsten ions*. Journal of Non-Crystalline Solids, 2006. **352**(28-29): p. 3121-3125.
261. Wang, C.Y., Shen, Z.X., and Chowdari, B.V.R., *Raman studies of Ag₂O center dot WO₃ center dot TeO₂ ternary glasses*. Journal of Raman Spectroscopy, 1998. **29**(9): p. 819-823.
262. Himei, Y., et al., *Coordination change of Te atoms in binary tellurite glasses*. Journal of Non-Crystalline Solids, 1994. **177**(0): p. 164-169.
263. Goldstein, J., et al., *Scanning electron microscopy and X-ray microanalysis*. 3rd Edition ed. New York, USA: Springer. 2003
264. Wittke, J.H. *Microprobe-SEM*. 2008; Available from: www4.nau.edu/microanalysis/microprobe-SEM/instrumentation.html.

265. West, A.R., *Basic solid state chemistry*. 2nd Edition ed. New York: John Wiley & Sons Inc. 1999
266. Chakravarthy, S.S., Jordan, E.H., and Chiu, W.K.S., *Thin film and substrate cracking under the influence of externally applied loads*. Engineering Fracture Mechanics, 2005. **72**(8): p. 1286-1298.
267. Hu, J.J., et al., *Low-loss high-index-contrast planar waveguides with graded-index cladding layers*. Optics Express, 2007. **15**(22): p. 14566-14572.
268. Battaglia, C., et al. *A new approach to light scattering from nanotextured interfaces for silicon thin-film solar cells*. in *Optical Nanostructures for Photovoltaics*. Optical Society of America.
269. Price, P.B. and Bergström, L., *Enhanced rayleigh scattering as a signature of nanoscale defects in highly transparent solids*. Philosophical Magazine A, 1997. **75**(5): p. 1383 - 1390.
270. Bai, S.N. and Tseng, T.Y., *Effect of alumina doping on structural, electrical, and optical properties of sputtered ZnO thin films*. Thin Solid Films, 2006. **515**(3): p. 872-875.
271. Irannejad, M., et al., *A parametric study of Er³⁺-ions doped Phospho-tellurite glass thin films by pulsed laser deposition*. Optical Materials. **33**(2): p. 215-219.
272. Williams, D.B. and Carter, C.B., *Transmission electron microscopy-a textbook for materials science*. New York and London: Plenum Press. 2003
273. Reimer, L. and Kohl, H., *Transmission electron microscopy: physics of image formation*. 5th Edition ed. Munster, Germany: Springer Science+Business Media, LLC. 2008
274. Giannuzzi, L.A. and Stevie, F.A., *A review of focused ion beam milling techniques for TEM specimen preparation*. Micron, 1999. **30**(3): p. 197-204.
275. Cayron, C. *TEM study of interfacial reactions and precipitation mechanisms in Al₂O₃ short fiber or high volume fraction SiC particle reinforced Al-4Cu-1Mg-0.5 Ag squeeze-cast composites*: Ingénieur Civil diplômé de l'Ecole des Mines de Nancy originaire de Dijon (France), PRÉSENTÉE AU DÉPARTEMENT DES MATÉRIAUX. 2000
276. Ward, M.B. *Manganese based nanoparticles via inert gas condensation*: University of Leeds, Institute for Materials Research, School of processing, environment and materials engineering. 2008
277. Rusop, M., et al., *Effect of Helium gas on the deposition of diamond like carbon thin films by pulsed laser ablation*. International Journal of Modern Physics B, 2002. **16**(6-7): p. 871-875.
278. Irannejad, M., et al., *Active Glass Waveguide Amplifier on GaAs by UV Pulsed Laser Deposition and Femtosecond Laser Inscription* Laser Physics Letter, 2012. **19**(5): p. 329-339.
279. Dong, J., et al., *Dual-pumped tellurite fiber amplifier and tunable laser using Er³⁺/Ce³⁺ codoping scheme* Photonics Technology Letters, IEEE, 2011. **23**(11): p. 736-738.
280. Okoshi, M., Kuramatsu, M., and Narumi, I., *Pulsed laser deposition of SiO₂ thin films with dimethylpolysiloxane targets*. Jpn.J. Appl. Phys., 2002. **41**(3A): p. 1395-1399.
281. Kiessig, H., *Interferenz von röntgenstrahlen an dünnen schichten*. Annalen der Physik, 1931. **402**(7): p. 769-788.

282. Meyer, K., *Characterization of the structure of binary zinc ultraphosphate glasses by infrared and Raman spectroscopy*. Journal of Non-Crystalline Solids, 1997. **209**(3): p. 227-239.
283. Brow, R.K., et al., *The short-range structure of sodium ultraphosphate glasses*. Journal of Non-Crystalline Solids, 1994. **177**: p. 221-228.
284. Henderson, L.J. and Keller, T.M., *Synthesis and characterization of poly(carborane siloxane acetylene)*. Macromolecules, 1994. **27**(6): p. 1660-1661.
285. Ardelean, I. and Horea, C., *FTIR spectroscopic investigations of MnO-P₂O₅-TeO₂ glasses*. Journal of Optoelectronics and Advanced Materials, 2006. **8**(3): p. 1111-1113.
286. Favia, P., Caporiccio, G., and D'Agostino, R., *Plasma deposition of thin films from a fluorine-containing cyclosiloxane*. Journal of Polymer Science Part A: Polymer Chemistry, 1994. **32**(1): p. 121-130.
287. Vedeanu, N., et al., *IR and Raman investigation of x(CuO center dot V₂O₅)(1-x) [P₂O₅ center dot CaF₂] glass system*. Journal of Optoelectronics and Advanced Materials, 2006. **8**(1): p. 78-81.
288. Dayanand, C., et al., *Structural investigations of phosphate glasses: a detailed infrared study of the x(PbO)-(1-x) P₂O₅ vitreous system*. Journal of Materials Science, 1996. **31**(8): p. 1945-1967.
289. Su, K., et al. *Siloxane materials for optical application*. in *ICO20: Materials and Nanotechnologies*. 2005. Changchun, China: Proceeding.
290. Nandi, P., et al., *Femtosecond laser written channel waveguides in tellurite glass*. Opt. Express, 2006. **14**(25): p. 12145-12150.
291. Berneschi, S., et al., *Ion beam irradiated channel waveguides in Er³⁺-doped tellurite glass*. Applied Physics Letters, 2007. **90**(12): p. 121136-121136-3.
292. Fernandez, T.T., et al., *Active waveguides written by femtosecond laser irradiation in erbium-doped phospho-tellurite glass*. Opt. Express, 2008. **16**(19): p. 15198-15205.
293. Lanata, M., et al. *Sputtered tellurite glass thin films for planar optical devices*. in *Transparent Optical Networks, 2008. ICTON 2008. 10th Anniversary International Conference on*. 2008.
294. Pietralunga, S.M., et al., *High-contrast waveguides in sputtered pure TeO₂ glass thin films*. Optics Express, 2008. **16**(26): p. 21662-21670.
295. Madden, S.J. and Vu, K.T., *Very low loss reactively ion etched Tellurium Dioxide planar rib waveguides for linear and non-linear optics*. Opt. Express, 2009. **17**(20): p. 17645-17651.
296. Vu, K. and Madden, S., *Tellurium dioxide Erbium doped planar rib waveguide amplifiers with net gain and 2.8dB/cm internal gain*. Opt. Express, 2010. **18**(18): p. 19192-19200.
297. Hunsperger, R.G., *Integrated Optics*: Springer Science+Business Media. 2009
298. Hensler, D.H., et al., *Optical propagation in sheet and pattern generated films of Ta₂O₅*. Appl. Opt., 1971. **10**(5): p. 1037-1042.
299. Nolte, S., et al., *Polarization effects in ultrashort-pulse laser drilling*. Applied Physics A: Materials Science & Processing, 1999. **68**(5): p. 563-567.
300. Yang, D., et al., *Radiation and gain behaviors in Tm³⁺-doped aluminum germanate substrate glasses and thermal ion-exchanged waveguide*. J. Opt. Soc. Am. B, 2010. **27**(5): p. 990-996.